Interaction ondes/interfaces en contexte sismique

Nathalie Favretto-Cristini

UNIVERSITE DE LA MEDITERRANEE - AIX-MARSEILLE II

INSTITUT DE MECANIQUE DE MARSEILLE

Habilitation à Diriger des Recherches

Interaction ondes / interfaces en contexte sismique

Nathalie FAVRETTO-CRISTINI

soutenue publiquement le 21 avril 2011 devant le jury composé de

Rapporteurs :	Michel DIETRICH	-	Directeur de Recherche CNRS & IFP Energies Nouvelles, Paris
	Dimitri KOMATITSCH	-	Professeur, GET Université P. Sabatier, Toulouse
	Manell ZAKHARIA	-	Professeur, NURC, La Spezia (Italie)
Examinateurs :	José CARCIONE	-	Directeur de Recherche, INOGS Trieste (Italie)
	Cédric MAURY	-	Professeur, Ecole Centrale de Marseille
	Bjorn URSIN	-	Professeur Vista, NTNU (Norvège)

Remerciements

C'est avec enthousiasme que j'aborde l'écriture de cette page de remerciements. C'est l'occasion pour moi d'avoir une pensée pour toutes celles et tous ceux qui m'ont accompagnée sur mon chemin de vie professionnel, et parfois également sur mon chemin de vie personnel.

Je dois mon orientation scientifique vers les géosciences à trois personnes.

Tout d'abord à *Eric de Bazelaire*, que j'ai entendu pour la première fois en conférence à Marseille en 1994. Son exposé sur les méthodes sismiques à des fins d'exploration de réservoirs m'avait enthousiasmée à la fois par le fond scientifique et par le côté convivial et blagueur de l'orateur. J'avais eu l'impression d'écouter le fils spirituel du Professeur Tournesol et de Raymond Devos... Plus tard, alors que je n'étais pas géophysicienne, il m'a témoigné une confiance absolue en m'"adoptant" immédiatement pour travailler avec lui sur des anomalies observées sur certaines images sismiques : c'était le début des études sur la diffusion d'interface et de mon aventure à Pau... C'était surtout le début d'une formidable amitié et d'une tendre complicité. Passer une journée entière à travailler avec Eric donnait généralement mal à la tête pour deux jours, si on n'en avait pas l'habitude ! Deux mille idées à l'heure fusaient en tout sens et on devait s'accrocher aux branches (comme il disait) pour suivre son raisonnement qu'il énonçait de manière sous-échantillonnée, son cerveau fonctionnant bien plus vite que sa langue. Lors de ces journées, il me faisait partager son immense savoir avec énormément de passion, expliquant inlassablement certaines notions jusqu'à ce que je les maîtrise. Véritable puits de science à formation résolument pluridisciplinaire, il m'a formée et guidée avec beaucoup d'enthousiasme, de joie de vivre, de curiosité et d'humour ponctué de ses célèbres contrepèteries. Témoignant une confiance envers moi qui n'a jamais défailli. Et jusqu'à son dernier souffle, il m'a transmis avec beaucoup d'affection tout ce qu'un "père" scientifique peut transmettre à sa "fille"... Cet "héritage" va bien au-delà de la science et nos très nombreuses discussions sur la vie au sens large, et sur la mort, restent à jamais gravées... Deux jours avant sa disparition et sentant sa fin proche, il m'avait assuré qu'il serait toujours là près de moi, prêt à me donner des coups de pieds aux fesses si je baissais les bras... ou tout simplement pour me dire qu'il serait fier de moi... Il est bien là.

Je ne sais comment remercier *Michel Jean* pour son conseil ô combien visionnaire qui, au détour d'une conversation téléphonique (à l'époque où il était Président de la section 9 du Comité National), m'a définitivement aiguillée vers les géosciences. J'ai fait sa connaissance en revenant quelques années plus tard au LMA et j'ai découvert un Grand Monsieur, profondément humain et attachant.

Enfin, je remercie du fond du cœur *Jean-Paul Montagner* pour avoir cru en moi, pour m'avoir encouragée et soutenue dans les moments quelque peu difficiles.

J'ai eu la chance de pouvoir soutenir devant un jury incroyable.

Je remercie tout particulièrement les trois rapporteurs pour leur grand enthousiasme à jeter un regard critique et avisé sur le manuscrit et pour l'intérêt qu'ils ont toujours porté à mes travaux. Que *Michel Dietrich* et *Dimitri Komatitsch* soient vivement remerciés pour leurs encouragements tout au long de ces années. *Manell Zakharia* était déjà présent dans mon jury de thèse en 1997 ; depuis, il a toujours été d'un grand soutien et je le remercie vraiment du fond du cœur pour nos échanges passionnants (qu'ils soient scientifiques ou plus personnels) et pour avoir fait le déplacement d'Italie.

Je voudrais également remercier chaleureusement les trois examinateurs qui ont tout de suite accepté avec enthousiasme de faire partie du jury. Tout d'abord, *Cédric Maury* (le Président) avec qui je partage (outre quelques cours) la curiosité pour les choses nouvelles. Ensuite, *Bjorn Ursin* qui a eu la gentillesse de décaler d'une semaine la fin de son séjour à Marseille pour pouvoir assister à la soutenance. Sa venue au LMA a été décidée lors d'un repas dans un restaurant de Barcelone (merci Christian Deplanté !) et les six mois passés en sa compagnie ont été très enrichissants sur le plan scientifique. Tusen Takk pour ses conseils, sa gentillesse et ses encouragements. Enfin, *José Carcione* qui a eu l'amitié de faire directement le trajet Argentine-Marseille via Rome (sans rentrer chez lui !) pour venir m'écouter et me juger. Je me souviens de son séjour à Pau en 2004. J'étais terriblement impressionnée et timide face à ce "monstre sacré" de la propagation des ondes. Je me souviens de ses encouragements d'alors... J'ai découvert par la suite un homme formidablement humain et gentil, à l'humour fin, qui diffuse sans compter son savoir et ses conseils. Peut-être m'apprendra-t'il également un jour à danser le tango ?

J'ai une pensée émue et particulière pour *Paul Cristini*, qui est avant tout mon compagnon de cœur, et qui est aussi mon compagnon de "tête". Mon âme amie. Il a toujours été présent à mes côtés, m'encourageant, croyant en moi, même dans les heures les plus sombres. Je ne serais pas grand-chose sans lui... Sur le plan scientifique, nous avons partagé (et partageons toujours) de belles aventures où ses compétences, sa culture, sa curiosité intellectuelle et sa créativité ont la part belle. Sur le plan humain, que dire... si ce n'est que je l'aime profondément pour ce qu'il est... Un Très Grand Merci pour tout.

Je voudrais avoir également une pensée pour tous mes autres compagnons de route. *Wasiu Makindé* qui est devenu un ami sincère et précieux, après avoir été mon étudiant. *Bertrand Nivière* (Maître Yoda), un ami qui a une richesse d'âme incroyable et avec qui j'ai beaucoup appris, et avec qui j'apprends toujours beaucoup d'ailleurs. Pas seulement sur la géologie... *Grégoire Le Touzé* qui a été un post-doctorant avec qui j'ai eu vraiment un grand plaisir à travailler. *Daniel Broseta* qui a suggéré ma participation dans le projet ANR EMSAPCO2 et qui m'a initiée aux problèmes thermodynamiques. *Fabio Cavallini*, un de mes coéquipiers travaillant sur les ondes de surface, qui avec son humour m'a déridée plus d'une fois dans les moments de doute. A *Didier Rappin* et *Christian Deplanté*, un Grand Merci pour ce moment d'intensité rare (professionnellement et émotionnellement parlant) partagé à Barcelone juste quelques heures avant le début du workshop...

Je voudrais remercier du fond du cœur *Frédéric Lebon* qui a lu la première version du manuscrit et qui a assisté à la première répétition de la soutenance. Je voudrais le remercier non seulement pour sa présence à mes côtés, mais aussi et surtout pour son soutien tellement précieux et son amitié. Je n'oublie pas bien sûr son humour irrésistible... Les mots sont forcément réducteurs et traduisent mal tout ce que l'on a dans le cœur... Un Grand Grand Merci...

Je n'oublie pas mes acolytes du laboratoire "Modélisation et Imagerie en Géosciences de Pau", du "Laboratoire de Mathématiques Appliquées" ou du "Laboratoire des Fluides Complexes et de leurs Réservoirs" de Pau. En particulier, *Hélène Barucq*, *Pascal Bruel* (avec qui on formait la bande CNRS), *Pascale et Guy Sénéchal* (qui m'ont beaucoup aidée dans les premiers temps difficiles de Pau), *Jean-Baptiste Daban* (que de bons moments passés en sa compagnie !), *Charles Revaux*...

Une pensée pour mes amis d'Elf/Total, en particulier *Béatrice Dérès* (on se connait depuis tellement longtemps, n'est-ce pas ? Un Grand Merci pour son amitié sincère et indéfectible...

et ses soins constants) et *Thierry Castex*. Merci aux personnes qui ont cru en moi et qui m'ont soutenue : *Jean-Marc Komatitsch*, *Claude Jablon*, *Philippe Jullien* et *Jérôme Guilbot*.

Depuis mon retour au LMA à Marseille, j'ai retrouvé avec bonheur certains collègues, et j'en ai découvert d'autres avec grand plaisir. Merci à tous ceux qui m'ont encouragée et soutenue. Je voudrais remercier tout particulièrement *l'équipe "Modélisation en Mécanique du Contact"* (et ses satellites), équipe adoptive pour le café et la bonne humeur du matin. Un Très Grand Merci également à *Michèle Laurent*, *Emmanuelle Paniagua*, *Alain Rimeymeille* et *Annie Fornacciari* pour leur aide précieuse dans la logistique liée à la HDR, et surtout pour leur soutien amical, toujours teinté de bonne humeur et de sourires.

J'ai eu la grande chance de rencontrer, de discuter et/ou de côtoyer des géophysiciens de renom. Parmi eux, je voudrais remercier tout particulièrement *J.P. Lindsey* pour son intérêt et son soutien pour nos travaux sur la définition du réflecteur sismique 3D. Un Grand Merci également à *Peter Hubral* pour ses encouragements (cela va bien au-delà de la science...). Merci au regretté *Gerard Hermann* et à *Norman Bleistein* (pour ses cours passionnants et son humanité révélée lors d'un déjeuner qui reste dans ma mémoire) pour leurs conseils et leurs encouragements.

J'ai de nombreux amis (pas forcément scientifiques) qui m'ont entourée tout au long de ces années et qui m'ont apportée joie de vivre et bouffées d'air pur. Outre *Fafa*, je voudrais remercier mes amis de Pau, en particulier *Nath et Jérôme* (présents à Marseille les jours précédents la soutenance pour m'encourager), *Cécé* (que de fous rires !), *Béatrice et François* et *Grégory et Elisabeth* (pour leur aide précieuse...), *Robert et Marido*, *Bernard et Françoise*, *Jean-Pierre et Claudie*, *Laurent et Nadège*, *Régis et Isabelle*... et mes amis de Marseille, tout particulièrement *Pierre-Olivier et Béatrice* (pour leur amitié sincère et leur soutien depuis notre retour à Marseille), *Marie et Bruno*, *Marianne et Flavien*, *Soso et Marc*...

Je termine enfin en ayant une pensée pour *mon père et ma sœur* (qui ne sont plus là), pour *ma mère et mon frère*.

A *Paul*, à *Pierre* (qui a fêté ses 16 ans le jour de la soutenance), à *Rémi* (qui a supporté stoïquement la soutenance et les questions en anglais, sans comprendre un traître mot de ce qui se disait !), et à ma petite princesse *Corentine*, je leur redis toute mon affection et mon amour, en les remerciant d'être là, tout près de moi. Je me nourris de votre amour...

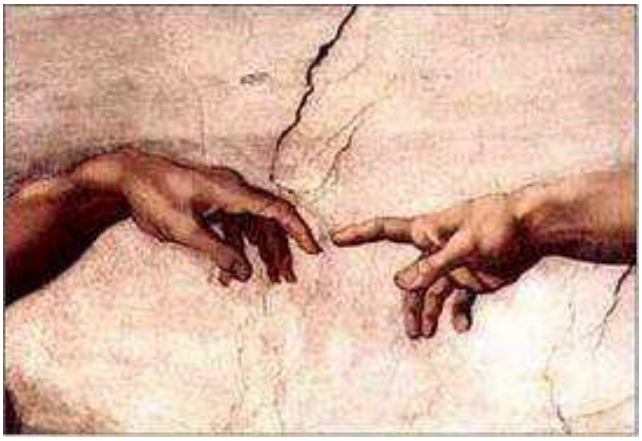

Représentation partielle du Tableau de Michelangelo "La Creazione di Adamo".

à Eric...

Résumé

Certains besoins économiques, sociétaux ou environnementaux nécessitent une caractérisation approfondie des structures géologiques du sous-sol. Parmi les différentes méthodes géophysiques, la sismique est sans doute celle qui est le plus souvent privilégiée. Imager et caractériser le sous-sol à partir de données réelles acquises sur le terrain est cependant un problème inverse généralement difficile à résoudre. Il l'est d'autant plus si le problème direct associé n'a pas été au préalable "maîtrisé" *a minima*, c'est-à-dire si l'on ne dispose pas d'une modélisation réaliste de la propagation des ondes. Pour cela, il semble essentiel, pour modéliser les données sismiques synthétiques afin de les rendre comparables aux données réelles, d'identifier et de comprendre en premier lieu les facteurs géologiques et/ou physiques de premier ordre qui influencent la propagation des ondes dans une configuration donnée. Cela suppose qu'on prenne en compte à la fois les lois de comportement des couches géologiques traversées et les lois de contact entre ces couches, mais aussi les limitations introduites par le système d'observation constitué par les ondes sismiques.

Ce mémoire décrit les travaux que j'ai menés essentiellement sur la compréhension et la modélisation de l'interaction ondes/interfaces en me basant sur des approches pluridisciplinaires. Outre l'aspect fondamental d'une meilleure connaissance des mécanismes physiques sous-jacents à la propagation des ondes dans des milieux complexes (*e.g.*, les résolutions sismiques verticale et latérale, la définition du réflecteur sismique 3D, la diffusion d'interface et l'influence de l'anisotropie sur les ondes de surface), des aspects plus appliqués, dédiés notamment à l'exploration de gisements énergétiques ou à la surveillance de réservoirs géologiques de stockage du CO2, ont été également développés.

Mots-clés

Onde sismique, onde réfléchie, onde diffractée, onde de surface, interface, réflecteur, zone de Fresnel, résolution, diffusion d'interface, anisotropie, modélisation, caractérisation, stockage géologique du CO2.

Interaction between waves and interfaces in seismics

Abstract

Many major challenges of the twenty-first century in the economic, social, or environmental fields, require a careful characterization of the geological structures of the Earth. Seismics is probably the most widely used technique to explore the environment at large scales. Imaging and characterizing the subsurface from real seismic data however is a difficult task, and the difficulty increases since the wave propagation in complex and heterogeneous natural systems is poorly understood. It is therefore essential to identify the geological features, which significantly influence the wave propagation in a given configuration, and to understand their interaction with the seismic waves. To model the wave characteristics one has to account for the complexity of natural environments through which the waves propagate, but also for the contact laws between the geological media, and for the limitations introduced by the seismic waves themselves.

This manuscript summarizes the work I have developed essentially on the understanding and on the modeling of the wave/interface interaction using multidisciplinary approaches. Besides basic knowledge of the physical mechanisms underlying the wave propagation in complex media (*e.g.*, the vertical and the lateral seismic resolutions, the definition of the 3D seismic reflector, the interface scattering, and the influence of the anisotropy on surface waves), applied works dedicated to the oil and gas exploration or to the monitoring of geological storage of CO2 have also been developed.

Keywords

Seismic wave, reflected wave, diffracted wave, surface wave, interface, reflector, Fresnel zone, resolution, interface scattering, anisotropy, modeling, characterization, geological storage of CO2.

Liste des sigles utilisés

2D/3D : deux dimensions / trois dimensions
ANR : Agence Nationale de la Recherche
ASA : Angular Spectrum Approach
AVA/AVO : Amplitude-versus-Angle / Amplitude-versus-Offset
B : Bruit
BENCHIE : BENCHmarks expérimentaux de laboratoire en environnements complexes à des fins de validation de codes de propagation d'ondes et d'ImageriE
BF : Basses Fréquences
BP : Bande Passante
BRGM : Bureau de Recherches Géologiques et Minières
CGG Véritas : Compagnie Générale de Géophysique Véritas
CND : Contrôle Non Destructif
CNRS : Centre National de la Recherche Scientifique
CO2 : dioxyde de carbone
EMSAPCO2 (projet ANR) : Développement des méthodes ElectroMagnétiques et Sismiques Actives et Passives pour la surveillance des réservoirs de stockage du CO2
EOR : Enhanced Oil Recovery (ou récupération assistée de pétrole)
FV : Fresnel Volume (ou Volume de Fresnel)
GPR : Ground Penetrating Radar (ou Radar géologique)
HF : Hautes Fréquences
LFC-R : Laboratoire des Fluides Complexes et leurs Réservoirs
LMA : Laboratoire de Mécanique et d'Acoustique
MIGP : Laboratoire de Modélisation et Imagerie en Géosciences de Pau
OASES (code) : Ocean Acoustic and Seismic Exploration Synthesis (code)
PSM : Pseudo-Spectral Method (ou méthode pseudo-spectrale Fourier-Chebyshev)
S : Signal
SEM : Spectral Element Method (ou méthodes d'éléments finis spectraux)
SPECFEM (code) : Spectral Finite Element Method (code)
WZ : Weathered Zone (ou zone altérée de surface)
ZFI ou IFZ : Zone de Fresnel à l'Interface ou Interface Fresnel Zone

Avant-propos

Après avoir soutenu une thèse en 1997 en Sciences pour l'Ingénieur, j'ai découvert les Sciences de la Terre en travaillant durant onze années au sein d'un laboratoire de Géosciences. L'immersion totale dans un univers nouveau a été très enrichissant à la fois sur les plans personnel et professionnel. J'ai toujours cherché à réinvestir les connaissances issues de ma formation initiale quand cela était possible et ainsi à combiner les deux disciplines pour tenter de résoudre certains problèmes. Ceci m'a conduit à emprunter des chemins de traverse qui m'ont parfois éloignée de la route... au risque de me perdre. Mais je demeure persuadée que les avancées significatives, surtout quand elles se trouvent à la marge, ne peuvent être réalisées qu'en osant et en confrontant les disciplines.

Ce mémoire récapitule l'essentiel de ces quatorze années de parcours scientifique pluridisciplinaire. Cependant j'ai choisi de ne pas décrire, par exemple, des travaux qui n'ont pas complètement abouti, soit parce que les pistes empruntées se sont au final avérées stériles, soit par abandon prématuré de la thématique suite aux discussions avec un des partenaires impliqués dans le Laboratoire de Modélisation et Imagerie en Géosciences de Pau. De la même façon, je n'ai pas jugé utile de décrire en détails les travaux pour lesquels mon implication a été de moindre importance.

Les travaux de recherche se mènent rarement seul ; ils sont souvent le fruit de collaborations fructueuses entre scientifiques. Aussi, au début de chaque chapitre, je mentionnerai les personnes avec lesquelles j'ai partagé ces aventures exploratoires. J'indiquerai également les publications et les principales communications associées à nos travaux qui sont toutes récapitulées en Annexe C. Le lecteur trouvera en Annexe D une copie des publications les plus significatives.

Enfin, pour conclure cet avant-propos, je citerai **Pierre Joliot (2001)** *La Recherche passionnément*, Editions Odile Jacob Sciences.

———————

"Comme dans toute forme d'art, la peinture par exemple, il existe un continuum entre l'oeuvre d'un Rembrandt et celle, également respectable, d'un peintre du dimanche. La beauté de notre métier réside dans le fait que les progrès de la science ne reposent pas uniquement sur les découvertes de quelques rares génies, mais également sur l'activité créatrice plus modeste pratiquée au quotidien de très nombreux chercheurs. [...] Une démarche créative suppose de privilégier, au moins transitoirement, une approche intuitive par rapport à une approche logique, rarement capable de générer des idées nouvelles. Quels que soient les domaines de la Science, la démarche logique doit intervenir a posteriori pour valider ou rejeter une idée originale. [...] L'activité créatrice doit conduire à une prise de risques permanente. Elle est indissociable du droit à l'échec et à l'erreur."

———————

Table des matières

Chapitre 1

Introduction générale

Les ondes sont largement utilisées dans différentes communautés (acoustique, CND, géophysique) pour inspecter de manière non invasive les milieux et matériaux, et plus particulièrement pour caractériser les structures et détecter les défauts présents. En géophysique, elles sont utilisées pour explorer la Terre, de la lithosphère (sismiques terrestre et marine) jusqu'au noyau (sismologie) à des fins de caractérisation et d'exploitation du sous-sol et de ses ressources naturelles, et plus globalement pour une meilleure compréhension de sa dynamique. Les ondes sismiques permettent ainsi d'étudier différentes problématiques d'intérêt majeur pour la société, liées pour certaines au domaine de l'énergie et de l'environnement : détection, caractérisation et suivi d'exploitation des réservoirs d'hydrocarbures et des ressources en eau, des réservoirs de stockage du CO2... Néanmoins, bien qu'elles soient un puissant outil d'investigation des milieux, les ondes ne constituent pas le socle d'une méthode absolue et toute puissante. Il faut garder à l'esprit que ce que nous observons au travers du filtre "ondes" est UNE représentation, mais en aucune manière l'unique représentation de la réalité (par analogie, *cf* Figure 1.1). En effet, la propagation des ondes est essentiellement influencée et limitée par leur façon d'interagir avec les milieux (leurs propriétés physiques et géométriques, et les hétérogénéités qui y sont présentes), qui elle-même est influencée par la mise en oeuvre de cette propagation sur le terrain (réponse de la source & des capteurs...). C'est la raison pour laquelle la confrontation des résultats issus de la propagation des ondes sismiques avec d'autres mesures issues de techniques complémentaires (GPR, électrique ...) est souvent recherchée en association avec un apport d'information géologique.

Figure 1.1 – *Représentation du Tableau de René Magritte "La Trahison des Images".*

En sismique, l'objectif est souvent d'identifier, d'imager et de caractériser les structures géologiques du sous-sol à partir de données réelles acquises sur le terrain. Ce problème inverse est généralement difficile à résoudre à cause de nombreuses incertitudes, dont certaines inhérentes aux hypothèses formulées a priori sur les propriétés physiques et géométriques du sous-sol et

sur les moyens de mesure utilisés. Il l'est d'autant plus si le problème direct associé n'a pas été au préalable "maîtrisé" *a minima*. Les algorithmes de modélisation de la propagation des ondes classiquement utilisés en sismique sont d'ordre et de complexité différents (*e.g.*, tracé de rayons, modélisation de Kirchhoff, ...), mais n'en demeurent pas moins que des approximations plus ou moins "réalistes" de la complexité de la propagation réelle. En effet, chaque type de modélisation a des limitations, soit par des simplifications parfois abusives de la propagation, soit par une description trop grossière de la réalité géologique, et de ce fait elles ne cherchent à représenter qu'un aspect de la propagation réelle des ondes. Ce fait est d'autant plus vrai que l'environnement géologique est complexe (*e.g.*, forts contrastes de vitesses, structures compliquées, topographie chahutée, plan de chevauchement...). Par ailleurs, les contraintes de temps de calcul, plus prononcées encore dans un contexte industriel, obligent à limiter la complexité des modèles afin de pouvoir conserver le processus itératif "modélisation/comparaison avec les données réelles/modification du modèle" pour une convergence plus rapide vers une représentation "réaliste" du sous-sol. Les questions que l'on peut alors se poser sont les suivantes : Qu'entend-on au juste par "réaliste" ? Comment modéliser "réaliste" ? Il semble qu'une représentation "réaliste" du sous-sol sous-entende une représentation géophysique/géologique cohérente. Cependant, le contraire est-il vérifié ? Par ailleurs, pour modéliser "réaliste", et donc rendre les données sismiques synthétiques comparables aux données réelles, il semble essentiel d'identifier et de comprendre en premier lieu les facteurs géologiques et/ou physiques de premier ordre qui influencent la propagation des ondes dans une configuration donnée. Cela suppose qu'on prenne en compte à la fois les lois de comportement des couches géologiques traversées et les lois de contact entre ces couches, mais aussi les limitations introduites par le système de "mesure" sismique (ce qui n'est pas toujours le cas).

Depuis quelques années, mon travail de recherche s'inscrit dans cette orientation. Il est essentiellement centré sur le problème de caractérisation des milieux géologiques, le but étant d'obtenir une meilleure estimation des propriétés de la sub-surface. La plupart des développements & applications concernent de près ou de loin le domaine pétrolier, de par l'historique du Laboratoire de Modélisation et Imagerie en Géosciences de Pau (MIGP, unité mixte de recherche tripartite Université de Pau/CNRS/Elf Exploration Production (puis TOTAL)), mais pas de manière exclusive. Les questions que je me suis posées jusqu'à présent sont multiples et toutes liées à l'aspect fondamental de la propagation des ondes, et plus particulièrement à celui de l'interaction ondes/interfaces. Par exemple, comment l'onde interagit avec une interface dans le sous-sol et comment l'isole-t'elle parmi le reste ? Comment l'onde, avec ses propres caractéristiques, perçoit-elle le sous-sol, *i.e.* ses hétérogénéités et les éléments géologiques qui le composent ? Qu'est-ce qu'un réflecteur sismique ? En contexte de sismique-réflexion, comment ce réflecteur influence-t'il le champ d'onde capté par les récepteurs en surface (en particulier les amplitudes), et par voie de conséquence l'estimation des propriétés des milieux ? Les "anomalies" ou les atténuations d'amplitude observées peuvent-elles toujours être attribuées à de l'absorption ? Comment le comportement mécanique intrinsèque des milieux et celui des interfaces modifient la propagation des ondes de volume et des ondes de surface et d'interface ?...

Pour tenter d'apporter un éclairage original sur ces questions fondamentales, je me suis appuyée sur des approches pluridisciplinaires (optique, mécanique, acoustique, CND, géophysique, traitement du signal et théorie de l'information) en tenant compte, autant que faire se peut, des limitations introduites par le système de "mesure" sismique. Outre l'aspect fondamental d'une meilleure connaissance des mécanismes physiques sous-jacents à la propagation des ondes dans des milieux complexes, des aspects plus appliqués, dédiés notamment à l'exploration de gisements énergétiques ou à la surveillance de réservoirs géologiques de stockage du CO2, ont

été également développés. Jusqu'à présent, mes travaux se sont donc principalement articulés autour de l'interaction ondes/interfaces déclinée sous trois thèmes principaux et une application spécifique.

Dans le thème "Réflecteur sismique et réflectivité équivalente" décrit dans le Chapitre 2, l'objectif fondamental est d'obtenir une meilleure compréhension de la propagation des ondes au voisinage des interfaces en tenant compte des limitations introduites par le système de "mesure" sismique, afin de proposer des améliorations aux techniques dites d'AVA ("Amplitude-versus-Angle ") wide-angle utilisées pour la caractérisation du sous-sol. Afin de comprendre comment une onde "isole" une interface sur laquelle elle va se réfléchir, nous avons revisité le concept de résolution verticale de la sismique. Puis à partir des concepts de volume de Fresnel et des lois de transmission et de réflexion des courbures de fronts d'onde, nous avons identifié pour chaque fréquence de la bande passante de la source sismique un volume spatial, autour de l'interface, qui affecte réellement la réponse de l'interface et donc l'amplitude du champ d'onde réfléchi. Le volume spatial ainsi défini représente un volume spatial minimal d'intégration et d'homogénéisation des propriétés autour de l'interface. Cela signifie que seules les hétérogénéités présentes dans ce volume contribuent physiquement à la réflexion des ondes et conditionnent (en partie) le comportement des formes d'onde enregistrées aux capteurs. Ne pas en tenir compte conduit systématiquement à des erreurs commises sur l'estimation des propriétés physiques des milieux naturels, et donc à une connaissance biaisée de notre environnement.

Les propriétés physiques et géométriques des milieux géologiques influencent significativement les ondes sismiques qui les traversent. Or, la sismique réflexion se focalise principalement sur les contrastes d'impédance pour imager les réflecteurs et illustrer la structure du sous-sol, en admettant souvent que les interfaces sont latéralement homogènes dans leurs propriétés géométriques et/ou physiques. De ce fait, les altérations des formes d'onde sont attribuées préférentiellement au contraste d'impédance aux interfaces et à la présence d'hétérogénéités dans le volume. Cependant, dans le cas où les interfaces ont des propriétés latéralement hétérogènes, l'hypothèse habituelle conduit à des estimations biaisées des paramètres du sous-sol. Nous nous sommes plus particulièrement intéressés aux effets, sur les données sismiques, du phénomène de diffusion d'interface (*i.e.*, diffusion des ondes par des interfaces latéralement hétérogènes de type surfaces d'érosion ou zones de décollements) qui est un processus physique généralement négligé dans les modélisations. Le Chapitre 3 lui est entièrement consacré.

Par définition, les ondes de surface sont des combinaisons d'ondes de volume (ondes de compression et de cisaillement qui se propagent à la surface d'un milieu. Par conséquent, elles sont très sensibles aux variations de l'état de la surface. Si ces ondes sont bien connues pour des milieux homogènes, élastiques et isotropes, il est plus difficile de les cerner en contexte anisotrope. En effet, même pour des symétries élevées (cubique ou hexagonale) où la physique de la propagation a été étudiée sur la base de méthodes analytiques et semi-analytiques, certaines controverses concernant les ondes de surface persistent et nécessitent une clarification des résultats de recherche publiés et de la terminologie utilisée. Par ailleurs, nous avons utilisé deux méthodes numériques "full-wave" 3D pour résoudre le problème de propagation des ondes de surface sans aucune approximation sur le type de symétrie des milieux anisotropes et sur l'orientation de la surface libre. Tout ce travail est résumé dans le Chapitre 4.

Enfin, le Chapitre 5 est consacré à la surveillance du stockage géologique du CO2 et au travail que nous avons réalisé dans le cadre du projet ANR EMSAPCO2 ("Développement des méthodes Electro-Magnétiques et Sismique Active et Passive pour la surveillance des réservoirs de stockage du CO2"). Nous avons plus particulièrement étudié la pertinence d'utiliser les réflexions non spéculaires des ondes sismiques pour détecter la présence de poches de CO2 qui aurait migré

à travers le sous-sol vers la surface et qui serait piégé au niveau des interfaces sous la roche couverture.

Je terminerai ce mémoire par quelques perspectives (non exhaustives) quant à l'évolution de mes recherches.

Chapitre 2

Qu'est-ce qu'un réflecteur sismique ?

Collaborations

E. de Bazelaire *(ancien Expert International Elf Exploration Production, puis TOTAL ; décédé le 28/06/2007)*
P. Cristini *(Chargé de Recherche CNRS, Laboratoire de Mécanique et d'Acoustique)*
C. Deplanté *(Ingénieur TOTAL)*
G. Le Touzé *(Post-doctorant, Laboratoire de Mécanique et d'Acoustique, 01/09/2008 - 31/08/2010)*
B. Nivière *(Maître de Conférences, Université de Pau et des Pays de l'Adour, Laboratoire des Fluides Complexes et leurs Réservoirs)*
D. Rappin *(Ingénieur TOTAL)*

Publications associées

cf Annexe C : [2], [3], [4], [12]
Une copie des articles [2], [4] et [12] a été placée en Annexe D.

Communications associées

cf Annexe C : [14], [16], [19], [20], [21], [24], [25]

———————

2.1 Introduction

La question posée dans le titre du chapitre est à la fois simple et très complexe, et la réponse est loin d'être triviale *a priori*. Cependant, si nous nous hasardons à fournir des éléments de réponse, ceux-ci vont être généralement fortement influencés (du moins dans un premier temps) par notre "métier" (géologue, géophysicien, mathématicien...). Par exemple, le mathématicien définira le réflecteur sismique comme une surface à courbure nulle (ou non) qui est le lieu d'une discontinuité des propriétés des milieux. Pour un géophysicien, ce sera une "surface" sur laquelle se réfléchissent les ondes du fait de la présence d'une rupture d'impédance entre les milieux. Ces définitions sont souvent incomplètes car elles font abstraction du système de "mesure" sismique et de ses limitations, et donc des caractéristiques intrinsèques de l'onde. Ces caractéristiques vont néanmoins fortement conditionner l'interaction "physique" de l'onde avec le milieu géologique traversé.

L'objectif final de notre étude était d'obtenir une meilleure compréhension de la propagation des ondes au voisinage des interfaces, afin de proposer le cas échéant des améliorations aux

techniques dites d'AVA [1] (*i.e.*, Amplitude-versus-Angle) utilisées pour la caractérisation du sous-sol [Castagna, 1993, Foster *et al.*, 2010]. Ce problème nous a renvoyés tout d'abord vers des considérations plus fondamentales, par exemple les résolutions verticale et latérale de la sismique, mais abordées sous l'aspect "amplitude" et pas uniquement sous l'aspect "temps de trajet", avant de proposer par la suite une définition originale du réflecteur sismique 3D. Comme nous allons le voir, cette nouvelle définition a un impact non négligeable sur les problèmes direct (modélisation de l'AVA) et inverse (estimation des propriétés des milieux).

2.2 Résolution verticale et Résolution latérale

Tout système de mesure (*e.g.*, l'oeil, le microscope...) possède des limites de résolution et donne par conséquent seulement une version "filtrée" de la réalité. Les ondes sismiques perçoivent la Terre à travers des "verres épais" selon le point de vue des géologues. Une bonne compréhension des limites de résolution de la sismique est nécessaire pour permettre, entre autres, de lever les ambiguïtés de l'interprétation géologique. Améliorer la résolution est donc un challenge important pour "voir" des unités stratigraphiques plus minces, des détails plus petits ou des changements latéraux dans les propriétés des roches. Ce sujet, toujours d'actualité, a fait jusqu'à présent l'objet de nombreuses publications. Malheureusement, les hypothèses initiales sous-jacentes aux différentes techniques développées ont souvent été oubliées au fil des années, ce qui a faussé certaines interprétations. Il nous a alors semblé intéressant, dans le cadre d'un tutorial invité (cf Annexe C [14]) présenté au workshop EAGE/SEG "Frequency attenuation and resolution of seismic data" à Barcelone en 2009, de repositionner ces hypothèses pour clarifier certaines "croyances" et dissiper certains malentendus.

Rappelons tout d'abord que la détection d'un évènement est avant tout un problème de rapport Signal (S)-sur-Bruit (B). D'après la Théorie du Signal, le signal est un évènement corrélé de trace en trace (*e.g.*, réflexions primaires, multiples...), le bruit (généralement aléatoire) étant tout le reste. Cependant, en traitement du signal sismique, tout signal indésirable (*e.g.*, multiples, ground roll...) est traité comme du bruit. La détection d'un signal avec un bon rapport S/B est chose aisée ; celle d'un signal faible reste possible si le signal source est connu. Quel que soit le rapport S/B, un évènement isolé est détecté s'il se trouve 20% au-dessus du seuil de bruit statistique. Mais un évènement qui est détectable peut, ou ne peut pas, être résolu.

La séparabilité qualitative (ou résolution) est la capacité à distinguer des éléments distincts proches l'un de l'autre. La séparabilité quantitative est la réponse à la question "Avec quelle précision peut-on déterminer la position de ces deux éléments adjacents ?". En sismique, le terme "résolution" fait référence aux problèmes de séparabilité qualitative uniquement, problèmes résolus selon différents critères dont les hypothèses ne sont pas toujours clairement définies. La résolution sismique est généralement liée à deux directions : la résolution verticale (en temps ou en profondeur) est la capacité à distinguer deux évènements sismiques proches correspondant

1. Les courbes AVA décrivent la variation, en fonction de l'angle d'incidence, de l'amplitude des ondes (réfléchies ou transmises) normalisée par l'amplitude de l'onde incidente. Elles représentent donc tout simplement les coefficients de réflexion ou de transmission des ondes. Les courbes AVO (*i.e.*, Amplitude-versus-Offset) décrivent la variation, en fonction de l'offset (ou distance entre la source et le récepteur), de l'amplitude des ondes (réfléchies ou transmises) normalisée par l'amplitude de l'onde incidente. Il est à noter que le passage de l'offset (donnée pouvant être parfaitement connue) à l'angle d'incidence nécessite de connaître au préalable la profondeur, par rapport au plan source-récepteur, de l'interface sur laquelle se réfléchit l'onde. Cette conversion offset-angle conduit inévitablement à des imprécisions (de quelques degrés) commises sur l'estimation de l'angle d'incidence. Par ailleurs, un échantillonnage régulier de l'offset (appliqué lors des acquisitions) ne conduit pas à un échantillonnage régulier de l'angle d'incidence.

à différentes profondeurs, tandis que la résolution latérale (de trace en trace) est la capacité à distinguer deux structures latéralement proches comme deux évènements adjacents distincts. Les objectifs géologiques sont de définir d'une part l'épaisseur des unités stratigraphiques, et d'autre part la taille surfacique des structures.

Il est fréquemment admis en sismique que la longueur d'onde limite le pouvoir de résolution et que le facteur clé pour améliorer la résolution est la fréquence [2] [Sheriff, 1977]. D'après le modèle de Widess [Widess, 1973], on définit la limite de résolution comme étant d'environ un quart de longueur d'onde dominante du signal [Sheriff, 1997], les hypothèses sous-jacentes étant que seul le lobe primaire est pris en compte et que les signaux à séparer ont la même amplitude [3]. Toutefois, il a été constaté que la résolution verticale pouvait être améliorée *à la fois* par des hautes fréquences (HF) et une large bande passante (BP) du signal [Kallweit et Wood, 1982]. Ceci est tout à fait vrai pour les Ricker, très largement utilisés en modélisation ou en traitement des signaux sismiques et qui ont la particularité intrinsèque d'établir une relation linéaire entre la fréquence centrale et la BP du signal. Mais quid des signaux autres que les Ricker ?

En traitement du signal radar et sonar, le principal outil pour définir la résolution est la fonction d'ambiguïté χ [de Coulon, 2000, Levanon et Mozeson, 2004]

$$\chi(\tau,\nu) = \int_{-\infty}^{+\infty} \tilde{r}^*(t)\ \tilde{r}(t+\tau)\ \exp(j\,2\pi\,\nu t)\ dt$$

où $\tilde{r}(t)$ est l'enveloppe complexe du signal analytique. Sa signification est que si deux cibles dont les échos, d'intensité comparable, diffèrent d'un retard τ et d'un décalage Doppler ν, elles ne peuvent pas être distinguées si $|\ \chi(\tau,\nu)\ |^2 = |\ \chi(0,0)\ |^2$ et difficiles à distinguer si $|\ \chi(\tau,\nu)\ |^2 \approx |\ \chi(0,0)\ |^2$. Hormis pour les streamers en sismique marine, il n'y a généralement pas d'effet Doppler. Aussi, en considérant $\nu = 0$, on obtient la fonction d'autocorrélation $R(\tau)$ de l'enveloppe complexe du signal analytique :

$$\chi(\tau,0) = \int_{-\infty}^{+\infty} \tilde{r}^*(t)\ \tilde{r}(t+\tau)\ dt = R(\tau)$$

qui doit se rapprocher le plus possible d'une impulsion de Dirac pour une bonne résolution de l'estimation de la distance entre les cibles, c'est-à-dire une large BP. Les Figures 2.1 et 2.2 montrent clairement que le paramètre clé pour la séparation des enveloppes de deux évènements sismiques est bien la BP du signal, et non la fréquence centrale. Plus la BP est large, meilleure est la résolution [Revaux, 2005]. En conséquence, il est équivalent d'étendre le spectre vers les basses fréquences (BF) que de l'étendre vers les HF pour améliorer la séparabilité des évènements [4]. La fréquence centrale indique seulement la quantité de BF qu'il est possible d'inclure dans le signal [5]. A noter qu'une des difficultés majeures pour la réalisation d'une acquisition large bande en sismique terrestre est assurément la présence de terrains altérés d'épaisseur variable, constitués de matériaux hétérogènes, non consolidés et partiellement saturés en fluide (zone

2. Nous verrons plus loin que cette erreur de jugement provient du fait qu'en sismique on utilise souvent des Ricker qui ont la particularité de relier linéairement la fréquence à la bande passante.

3. Quid si les signaux ont des amplitudes différentes ? Le critère de Rayleigh est alors difficilement applicable. Il faut alors intégrer dans l'étude les lobes secondaires.

4. A noter que lorsqu'on enrichit la BP par des HF, on risque généralement d'augmenter dans le même temps le bruit, ce qui va diminuer du coup le rapport S/B et donc la détection des évènements. On a tout intérêt à préserver le rapport S/B [Rappin *et al.*, 2009b].

5. Enrichir de quelques hertz en BF la BP ne change pas fondamentalement la fréquence dominante du signal. Par contre, cela augmente considérablement le nombre des octaves utiles et cela conduit à une meilleure résolution. [Kallweit et Wood, 1982]

vadose) qui atténuent les HF via différents mécanismes (atténuation intrinsèque, diffusion, ...) (*cf.* Chapitres 3 et 4). D'autres causes (*e.g.*, les interférences destructives...) réduisent également la BP, induisant par là-même une baisse de la résolution. Après acquisition des signaux, le traitement sismique essaie de compenser cet effet soit en identifiant la cause (tâche ardue !) puis en modélisant ses effets avant de corriger les données, soit en travaillant en aveugle (blind deconvolution ...). Une autre possibilité intéressante a été récemment proposée : fusionner deux acquisitions avec des BP différentes [Deplanté, 2009]. Notons enfin qu'il est difficile d'émettre efficacement des fréquences de quelques Hertz : même si les géophones conventionnels peuvent enregistrer des signaux de 4 Hz, il faut des vibreurs spéciaux pour émettre ces basses fréquences sans distortion.

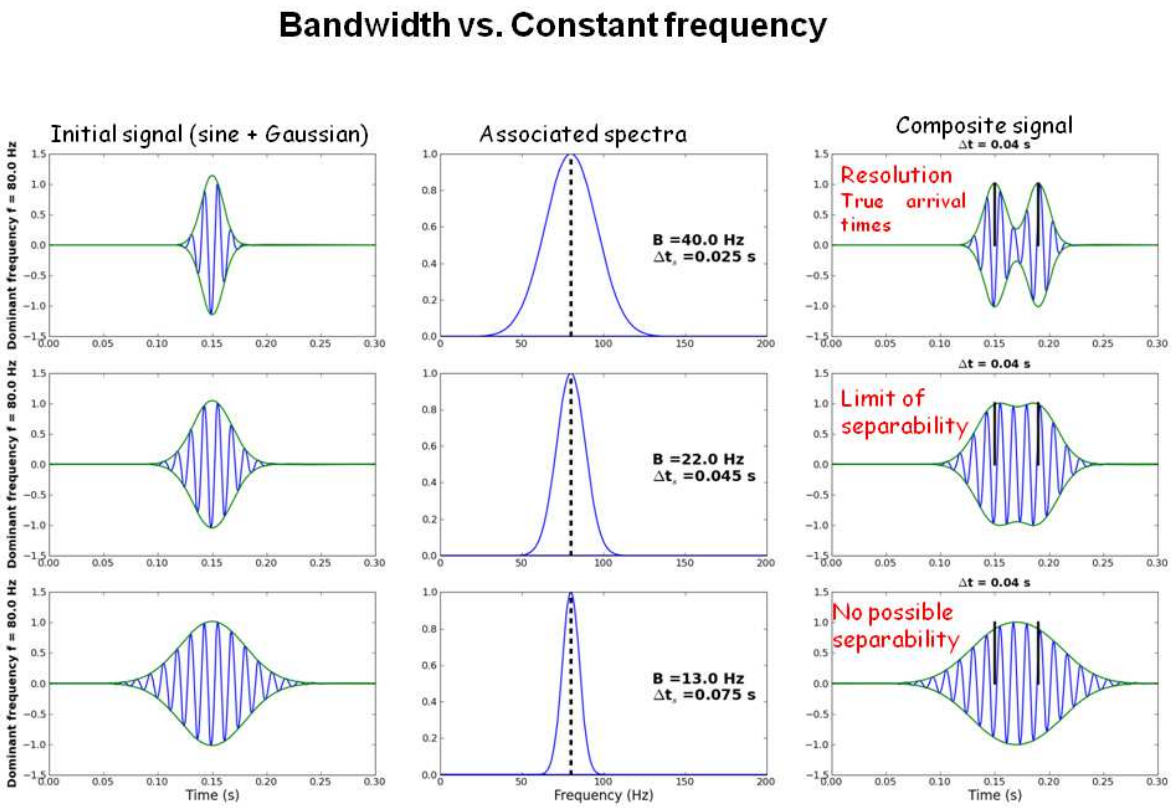

FIGURE 2.1 – *Résolution pour des signaux (de même amplitude) à phase non nulle avec différentes bandes fréquentielles. Gauche : trois signaux, avec leur enveloppe, composés du même signal sinusoïdal de fréquence $f = 80Hz$ convolué avec différentes gaussiennes dont la largeur définit la bande fréquentielle B. Centre : spectres associés. Droite : signaux, avec leur enveloppe, composés de la somme du signal (de gauche) et du même signal mais retardé de $\Delta t = 0.04\,s$. Les lignes noires épaisses indiquent le temps d'arrivée des deux signaux supposés être réfléchis par deux interfaces.*

La résolution latérale est caractérisée par la distance minimale entre deux caractéristiques le long d'une même interface telle que ces deux caractéristiques peuvent être identifiées plutôt qu'une seule. Il est bien connu que la Zone de Fresnel à l'Interface (ZFI ou IFZ) [6] est l'essence

6. Du fait du contenu BF des données sismiques, il est admis que les ondes ne se propagent pas uniquement

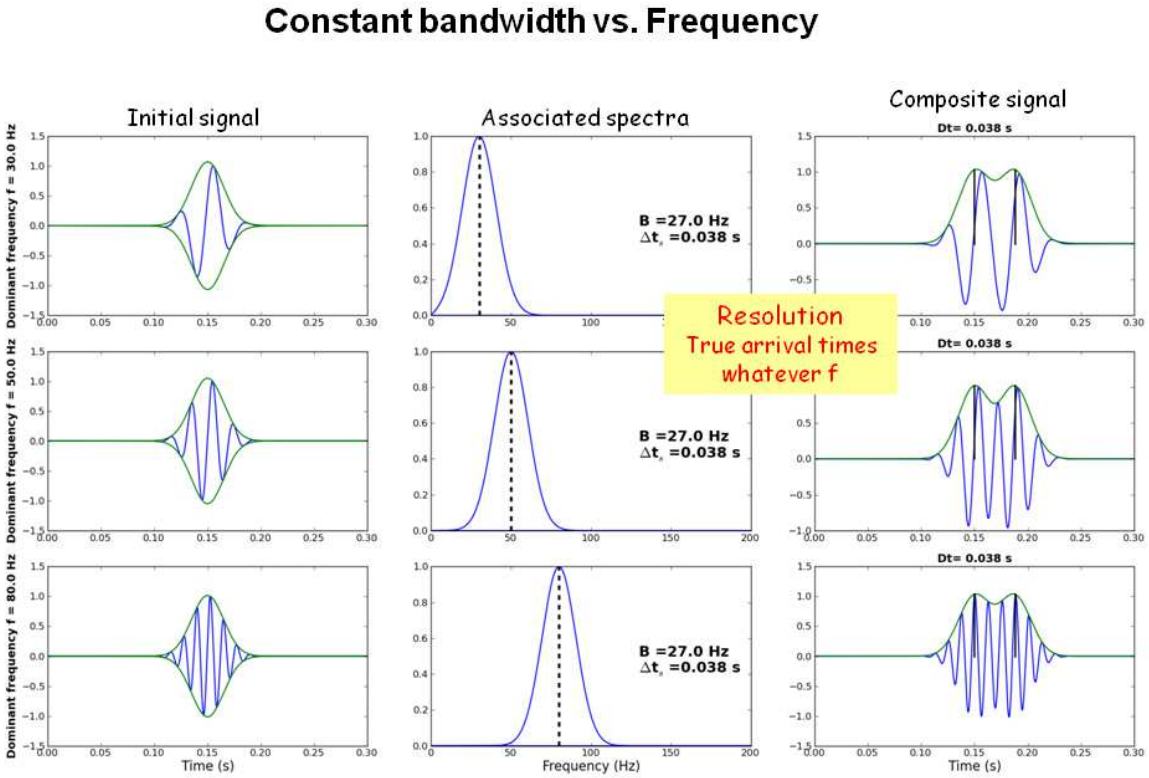

FIGURE 2.2 – *Résolution pour des signaux (de même amplitude) à phase non nulle avec différentes fréquences centrales. Gauche : trois signaux, avec leur enveloppe, composés de signaux sinusoïdaux de fréquences différentes convolués avec la même gaussienne dont la largeur définit la bande fréquentielle $B = 27$ Hz. Centre : spectres associés. Droite : signaux, avec leur enveloppe, composés de la somme du signal (de gauche) et du même signal mais retardé de $\Delta t = 0.038\,s$. Les lignes noires épaisses indiquent le temps d'arrivée des deux signaux supposés être réfléchis par deux interfaces.*

même de la résolution latérale puisqu'elle détermine la résolution spatiale avec laquelle d'importants changements dans les propriétés de l'interface peuvent être observés. Concrètement, pour que deux évènements soient visuellement indépendants le long d'une même interface, ils doivent être séparés latéralement par approximativement le rayon de la ZFI. Il est à noter que le diamètre de la ZFI peut varier considérablement selon la courbure de l'interface (*cf* Figure 2.3). La ZFI est minimale dans le cas d'un anticlinal et maximale dans le cas d'un synclinal. A noter que dans le cas d'un synclinal, la ZFI est d'autant plus grande que le rayon de courbure

le long d'un rayon, mais qu'un volume fini autour de ce rayon participe activement à cette propagation. Le (1^{er}) Volume de Fresnel (FV) peut être vu comme une zone d'interférences constructives qui contribue au champ d'onde réfléchi pour chaque fréquence [Favretto-Cristini *et al.*, 2009]. La réflexion des ondes sur une interface résulte d'une intégration sur une zone spécifique (*i.e.*, la Zone de Fresnel à l'Interface (ZFI ou IFZ)) qui est définie par l'intersection du FV par cette interface. Les dimensions de la ZFI dépendent de plusieurs paramètres, parmi lesquels la fréquence, l'offset (*i.e.*, la distance source-récepteur), la localisation en profondeur de l'interface, les propriétés des milieux en contact, la courbure de l'interface... J'invite le lecteur à consulter l'article [Favretto-Cristini *et al.*, 2009] placé en Annexe D pour plus de détails.

de l'ellipsoïde de révolution, décrivant l'isochrone pour le couple S(ource)-R(écepteur) relatif à la réflexion spéculaire SMR (M étant le point d'impact de l'onde sur l'interface), tend vers le rayon de courbure de l'interface [7]. Alors que ses dimensions n'avaient été approchées que de manière empirique et pour des offsets nuls, nous avons pu les évaluer analytiquement, dans les directions, du plan de l'interface, incluse dans le plan d'incidence et perpendiculaire au plan d'incidence, pour des offsets quelconques [Favretto-Cristini *et al.*, 2009]. Il faut garder à l'esprit que la ZFI définit la résolution uniquement pour des données non migrées. La résolution latérale de la sismique est donnée *in fine* par la migration (*cf* Figure 2.4) [Berkhout, 1984].

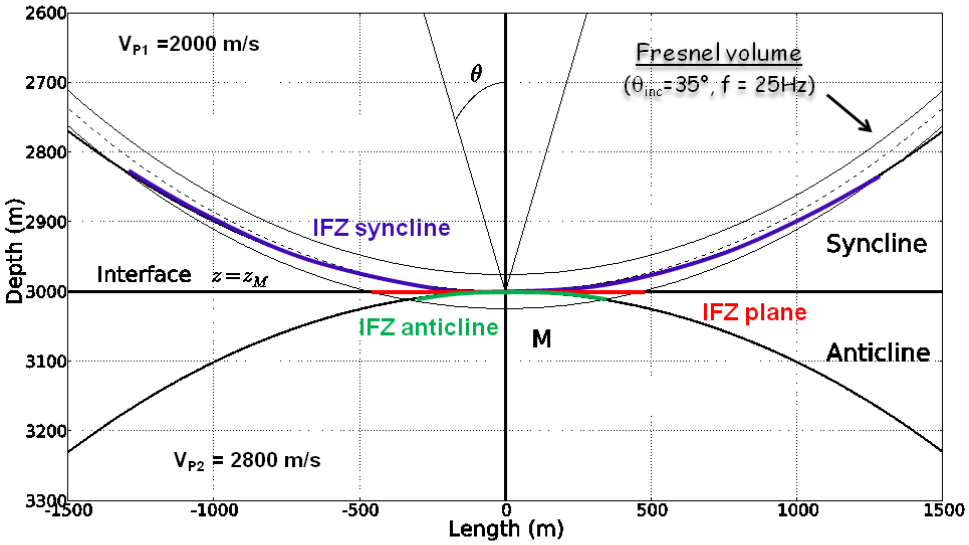

FIGURE 2.3 – *Illustration de l'influence de la courbure de l'interface entre deux milieux homogènes, isotropes et élastiques sur les dimensions de la Zone de Fresnel à l'Interface (ZFI ou IFZ), associée à la réflexion P-P sur cette interface.*

2.3 Réflecteur sismique 3D et Réflectivité équivalente

Une fois l'interface isolée, l'onde sismique se réfléchit sur cette interface avant d'atteindre les capteurs en surface. Nous avons l'habitude de décrire mathématiquement ce processus en considérant implicitement que la fréquence de la source est infinie. Or, les fréquences sismiques étant basses (typiquement, entre 5 et 80 Hz pour la sismique terrestre), le point d'impact des ondes sur les interfaces ne peut pas être considéré comme ponctuel. Lindsey a montré que la ZFI est une notion importante à prendre en compte dans le processus de réflexion des ondes sur une interface [Lindsey, 1989]. Les travaux complémentaires de Kvasnička et Červený ont mis en lumière une zone sous-jacente à l'interface qui participe également à ce processus

7. Dans ce cas, on peut assister à une amplification de l'amplitude (ponctuellement) au niveau d'un capteur, car l'ouverture angulaire d'émission en provenance de l'interface est très grande. Il faut garder cela à l'esprit lorsqu'on analyse des données acquises en tectonique complexe.

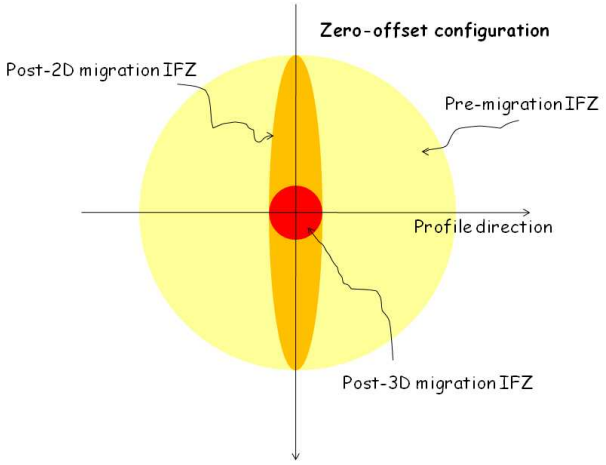

FIGURE 2.4 – *Résolution latérale après migration dans une configuration zéro-offset. Dans un contexte de pré-migration, la résolution latérale est donnée par la Zone de Fresnel à l'Interface (IFZ). La migration 2D réduit la taille de l'IFZ uniquement dans la direction du profil sismique, tandis que la migration 3D réduit l'IFZ à une toute petite zone.*

[Kvasnička et Červený, 1996]. Mais ces travaux sont essentiellement motivés par des considérations sur les temps de trajet des ondes, et non sur les amplitudes, et ne répondent donc pas à la question fondamentale : Qu'est-ce qu'un réflecteur sismique ? Ou reformulée autrement : Quelle est la zone spatiale autour de l'interface qui interagit avec le champ d'onde incident, définit ainsi sa réflectivité, et affecte par conséquent le champ d'onde réfléchi ?

A partir des concepts de Volume de Fresnel[8] (VF) [Kravtsov et Orlov, 1990] et des lois de transmission et de réflexion des courbures de fronts d'onde [Hubral et Krey, 1980], nous avons identifié pour chaque fréquence de la bande passante de la source sismique un volume spatial, autour de l'interface (plane, ou de type synclinal ou anticlinal), qui affecte réellement la réponse de l'interface (*i.e.*, sa réflectivité), et donc le champ d'onde réfléchi (*cf* Figure 2.5). Ce volume a pour extension latérale maximale la ZFI, pour laquelle nous avons déterminé analytiquement ses dimensions quelle que soit la courbure de l'interface et pour des offsets quelconques. Il a pour épaisseur maximale une distance qui peut être équivalente aux longueurs d'onde mises en jeu lorsque les angles d'incidence sont proches de l'angle critique. Ce volume est plus grand que celui décrit précédemment dans la littérature qui ne considère en fait que la partie spatiale sous-jacente à l'interface "mathématique" (car c'est la seule qui est impliquée dans les mesures de temps de trajet des réflexions). Précisons que la partie située au-dessus de l'interface "mathématique" doit être obligatoirement prise en compte si les amplitudes des ondes sont traitées. Le volume spatial ainsi défini représente un volume spatial minimal d'intégration et d'homogénéisation (partielle ou totale ?) des propriétés autour de l'interface : cela signifie que seules les hétérogénéités présentes dans ce volume contribuent physiquement à la réflexion des ondes et conditionnent le comportement des formes d'onde enregistrées aux capteurs[9]. Ne pas tenir compte de ce volume

8. Il semblerait qu'il y ait une analogie entre le Volume de Fresnel et le volume de confusion connu en traitement sonar.

9. En partie seulement, car les hétérogénéités présentes dans le VF conditionnent également le comportement des formes d'onde enregistrées aux capteurs.

spatial pourrait conduire à des erreurs systématiques commises sur l'estimation des propriétés physiques des milieux naturels, et donc à une connaissance biaisée de notre environnement.

Ces résultats tout à fait originaux, qui corrigent et étendent les résultats publiés antérieurement par Červený et ses collaborateurs et Lindsey, ont fait l'objet d'une publication dans la revue "Geophysics" [Favretto-Cristini *et al.*, 2009] et d'une distinction dans la section "Geophysics Bright Spots" de la revue "The Leading Edge" en février 2009.

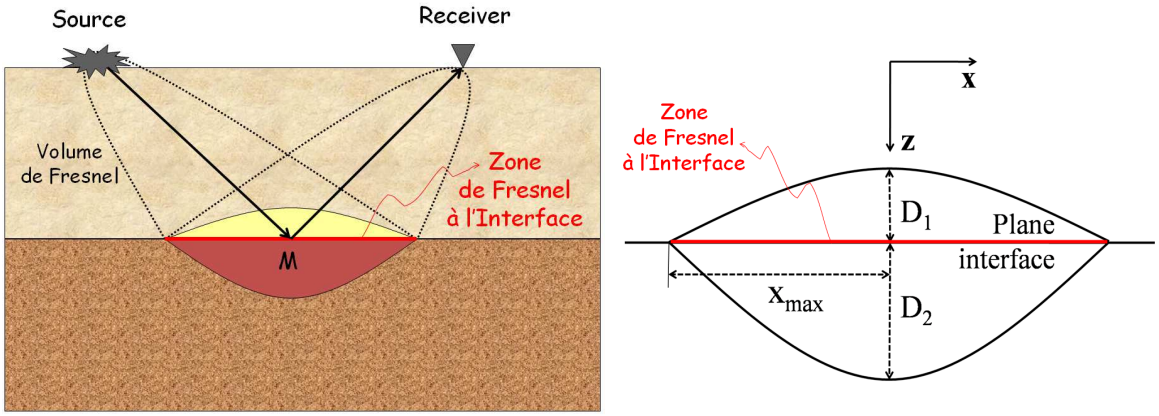

FIGURE 2.5 – *Gauche : Représentation, dans le plan d'incidence, du Volume de Fresnel impliqué dans la réflexion des ondes sur l'interface plane au point M. Droite : Zoom sur le volume spatial autour de l'interface plane qui affecte réellement la réponse de l'interface (i.e., sa réflectivité), et donc le champ d'onde réfléchi.*

2.4 Implications sur les problèmes direct et inverse

Lorsqu'il n'y a pas d'hétérogénéités présentes dans le volume spatial défini précédemment, seule la ZFI contribue de manière significative au champ d'onde réfléchi. Pour démontrer cela, nous avons calculé l'amplitude d'une onde P émanant d'un point source et enregistrée au récepteur après avoir été réfléchie spéculairement par une interface plane entre deux milieux élastiques homogènes isotropes. Ce problème pouvant être considéré comme un problème de diffraction par la ZFI, nous avons appliqué l'Approche "Angular Spectrum" (ASA) combinée au concept de ZFI pour obtenir la solution analytique 3D [Favretto-Cristini *et al.*, 2007a, Favretto-Cristini *et al.*, 2007b] [10]. La variation de l'amplitude de l'onde réfléchie obtenue par l'ASA, en fonction de l'angle d'incidence (*i.e.*, la courbe AVA) a été comparée avec le coefficient de réflexion ondes planes, donné par les équations de Zoeppritz [Aki et Richards, 2002], et la solution exacte obtenue par un code numérique 3D (OASES) utilisé en acoustique sous-marine (*cf* Figure 2.6). A noter que la solution en ondes sphériques obtenue par le code OASES a été corrigée de la divergence géométrique des fronts d'onde. Pour de faibles angles subcritiques, le coefficient de réflexion ondes planes (qui varie très peu) et la solution exacte sont quasiment identiques. L'effet de la ZFI sur l'amplitude est donc négligeable. Par contre, proche de l'angle critique où le coefficient de réflexion ondes planes varie très fortement et est très différent de la solution exacte, l'effet de la ZFI est très important, et notre approximation ASA combinée au concept de la ZFI donne de très bons résultats. Au-delà de l'angle critique, néanmoins, la solution approchée

10. J'invite le lecteur à consulter l'article [Favretto-Cristini *et al.*, 2007a] en Annexe D.

s'éloigne de la solution exacte. Cela provient du fait que nous ne calculons que l'amplitude de l'onde réfléchie alors que le code calcule l'amplitude de l'interférence onde réfléchie/onde conique. Il serait intéressant de calculer par notre approche l'amplitude résultante de cette interférence en intégrant le fait que chaque onde (réfléchie et conique) possède sa propre ZFI. Il est à noter que notre approche est complémentaire à la méthode initialement développée par Klem-Musatov et Aizenberg [Klem-Musatov et Aizenberg, 1985, Ayzenberg *et al.*, 2009]. Elle est par ailleurs équivalente au calcul du coefficient de réflexion des ondes sphériques [Dettmer *et al.*, 2007]. Cependant, contrairement à ce dernier qui nécessite l'évaluation d'une intégrale de $+\infty$ à $-\infty$, notre méthode se limite à une intégration sur la zone "physique" de l'interface qui interagit avec l'onde, ce qui réduit le temps de calcul.

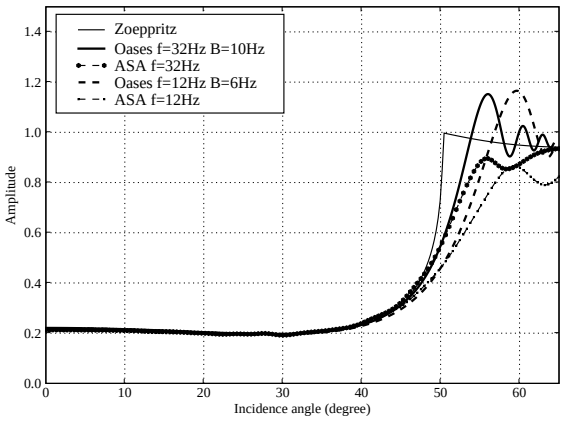

FIGURE 2.6 – *Variation de l'amplitude de l'onde réfléchie P-P par une interface plane en fonction de l'angle d'incidence. Comparaison entre le coefficient de réflexion ondes planes (Zoeppritz), les amplitudes corrigées de la divergence géométrique associées aux solutions exactes (OASES), et les amplitudes associées aux solutions approchées (ASA) pour différentes fréquences centrales et différentes bandes passantes de la source.*

Nous avons également abordé le problème inverse en cherchant à évaluer quelle était l'erreur commise sur les paramètres (*e.g.*, vitesse des ondes P et S et densité) des milieux en contact si on prenait (ou non) en compte la ZFI dans les calculs. Admettons que l'on veuille évaluer ces paramètres, à partir des courbes AVA grands angles acquises in situ (donc intégrant naturellement les VF et ZFI), mais corrigées de la divergence géométrique des fronts d'onde, et en utilisant un algorithme d'inversion basé sur les équations de Zoeppritz. On a montré que pour des études AVA grands angles (*i.e.*, pour des angles d'incidence pouvant aller jusqu'à 50° ou 60°) on commettrait des erreurs d'estimation pouvant atteindre 4% pour la densité, 14% pour la vitesse des ondes P et 73% pour la vitesse des ondes S en BF [Favretto-Cristini *et al.*, 2008] [11]. Ces erreurs sont plus importantes en BF qu'en HF. Notons que ces erreurs ont été estimées pour une configuration "académique", à savoir une interface sans hétérogénéités entre deux milieux élastiques homogènes isotropes. On peut penser qu'elles seront du même ordre de grandeur, voire plus importantes, dans le cas de milieux plus complexes. Par contre, l'utilisation de notre approximation, basée sur la combinaison équations de Zoeppritz / ZFI, limite considérablement les erreurs commises sur l'estimation des propriétés, en particulier sur la vitesse des ondes P (erreur inférieure à 9%) et sur la vitesse des ondes S (erreur inférieure à 4%). Par ailleurs, le fait de

11. J'invite le lecteur à consulter cet article en Annexe D

disposer d'un algorithme de modélisation quasi-analytique "simple", basé sur la combinaison de la ZFI et de coefficients de réflexion ondes planes connus pour des configurations types, pourrait sans doute être bénéfique en vue d'une stratégie d'inversion peu coûteuse en temps de calcul. Dans tous les cas, cela mérite plus ample réflexion.

2.5 Conclusions et Problèmes ouverts

Afin de comprendre comment une onde interagit avec une interface sur laquelle elle va se réfléchir, nous avons revisité le concept de résolution verticale de la sismique : contrairement à la pensée commune, ce n'est pas la fréquence mais bien la bande passante sismique qui est le paramètre le plus important. Plus la bande passante sera grande, mieux les interfaces proches pourront être distinguées. On doit donc veiller à enrichir la bande à la fois avec des hautes fréquences et des basses fréquences, tout en gardant à l'esprit que les HF peuvent parfois être fortement atténuées par différents mécanismes tels que par exemple l'absorption ou la diffusion.

La résolution latérale de la sismique est liée (avant migration) à la Zone de Fresnel à l'Interface (ZFI). Nous avons pu évaluer analytiquement les dimensions de la ZFI pour des angles d'incidence subcritiques quelconques et pour des interfaces de type plan, anticlinal et synclinal. Il serait intéressant de généraliser cette étude en considérant des interfaces à courbure quelconque dans les plans d'incidence et perpendiculaire au plan d'incidence.

Par ailleurs, nous avons identifié le volume spatial (localisé autour de l'interface) d'interaction avec les ondes qui contribue physiquement à la réflexion. Ne pas en tenir compte dans les modélisations conduit à des erreurs systématiques sur l'estimation des propriétés physiques des milieux naturels, et donc à une connaissance biaisée de l'environnement. Ce volume, qui définit ce qu'est un réflecteur sismique, est aussi un volume spatial minimal d'intégration et d'homogénéisation des propriétés autour de l'interface. Les hétérogénéités présentes dans ce volume conditionnent le comportement des formes d'onde enregistrées aux capteurs. Afin de nous rapprocher un peu plus de la réalité géologique, il serait particulièrement intéressant de déterminer les dimensions du réflecteur sismique, par exemple dans le cas de milieux anisotropes en contact, l'anisotropie de vitesses pouvant résulter de la lithologie ou de la fracturation des milieux. La question sous-jacente est la suivante : l'anisotropie réduit-elle le volume spatial minimal d'intégration des propriétés autour de l'interface ? Par ailleurs, il semble nécessaire d'étudier une configuration (type) multi-échelles d'hétérogénéités pouvant être présentes au sein de ce volume, afin d'y associer une réflectivité "équivalente". Cela nécessite une approche intégrée géologie/mécanique du contact/géophysique. Même si ce processus semble fortement dépendant du milieu géologique étudié, on pourrait sans doute poser certains jalons assez généraux pour cerner cette problématique.

Chapitre 3

La diffusion d'interface

Collaborations

E. de Bazelaire *(ancien Expert International Elf Exploration Production, puis TOTAL ; décédé le 28/06/2007)*
W. Makindé *(Thèse Université de Pau et des Pays de l'Adour soutenue le 25/02/2004 ; actuellement ingénieur TOTAL)*

Publications associées

cf Annexe C : [5], [6], [13], [58], [59], [60]
Une copie des articles [5], [6] et [13] a été placée en Annexe D.

Communications associées

cf Annexe C : [17], [18], [26], [27], [28], [29], [30], [31], [32]

———————

3.1 Introduction

L'amplitude et la phase des signaux sismiques sont deux paramètres importants exploités au cours des processus d'interprétation et d'inversion. Ces deux paramètres sont affectés, tout le long de la propagation des champs d'onde incident et réfléchi, par certains effets qui dépendent du contexte géologique, de sa forme structurale, de la lithologie, des fluides en présence...

Par exemple, les causes des baisses d'amplitude le long du trajet de l'onde sismique entre la source et le récepteur sont nombreuses et ont été identifiées dans leur grande majorité par Sheriff [Sheriff, 1975]. On peut citer par exemple les causes d'atténuation "intrinsèque", liées essentiellement à des phénomènes dissipatifs à l'échelle microscopique qui induisent des effets macroscopiques pouvant être représentés par de la viscoélasticité ou de la poro-élasticité (*e.g.*, mouvement grain-grain, mouvement de fluide dans les roches partiellement saturées, comportement anélastique de la roche...). On peut également citer les causes d'atténuation "apparente" liées à la divergence géométrique des fronts d'onde et à des phénomènes complexes de propagation des ondes (*e.g.*, diffractions par des hétérogénéités à l'échelle des longueurs d'onde, interférences destructives...). Le traitement classique des signaux se concentre essentiellement sur les effets géométriques "simples" tels que la courbure des interfaces, supposée être corrigée par la migration, et regroupe souvent (sans vraiment les identifier) les autres causes de baisse de l'amplitude sous une atténuation apparente compensée par l'application de facteurs de qualité Q [Aki et Richards, 2002]. Néanmoins, des mesures additionnelles obtenues en puits et des modélisations ont prouvé que l'absorption due à des phénomènes dissipatifs n'était pas toujours la cause dominante de l'atténuation des amplitudes, et que d'autres phénomènes, liés plutôt à la

propagation des ondes, pouvaient être mis en cause tels que, par exemple, la diffusion d'interface [Rappin *et al.*, 2009a]. Il a d'ailleurs été montré dans ce cas précis que les compensations basées sur le facteur Q avaient très peu d'effet sur l'atténuation des amplitudes induite par la diffusion d'interface [Rappin et Barnes, 2008].

Il semble alors indispensable d'identifier les causes des "anomalies" d'amplitude des signaux sismiques dans un environnement donné pour corriger les données afin d'améliorer l'efficacité des techniques d'imagerie conventionnelles et des techniques visant à quantifier les propriétés des milieux géologiques. Cette identification passe avant tout par une connaissance des mécanismes physiques sous-jacents. De notre côté, nous nous sommes focalisés sur le phénomène de diffusion des ondes par des interfaces aux caractéristiques (géométriques et/ou physiques) latéralement hétérogènes (*i.e.*, la diffusion d'interface) et sur ses effets potentiels sur les données sismiques.

3.2 Diffusion de phase et Diffusion d'amplitude

Il existe deux types de diffusion d'interface, *i.e.* la diffusion de phase et la diffusion d'amplitude, qui peuvent exister séparément ou cohabiter selon la structure et l'histoire des milieux géologiques.

Typiquement, la diffusion de phase apparaît lorsqu'un front d'onde rencontre une surface de discontinuité d'impédance dont le relief varie spatialement de façon aléatoire et a une amplitude non "négligeable" comparée à la longueur d'onde dominante du spectre du signal incident. Outre le fait de transformer une partie de l'énergie incidente en bruit (qui apparaît sur tous les offsets), le diffuseur de phase (*i.e.*, l'interface rugueuse) introduit un déphasage spatialement aléatoire sur les fronts d'onde réfléchis et transmis, ce qui conduit à l'existence d'un champ cohérent (dans les directions spéculaires) mais aussi à l'existence d'un champ incohérent (diffractions dans les directions non spéculaires). Ce déphasage est difficilement prévisible sans connaissance *a priori* du profil de la surface rugueuse. Précisons que la notion de rugosité n'est pas une propriété intrinsèque du milieu, elle dépend de l'échelle d'observation. En effet, les caractéristiques de l'onde incidente influencent de manière cruciale le comportement des ondes. La fréquence et l'angle d'incidence déterminent une rugosité "effective" de la surface et la façon dont l'énergie est diffusée par cette surface (*cf* Figure 3.1). Une surface apparaît d'autant plus rugueuse que la longueur d'onde incidente λ_{inc} est petite ou que l'angle d'incidence α_{inc} (défini par rapport à la normale à l'interface) tend vers zéro [Ogilvy, 1991]. Le critère de Rayleigh

$$\Delta h < \frac{\lambda}{8 \cos \alpha_{inc}}$$

définit la limite des hauteurs de rugosité en-dessous de laquelle la surface peut apparaître lisse [Ishimaru, 1978, Ogilvy, 1991]. C'est ainsi qu'à incidence normale une surface sera vue comme lisse par l'onde incidente si la hauteur de ses rugosités est inférieure à $\lambda_{inc}/8$.
Le diffuseur de phase le plus connu en sismique est certainement la zone altérée de surface (ou "weathered zone" en anglais). Les discordances angulaires, les interfaces sel-couches le long des dômes de sel ou sous les surplombs (*i.e.*, "overhangs"), et les olistostromes constituent également de bons diffuseurs de phase (*cf* Figure 3.2). Quand la diffusion de phase existe, elle est souvent très forte et son effet est d'autant plus grand qu'on s'éloigne de l'interface, un peu à la manière du verre dépoli en optique [Born et Wolf, 1999].

La diffusion d'amplitude apparaît lorsqu'un front d'onde rencontre une surface de discontinuités d'impédance dont les valeurs varient spatialement de façon aléatoire. Elle est dite pure si la surface de contact n'introduit pas de variation latérale de phase dans les champs d'onde, *i.e.*

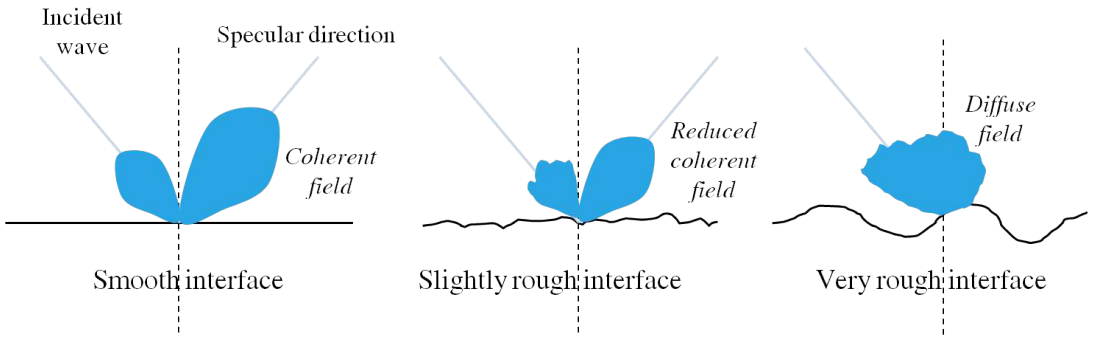

FIGURE 3.1 – *Représentation schématique de la distribution de l'énergie diffusée en fonction de la rugosité de surface. (Adapté de [Ogilvy, 1991])*

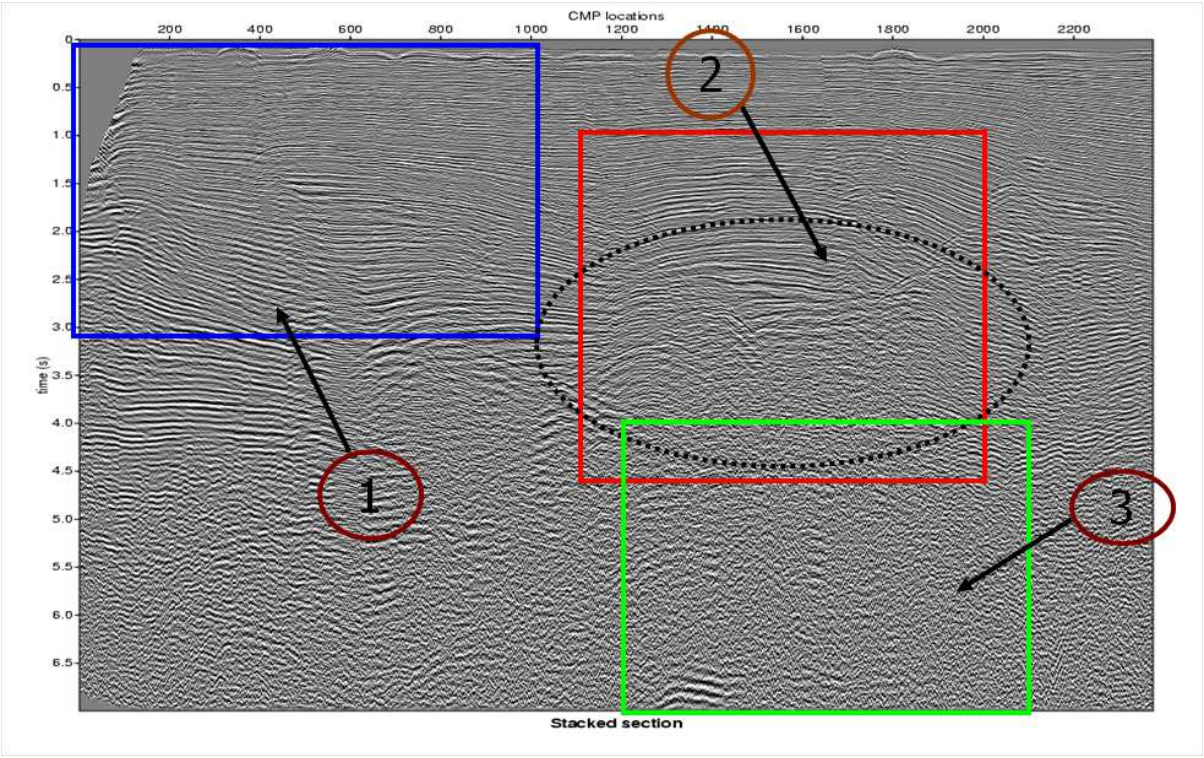

FIGURE 3.2 – *Illustration du phénomène de diffusion de phase sur des données sismiques réelles (Delta du Niger). Dans la zone 1, on note une bonne cohérence latérale des évènements et de la phase des signaux, tandis que dans la zone 3 les évènements ont un caractère totalement aléatoire. Dans la zone 2, on peut facilement distinguer la position du diffuseur de phase. (Source : [Makindé, 2004])*

si la surface est lisse. Le diffuseur d'amplitude introduit une variation d'amplitude relative entre deux parties consécutives du front d'onde réfléchi ou transmis, sans qu'il y ait variation latérale des phases.

Les discontinuités d'impédance qui génèrent de la diffusion d'amplitude sont essentiellement dues aux décollements des couches qui se superposent. Lorsqu'une couche se dépose sur une couche sous-jacente déposée précédemment, deux cas de figure peuvent se présenter. Dans le 1^{er} cas, la couche sous-jacente est ancienne ; elle est partiellement érodée car il y a eu régression

puis transgression de la mer. L'état de surface de cette couche a ainsi des propriétés de dureté superficielle qui varient spatialement de façon aléatoire au gré des oxydations, des dissolutions et de toute autre altération. La nouvelle couche qui se dépose, même si elle est homogène et de même impédance acoustique que la couche sous-jacente, va engendrer des discontinuités d'impédance de contact qui varient spatialement de façon aléatoire. Les deux couches ne sont pas "collées" de façon uniforme et la diffusion d'interface apparaît, comme par exemple dans les séries deltaïques (*cf* Figure 3.3). Dans le 2^e cas, la couche sous-jacente vient d'être déposée. La nouvelle couche qui se dépose est composée de matériaux d'origine différente ; en particulier, sa dureté n'est pas la même. Cependant, comme ce nouveau matériau est déposé directement sur celui de la couche sous-jacente, l'adhérence entre les deux couches est parfaite et la diffusion d'interface est négligeable, jusqu'au jour où il y a déformation des couches par tectonisation, soit en traction, soit en compression. Les plissements ainsi engendrés provoquent des mouvements plan-sur-plan entre les couches successives qui vont donc se décoller (*e.g.*, des niveaux de décollement). Les nouvelles surfaces en contact auront une adhérence, due principalement à la pression géostatique, qui va varier spatialement de façon aléatoire au gré des micro-reliefs apparus latéralement lors du dépôt. L'interface devient donc diffusante. La diffusion d'amplitude est d'autant plus forte que la tectonisation a été poussée, comme par exemple dans les séries chevauchantes.

3.3 Les effets du diffuseur de phase

Les rugosités de surface apparaissent dans la nature à toutes les échelles mais, d'après le critère de Rayleigh, leur influence sur la propagation des ondes sismiques est sensée ne devenir considérable que lorsque les hauteurs de rugosités atteignent $1/8^e$ de la longueur d'onde incidente en incidence normale [Ogilvy, 1991]. En effet, en-deçà, les ondes "voient" le milieu comme un milieu lisse. Par exemple, seules les surfaces dont les hauteurs de rugosités sont inférieures à 3 mètres peuvent être considérées comme lisses par une onde de fréquence centrale 60 Hz qui traverse un milieu avec une vitesse de compression de 1500 m/s. Cette limite est revue à la hausse si la vitesse de propagation est plus rapide ou si la fréquence est plus basse. Ainsi, seules les surfaces dont les hauteurs de rugosités sont inférieures à 38 mètres peuvent être considérées comme lisses par une onde de fréquence centrale 10 Hz et de vitesse de compression de 3000 m/s !

Pourtant peu de travaux rendent compte de l'influence de ces rugosités sur la propagation des ondes réfléchies enregistrées en sismique réflexion. Les rares études numériques sont limitées la plupart du temps à des configurations 2D, voire 2,5D, car les études 3D coûtent cher numériquement, même si de nos jours la puissance de calcul tend à s'améliorer grandement d'année en année. Ne pas modéliser les effets de la diffusion des ondes sismiques par les interfaces rugueuses en 3D n'est pourtant guère réaliste d'un point de vue géologique et géophysique, car la diffusion de phase est résolument un phénomène physique 3D.

Dans le cadre de la thèse de W. Makindé que j'ai co-encadré au cours des deux dernières années, nous avons montré à l'aide de simulations numériques 3D (schéma aux différences finies) de quelle façon la diffusion des ondes par des interfaces rugueuses aléatoires affecte les images sismiques 3D [Makindé *et al.*, 2005] [1]. Du fait de la convolution spatiale du champ d'onde incident par la fonction décrivant la surface rugueuse aléatoire, une partie de l'énergie incidente est convertie en énergie diffusée par les rugosités, ce qui se traduit par du bruit sur les images, masquant du coup les réflexions non seulement sur les interfaces rugueuses mais également celles

1. J'invite le lecteur à consulter cet article en Annexe D.

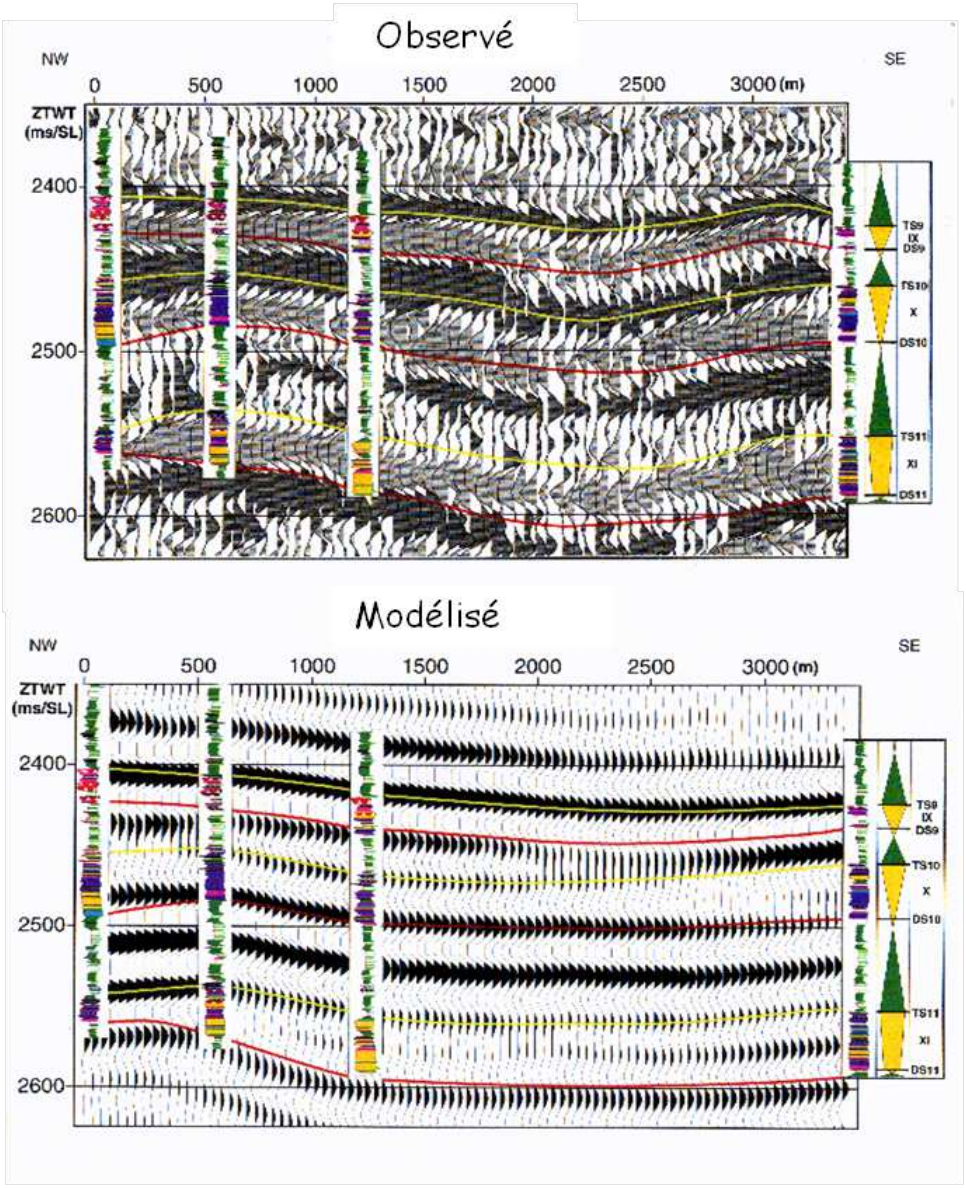

FIGURE 3.3 – *Illustration du phénomène de diffusion d'amplitude sur des données sismiques réelles (Delta du Niger). Dans les séries deltaïques, la diffusion peut parfois faire apparaître sur les sections sismiques des évènements qui ne sont pas des réflexions classiques (car pas de contraste d'impédance observé dans les logs de puits), mais qui correspondent à un hiatus temporel dans la séquence des dépôts (surfaces d'érosion maximale). De ce fait, les évènements sismiques (notamment leurs amplitudes et leur contenu fréquentiel) sont mal simulés si la diffusion d'interface n'a pas été au préalable identifiée et prise en compte dans les algorithmes de modélisation. (Adapté de [Schulbaum, 1996])*

sur les interfaces situées au-dessous (*cf* Figure 3.4). Cet effet est notable dès que les hauteurs de rugosité atteignent $\lambda_{inc}/10$ (h = 20 m sur la Figure 3.4), ce qui modifie légèrement la limite du critère de Rayleigh. Il s'accroît avec l'augmentation de la hauteur des rugosités pour devenir très important lorsque les hauteurs sont égales à $1/4$ ou $1/5$ de la longueur d'onde incidente. Par ailleurs, nous avons montré que pour obtenir des effets de la diffusion des ondes sur les images

sismiques synthétiques, comparables dans le cas de modèles numériques 2D et 3D, il faut nécessairement considérer des hauteurs de rugosité au moins trois fois plus grandes en 2D qu'en 3D, ce qui constitue un résultat important pour la sismique numérique. En conséquence, les études menées en 2D dans la littérature, qui considèrent des hauteurs de rugosité mal définies, ne reflètent généralement pas la réalité de la propagation des ondes sismiques.

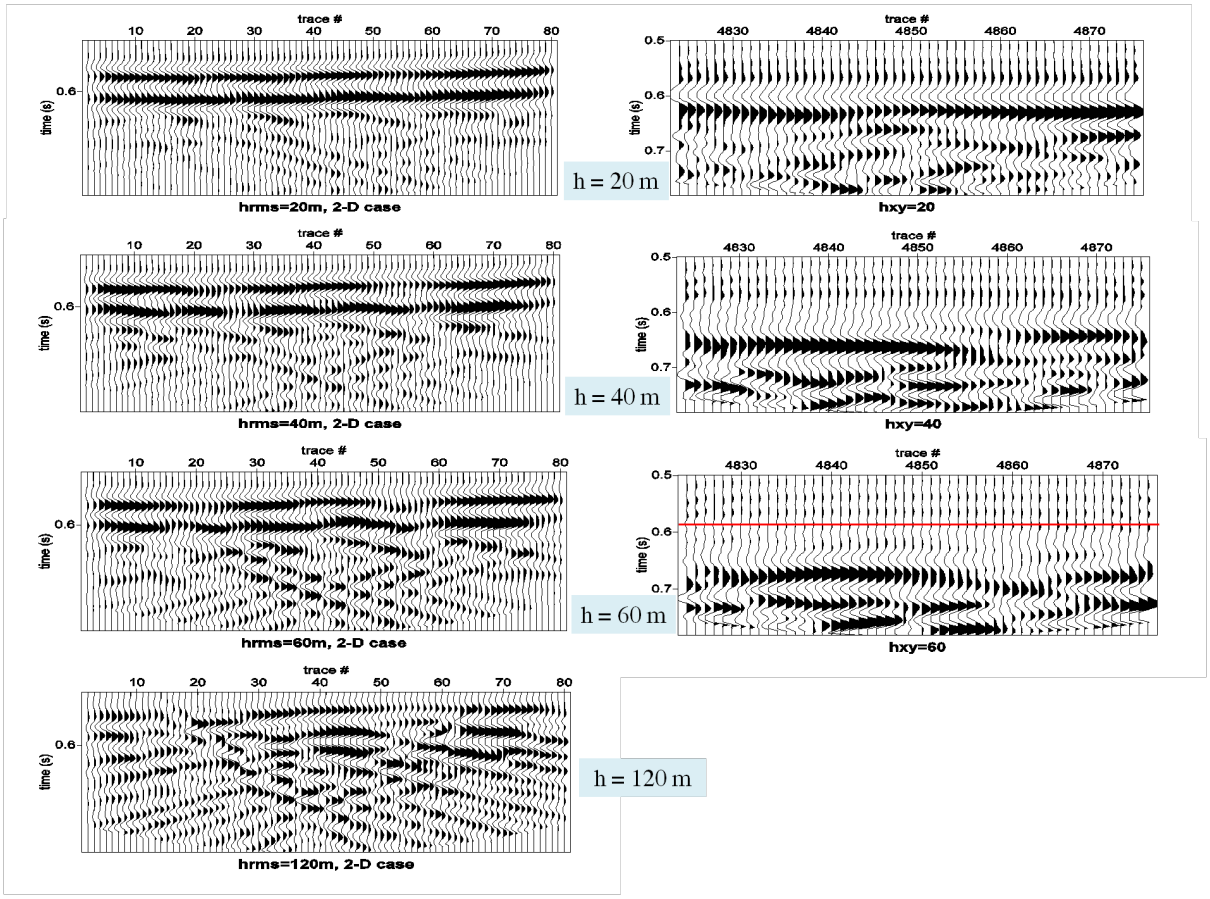

FIGURE 3.4 – *Comparaison entre les sismogrammes synthétiques obtenus dans des configurations 2D (gauche) et 3D (droite) pour différentes hauteurs h de rugosité de surface. En 3D, l'interface rugueuse n'est plus du tout visualisée et les effets de la diffusion sont beaucoup plus prononcés.*

3.4 Les effets du diffuseur d'amplitude

Le diffuseur d'amplitude est généralement une distribution de "mauvais" contacts mécaniques entre les milieux géologiques, induite soit par un dépôt de couche sur une surface ancienne érodée (*cf* Figure 3.3), soit par une forte tectonisation engendrant des zones ou des niveaux de décollement (*cf* Figure 3.5). Par souci de simplification, nous appellerons ci-après "zones de décollement" indifféremment les niveaux de décollement et les zones de mauvais contacts mécaniques[2].

Les zones de décollement, généralement remplies de gaz, de fluide, de calcite ou de débris, perturbent de manière significative la propagation des ondes sismiques. Nous avons suggéré

2. Même si cela n'est pas assimilable. Que mes collègues géologues veuillent bien me pardonner...

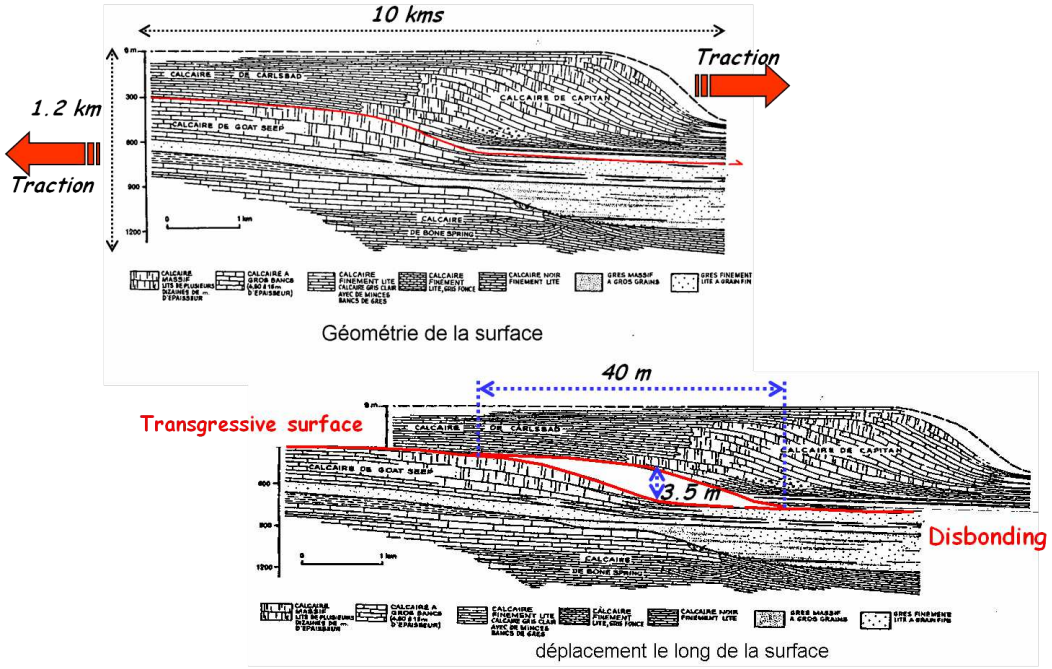

FIGURE 3.5 – *Illustration du mécanisme donnant naissance à des niveaux de décollement.*

que ces zones le long des interfaces pouvaient être comparées, par analogie avec l'acoustique ou l'optique, à un réseau de diffraction [Favretto-Cristini et de Bazelaire, 2003] [3]. Pour prendre en compte ses effets, les propriétés de ce réseau ne doivent pas être homogénéisées, comme cela est fait habituellement, même si les longueurs caractéristiques des décollements semblent très faibles devant celles des ondes sismiques [Baik et Thompson, 1984, Margetan *et al.*, 1988, Rokhlin et Wang, 1991]. La répartition de ces décollements le long d'une même interface peut être assimilée à une interface latéralement hétérogène. Si la répartition des décollements est aléatoire, les ondes de volume sont diffractées dans toutes les directions, ce qui se traduit par du "bruit" sur les sections sismiques (de manière assez similaire à celui engendré par des interfaces rugueuses aléatoires). Si au contraire les décollements sont distribués suivant un arrangement quasi-répétitif (ou perçu comme tel), les ondes peuvent être diffractées dans le milieu dans certaines directions seulement, selon le rapport entre la longueur d'onde sismique incidente et la longueur d'onde spatiale du réseau. Si on suppose que l'onde incidente, à contenu spectral borné, définit elle-même les propriétés du réseau quand elle arrive au voisinage de l'interface, et donc que les propriétés du réseau évoluent avec la fréquence, la diffraction "ordonnée" des ondes se fera dans toutes les directions de l'espace et sera détectée par tous les capteurs. Des phénomènes d'interférences apparaîtront tout le long d'un horizon sismique et pour toute la bande passante sismique, mais ils peuvent être interprétés à tort comme étant des multiples.

Nous appuyant sur ces hypothèses et considérant dans un 1^{er} temps un réseau de décollement périodique, nous avons développé une approche analytique 2D qui permet de décrire tous les phénomènes de propagation au voisinage de ces zones [Favretto-Cristini, 2004] [4]. Cette approche s'appuie sur une méthode qui exploite des propriétés particulières des fonctions de Legendre de $1^{ère}$ espèce, qui sont impliquées dans la formulation des coefficients des séries de Fourier qui décrivent les champs diffractés (théorème de Floquet) [Danicki, 1999]. Ces propriétés particulières

3. J'invite le lecteur à consulter cet article en Annexe D.
4. J'invite le lecteur à consulter cet article en Annexe D.

permettent de définir des fonctions capables de modéliser proprement le champ élastique dans le système considéré, en satisfaisant non seulement implicitement les conditions aux frontières mixtes à l'interface, mais en préservant également implicitement le caractère singulier des champs d'onde aux bords des différents domaines de l'interface. La troncature des séries de Fourier qui décrivent les champs diffractés s'effectue essentiellement à partir de considérations physiques et mathématiques. À partir de la résolution du système linéaire d'équations non homogènes obtenu, une solution asymptotique au problème de propagation des ondes diffractées par les décollements entre deux milieux élastiques différents est déterminée. Tout le problème repose alors sur le choix judicieux de combinaisons des coefficients des séries de Fourier (décrivant les champs diffractés), écrits sous la forme de séries de fonctions de Legendre, afin d'intégrer implicitement la nature du contenu des décollements (*e.g.*, du gaz ou du liquide). Cette approche analytique nous a permis de quantifier l'énergie attribuée aux différentes ondes (réflexions et transmissions spéculaires et non spéculaires induites par les décollements) pour différentes caractéristiques des décollements telles que la longueur, le contenu et la répartition le long de l'interface, et en fonction de l'angle d'incidence (*cf* Figure 3.6). En présence de gaz dans les décollements, nous avons montré que l'énergie des ondes réfléchies spéculaires pouvait être largement sous-estimée, puisque les modélisations prennent en compte uniquement les impédances des milieux en contact en négligeant généralement le contraste d'impédance entre les hétérogénéités de l'interface et les milieux (*cf* Figure 3.7). Ceci est d'autant plus vrai que la concentration de zones de décollement à l'interface est importante. Ces 1^{ers} résultats analytiques semblent en bon accord avec les données réelles observées considérées comme anomaliques (*cf* Figure 3.3). Par ailleurs il est à noter qu'en présence de liquide (*e.g.*, eau) dans les décollements, l'énergie des ondes réfléchies spéculaires est sensiblement égale à celle obtenue en l'absence de décollements à l'interface. Néanmoins, l'énergie attribuée aux ondes S transmises est paradoxalement plus importante. Ces résultats semblent concorder avec les anomalies d'amplitude observées parfois *in situ* (*cf* Figure 2 de [Favretto-Cristini et de Bazelaire, 2003] où l'on peut observer une disparition des ondes P associée à une forte transmission des ondes S dans des zones de diffuseurs saturés en eau).

Malgré ses avantages, l'approche décrite ci-dessus demeure malgré tout une approche analytique, avec tout ce que cela comporte comme limitations pour étudier des configurations plus complexes. Nous nous sommes donc orientés depuis quelque temps vers une approche numérique (*cf* Chapitre 5).

3.5 Conclusions et Perspectives

La diffusion d'interface, qu'elle soit de phase ou d'amplitude, est un phénomène physique qu'il ne faut pas négliger dans certaines configurations géologiques. Elle peut considérablement affecter la propagation des ondes et les images sismiques, soit en introduisant du bruit aléatoire sur toutes les traces, soit en redistribuant différemment l'énergie incidente et donc en modifiant en particulier les amplitudes des ondes réfléchies spéculaires.

Les perspectives de ce travail sont nombreuses et couplées à celles énoncées en conclusion du Chapitre 2. Nous savons que la propagation et la réflexion des ondes sismiques *in situ* (propagation 3D) n'est véritablement influencée que par les Volumes de Fresnel et par un volume autour de l'interface limité latéralement par la Zone de Fresnel à l'Interface (ZFI). Ce volume d'intégration et d'homogénéisation des hétérogénéités de contact évolue en fonction de la bande fréquentielle de la source et de sa position, de la position des récepteurs et de l'angle d'incidence, mais aussi des propriétés des milieux en contact. Au vu de sa taille, il pourrait contenir plusieurs

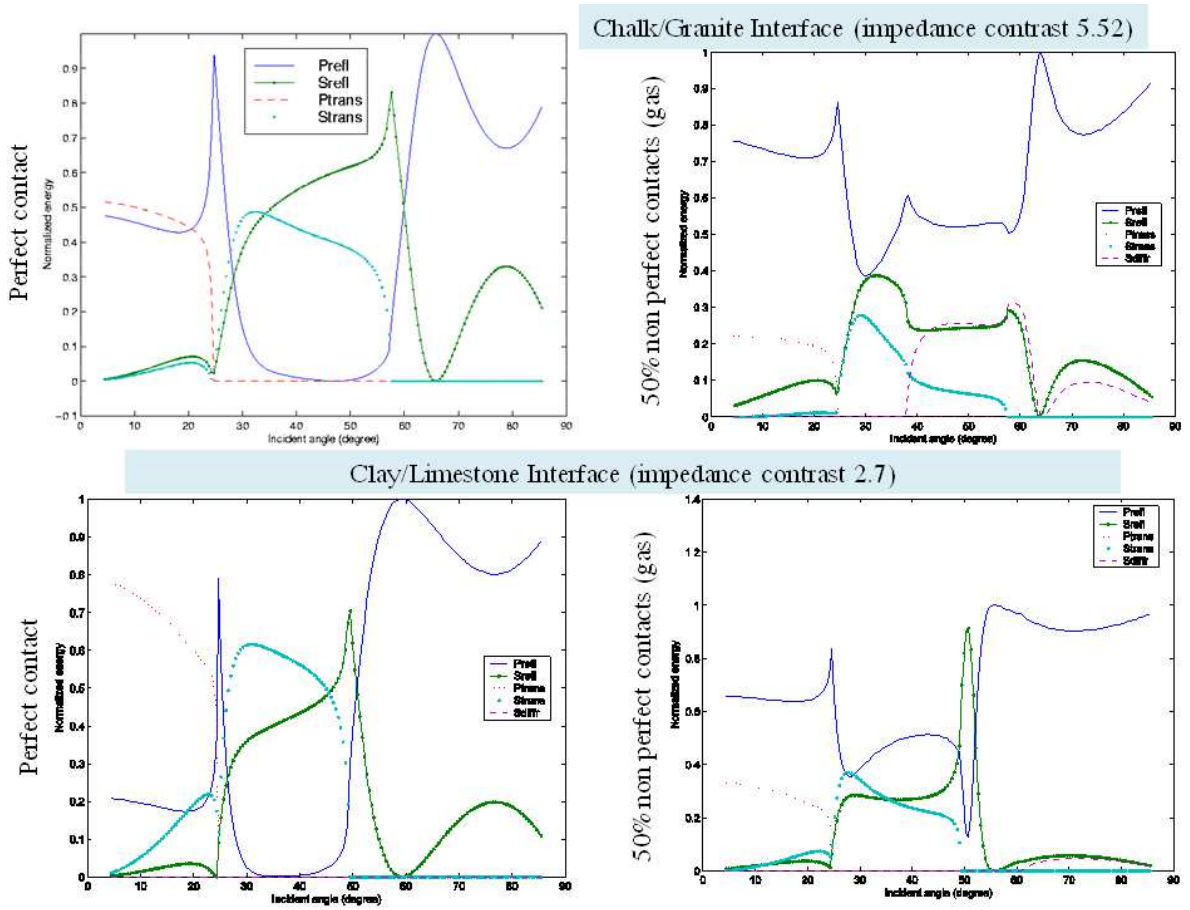

FIGURE 3.6 – *Courbes AVA (Amplitude-versus-Angle) associées aux ondes P et S réfléchies et transmises par deux types d'interface (craie/granite et argiles/calcaire) et pour deux types de contact (contact parfait et 50% de cracks remplis de gaz) entre les milieux. En présence de cracks ou décollements, l'amplitude des ondes P réfléchies spéculaires augmente considérablement tandis qu'apparaît une onde diffractée propagative d'énergie parfois non négligeable.*

décollements répartis de manière quasi-répétitive le long de l'interface comme déjà observé *in situ* (*cf* Figure 3.8). Néanmoins, il serait intéressant d'aller plus avant dans nos réflexions, en procédant tout d'abord à une caractérisation structurale multi-échelle des zones en présence de ces décollements pour élaborer une paramétrisation pertinente des objets géologiques (en particulier, en termes de définition de réseaux de décollements, géométrie, espacement, symétrie, longueurs caractéristiques...). Cela nous aiderait à identifier pour toute la bande passante sismique les interactions possibles entre hétérogénéités et ondes, avant de pouvoir définir par la suite une loi de contact à l'interface et de l'implémenter dans un code numérique 3D de propagation d'ondes. Cela suppose donc une approche intégrée géologie/mécanique du contact/géophysique.

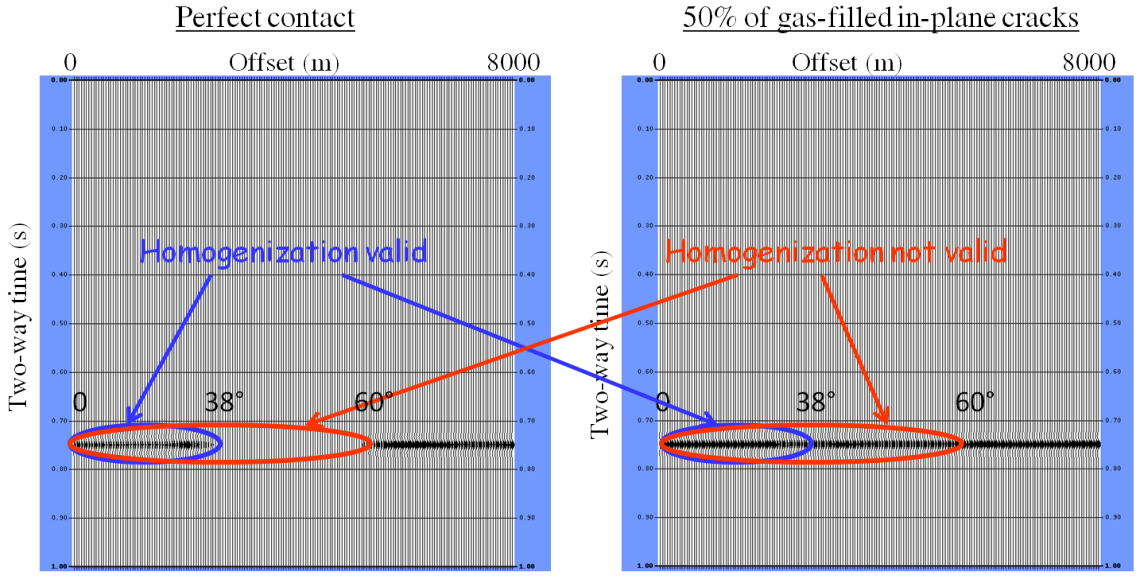

FIGURE 3.7 – *Sismogrammes synthétiques représentant l'onde P réfléchie spéculairement sur une interface craie/granite. L'onde P réfléchie spéculaire est l'onde qui est traitée préférentiellement en sismique réflexion. Gauche : résultats que l'on obtient habituellement à l'aide des simulations numériques traditionnelles en considérant le cas d'une interface avec un contact parfait entre les milieux. Droite : résultat obtenu en tenant compte des diffractions d'ondes engendrées par la présence, à l'interface, de 50% de décollements remplis de gaz. L'amplitude des ondes P réfléchies spéculaires, bien modélisée pour des angles d'ouverture petits, devient largement sous-estimée pour des angles d'ouverture plus grands, notamment au-delà de l'angle de génération de l'onde diffractée propagative.*

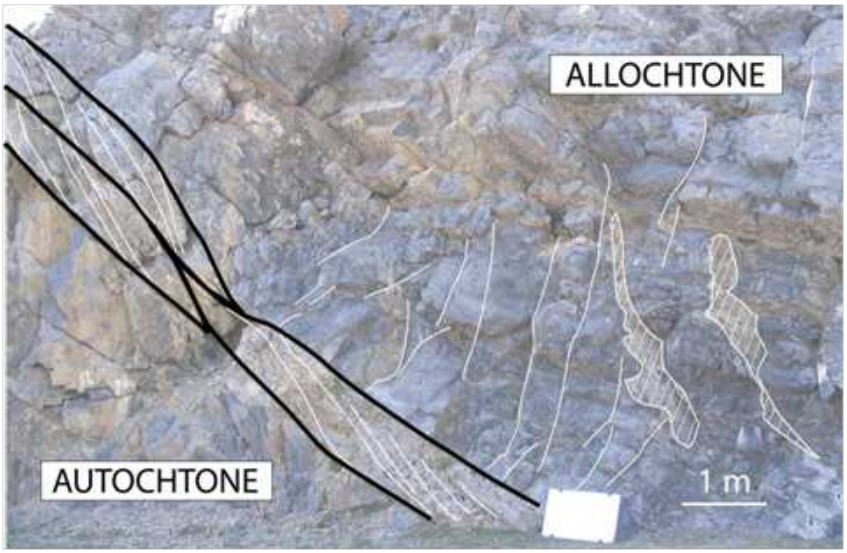

FIGURE 3.8 – *Exemple de faille inverse à la Pierre Saint-Martin (Pyrénées-Atlantiques), analogue à un niveau de décollement. La zone de décollement est constituée d'un empilement de sigmoïdes de déformation de différentes longueurs et épaisseurs dont la courbure et l'orientation de l'axe long sont vraisemblablement reliées à l'intensité de la déformation. Ces sigmoïdes simples s'empilent et s'emboîtent dans des sigmoïdes composites d'ordre supérieur qui vont venir déterminer l'épaisseur du niveau de décollement au sens strict. Mais à plus grande échelle, ces sigmoïdes apparaissent elles-mêmes affectées d'une schistosité oblique par rapport à leur axe long. En fonction de la longueur d'onde incidente, chacune de ces interfaces (sigmoïdes de différents ordres ou bien schistosité) va jouer le rôle de zones de mauvais contact mécanique ou bien être inopérante. On remarquera également la fracturation 3D associée présente dans l'allochtone. (Photo de Bertrand Nivière, Université de Pau et des Pays de l'Adour)*

Chapitre 4

Les ondes de surface en milieu anisotrope

Collaborations

J. Carcione *(Directeur de Recherche, Istituto Nazionale di Oceanografia e di Geofisica Sperimentale - Trieste, Italie)*
F. Cavallini *(Chercheur, Istituto Nazionale di Oceanografia e di Geofisica Sperimentale - Trieste, Italie)*
D. Komatitsch *(Professeur Université Paul Sabatier Toulouse, Laboratoire Géosciences Environnement Toulouse)*

Publications associées

cf Annexe C : [10], [11]
Une copie de l'article [10] a été placée en Annexe D.

———————

4.1 Introduction

Les données de sismique-réflexion acquises en environnement terrestre sont souvent polluées par du bruit cohérent [1], dénommé le "ground-roll", qui est généré par la propagation d'ondes de surface dispersives le long de la zone superficielle du sous-sol. Cette zone altérée est généralement fortement hétérogène avec des propriétés spatio-temporelles variables en fonction de facteurs externes comme, par exemple, les conditions météorologiques (d'où son nom anglophone, "weathered zone" ou WZ). La contamination des données par le ground-roll est particulièrement nuisible dans la mesure où les fortes amplitudes des signaux basses fréquences (BF) des ondes de surface (typiquement, des modes de Rayleigh) dégradent la qualité globale des données et peuvent masquer des informations importantes sur les réflecteurs à la fois dans le domaine spatio-temporel (x,t) et le domaine fréquences-nombres d'onde (f,k) (*cf* Figure 4.1). La suppression de ce bruit cohérent sur les données sismiques est par conséquent un prérequis essentiel pour imager correctement le sous-sol et sa subsurface.

Pour réaliser cette opération, plusieurs techniques évoluant dans différents domaines (méthodes f-k, Tau-p...) ont été développées [Henry, 1994], parmi lesquelles les techniques conventionnelles, reposant sur la séparation fréquentielle entre le signal et le ground-roll (BF), qui peuvent se révéler parfois inefficaces dans le cas d'études de réflecteurs profonds [Welford et Rongfeng, 2004]. D'autres utilisent un filtrage automatique adapté du ground-roll

1. En sismique, le signal dit "utile" fait référence principalement aux réflexions, tandis que tout ce qui est "inutile" (*e.g.*, les multiples, le ground-roll...) est appelé "bruit", qu'il soit cohérent ou non.

en tenant compte de sa variabilité spatiale, ce qui permet d'obtenir des résultats sensiblement meilleurs que le filtrage f-k, surtout en termes de préservation d'amplitudes des ondes de volume dans le cône des proches offsets [Meur *et al.*, 2010].

A l'heure actuelle, une autre possibilité est étudiée pour s'affranchir des effets de la WZ sur la propagation des ondes sismiques (*cf* aussi le projet ANR EMSAPCO2, Chapitre 5). Elle utilise le concept de "source virtuelle" qui repose sur le principe de focalisation par retournement temporel, largement étudié en imagerie médicale ou en acoustique sous-marine. Déclinée à la sismique, la méthode ne nécessite d'enterrer que des capteurs (et non des sources qui demeurent, elles, conventionnelles) et permet de reconstruire par synthèse les sismogrammes qui auraient été créés par une source fictive à l'emplacement des capteurs enterrés [Bonneau *et al.*, 2010]. Cela permet ainsi de s'affranchir des variations de positionnement des capteurs et de la sensibilité aux changements de surface, tout en réduisant les coûts en évitant l'enterrement des sources vibratoires.

Du fait de sa forte variabilité en termes de caractéristiques spatiales et physiques, la WZ a un impact considérable sur la propagation des ondes dans la proche surface, impact qui demeure toutefois aujourd'hui encore mal connu même dans les zones de tectonique calme. Dans les méthodes conventionnelles d'imagerie sismique du sous-sol, un des problèmes récurrents est l'absence de modèles de vitesse suffisamment fiables pour décrire la zone altérée de surface, ce qui conduit à des simulations quelque peu biaisées de la propagation des ondes. A l'inverse, l'analyse du ground-roll permettrait d'obtenir des informations sur les propriétés (liées aux ondes S) de la WZ. Tout le problème consiste donc à étudier conjointement la structure de la WZ et la propagation des ondes de surface dans cette zone. Dans ce cadre, nous avons choisi dans un premier temps de nous focaliser sur le caractère anisotrope de la WZ[2] et d'étudier en détails les conditions d'existence et les propriétés des ondes qui peuvent s'y propager.

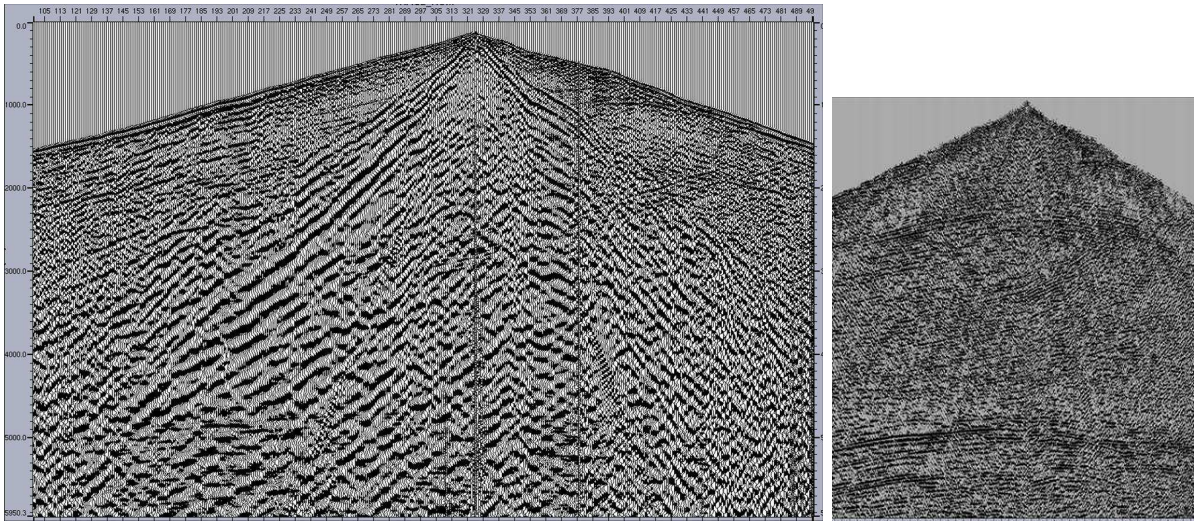

FIGURE 4.1 – *Gauche : Illustration de l'impact du ground-roll (représenté sous la forme d'un cône) sur les données sismiques brutes. Droite : Données sismiques similaires après "filtrage" du ground-roll. (Source : GeoApex Technology Inc).*

2. Il est bien entendu que dans la hiérarchie des difficultés liées à la connaissance de la WZ, l'anisotropie se place après certaines autres caractéristiques telles que, par exemple, l'hétéogénéité...

4.2 Clarification de la terminologie et Simulation de la propagation

Un demi-espace élastique homogène isotrope peut supporter trois types d'ondes de volume : une onde P et deux ondes S (SV et SH), dont le vecteur polarisation est soit parallèle (cas de l'onde P), soit perpendiculaire (pour les ondes S) au vecteur lenteur. La polarisation des ondes S, par rapport à la surface libre du demi-espace, est soit verticale (pour l'onde SV), soit horizontale (pour l'onde SH). Seules les ondes P et SV peuvent être couplées à la surface (plane) libre d'un solide élastique homogène isotrope. Une onde de surface de type Rayleigh, résultant de la combinaison linéaire des ondes de volume non homogènes P et S, se propage alors le long de la surface du demi-espace isotrope, sans dispersion et avec une vitesse constante proche de la vitesse des ondes S dans le milieu. L'énergie transportée par cette onde de surface, dont la polarisation est elliptique dans le plan sagittal, est concentrée dans une couche, d'épaisseur une longueur d'onde, juste sous la surface libre. Un point source génère, outre les fronts d'onde P et S et le front d'onde de Rayleigh, une onde latérale S qui connecte les ondes P et S.

En présence d'anisotropie, la propagation d'ondes présente des différences notables par rapport au cas isotrope. Le vecteur polarisation des trois ondes de volume n'est ni nécessairement parallèle, ou perpendiculaire au vecteur lenteur. Excepté pour des directions de propagation spécifiques, l'onde quasi-P (qP) et les ondes quasi-S (qS) peuvent être couplées à la surface d'un demi-espace élastique, et contrairement au cas isotrope, l'onde de surface en milieu anisotrope peut résulter de la combinaison linéaire de trois, deux, ou même une seule, onde(s) de volume non homogène(s). Le comportement anisotrope du milieu modifie donc considérablement l'existence et la structure des ondes de surface qui se propagent à la surface libre d'un milieu. Le changement le plus flagrant est certainement le fait qu'un milieu anisotrope, contrairement au cas isotrope, peut supporter de nombreuses ondes de surfaces supersoniques (*i.e.*, des ondes de surface ayant dans leurs composantes au moins une onde de volume homogène)[3]. En outre, les propriétés des ondes de surfaces dépendent essentiellement de l'orientation de la surface libre ainsi que de leur direction de propagation.

L'anisotropie induit par conséquent des difficultés, parfois considérables, pour étudier explicitement et analytiquement la propagation des ondes. Même si des tentatives pour obtenir des équations séculaires explicites ont été couronnées de succès, la plupart ont été obtenues uniquement pour des anisotropies spécifiques avec un haut degré de symétrie. Peu de problèmes en élastodynamique ont des solutions analytiques, aussi ils sont souvent étudiés au moyen d'approches semi-analytiques. Néanmoins, des doutes persistent sur la fiabilité de leurs solutions. Les simulations numériques deviennent par conséquent très attractives pour décrire la propagation des ondes de surface générée par un point source à une surface libre qui peut différer d'un plan de symétrie d'un milieu anisotrope. Être capable de simuler numériquement et de manière précise la propagation des ondes est essentiel non seulement pour le domaine de la sismique, mais aussi pour les domaines de la sismologie et des ultrasons, où les matériaux possèdent généralement des propriétés anisotropes décrites dans leur forme la plus générale, *i.e.*, par 21 coefficients élastiques.

Dans un premier temps, nous avons passé en revue les propagations harmoniques et transitoires des ondes à la surface de milieux anisotropes (*e.g.*, milieux cubiques, hexagonaux...), en clarifiant par la même occasion la terminologie, souvent confuse et parfois contradictoire,

3. Le caractère supersonique ou subsonique d'une onde de surface en contexte anisotrope est lié à la notion d'onde de volume limite. J'invite le lecteur à consulter [Favretto-Cristini *et al.*, 2011] en Annexe D, et plus particulièrement ses pages 654-655 pour de plus amples explications.

attribuée aux différents types d'ondes de surfaces [Favretto-Cristini *et al.*, 2011] [4].

Par la suite, nous avons utilisé deux méthodes numériques "full-wave" 3D pour résoudre le problème de propagation des ondes de surface sans aucune approximation sur le type de symétrie des milieux anisotropes et sur l'orientation de la surface libre. Ces deux méthodes, *i.e.*, la méthode pseudo-spectrale Fourier-Chebyshev (PSM) et la méthode des éléments finis spectraux (SEM), sont très précises car elles reposent sur des approximations spectrales d'ordre élevé du champ d'onde pour calculer les dérivées spatiales. La PSM est basée sur des opérateurs différentiels globaux pour lesquels le champ est décrit en termes de polynômes de Fourier et de Chebyshev [Priolo *et al.*, 1994, Carcione, 2007], tandis que la SEM est une extension de la méthode des éléments finis qui utilise les polynômes de Legendre comme fonctions d'interpolation [Komatitsch et Vilotte, 1998, Komatitsch *et al.*, 2000]. Très flexibles, les deux méthodes peuvent obtenir les solutions pour des milieux hétérogènes quelconques car l'espace est discrétisé suivant un maillage dont les points de la grille peuvent avoir des valeurs différentes de propriétés élastiques. Nos simulations se sont dans un premier temps focalisées sur les milieux de symétries cubique et hexagonale (cuivre, apatite et zinc) pour pouvoir les comparer à des solutions analytiques connues, avant de traiter dans un second temps des cas plus complexes de milieux hétérogènes, pour lesquels il n'existe pas de solution analytique, montrant ainsi que les algorithmes peuvent également traiter de grandes variations d'impédance aux interfaces [Komatitsch *et al.*, 2011].

A des fins d'illustration, la Figure 4.2 représente des instantanés aux temps de propagation 28 μs, 34μs, 40μs et 46μs, calculés en utilisant la SEM, à la surface (001) d'un cristal de cuivre 3D. La source placée en surface a pour fréquence centrale 200 kHz. Outre les fronts d'onde associés aux ondes P, SV et SH, le front d'onde de Rayleigh, dominant, peut clairement être observé. La Figure 4.3 présente une comparaison d'un instantané, obtenu par la PSM, à la surface libre (100) d'un cristal de cuivre avec les fronts d'onde obtenus par [Deschamps et Huet, 2009] au moyen du formalisme des ondes planes non homogènes. On peut noter en particulier le bon accord correspondant au prolongement des points de rebroussement qS, dû à des phénomènes de diffraction, formant ainsi deux quasi-ellipses. Dans la mesure où la simulation est 2D avec la source (de fréquence dominante 200 kHz) placée au centre du modèle, seules les ondes de volume sont imagées, d'où la différence observée avec l'instantané de la Figure 4.2 qui est, lui, dominé par les ondes de surface.

4.3 Conclusions et Perspectives

La présence de ground-roll sur les données sismiques terrestres est particulièrement nuisible pour une bonne imagerie du sous-sol et de sa subsurface. Que l'on veuille obtenir de ce bruit cohérent dispersif des informations sur les propriétés physiques du sous-sol, ou que l'on veuille l'éliminer pour améliorer l'interprétation sismique, il est nécessaire de comprendre au préalable les phénomènes physiques sous-jacents afin de pouvoir le simuler avec réalisme. Dans ce cadre, nous avons étudié la physique de la propagation des ondes de surface à la surface libre d'un milieu élastique anisotrope, et nous avons utilisé des algorithmes numériques qui permettent de simuler en 3D et avec une grande précision cette propagation.

Ce travail constitue la première étape d'un projet sur l'étude des ondes de surface et d'interface dans les milieux complexes (anisotropes, poreux...) qui trouve des applications en exploration sismique. Dans ce cadre, il serait intéressant d'étendre notre étude académique, par exemple au

4. J'invite le lecteur à consulter cet article en Annexe D.

cas des ondes de type Stoneley-Scholte. Par ailleurs, l'exploration sismique des régions arctiques, au-delà des problèmes logistiques, peut par exemple présenter des difficultés liées à la grande complexité de la proche surface. Les dépôts successifs et l'érosion glaciaire ont produit une géomorphologie complexe avec de rapides changements lithologiques. En outre, la présence de permafrost et de couches de glace saisonnières induisent des variations rapides et importantes, à la fois latérales et verticales, des propriétés élastiques de la subsurface au niveau de la transition entre les zones gelées et les zones dégelées. Ceci induit des variations latérales extrêmes des signaux sismiques, avec la présence de bruit cohérent à forte amplitude généré par la propagation des ondes de surface ou des ondes de plaque (de type ondes de Lamb) [Strobbia *et al.*, 2009].

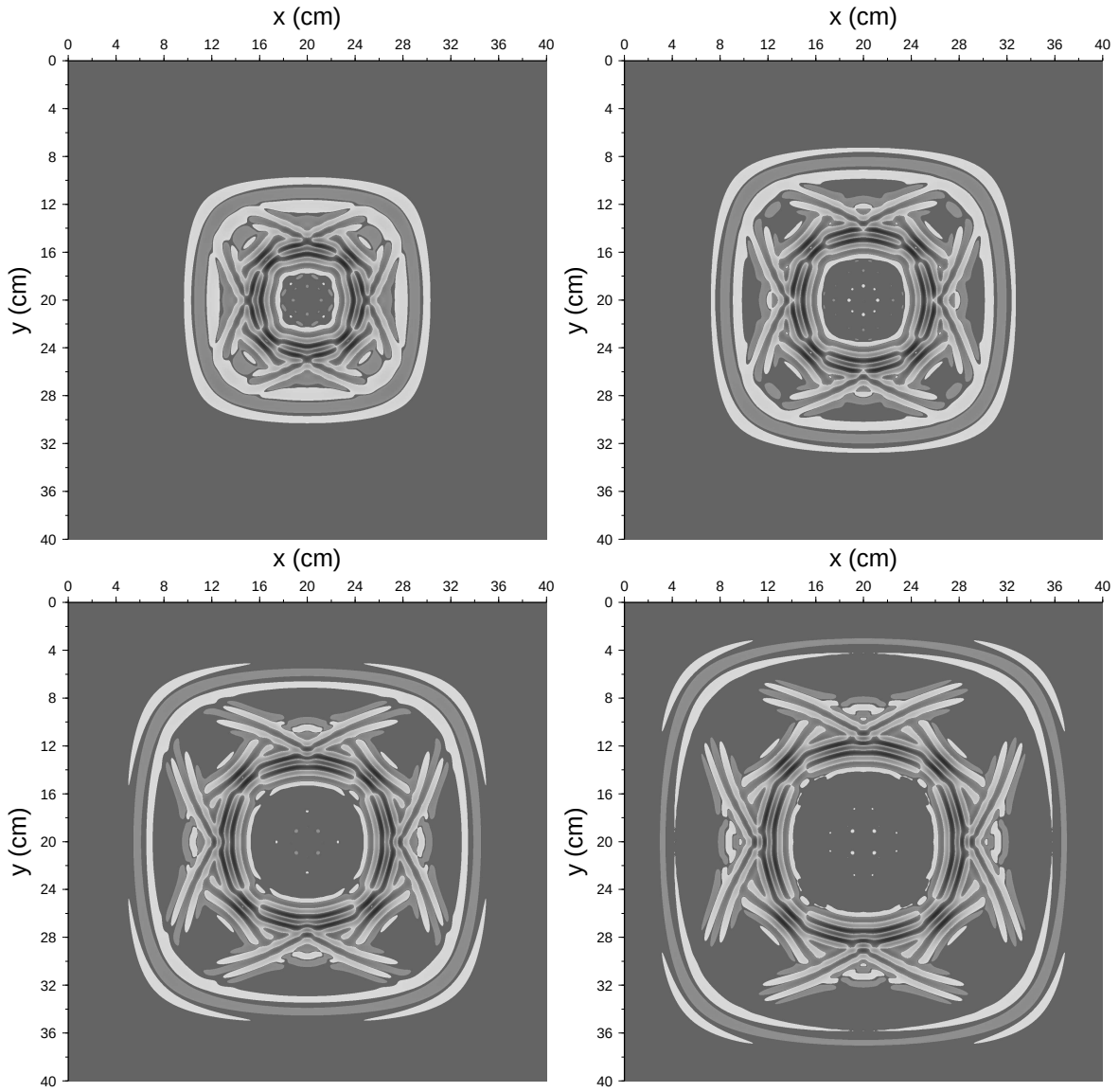

FIGURE 4.2 – *Instantanés aux temps de propagation 28µs, 34µs, 40µs et 46µs (calculés en utilisant la SEM 3D) à la surface (001) d'un cristal de cuivre. La source placée en surface a pour fréquence centrale 200 kHz.*

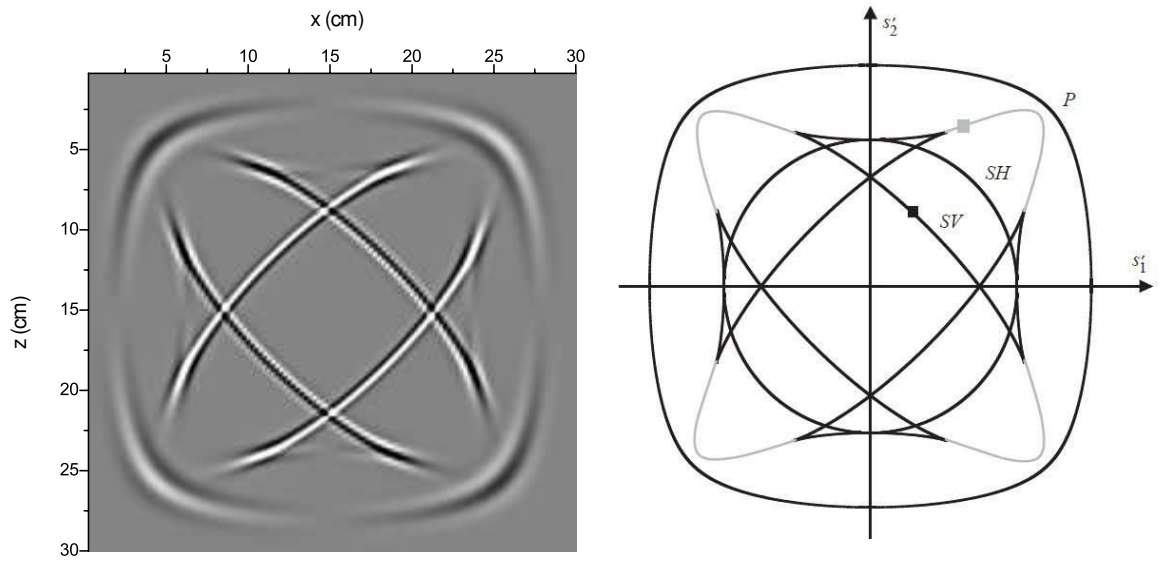

FIGURE 4.3 – *Gauche : Instantané au temps de propagation 36µs (obtenue avec la PSM 2D) à la surface libre (010) d'un cristal de cuivre. Une force verticale avec une fréquence dominante de 200 kHz est appliquée en son centre. Droite : Courbes polaires de la vitesse de l'énergie dans le plan de la surface libre (D'après [Deschamps et Huet, 2009]). Les lignes noires et grises correspondent aux ondes de volume limites exceptionnelles homogènes et non homogènes.*

Chapitre 5

La surveillance du stockage géologique du CO2

Collaborations

J. Blanco *(Physeis Consultant)*
D. Broseta *(Professeur, Université de Pau et des Pays de l'Adour, Laboratoire des Fluides Complexes et leurs Réservoirs)*
P. Cristini *(Chargé de Recherche CNRS, LMA)*
P. Khalid *(Doctorant, Université de Pau et des Pays de l'Adour, Thèse soutenue le 06/01/2011)*
G. Le Touzé *(Post-doctorant, LMA, 01/09/2008 - 31/08/2010)*

Publications associées

cf Annexe C : [1], [57]

Communications associées

cf Annexe C : [22], [23]

5.1 Introduction

Les enjeux de la réduction des gaz à effet de serre dans l'atmosphère sont fondamentaux pour la préservation du climat et l'intégrité des océans. En France, l'objectif d'ici 2050 est de diviser par quatre les émissions des gaz à effet de serre. Parmi ceux-ci se trouve le CO2, un gaz présent naturellement dans l'atmosphère à un taux raisonnable et qui s'échange entre les différents compartiments terrestres (océan, biomasse..). Cependant, depuis la révolution industrielle, l'activité humaine dégage des quantités de CO2 de plus en plus importantes et les réservoirs naturels à la surface du globe ne peuvent malheureusement plus accomoder cette croissance d'origine anthropique. En conséquence, on assiste à une augmentation continue de la concentration en CO2 dans l'atmosphère. A titre d'exemple, en 2009 a été atteint le record de 388 ppm de CO2 présent dans l'atmosphère [1], quantité jamais observée depuis 800 000 ans.

Depuis les années 90, une prise de conscience collective à l'échelle mondiale, du moins des scientifiques, a permis d'engager une réflexion sur les moyens à mettre en place pour lutter efficacement contre l'augmentation de CO2 dans l'atmosphère. Il est certain que nos modes de vie actuels sont très fortement dépendants des énergies fossiles, et il est complètement illusoire de penser que nos sociétés puissent se passer totalement (du moins à court terme) de ces énergies. Néanmoins, des mesures sont proposées pour diminuer leur utilisation et/ou les rendre

1. Rapport de l'Académie des Sciences (Institut de France) du 26 octobre 2010 "Le changement climatique".

"propres" [2], parmi lesquelles encourager la diminution de consommation énergétique, améliorer l'efficacité énergétique, promouvoir les énergies renouvelables ou faiblement émettrices de CO2, accroître la surface de la biomasse, stocker le CO2 dans des réservoirs géologiques souterrains... Si prometteuses soient-elles, aucune de ces solutions prises séparément n'est une solution miracle qui pourra résoudre à elle seule le problème global. Seule une combinaison de ces mesures peut être efficace.

La séquestration géologique est considérée par la communauté internationale comme l'un des moyens potentiellement efficaces pour réduire le taux de CO2 dans l'atmosphère. Le gaz est capté directement à la sortie des sources d'émission conséquente (*e.g.*, les centrales thermiques, les usines sidérurgiques, les raffineries et les cimenteries qui génèrent près de la moitié de la totalité des émissions de CO2), puis transporté à l'état supercritique (*i.e.*, à une température supérieure à 31°C et une pression supérieure à 74 bars) essentiellement par gazoducs, avant d'être stocké dans des réservoirs géologiques profonds pour de très longues périodes. Même si le principe apparaît simple, les problèmes potentiels posés par cette technique sont néanmoins nombreux et concernent tous les stades du processus, de la capture (par procédés post-combustion, oxy-combustion ou précombustion) à la surveillance du site de stockage, en passant par le transport, l'injection et la séquestration du CO2. Cela nécessite donc un examen approfondi des différentes étapes et la définition de critères de sécurité associés.

Avant toute chose, le site potentiel de stockage doit être rigoureusement sélectionné : il doit, si possible, se situer près d'une source d'émission importante de CO2 et avoir bien évidemment une capacité de stockage élevée. Les sites intéressants peuvent être en environnement onshore ou offshore et sont généralement de type aquifères salins profonds (*e.g.*, le site pilote emblématique de Sleipner en Mer du Nord (*cf* Figure 5.1)), champs d'hydrocarbures déplétés en fin d'exploitation (*e.g.*, le site de Weyburn au Canada pour lequel l'injection de CO2 participe à la récupération assistée de pétrole (EOR), ou le site de Rousse en France), ou veines de charbon non exploitées (*e.g.*, le projet RECOPOL en Pologne) [Chadwick, 2008].

La caractérisation du site est une étape cruciale qui permet de définir de manière optimale les paramètres qui vont influencer l'injectivité (*i.e.*, les caractéristiques de la formation géologique, la présence d'hétérogénéités, les variations de la perméabilité, le comportement in situ du CO2 avec les fluides de la formation, les effets de la pression sur l'intégrité de la roche couverture, le nombre, l'espacement et l'orientation des puits...), mais aussi d'anticiper les risques associés à l'injection et au stockage du CO2 et de prédire le comportement du réservoir sur le long terme. Ces risques sont essentiellement d'origine géomécanique et concernent les zones de "faiblesse" (*i.e.*, les puits, les failles et la roche couverture). Les fortes pressions mises en jeu lors de l'injection du CO2 peuvent créer ou réactiver des failles ou des systèmes de fractures qui peuvent devenir ainsi des chemins potentiels de fuite du gaz vers les formations géologiques supérieures. Les risques sont également d'origine géochimique : les fluides à forte salinité enrichis de CO2 sont fortement corrosifs et peuvent endommager les puits, le réservoir ou la roche couverture.

La surveillance (ou monitoring) 4D des réservoirs de CO2 consiste à comparer les acquisitions géophysiques 3D réalisées à différentes étapes du stockage à des données de référence (lignes de base) acquises avant injection durant des mois. Cela permet d'assurer le suivi de la géométrie et du volume de la bulle de CO2 dans la formation de stockage (*cf* Figure 5.2) et de détecter

2. Depuis quelques années en France, le Programme Interdisciplinaire Energie (PIE), très actif, regroupe régulièrement des scientifiques et industriels de différentes disciplines pour réfléchir et proposer des solutions, au travers de projets innovants, sur différents aspects allant des bioénergies aux aspects socio-économiques, en passant par la thermique, l'électricité, le photovoltaïque, la production et le stockage d'H2, le solaire, le nucléaire, le captage et le stockage du CO2...

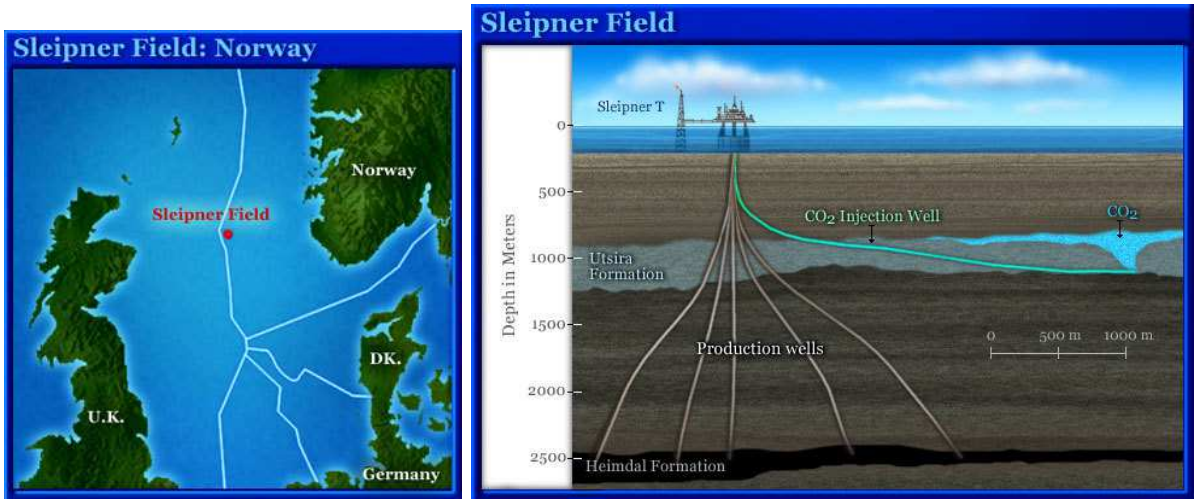

FIGURE 5.1 – *Site offshore de Sleipner en Mer du Nord, situé à 250 kilomètres à l'ouest de Stavanger en Norvège. Le projet Sleipner constitue le premier exemple de stockage de CO2 dans un aquifère salin profond. Statoil exploite le gaz naturel de la formation de Heimdal. Comme ce gaz est inutilisable en l'état puisqu'il contient près de 9% de CO2, on procède à sa séparation du CO2 avant de réinjecter ce CO2 dans la formation d'Utsira composée d'une couche de grès épaisse de 200 mètres et gorgée d'eau salée. La formation d'Utsira a une porosité et une perméabilité élevées, si bien que le CO2 se déplace rapidement sur le côté ou vers le haut. Entre 1996 et 2008, environ 11 millions de tonnes de CO2 ont été injectés dans la formation Utsira. (Source : SEED).*

précocement d'éventuelles fuites vers les formations supérieures, afin de pouvoir y remédier rapidement et efficacement. Dans ce cadre, les méthodes géophysiques actives ou passives, de type électrique, gravimétrie, électromagnétique, sismique ou microsismique, apparaissent comme des outils particulièrement intéressants car elles ont l'avantage de proposer une vision à l'échelle du réservoir.

5.2 Le projet EMSAPCO2

Le monitoring des réservoirs de CO2 est un élément clé des directives de la Commission Européenne (*cf* CO2 GeoNet Joint Researches...). Outre l'absolue nécessité d'assurer que les opérations de stockage auront un impact négligeable sur la santé et la sécurité des hommes, de la faune et de la flore, ainsi que sur l'environnement (notamment sur les ressources en eau du sous-sol), il est important, pour l'acceptabilité sociétale et pour un déploiement large de la méthodologie, de prouver que tous les risques potentiels ont été examinés et minimisés (*i.e.*, choix scientifique du meilleur site de stockage et du plus sûr, techniques développées pour surveiller la sécurité du site durant l'injection et la post-injection...), et surtout qu'il existe des stratégies en cas de fuites et des technologies de remédiation. Malheureusement les critères sont nécessairement spécifiques au site de stockage et toutes les possibilités de sites doivent être envisagées en recherche amont.

De 2005 à 2008, l'Agence Nationale de la Recherche (ANR) a financé dans le cadre du programme thématique "Captage et Stockage du CO2" plusieurs projets explorant les techniques (et les risques associés) de captage, de transport, d'injection et de stockage du CO2, ainsi que

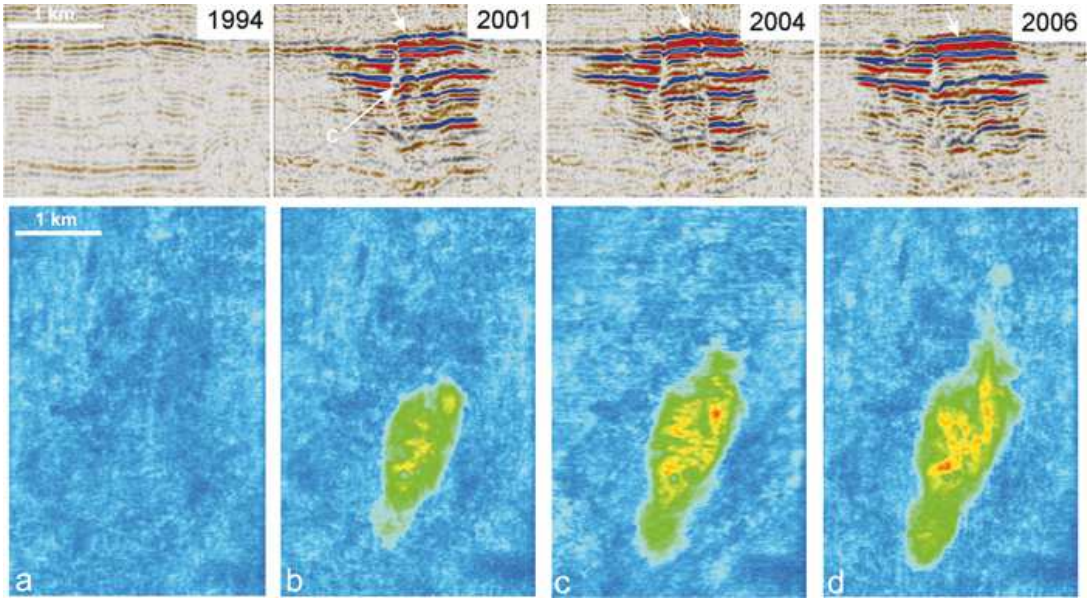

FIGURE 5.2 – *Monitoring sismique 4D de la formation d'Utsira à Sleipner. Les données sismiques ont été acquises avant injection (1994) et après injection (2001, 2004, 2006). Sur les images du haut, les réflexions observées proviennent des lieux où le CO2 s'est accumulé, c'est-à-dire essentiellement autour et au-dessus du point d'injection dans des fines couches d'argiles. On voit que le CO2 est confiné dans le réservoir sous la roche couverture. Les images du bas représentent les amplitudes absolues (cumulées pour toutes les couches) illustrant le développement de la bulle de CO2 au cours du temps. (Source : British Geological Survey).*

quelques projets traitant des techniques de surveillance des sites et de leur mise en oeuvre sur le terrain. Le Projet ANR EMSAPCO2 (« Développement des méthodes Electro-Magnétiques et Sismique Active et Passive pour la surveillance des réservoirs de stockage du CO2 », décembre 2007-septembre 2010), coordonné par la CGG Véritas, faisait partie de ceux-là. Ce projet impliquait partenaires académiques et industriels (CGG Véritas, BRGM, Institut Français du Pétrole et Energies Nouvelles, Magnitude, Institut Langevin (Laboratoire Ondes et Acoustique), Université de Pau (Laboratoire des Fluides Complexes et leurs Réservoirs - LFC-R), CNRS (LMA)) et avait pour objectif de tester la sensibilité des méthodes géophysiques à la présence de CO2, aux variations de paramètres internes ou externes au stockage... Le projet EMSAPCO2 était en ce sens complémentaire aux projets GEOCARBONE PICOREF (2005) et GEOCARBONE MONITORING (2005), et au projet HPPPCO2 (2007). Il s'articulait autour de quatre tâches (faisabilité sismique, applicabilité pratique de l'électromagnétisme, micro-sismique à partir d'antennes, source virtuelle) et le LMA était impliqué dans deux d'entre elles (tâches 1 et 3). J'étais responsable scientifique pour l'Université de Pau (laboratoires LFC-R et MIGP) jusqu'à mon départ de Pau et le transfert de ce projet sur Marseille ; j'étais responsable scientifique pour le LMA par la suite.

Je ne décrirai pas la tâche 3 qui concerne plus particulièrement P. Cristini, G. Le Touzé et J. Blanco et pour laquelle mon implication (principalement de l'expertise et de l'accompagnement) a été moindre. Néanmoins, dans le cadre du post-doctorat de G. Le Touzé, un algorithme de décomposition morphologique des signaux sismiques sur une antenne de capteurs (*cf* Figure 5.3), intitulé logiciel "ArrayChirpDecomp" (déposé en août 2010), a été développé pour la détection, le filtrage et la caractérisation des événements micro-sismiques (*i.e.*, évènements

sismiques naturels induits par l'évolution du comportement géomécanique du réservoir et/ou de sa couverture) dans le cadre d'une surveillance de réservoir de stockage de CO2. Il peut également s'appliquer à toutes données issues de propagation d'ondes (sismiques, acoustiques...). L'algorithme a pour base des techniques de décomposition atomique Matching Pursuit. On part du principe que les signaux sismiques de l'antenne sont composés d'évènements (de différentes ondes) que l'on retrouve d'une trace à l'autre sur l'antenne avec certaines variations (décalage temporel, déphasage...). L'algorithme de décomposition cherche à extraire les ondes en exploitant les informations communes entre les traces, tout en autorisant des degrés de liberté pour certains paramètres susceptibles d'évoluer entre les traces (position temporelle, phase...). Cet algorithme comporte plusieurs innovations, dont une optimisation récursive de la décomposition Matching Pursuit, et a été testé avec succès sur des données synthétiques et réelles. Outre son efficacité à caractériser les arrivées pour un événement donné, l'algorithme a montré de manière inattendue ses capacités de débruitage dans le cas de bruit cohérent (bruit de capteur). Cette étude a fait l'objet d'une collaboration avec la société Physeis Consultant (J. Blanco) et des publications communes, dont [Touzé *et al.*, 2010].

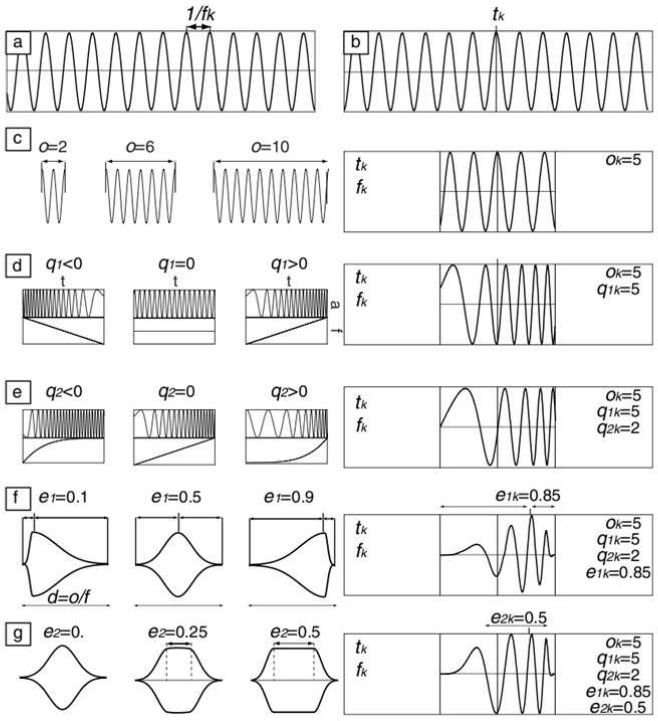

FIGURE 5.3 – *Dictionnaire de chirplets utilisé pour la décomposition morphologique des signaux. Les attributs morphologiques sont (a) une fréquence centrale, (b) un temps d'arrivée (position du centre de l'enveloppe), (c) une durée, (d) un taux de modulation de fréquence, (e) un type de modulation de fréquence, (f) une asymétrie d'enveloppe, (g) un plateau constant de l'enveloppe. D'après [Bardainne, 2005]*

Par ailleurs, j'ai collaboré avec d'autres partenaires (D. Broseta et ses collaborateurs du Laboratoire LFC-R) à la description des propriétés sismiques des réservoirs faiblement saturés en gaz, en particulier dans des conditions proches du point bulle, dans le cadre de la tâche 1. L'intérêt de cette étude résidait dans la définition de marqueurs pertinents pour la détection de fuites de CO2. Il a été suggéré qu'au voisinage du point critique (31°C, 74 bars pour le CO2

pur, ce qui correspond à environ 800-1000 m de profondeur), l'approche Gassmann-Wood qui fait l'hypothèse de "phases gelées" (*i.e.*, transfert de masse et de chaleur négligeable entre les phases sur une échelle de temps comparable à la période sismique) pouvait ne pas être valide pour décrire correctement les propriétés sismiques des fluides enrichis en CO2. Aux fréquences sismiques basses, il semble qu'il faille plutôt orienter la modélisation vers une approche thermodynamique (du type Landau-Lifshitz) qui prenne en compte les échanges de matière et de chaleur au passage des ondes, et de ce fait, qui décrit l'équilibre thermodynamique entre les phases [Nichita *et al.*, 2010, Khalid, 2011]. Cette approche pourrait expliquer la décroissance brutale de la vitesse des ondes P observée sur les données réelles en contexte de réservoirs faiblement saturés en gaz (réservoirs de stockage de CO2 lors de l'injection, phénomène de "Fizz water"...) (*cf* Figure 5.4). La collaboration avec D. Broseta s'est traduit par des communications communes (*cf* Publications [22], [23] en Annexe C).

Mon implication dans le projet EMSAPCO2 a concerné plus particulièrement la tâche 1. En collaboration avec P. Cristini, nous avons évalué la pertinence d'utiliser les réflexions spéculaires et non spéculaires des ondes sismiques comme outil d'analyse et de monitoring du stockage de CO2. En particulier, nous avons cherché à savoir si ces ondes pourraient renseigner sur l'existence de poches de CO2 qui aurait migré à travers le sous-sol vers la surface et qui serait piégé au niveau des interfaces sous la roche couverture.

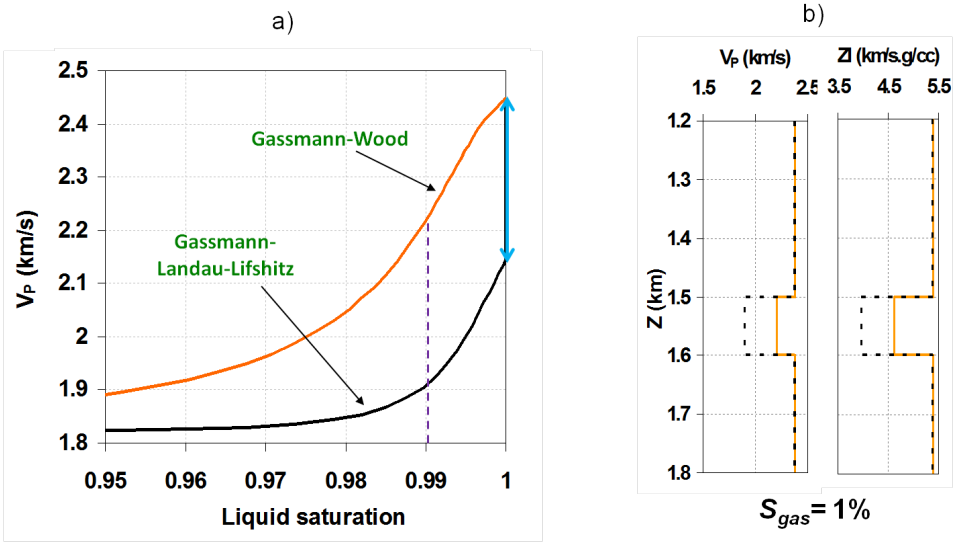

FIGURE 5.4 – *Paramètres sismiques d'un milieu poreux saturé par un mélange variable eau+CO2, pour des fréquences sismiques basses et des conditions proches du point bulle : comparaison des résultats issus des méthodes de Gassmann-Wood et de Gassmann-Landau-Lifshitz (équilibre thermodynamique). a) Vitesse des ondes P en fonction de la saturation en eau. A noter la discontinuité de la vitesse pour une saturation en CO2 proche de 0% prédite par la méthode de Gassmann-Landau-Lifshitz (dans ce cas, la compressibilité du gaz est augmentée, et la vitesse des ondes P réduite, à cause de la conversion du gaz en liquide quand la pression augmente). b) Vitesse des ondes P et impédance pour une saturation en gaz de 1%. D'après [Broseta* et al.*, 2009].*

5.3 Influence des poches de CO2 sous la roche couverture

Nous nous sommes placés dans un contexte de post-injection. Pour simplifier le problème, nous avons supposé d'une part, que le CO2 s'était diffusé (plus ou moins) uniformément dans le réservoir poreux avant de migrer massivement vers la surface du réservoir, et d'autre part, que cette migration donnait lieu ainsi à une accumulation de CO2 au sommet du réservoir sous la roche couverture sous la forme de zones compactes mais divisées (ci-après désignées bulles). Par ailleurs, nous avons considéré que la saturation en CO2 dans les bulles était plus importante que celle dans le réservoir et que leurs dimensions s'agrandissaient au fil du temps (*cf* Figure 5.5). Dans un premier temps, nous n'avons pas fait d'hypothèses a priori sur la nature et la géométrie du réservoir de stockage (*e.g.*, aquifère, piège structural de type anticlinal...). Néanmoins, il est à noter que dans le cas d'un réservoir structural de type anticlinal, la géométrie des bulles de CO2 suivront les courbures de l'anticlinal dans les directions longitudinale et transversale au plan d'incidence, d'où une possibilité de création de bulles étirées suivant une direction privilégiée. Par contre, nous avons fait l'hypothèse que la roche couverture est suffisamment mince pour pouvoir être représentée par une surface dans les modélisations.

Avant de modéliser la propagation des ondes sismiques au voisinage de l'interface représentant la roche couverture, et d'étudier ainsi l'impact de la présence des bulles de CO2 sous cette interface sur les attributs sismiques, il était impératif d'identifier au préalable les longueurs caractéristiques mises en jeu dans le problème, en particulier la zone spatiale de l'interface qui affecte le champ d'onde réfléchi (*i.e.*, la zone de Fresnel à l'interface). En effet, seules les bulles de CO2 présentes dans cette zone affecteront réellement la réponse de l'interface (*cf* Chapitre 2).

Par souci de simplification, nous avons supposé par la suite que la distribution de bulles était périodique (ou quasi-périodique) le long de l'interface, ou tout du moins à l'intérieur de la Zone de Fresnel à l'Interface[3]. Il est bien connu en acoustique, en contrôle non destructif et en optique, qu'une distribution de propriétés (physiques et/ou géométriques) latéralement hétérogènes agit généralement comme un réseau de diffraction qui, par interférences constructives et destructives, va générer non seulement les réflexions habituelles, dites "spéculaires" (ou diffractions d'ordre 0), mais également des réflexions dites "non spéculaires" (ou diffractions d'ordre élevé $\pm$ 1, $\pm$ 2...) propagatives. Bien entendu, les ondes diffractées d'ordre 0 demeurent les plus énergétiques, cependant certaines ondes diffractées d'ordre élevé peuvent transporter suffisamment d'énergie pour être enregistrées aux capteurs positionnés en surface, et ainsi fausser l'interprétation et le bilan énergétique si l'on n'en tient pas compte (*cf* Chapitre 3). Par conséquent, dans le cadre de notre problématique, il était intéressant de déterminer si les réflexions non spéculaires engendrées par la présence des bulles de CO2 sous la roche couverture pouvaient être un moyen de surveillance du stockage du CO2. Pour que le réseau de diffraction soit pleinement actif et puisse générer des ondes diffractées d'ordre élevé, la zone de Fresnel à l'interface doit contenir un nombre suffisant (au moins une dizaine pour un résultat optimal) de bulles de CO2. Par ailleurs, le rapport entre la longueur d'onde spatiale Λ du réseau et la longueur d'onde incidente λ_{inc} va conditionner fortement le régime de diffraction. Par exemple, si $\Lambda \ll \lambda_{inc}$, le régime quasi-statique s'applique, les diffractions d'ordre élevé sont évanescentes (à fort taux d'évanescence) et la réflectivité de l'interface s'obtient en homogénéisant ses propriétés ; pour $\Lambda \geq \lambda_{inc}$, le réseau est actif, les diffractions d'ordre élevé sont propagatives et la réflectivité de l'interface ne peut plus être obtenu simplement en homogénéisant ses propriétés [Baik et Thompson, 1984].

3. Cela peut être considéré comme un scénario possible.

L'existence et la direction de propagation des différentes ondes diffractées d'ordre 0 et d'ordre élevé peuvent être facilement prédites par des techniques graphiques classiques reposant sur les surfaces de lenteur [Crandall, 1970]. Le principe est que les vecteurs d'onde $k^n_{P,S\,diff}$ des ondes P et S diffractées d'ordre n sont définis tels que leurs composantes horizontales $p^n_{P,S\,diff}$ doivent satisfaire la condition (analogie avce la loi de Bragg) :

$$p^n_{P,S\,diff} = p_{inc} + n\,\frac{2\pi}{\Lambda}$$

où p_{inc} est la composante horizontale du nombre d'onde incident, n est un entier relatif qui caractérise l'ordre de diffraction. Dans le cadre de notre problématique, nous avons considéré une configuration type de réservoir de stockage de CO2 constitué par des grès et surmonté par des marnes. Par souci de simplification, nous avons supposé que les grès ne contenaient pas de CO2, ce dernier étant concentré au voisinage de l'interface marnes/grès sous forme de bulles constituées de grès saturés par un mélange variable d'eau et de CO2 et distribuées suivant une périodicité $\Lambda = \lambda_{inc}$.

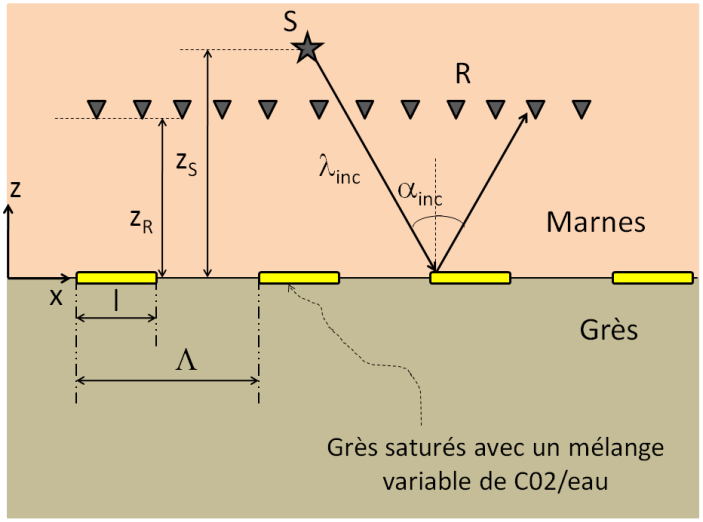

FIGURE 5.5 – *Configuration de l'étude*

La Figure 5.6 prédit l'existence et la direction de propagation des ondes P et S réfléchies et transmises (d'ordre $n = 0$) et des ondes diffractées P et S d'ordre élevé ($n \neq 0$) par l'interface marnes/grès (*cf* Tableau 5.1) avec un réseau de diffraction tel que $\Lambda = \lambda_{inc}$, pour deux angles d'incidence $\alpha_{inc} = 0$ et $\alpha_{inc} = 45°$, et lorsque l'onde incidente est une onde P dans les marnes. Nous constatons que même lorsque l'onde P frappe l'interface sous incidence normale, deux ondes S diffractées propagatives d'ordre $\pm$ 1 pourront être observées sur les capteurs, selon l'énergie qu'elles transporteront. Cette énergie sera essentiellement conditionnée par le contraste d'impédance entre le contenu des bulles et les milieux environnants et la concentration de bulles à l'interface . A noter que si l'onde incidente est une onde S, des résultats similaires sont obtenus.

La configuration choisie pour la modélisation numérique est décrite dans la Figure 5.5. La source S qui est une source ponctuelle explosive est située à $x_S = 3\,190\,m$ et $z_S = 2\,000\,m$, tandis que la ligne de récepteurs R (au nombre de 191 répartis tous les 20 mètres) est localisée à $z_R = 1\,500\,m$ et couvre la zone $x_R = 2\,000\,m$ à $x_R = 5\,800\,m$. Les récepteurs R sont situés légèrement plus bas que la source afin de pouvoir discriminer les différentes arrivées des ondes.

Milieux / Propriétés	Densité ρ (kg/m^3)	Vitesse V_P (m/s)	Vitesse V_S (m/s)
Marnes	1 900	2 000	1 200
Grès	2 050	2 050	600

TABLE 5.1 – *Propriétés des milieux (marnes et grès).*

Nous avons fait l'hypothèse d'une interface plane avec des bulles à géométrie très étirée dans une direction (*i.e.*, la géométrie "strip-cracks" qui est de dimension infinie, ou au moins égale au diamètre de la zone de Fresnel à l'interface dans la direction perpendiculaire au plan d'incidence, et de dimension finie mais variable dans la direction incluse dans le plan d'incidence). Le problème considéré peut être ramené à un problème 2D. Par ailleurs, nous avons considéré deux fréquences centrales pour la source (20 Hz et 40 Hz), différents contenus (*cf* Tableau 5.2) et différentes concentrations de bulles, tout en conservant les spécificités du réseau $\Lambda = \lambda_{inc}$. Le code utilisé pour la modélisation numérique 2D de la propagation des ondes dans la configuration choisie est le code SPECFEM basé sur les éléments finis spectraux [Komatitsch et Vilotte, 1998]. Toute la difficulté réside dans la création du maillage de la configuration. Par ailleurs, les temps de calcul sont typiquement de 3 heures pour la fréquence 20 Hz, et 10 heures pour la fréquence 40 Hz, sur 2 processeurs Xeon W5580 à 4 cœurs. Nous présentons ci-après quelques résultats issus de la modélisation.

Propriétés / Concentration en CO2	0%	10%	40%
Densité ρ (kg/m^3)	2 050	2 000	1 950
Vitesse V_P (m/s)	2 050	1 450	1 300
Vitesse V_S (m/s)	600	600	650

TABLE 5.2 – *Propriétés des grès saturés par un mélange variable d'eau et de CO2 (réservoir de Sleipner, $T = 37°C$, $P = 10\,MPa$). D'après [Lumley et al., 2008]*

La Figure 5.7 décrit le sismogramme représentant le champ de pression à la fréquence 20 Hz pour un réseau de 50% de bulles contenant 40% de CO2 à l'interface. On peut noter les effets du réseau de diffraction en particulier en-dessous de la réflexion P-S sur l'interface marnes/grès.

Les Figures 5.8 à 5.13 représentent les composantes suivant x ou z du déplacement enregistré sur différents capteurs situés soit à gauche, soit à droite, soit à la (quasi-)verticale de la source pour les fréquences 20 Hz et 40 Hz. Les images du haut montrent les composantes du déplacement dit "de référence" (*i.e.*, sans réseau de bulles à l'interface), tandis que les images sous-jacentes illustrent la différence entre les composantes du déplacement de référence et les composantes du déplacement enregistré pour différents cas d'interfaces, *i.e.*, différentes concentrations de bulles (10%, 50% ou 80%) et différents contenus (10% ou 40% de CO2). Sur les images de référence, nous pouvons observer les arrivées des réflexions P-P suivies des réflexions P-S, mais aucune diffraction. Sur les autres images, nous constatons d'une part d'infimes différences associées aux réflexions P-P et aux réflexions P-S qui sont constantes quels que soient la concentration des bulles et leur contenu, et qui correspondent à des erreurs numériques et en aucun cas à un phénomène physique. D'autre part, nous pouvons noter une différence beaucoup plus importante correspondant à la génération de diffractions d'ordre élevé générées par le réseau de bulles après les arrivées des réflexions P-P et P-S. Pour un capteur donné, cette différence est généralement plus importante sur la composante x du déplacement que sur la composante z. Ceci est logique puisque les ondes diffractées d'ordre élevé sont majoritairement des ondes S. En outre, pour une

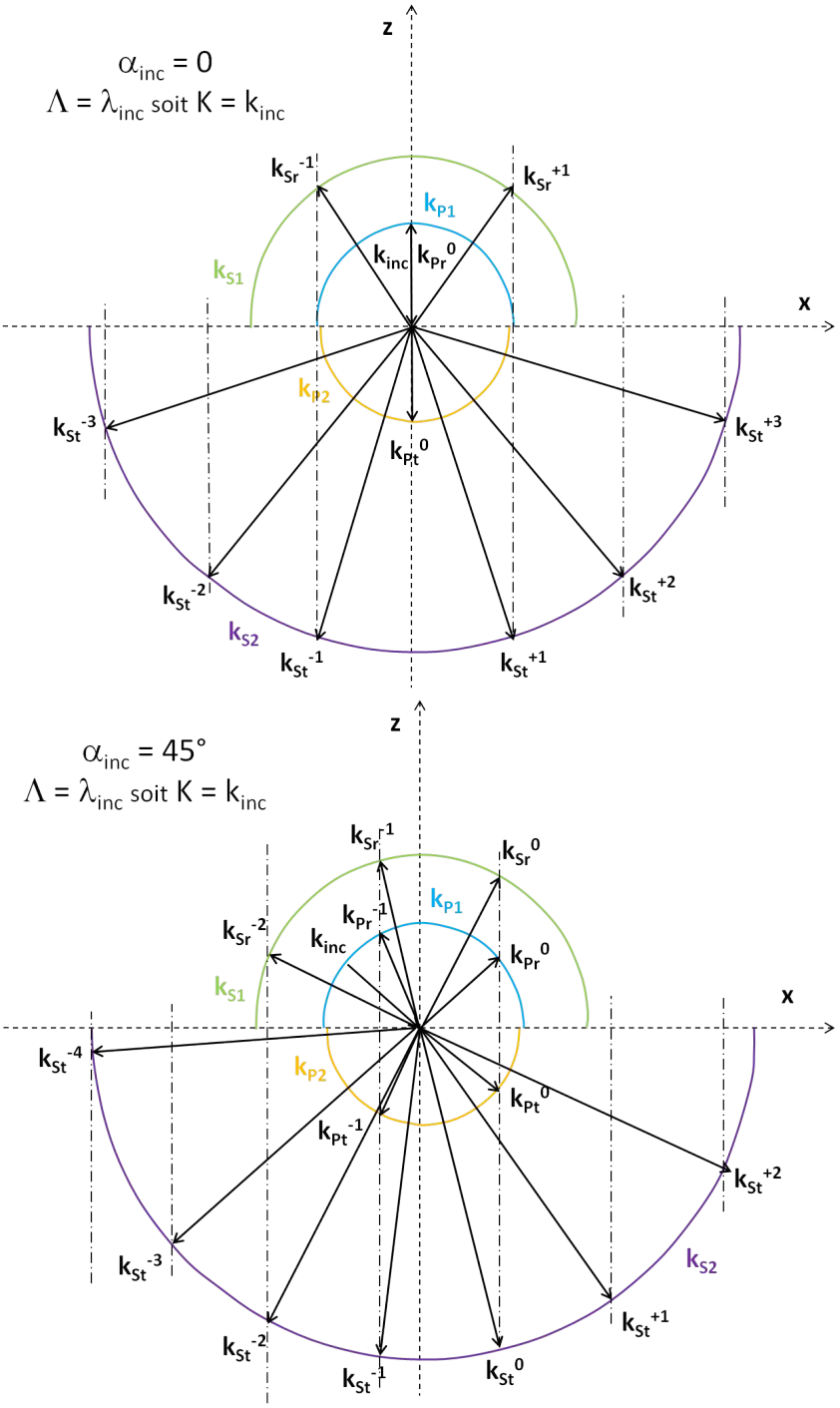

FIGURE 5.6 – *Existence et direction de propagation des ondes P et S réfléchies et transmises (d'ordre $n = 0$) et des ondes diffractées P et S d'ordre élevé ($n \neq 0$) par l'interface marnes/grès (cf propriétés des milieux dans le Tableau 1) avec un réseau de diffraction tel que $\Lambda = \lambda_{inc}$, pour deux angles d'incidence $\alpha_{inc} = 0$ et $\alpha_{inc} = 45^{\circ}$. L'onde incidente est une onde P dans les marnes.*

concentration donnée de bulles à l'interface, cette différence augmente avec le taux de CO2 dans les bulles. Enfin, pour une concentration en CO2 donnée, la différence dans les composantes

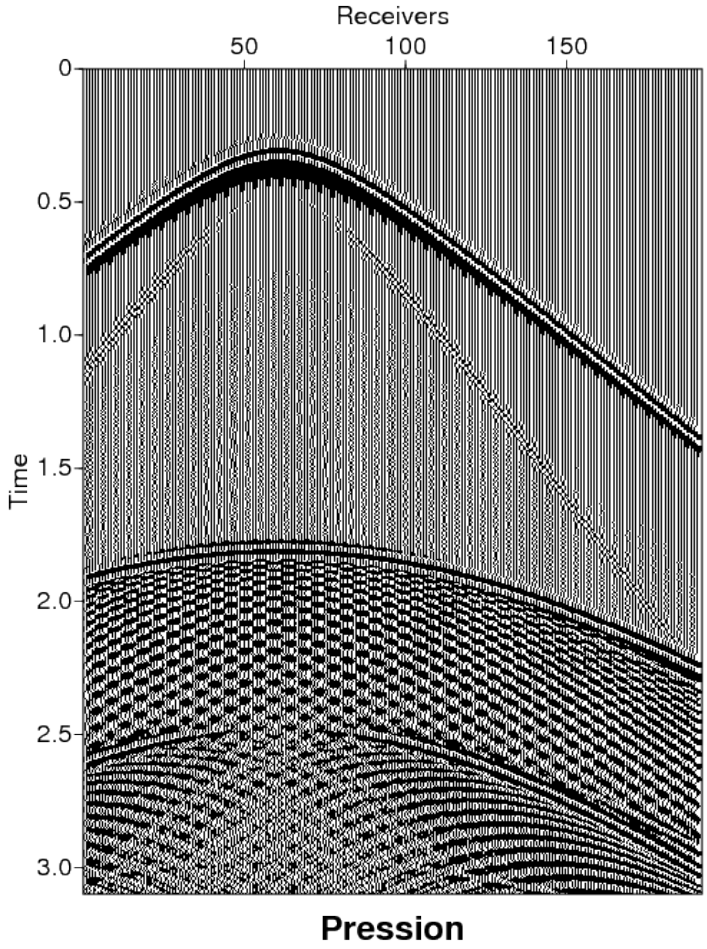

FIGURE 5.7 – *Sismogramme représentant le champ de pression à la fréquence 20 Hz pour un réseau à l'interface de 50% de bulles contenant 40% de CO2.*

du déplacement augmente avec la concentration de bulles à l'interface, avec cependant un pic plus prononcé pour une concentration de 50% de bulles (phénomène de résonance). A noter que les effets sont plus prononcés pour la fréquence 40 Hz (avec la présence de paquets d'onde), particulièrement pour le capteur situé quasiment à la verticale de la source (notamment pour la composante x du déplacement enregistré). Ceci peut s'expliquer par le fait qu'à 40 Hz le nombre de bulles présentes dans la zone de Fresnel à l'interface est plus important qu'à 20 Hz, ce qui va favoriser l'activité cohérente du réseau et donc une génération plus efficace des ondes diffractées.

La Figure 5.14 représente les sismogrammes, pour les composantes x et z du déplacement, résultant de la différence entre le sismogramme de référence obtenu pour le cas de l'interface sans réseau de bulles et le sismogramme obtenu pour le cas d'une interface avec un réseau de 50% de bulles contenant 40% de CO2 pour la fréquence 40 Hz. On peut noter les diffractions d'ordre élevé générées par le réseau de bulles, ainsi qu'un changement important dans l'amplitude des ondes P et S réfléchies spéculaires (ordre 0 de la diffraction). Cela signifie que le réseau de bulles va non seulement générer des ondes supplémentaires aux ondes "classiques" (P et S réfléchies et transmises), mais également affecter les énergies attribuées aux différentes ondes propagatives.

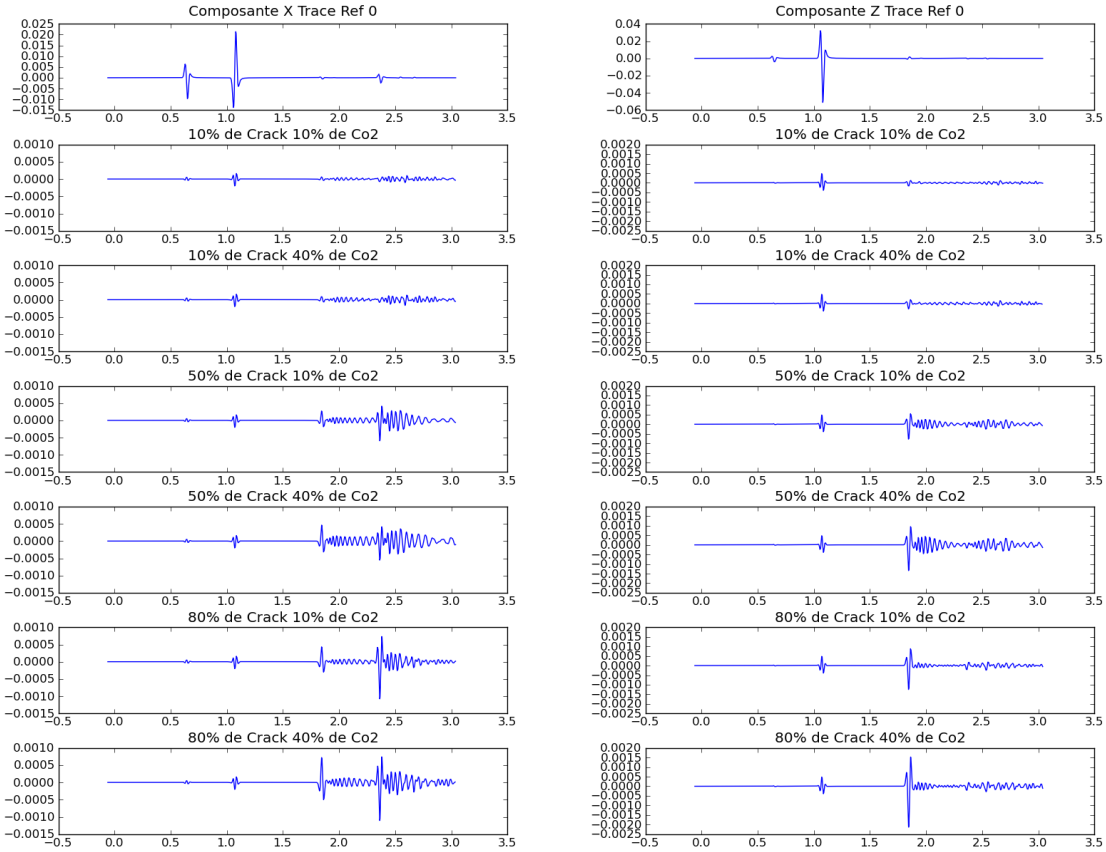

FIGURE 5.8 – *Composantes suivant x et z du déplacement enregistré sur le premier capteur situé à $x_R = 2\,000\,m$ (à gauche de la source) pour la fréquence 20 Hz. En haut : déplacement dit "de référence" (sans réseau de bulles à l'interface). Images suivantes : différence entre le déplacement de référence et le déplacement enregistré pour différents cas d'interfaces (différentes concentrations de bulles et différents contenus).*

Ces résultats montrent que les diffractions d'ordre élevé générées par le réseau de poches de CO2 qui apparaissent sur les sismogrammes peuvent être un premier indicateur de la présence d'une distribution de gaz sous la roche couverture et pourraient constituer une voie nouvelle pour le monitoring sismique. Cependant, une étude plus poussée serait nécessaire pour confirmer ces premières impressions.

5.4 Conclusions

La mise en œuvre de techniques de surveillance des réservoirs de stockage du CO2, apportant la preuve du confinement du gaz, constitue un enjeu majeur pour l'acceptabilité des projets de séquestration par l'opinion publique. Le monitoring géophysique 4D, dont le principal atout est de proposer une vision à l'échelle du réservoir, doit être validé théoriquement avant d'être éprouvé ultérieurement sur un site pilote, afin de montrer qu'il peut détecter en amont les phénomènes liés à la vie du réservoir.

Le projet ANR EMSAPCO2 avait pour objectif de contribuer à apporter une réponse à la demande de sécurité et de fiabilité des stockages en analysant la faisabilité de différentes techniques

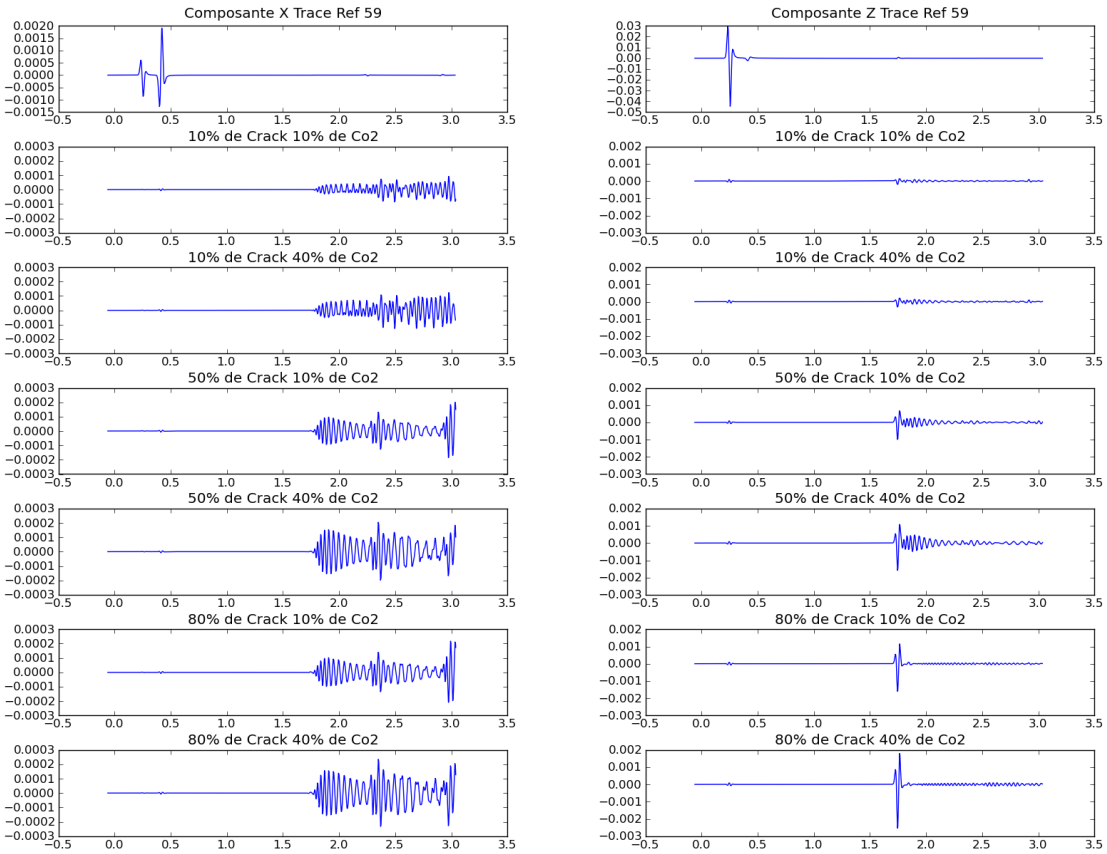

FIGURE 5.9 – *Composantes suivant x et z du déplacement enregistré sur le capteur placé à la quasi-verticale de la source pour la fréquence 20 Hz. En haut : déplacement dit "de référence" (sans réseau de bulles à l'interface). Images suivantes : différence entre le déplacement de référence et le déplacement enregistré pour différents cas d'interfaces (différentes concentrations de bulles et différents contenus).*

géophysiques pour assurer la surveillance et le suivi du CO2 injecté. Dans ce cadre, nous avons évalué plus particulièrement la possibilité d'utiliser les réflexions non spéculaires engendrées par la présence de poches de gaz piégées sous la roche couverture, après migration du CO2 vers la surface du réservoir, pour améliorer l'interprétation sismique et suivre les changements à l'intérieur du réservoir. Il semble que ces réflexions qui apparaissent sur les sismogrammes peuvent être un premier indicateur de la présence d'une distribution de gaz sous la roche couverture et pourraient constituer une voie nouvelle pour le monitoring sismique. Cependant, ces premiers résultats nécessitent encore d'être affinés. Par ailleurs, il serait intéressant de considérer dans nos modélisations une répartition aléatoire de bulles de CO2 sous la roche couverture.

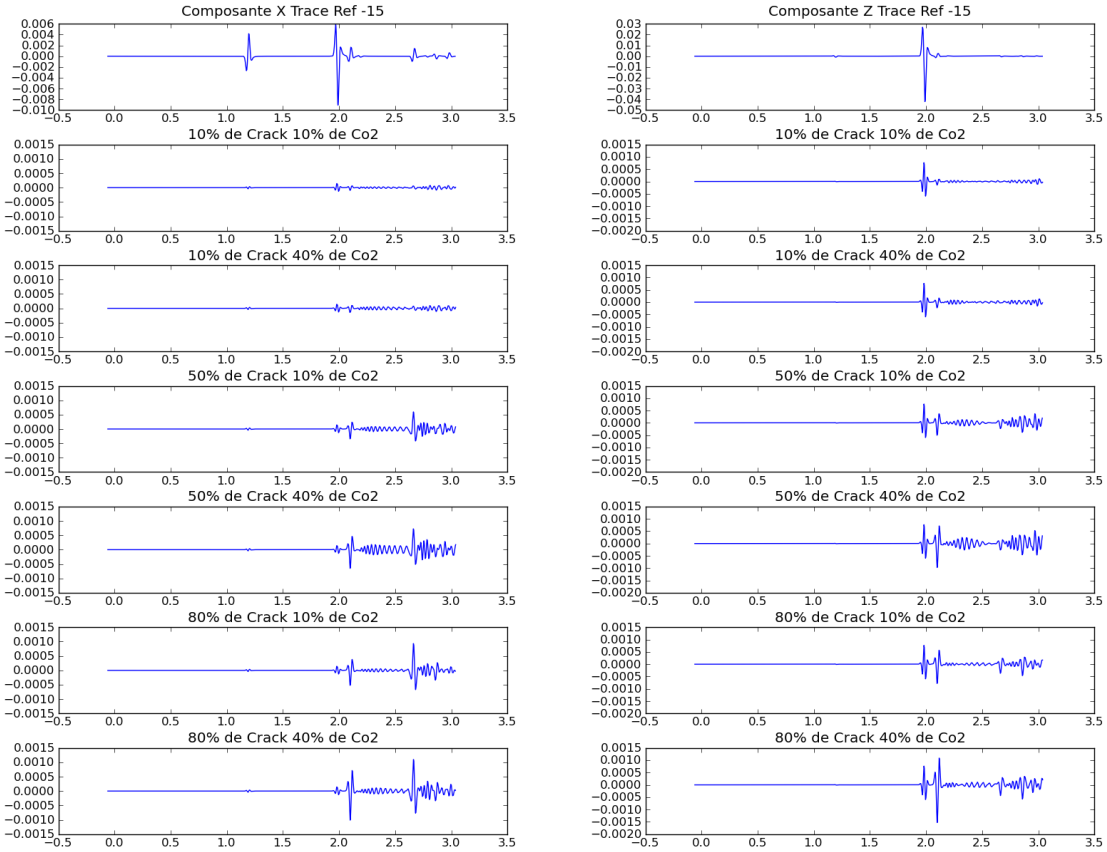

FIGURE 5.10 – *Composantes suivant x et z du déplacement enregistré sur le premier capteur situé à $x_R = 5\,500\,m$ (à droite de la source) pour la fréquence 20 Hz. En haut : déplacement dit "de référence" (sans réseau de bulles à l'interface). Images suivantes : différence entre le déplacement de référence et le déplacement enregistré pour différents cas d'interfaces (différentes concentrations de bulles et différents contenus).*

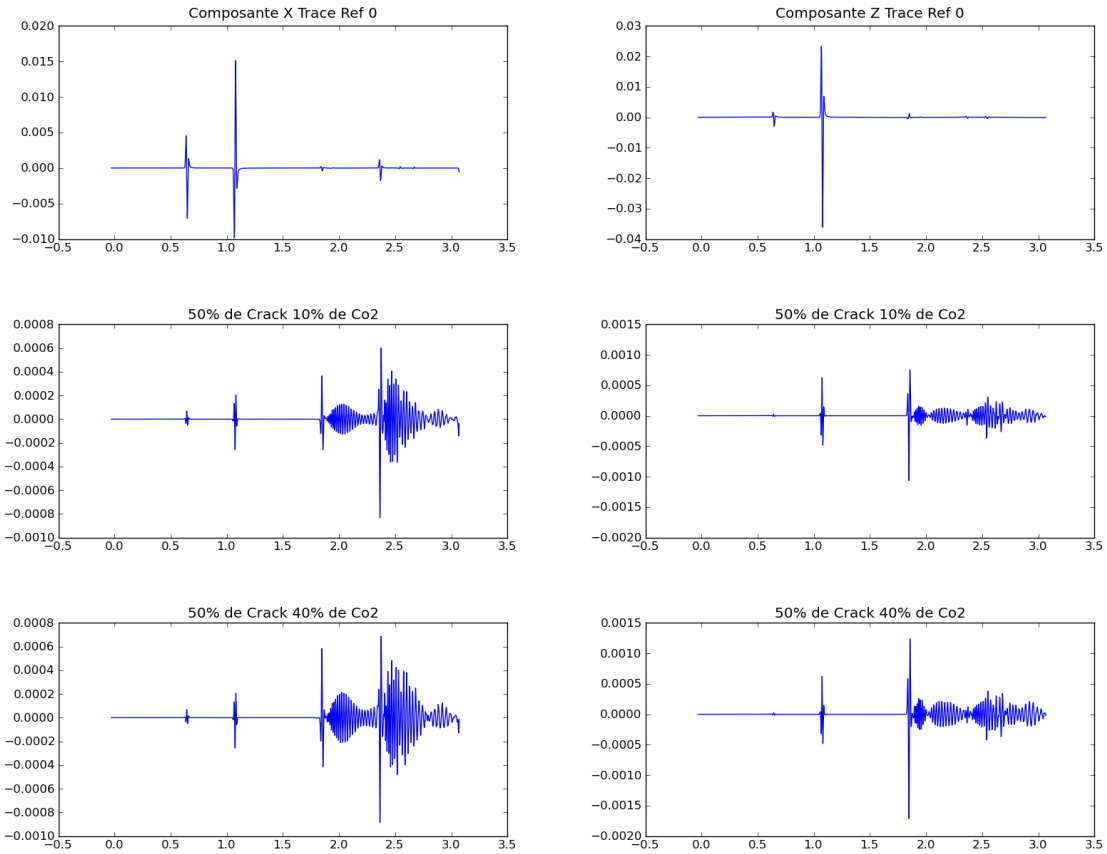

FIGURE 5.11 – *Composantes suivant x et z du déplacement enregistré sur le premier capteur situé à $x_R = 2\,000\,m$ (à gauche de la source) pour la fréquence 40 Hz. En haut : déplacement dit "de référence" (sans réseau de bulles à l'interface). Images suivantes : différence entre le déplacement de référence et le déplacement enregistré pour une concentration de 50% de bulles et différents contenus.*

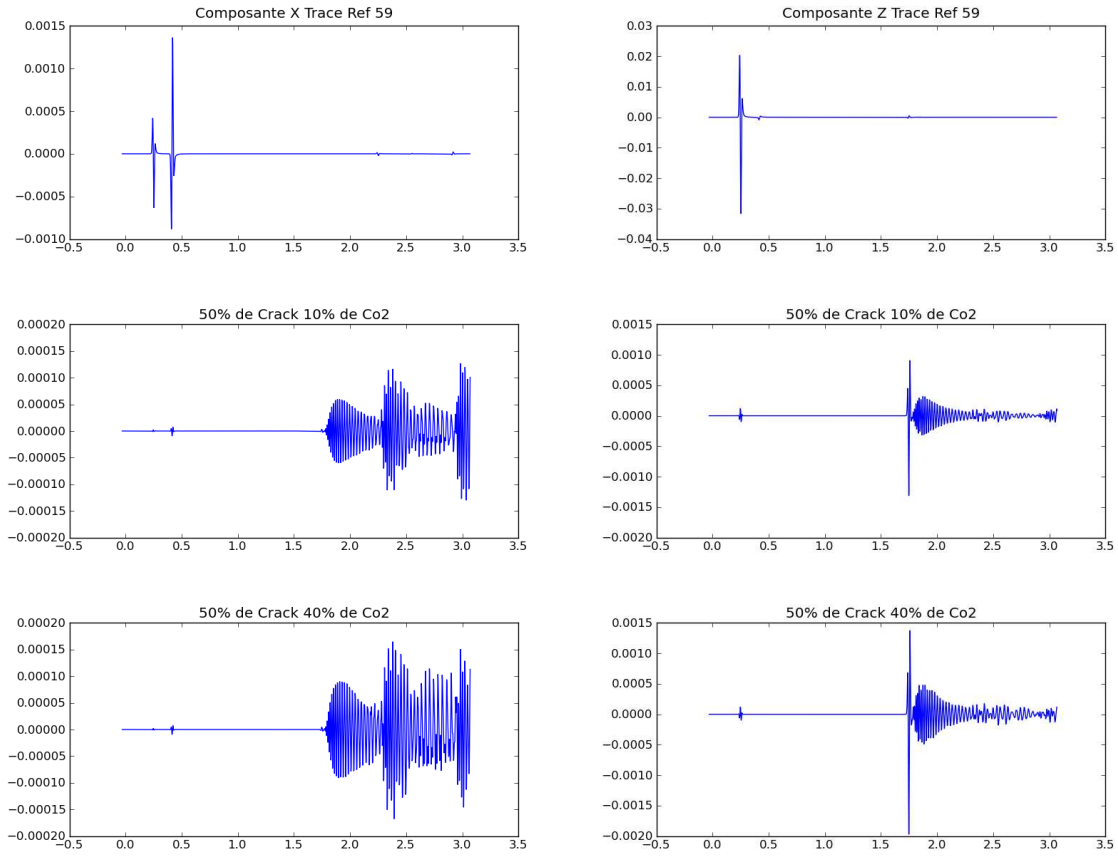

FIGURE 5.12 – *Composantes suivant x et z du déplacement enregistré sur le capteur situé à la quasi-verticale de la source pour la fréquence 40 Hz. En haut : déplacement dit "de référence" (sans réseau de bulles à l'interface). Images suivantes : différence entre le déplacement de référence et le déplacement enregistré pour une concentration de 50% de bulles et différents contenus.*

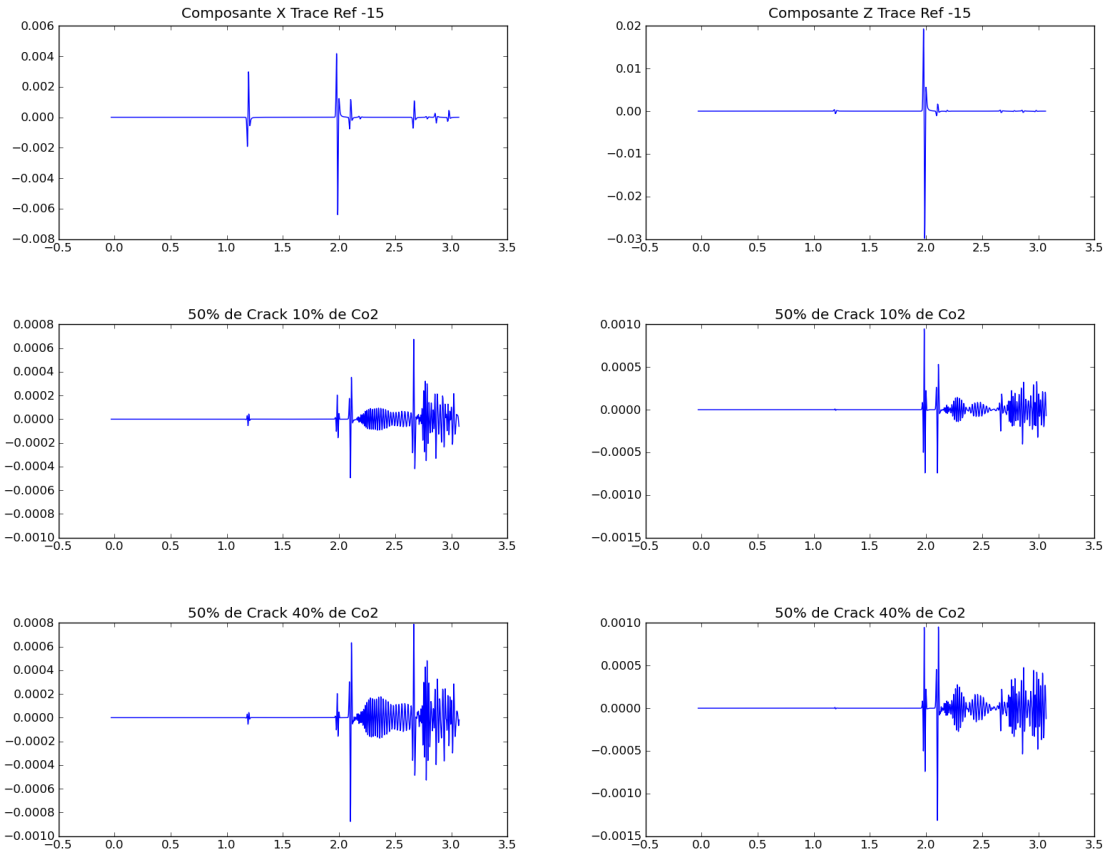

FIGURE 5.13 – *Composantes suivant x et z du déplacement enregistré sur le premier capteur situé à $x_R = 5\,500\,m$ (à droite de la source) pour la fréquence 40 Hz. En haut : déplacement dit "de référence" (sans réseau de bulles à l'interface). Images suivantes : différence entre le déplacement de référence et le déplacement enregistré pour une concentration de 50% de bulles et différents contenus.*

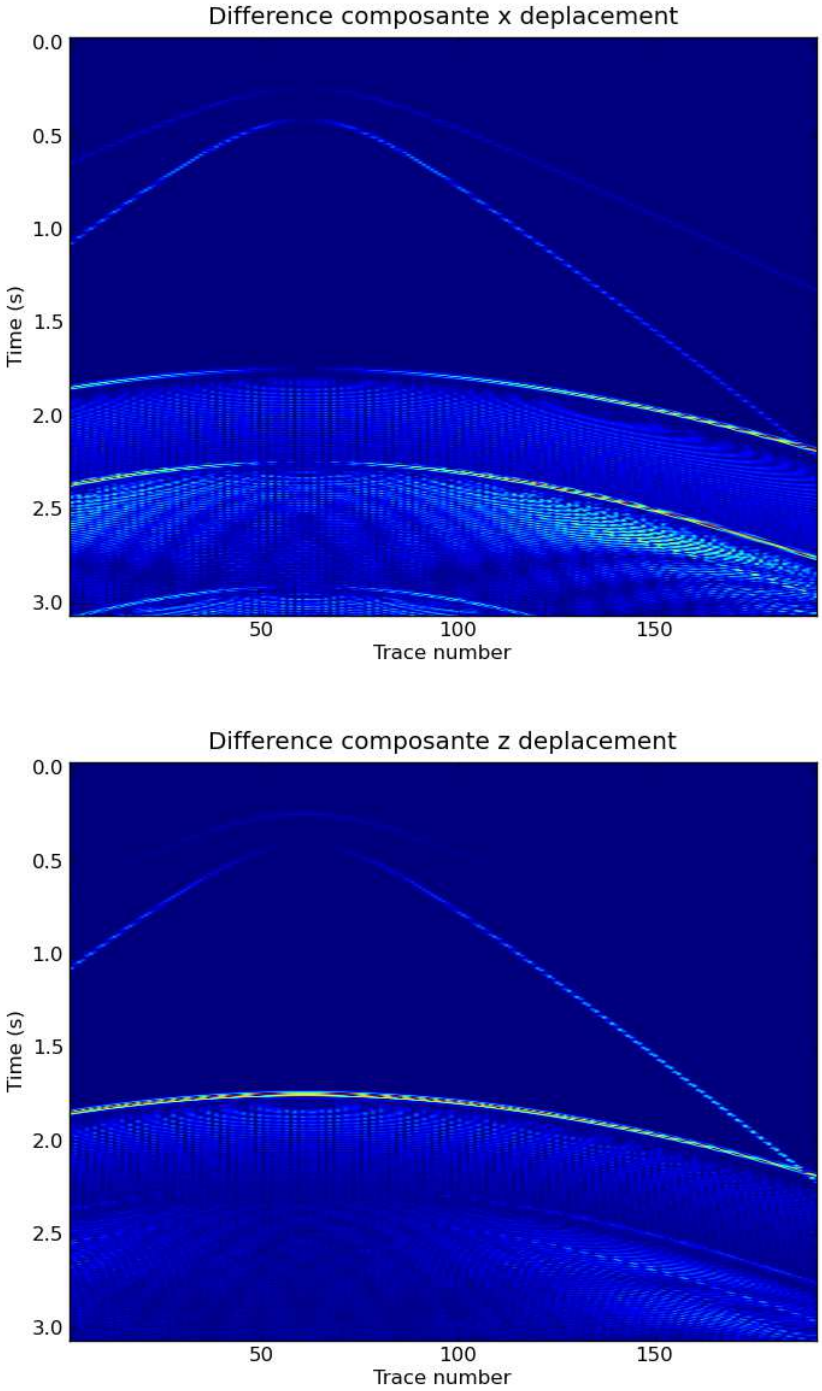

FIGURE 5.14 – *Sismogrammes résultant de la différence entre le sismogramme de référence obtenu pour le cas de l'interface sans réseau de bulles et le sismogramme obtenu pour le cas d'une interface avec un réseau de 50% de bulles contenant 40% de CO2 pour la fréquence 40 Hz. Haut : composante x du déplacement. Bas : composante z du déplacement.*

Chapitre 6

Extension et Perspectives

Une meilleure connaissance des mécanismes physiques de 1^{er} ordre qui influencent la propagation des ondes dans les milieux géologiques est une plus-value indispensable pour tendre vers une meilleure caractérisation du sous-sol. Au travers de ce mémoire, j'ai montré que le problème de l'interaction entre les ondes et les interfaces ne devait pas être sous-estimé et qu'il devait être abordé de manière pluridisciplinaire en tenant compte des limitations introduites par le système d'observation constitué par les ondes sismiques. Les travaux présentés ici n'ont pas d'autre prétention que de proposer des pistes d'investigation. Beaucoup reste encore à faire pour approcher la complexité de la réalité physique afin de l'intégrer de manière pertinente dans les simulations de la propagation des ondes sismiques. Mes perspectives de recherche se situent principalement dans la continuité de ces études. Elles s'enrichissent cependant des possibilités nouvelles offertes par la présence, au sein du Laboratoire de Mécanique et d'Acoustique de Marseille, de compétences scientifiques dans le domaine de la mécanique et de dispositifs expérimentaux de grande qualité (cuves).

Je me focaliserai dans ce chapitre uniquement sur deux thématiques, développées depuis quelques mois. D'autres, concernant notamment la propagation des ondes d'interface, ont également des places de choix dans mon activité.

6.1 Réflectivité d'une interface latéralement hétérogène

Outre le travail à poursuivre pour décrire le volume d'interaction autour de l'interface qui participe activement au processus de réflexion des ondes sur une interface entre deux milieux anisotropes (résultant par exemple d'une fracturation), il sera important de poursuivre en parallèle la réflexion sur l'état du contact entre les couches géologiques et sur son influence sur la propagation des ondes. Cette réflexion se doit d'être menée en particulier en collaboration avec des géologues structuralistes et des mécaniciens du contact. Une des questions essentielles est celle-ci : quel est l'impact, sur le champ d'onde réfléchi enregistré aux capteurs, des hétérogénéités du contact par rapport à celles localisées au sein des volumes des milieux (*e.g.*, fractures, porosité...) ? Pour y répondre, nous devons nous focaliser dans un 1^{er} temps sur les lois qui régissent la propagation des ondes au passage de la zone de contact hétérogène (interface). Pour cela, nous devons considérer un analogue terrain (*e.g.*, celui représenté sur la Figure 3.5) et découper le problème en problèmes intermédiaires plus simples avant de le complexifier progressivement. Tout au long de la démarche, nous devons veiller à conserver un bon compromis entre simplification du modèle (pour pouvoir le résoudre) et complexité des milieux réels (pour préserver les phénomènes physiques de 1^{er} ordre). Les hétérogénéités du site géologique naturel choisi devront être mesurées in situ et caractérisées à différentes échelles. Nous devrons identifier pour toute la bande passante sismique les hétérogénéités susceptibles d'interagir avec les ondes sismiques et de conditionner leur propagation. Cette caractérisation multi échelles servira de paramètres d'entrée réalistes à la modélisation des lois de contact entre les milieux géologiques, en vue d'une intégration dans un code numérique de propagation d'ondes. Les lois de contact décri-

vant les défauts d'adhésion dans des matériaux multicouches ont été particulièrement étudiées en Contrôle Non Destructif (CND). Les longueurs d'onde ultrasonores étant souvent grandes devant l'épaisseur des défauts, la zone d'adhésion est remplacée par une interface d'épaisseur nulle munie d'un ensemble de conditions d'interface adéquates décrivant des propriétés moyennes de contact. En élastodynamique, les conditions linéaires de type masse-ressort sont largement utilisées en CND pour décrire les collages ou en géosciences pour modéliser les fractures, car elles permettent de décrire simplement tout un continuum de situations physiques comprises entre les trois cas limites : contact soudé, glissement sans frottement, décollement total. Néanmoins, les méthodes utilisées en CND et basées sur ces modèles linéaires de contact échouent souvent à détecter des défauts d'adhésion en contact partiel. Il est pourtant essentiel dans certains cas de pouvoir conserver cette particularité géométrique dans les lois de contact car un réseau de défauts en contact partiel peut engendrer des phénomènes physiques de $1^{ère}$ importance qui n'apparaîtraient pas autrement (*cf* Chapitre 3). Par conséquent, pour définir les lois de contact correspondant au site géologique choisi, il serait sans doute intéressant d'avoir recours à des méthodes de type asymptotique issues de la mécanique des milieux continus. Dans ces méthodes, l'épaisseur de la zone de contact est considérée comme un petit paramètre. Lorsque l'on passe à la limite sur ce petit paramètre une "mémoire" des hétérogénéités et des caractéristiques de la zone de contact originelle (du type longueur et orientation moyennes des fissures, endommagement, géométrie...) est conservée [Lebon *et al.*, 2004] [1]. Le modèle limite est en général beaucoup plus simple à mettre en œuvre numériquement, mais contient tout de même un certain nombre de grandeurs représentatives du milieu. Comme précisé ultérieurement, il faut élaborer dans un 1^{er} temps un modèle de contact simple avant de le complexifier en fonction de la description géologique multi-échelle. On devrait aboutir *in fine* à des lois de contact plus "réalistes" du point de vue des ondes sismiques, lois qui définiront la réflectivité de l'interface et que l'on pourra intégrer dans des codes numériques de propagation d'ondes.

6.2 Le projet BENCHIE

... ou le projet "BENCHmarks expérimentaux de laboratoire en environnements complexes à des fins de validation de codes de propagation d'ondes et d'ImageriE".

Dans les zones géologiques complexes où les changements structuraux et les variations de topographie sont rapides et parfois abrupts, il est difficile de retrouver directement à partir des profils sismiques la vraie géométrie des structures géologiques. Pour résoudre ce problème (inverse), il est nécessaire de bien résoudre au préalable le problème direct, *i.e.* modéliser de manière réaliste la propagation des ondes sismiques en 3D. Pour cela, différents codes basés sur différentes techniques (tracé de rayons, schémas aux différences finies, éléments finis, éléments finis spectraux, intégrales de Kirchhoff ...) ont été développés et sont, à des fins de validation, généralement confrontés à d'autres méthodes "validées" sur une configuration synthétique test représentant un environnement géologique spécifique. Cette démarche, bien que courante, possède néanmoins des limitations, en particulier lorsque la propagation des ondes se produit dans un environnement complexe qui contient des réflecteurs à forts contrastes et à topographie irrégulière. En effet, nous ne savons pas quel est le code qui *in fine* s'approche au mieux de la "vraie" solution. Une autre démarche consiste à valider ces codes via une confrontation directe aux données réelles acquises in situ. Malheureusement, le fait de ne pas connaître parfaitement l'environnement géologique dans lequel se propagent les ondes rend difficile l'interprétation des

1. *cf* toutes les réferences dans cet article.

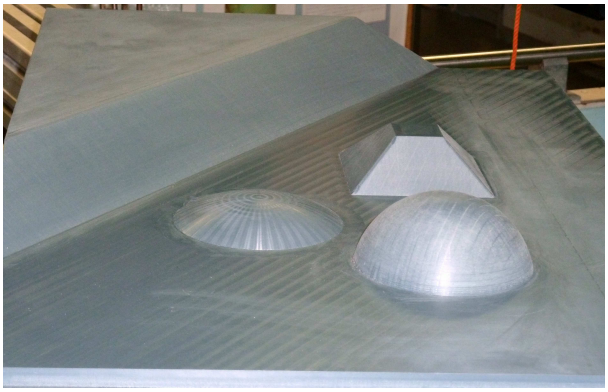

FIGURE 6.1 – *Le « Modèle Marseille » : maquette de « milieu géologique » présentant de fortes topographies 3D (faille, dôme plein, pyramide, dôme tronqué). Le facteur d'échelle par rapport à la configuration réelle équivalente est de 1 : 10 000.*

résultats. Aussi, le fait de disposer de mesures de référence calibrées acquises dans des configurations très complexes, mais contrôlées, constituerait une alternative particulièrement intéressante pour la validation de ces codes numériques.

L'objectif de ce projet international est précisément d'apporter cette alternative originale pour la sismique en proposant d'éprouver différentes familles de méthodes numériques, largement utilisées en sismique, par des benchmarks expérimentaux de laboratoire en environnements complexes (mais contrôlés). Le 1^{er} objectif est de réaliser en cuve différents benchmarks expérimentaux en configuration de sismique marine (offset nul, campagne AVA). Un 1^{er} modèle géologique présentant de fortes topographies 3D a été réalisé à partir de PVC (*cf* Figure 6.1). Il s'inspire largement du modèle de French [French, 1974], mais présente néanmoins quelques originalités, notamment un dôme tronqué et une pyramide tronquée. Des mesures ultrasonores de la réflexion des ondes sur chaque point de la surface du modèle immergé sont effectuées par différents capteurs dans la gamme fréquentielle 300 kHz – 1,2 MHz. L'analyse de ces mesures devrait permettre dans un 1^{er} temps de mieux cerner les mécanismes physiques mis en jeu dans l'interaction des ondes avec les surfaces irrégulières à forte topographie 3D qui engendrent la présence de zones d'ombre, de diffractions, de caustiques... Le 2^{nd} objectif du projet est de définir les domaines de validité respectifs de différentes familles de méthodes numériques utilisées en sismique. Pour cela, des simulations numériques basées sur différentes techniques (Tip-wave superposition method [Ayzenberg *et al.*, 2007, Ayzenberg *et al.*, 2009], Reciprocal plane-wave expansion method and Surface-integral methods [Ursin et Tygel, 1997, Tygel et Ursin, 1999, Schleicher *et al.*, 2001, Ursin, 2004], Spectral element method [Komatitsch et Vilotte, 1998, Komatitsch *et al.*, 2002, Cristini et Komatitsch, 2007]) seront réalisées en respectant les conditions des expériences en cuve (domaine fréquentiel, caractéristiques des sources et capteurs, dimensions et propriétés physiques du modèle...). La comparaison des données synthétiques et des données expérimentales permettra de mettre en lumière les qualités et défauts respectifs des différentes familles de méthodes numériques. Au-delà de cet état des lieux très important pour la communauté géophysicienne, il devrait en résulter une réflexion de fond sur la stratégie d'évolution de ces méthodes vers une simulation plus performante (en précision et en rapidité) de la propagation des ondes (problème direct) et de l'imagerie sismique (problème inverses), d'intérêt majeur pour les applications environnementales et industrielles.

Annexe A

Curriculum Vitae

Nathalie Favretto-Cristini

Chargée de recherche CNRS 1ère classe
Laboratoire de Mécanique et d'Acoustique (LMA - UPR 7051)
31, chemin Joseph-Aiguier, 13402 Marseille Cedex 20
E-mail : favretto@lma.cnrs-mrs.fr

ÉTAT CIVIL

Née le 26 novembre 1970 à Marseille
Nationalité française
Mariée, 3 enfants

FORMATION UNIVERSITAIRE

1991 et 1992 : *Licence et Maitrise de Mécanique* – Université d'Aix-Marseille II.

1993 : *DEA de Mécanique, filière Acoustique et Dynamique des Vibrations* – Université de la Méditerranée. Mention AB.

Janv. 1997 : *Doctorat, spécialité "Mécanique" mention "Acoustique et Dynamique des Vibrations"* – Université de la Méditerranée.
Thèse intitulée "Utilisation des ondes de type Stoneley-Scholte et Love pour la caractérisation acoustique des sédiments marins" sous la direction de J.-P. Sessarego au Laboratoire de Mécanique et d'Acoustique. Mention "Très Honorable avec les Félicitations du Jury".

PARCOURS PROFESSIONNEL

Juin 1997 - Sept. 1999 : *Post-doctorante* au Laboratoire d'Imagerie Géophysique de Pau (IGP, UMR 5831 tripartite CNRS-Université de Pau-Elf Exploration Production) de l'INSU (CNRS).
Stage intitulé "Étude de la diffusion des ondes aux interfaces entre deux solides en contact non uniformément soudé" sous la direction de E. de Bazelaire (Elf Exploration Production) et H. Perroud (Université de Pau).

Oct. 1999 – Sept. 2004 : *Chargée de recherche* 2^{e} *classe* au Laboratoire d'Imagerie Géophysique de Pau.

Oct. 2004 - Août 2008 : *Chargée de recherche* 1ère *classe* au Laboratoire d'Imagerie Géophysique de Pau, devenu entre-temps Laboratoire de Modélisation et Imagerie en Géosciences de Pau

(MIGP, UMR 5212 tripartite CNRS-Université de Pau-Total) de l'INSU (CNRS).

2003 – 2004 : *Collaborateur extérieur* de l'Equipe de Recherche Technologique "Propagation d'ondes", adossée au Laboratoire de Mathématiques Appliquées de l'Université de Pau.

2004 – 2007 : *Membre fondateur du Projet INRIA "MAGIQUE-3D"* (Modélisation Avancée en Géophysique 3D), devenu Action INRIA "MAGIQUE-3D" (dir. H. Barucq, Pau) au 1er Janvier 2005. (http ://uppa-inria.univ-pau.fr/m3d/)

Sept. 2008 - ... : *Chargée de recherche* $1^{ère}$ *classe* au Laboratoire de Mécanique et d'Acoustique de Marseille (LMA, UPR7051) de l'INSIS (CNRS).

Annexe B

Bilan d'activités

B.1 Encadrement de la recherche

THESE / POST-DOCTORAT

Sept. 08-Sept. 10 : Grégoire Le Touzé (Post-doctorat – Financement ANR EMSAPCO2) : "Identification, caractérisation et classification d'évènements micro-sismiques, et approche d'une solution quantitative du mécanisme au foyer" (co-encadré avec J. Blanco et P. Cristini).

Janv – Juin 2005 : Dorin Mogos-Niverlais (Thèse Université de Pau et des Pays de l'Adour - Financement Total) : "Effet de la zone superficielle altérée et de la topographie sur la propagation des ondes sismiques" (dir. D. Komatitsch, co-encadré avec P. Cristini). Thèse abandonnée en juin 2005 suite à la démission de l'étudiant pour suivre une autre formation.

2000-2004 : Wasiu Makindé (Thèse Université de Pau et des Pays de l'Adour - Financement TotalFinaElf Nigeria) : "Amélioration de l'imagerie sismique sous des sédiments sous-compactés et des argiles mobiles en Delta du Niger" (dir. E. de Bazelaire). Thèse soutenue le 25 février 2004.

STAGES

3e cycle

1998 : Bruno Lombard (DEA Acoustique et Dynamique des Vibrations, Université de la Méditerranée – 4 mois) : "Etude des défauts d'adhésion entre couches sédimentaires" (co-encadré avec J.-P. Sessarego).

2nd cycle

2003 : Sotheavy Loch (Maîtrise Sciences de la Terre, Université de La Rochelle - 2 mois) : "Etude expérimentale de la diffraction d'ondes élastiques par un réseau périodique de cavités à l'interface entre deux milieux solides" (co-encadré avec J.-B. Daban).

1er cycle

2009 : Marion Paci (IUT Mesures Physiques, Université Paul Cézanne - 3 mois) : "Mesures physiques en Acoustique Sous-Marine".

2009 : Adrien Perrier (IUT Mesures Physiques, Université Paul Cézanne - 3 mois) : "Mesures physiques en Sismique-Réflexion".

B.2 Enseignement

2002 : Dispense de cours au Laboratoire de Mathématiques Appliquées (Université de Pau et des Pays de l'Adour) : Mécanique des Milieux Continus, Propagation des ondes, Ondes de surfaces et d'interface (9h à destination de chercheurs et enseignants-chercheurs).

2005 : Chargée de cours du Master 2 Recherche "Mathématiques Appliquées" (Université de Pau et des Pays de l'Adour) : Propagation des ondes (9h de CM).

2006 : Chargée de cours du Master 2 Recherche "Génie Pétrolier" (Université de Pau et des Pays de l'Adour) : Propagation des ondes sismiques au voisinage des interfaces (3h de CM dans le module "Interprétation sismique").

2007 : Chargée de cours du Master 2 Recherche "Génie Pétrolier" (Université de Pau et des Pays de l'Adour) : Propagation des ondes sismiques au voisinage des interfaces (3h de CM dans le module "Interprétation sismique").

2008 -. . . : Chargée de cours du Master 2 Recherche "Mécanique, Physique et Ingénierie" spécialité Acoustique (Universités d'Aix-Marseille / Centrale Marseille) : Introduction à la géophysique (8h de CM dans le module "Sondages acoustique et géophysique").

2010 -. . . : Chargée de cours et de TD du Master 2 Recherche "Mécanique, Physique et Ingénierie" spécialité Acoustique (Universités d'Aix-Marseille / Centrale Marseille) – Propagation d'ondes de surface et d'interface (10h de CM et 2h de TD dans le module "Acoustique Générale")

B.3 Administration et Organisation de la recherche

GESTION DE PROJETS

Projet ANR Thématique CO2 : "EMSAPCO2" (Déc. 2007- Sept. 2010, Développement des méthodes EM et Sismique Active et Passive pour la surveillance des réservoirs de stockage du CO2). Projet porté par F.-X. Grésillon (CGG Véritas) et impliquant partenaires industriels et académiques (CGG Véritas, BRGM, Institut Français du Pétrole, Magnitude, Institut Langevin (LOA), Université de Pau (LFC-R) et CNRS (LMA)).

Responsable scientifique et technique des volets "Faisabilité sismique : Influence des poches de CO2 localisées aux interfaces », « Micro-sismique à partir d'antennes : Identification, caractérisation et classification d'évènements micro-sismiques » et « Micro-sismique à partir d'antennes : Approche d'une solution quantitative du mécanisme au foyer », développés par le LMA dans le cadre du projet ANR EMSAPCO2 (Déc. 2007- Sept. 2010).

Responsable scientifique CNRS-LMA de la Prestation de service réalisée par la société «Physeis Consultant » (Nov. 2008 – Février 2010) dans le cadre du projet ANR EMSAPCO2 : « Contribution au traitement des évènements micro-sismiques liés au stockage de CO2 et à une approche quantitative du mécanisme au foyer ».

INSTANCES DE LA RECHERCHE OU DE L'ENSEIGNEMENT SUPERIEUR

Membre (élue) du Conseil de la Fédération de Recherche "Institut Pluridisciplinaire de Recherche Appliquée dans le domaine du Génie Pétrolier" (IPRA, CNRS-FR 2952, Université de Pau) de

2007 à Août 2008 (démission pour cause de mobilité vers le LMA Marseille).

Membre (suppléante) de la Commission de spécialistes 35-36-37 de l'Université de Pau en 2008.

Membre du Conseil Scientifique et Technologique du Centre de Transfert Technologique du Mans, et Rapporteur du Département Acoustique et Vibrations en 2009.

Membre (nommée) de la Commission Bibliothèque IPRA du Service Commun de Documentation de l'Université de Pau de 2006 à Août 2008 (démission pour cause de mobilité vers le LMA Marseille).

Membre (nommée par la Fédération de Recherche IPRA) du Comité Technique du Club Géosciences Pau (http ://www.club-geosciences.org/fr/le-club.html) de Mars 2006 à Décembre 2007.

Membre (nommée) du Comité de Projet Scientifique de l'Association "Propriétés psychosensorielles des matériaux" (Université de Pau / Ecole des Mines d'Alès / Partenaires privés) d'Octobre 2002 à Janvier 2004.

VIE COLLECTIVE

Responsable "Documentation scientifique" du laboratoire MIGP et du département Géosciences de l'Université de Pau du 01/01/2000 au 31/08/2008.

Responsable de l'OR "Interaction ondes sismiques-interfaces en contexte géologique complexe" du LMA Marseille depuis janvier 2009.

ORGANISATION DE WORKSHOPS/CONGRES

Co-organisation et animation de la session "Géophysique et Sismique" du 10^e Congrès Français d'Acoustique, Lyon (France), 16 avril 2010.

Membre du comité d'organisation de l'EAGE/SEG Research Workshop "Frequency attenuation and resolution of seismic data", Barcelona (Espagne), 14-15 septembre 2009. Patronage conjoint des Sociétés Européenne et Américaine de Géophysique (EAGE et SEG).

Membre du comité d'organisation du Workshop International "Mesh creation, domain decomposition and parallel computing in 3D Geophysics", Pau (France), 21−22 octobre 2005.

Membre du comité d'organisation de la Réunion thématique du GDR Ondes (CNRS) "Propagation des ondes sismiques : modèles et applications", Paris (France), 24-25 mai 2004.

DIVERS

Membre de jury de thèse de F. Bouchaala ("Modélisation de la propagation des ondes sismiques dans les milieux viscoélastiques : application à la détermination de l'atténuation des milieux sédimentaires" - Université de Bretagne Occidentale) en mai 2008.

Rapporteur pour les revues "Communications in Computational Physics", "Optics Communications", "Acta Acustica united with Acustica" et "Mathematics and Computers in Simulation" (special issue).

B.4 Distinction

Citation de la publication "Favretto-Cristini *et al.* Geophysics 74 (2009)" dans la section "Geophysics Bright Spots" de la revue scientifique The Leading Edge (février 2009) éditée par The

Society of Exploration Geophysicists (SEG).

B.5 Diffusion et vulgarisation scientifique

Nombreuses conférences pédagogiques dans les lycées ou classes préparatoires de Pau autour du thème "Détermination de la nature du sous-sol (terrestre ou marin) grâce à la propagation des ondes sismiques".

Conférences pédagogiques au "3e Carrefour des métiers scientifiques et technologiques", 17 nov. 2008, Muséum d'Histoire Naturelle, Marseille.

Diffusion scientifique auprès de lycéens pour leur TPE ou d'étudiants en classes préparatoires pour leur TIPE.

Accueil de 10 collégiens pour leur stage en entreprise entre 2002 et 2010.

Cours (6h) de propagation des ondes en classe de CM1/CM2 en 2004 (Ecole Elémentaire d'Applications Bouillerce, Pau).

TP (6h) de mécanique des fluides (style "Main à la Pâte") en 3^e année de maternelle en 2000 (Ecole Maternelle Bosquet, Pau).

Annexe C

Publications et Communications

REVUES INTERNATIONALES A COMITE DE LECTURE

Articles publiés

[1] Favretto-Cristini N., Komatitsch D., Carcione J.M. & Cavallini F. (2011) Elastic surface waves in crystals. Part 1 : Review of the physics. *Ultrasonics* 51, 653-660.

[2] Le Touzé G., Cristini P., Favretto-Cristini N. & Blanco J. (2010) Wavefield extraction using multi-channel chirplet decomposition. *Journal of the Acoustical Society of America* 127(4), EL140-EL145.

[3] Favretto-Cristini N., Cristini P. & de Bazelaire E. (2009) What is a seismic reflector like ? *Geophysics* 74(1), T13-T23.

[4] Favretto-Cristini N., Cristini P. & de Bazelaire E. (2007) Some reflections on reflectors and wave amplitudes. *Acta Acustica united with Acustica* 93(6), 909-916.

[5] Favretto-Cristini N., Cristini P. & de Bazelaire E. (2007) Influence of the Interface Fresnel zone on the reflected P-wave amplitude modelling. *Geophysical Journal International* 171, 841-846.

[6] Makinde W., Favretto-Cristini N. & de Bazelaire E. (2005) Numerical modeling of interface scattering of seismic wavefield from a random rough interface in acoustic medium : comparison between 2D and 3D cases. *Geophysical Prospecting* 53(3), 373-397.

[7] Favretto-Cristini N. & de Bazelaire E. (2003) PP amplitude bias caused by interface scattering : are diffracted waves guilty ? *Geophysical Prospecting* 51, 99-115.

[8] Favretto-Anrès N. & Sessarego J.-P. (1999) Identification of shear wave parameters of viscoelastic solids by laboratory measurements of Stoneley-Scholte waves. *Acta Acustica united with Acustica* 85, 505-516.

[9] Favretto-Anrès N. & Rabau G. (1997) Excitation of the Stoneley-Scholte wave at the boundary between an ideal fluid and a viscoelastic solid. *Journal of Sound and Vibration* 203(2), 193-208.

[10] Favretto-Anrès N. (1996) Theoretical study of the Stoneley-Scholte wave at the interface between an ideal fluid and a viscoelastic solid. *Acta Acustica united with Acustica* 82(6), 829-838.

Article accepté

[11] Komatitsch D., Carcione J.M., Cavallini F. & Favretto-Cristini N., Elastic surface waves in crystals. Part 2 : Cross-check of two full-wave modeling methods. Accepté à *Ultrasonics* le 2 mai 2011.

CONTRIBUTION A UN OUVRAGE (AVEC COMITE DE LECTURE)

[12] Favretto-Cristini N., Cristini P. & de Bazelaire E. (2008) On the influence of the Interface Fresnel zone for estimating media parameters from seismic Amplitude-versus-Angle curves. In *Theoretical and Computational Acoustics 07*, M. Taroudakis and P. Papadakis (eds), 139-148.

[13] Favretto-Cristini N. (2004) Wave scattering by a periodic array of in-plane cracks at the interface between dissimilar media. In *Monografias del Seminario Matematico Garcia de Galdeano* vol. 31, VIII Jornadas Zaragoza-Pau de Matemática Aplicada y Estadística, M.C. López de Silanes et al. (eds), 469-478.

CONFERENCES INVITEES

Lorsque plusieurs auteurs sont mentionnés dans les présentations orales qui suivent, le nom de l'orateur est souligné.

[14] Favretto-Cristini N., Deplanté C., Rappin D., Cristini P. & Le Touzé G. (2009) Tutorial : Seismic resolution : sweet dreams, reality and pittfalls... *EAGE/SEG Research Workshop "Frequency attenuation and resolution of seismic data"*, Barcelona (Espagne), 14-15 septembre 2009.

[15] Rappin D., de Bazelaire I., Favretto-Cristini N. & Cristini P. (2009) Tribute to Eric de Bazelaire. *EAGE/SEG Research Workshop "Frequency attenuation and resolution of seismic data"*, Barcelona (Espagne), 14-15 septembre 2009.

[16] Favretto-Cristini N. & Cristini P. (2009) Quel est le volume spatial autour d'une interface intervenant dans le processus de réflexion des ondes ? *Réunion thématique "Réflectométrie(s)" du GDR Ondes*, Paris (France), 18 mai 2009.

[17] Favretto-Cristini N. (2003) Wave diffraction by a periodic array of in-plane cracks at the interface between dissimilar elastic media : a multi-scale problem in geophysics. *VIII Jornadas Zaragoza-Pau de Matemática Aplicada y Estadística*, Jaca (Espagne), 17 septembre 2003.

[18] Favretto-Cristini N., Cristini P., Komatitsch D. & Barucq H. (2003) Conférence plénière : Modélisation et imagerie en sismique : les acquis, les attentes. $1^{ère}$ *Réunion générale "Interférences d'ondes" du GDR Ondes*, Marseille (France), 08 décembre 2003.

CONFERENCES DANS DES CONGRES AVEC ACTES

Lorsque plusieurs auteurs sont mentionnés dans les présentations orales qui suivent, le nom de l'orateur est souligné.

[19] Cristini P., Le Touzé G. & Favretto-Cristini N. (2010) Envelope of signal and bandwidth : the key parameters for vertical seismic resolution. 10^{e} *Congrès Français d'Acoustique*, Lyon (France), 12-16 avril 2010.

[20] Cristini P., Le Touzé G. & Favretto-Cristini N. (2009) Complex seismic trace, bandwidth and vertical resolution. *EAGE/SEG Research Workshop "Frequency attenuation and resolution of seismic data"*, Barcelona (Espagne), 14-15 septembre 2009.

[21] Favretto-Cristini N. & Cristini P. (2009) Caractérisation du réflecteur sismique en contexte isotrope. 19^{e} *Congrès Français de Mécanique*, Marseille (France), 24-28 août 2009.

[22] Khalid P., Broseta D., Nichita D., Galliéro G., Favretto-Cristini N. & Blanco J. (2009) Vitesses et impédances sismiques en milieu poreux faiblement saturé en gaz. 19^{e} *Congrès Français de Mécanique*, Marseille (France), 24-28 août 2009.

[23] Broseta D., Khalid P., Nichita D., Favretto-Cristini N. & Blanco J. (2009) A new look at seismic properties of low gas-saturated reservoirs. 71^{st} *EAGE (European Association of Geos-*

cientists and Engineers) Conference & Exhibition, Amsterdam (The Netherlands), 8 - 11 June 2009.

[24] Cristini P., Favretto-Cristini N. & de Bazelaire E. (2008) What is the spatial volume involved in wave reflection from flat and curved interfaces ? *ACOUSTICS'08*, Paris (France), 29 juin – 4 juillet 2008.

[25] Favretto-Cristini N., Cristini P. & de Bazelaire E. (2007) On the use of the Interface Fresnel zone concept for estimating the media properties from the AVA curves. 8^{th} *International Conference on Theoretical and Computational Acoustics*, Heraklion (Crete), 2-5 juillet 2007.

[26] Favretto-Cristini N. (2004) Wave scattering from "fractured" interfaces. 1^{st} *General Assembly of European Geosciences Union (EGU)*, Nice (France), 25-30 avril 2004.

[27] Makinde W., de Bazelaire E. & Favretto-Cristini N. (2003) Interface scattering of seismic wavefield from a 3D random interface. 65^{th} *Conference and Exhibition of European Association of Geoscientists and Engineers*, Stavanger (Norway), 2-5 juin 2003.

[28] Favretto-Cristini N. & de Bazelaire E. (2001) The role of interface waves and diffracted waves in the amplitude scattering phenomenon. 7^{th} *International Congress of the Brazilian Geophysical Society*, Workshop "Seismic Imaging and Inversion", Salvador da Bahia (Brasil), 28-31 octobre 2001. Proceedings vol.1, pp 1747-1750.

[29] Favretto-Cristini N. & de Bazelaire E. (2001) Amplitude scattering phenomenon : is interface wave propagation guilty ? *EAGE/SEG Research Workshop on "Reservoir Rocks"*, Pau (France), 30 avril-4 mai 2001. Proceedings of the European Association of Geoscientists and Engineers (eds), ISBN 90-73781-16-7.

[30] Favretto-Cristini N. & de Bazelaire E. (2001) PP amplitude bias caused by interface scattering. Part I : Amplitude scattering phenomenon. 2^{nd} *Wave Inversion Technology Workshop "Seismic True Amplitudes"*, Karlsruhe (Germany), 18-20 février 2001.

[31] Favretto-Cristini N. & de Bazelaire E. (2001) PP amplitude bias caused by interface scattering. Part II : Are interface wave propagation and diffracted waves guilty ? 2^{nd} *Wave Inversion Technology Workshop "Seismic True Amplitudes"*, Karlsruhe (Germany), 18-20 février 2001.

[32] Favretto N., de Bazelaire E. & Perroud H. (1999) PP amplitudes bias caused by interface scattering. 69^{th} *Annual Meeting of SEG*, Workshop "Is true amplitude processing and imaging possible in 3D ?", Houston (USA), 4 novembre 1999.

[33] Favretto-Anrès N., de Bazelaire E. & Perroud H. (1998) Propagation of Stoneley waves along a sediment/rocky bottom "imperfect" interface - Application to marine geophysics. In A. Alippi and G.B. Cannelli (eds), 4^{th} *European Conference on Underwater Acoustics*, CNR-IDAC, vol. 1, pp. 327-332. Rome (Italy), 21-25 septembre 1998.

[34] Favretto-Anrès N. & Sessarego J.-P. (1997) Caractérisation acoustique des paramètres de cisaillement des sédiments par ondes d'interface. In G. Canévet, G.Mangiante et S. Meunier (eds), 4^{e} *Congrès Français d'Acoustique*, vol. 2, pp. 1129-1132. SFA/Technea, Toulouse. Actes du colloque, Marseille (France), 14-18 Avril 1997.

[35] Favretto-Anrès N. & Sessarego J.-P. (1996) The Stoneley-Scholte wave and the Love waves : combination of inhomogeneous plane waves - Application to the acoustical characterization of the sediments. In J.-S. Papadakis (ed.), 3^{rd} *European Conference on Underwater Acoustics*, IACM-FORTH, vol.2, pp. 595-600. Héraklion (Crete), 24-28 juin 1996.

[36] Favretto N. (1994) The Stoneley-Scholte wave : combination of three heterogeneous plane waves. *IEEE Oceans-Osates*, vol.1, pp. 795-800. Brest (France), 13-16 septembre 1994.

CONFERENCES DANS DES COLLOQUES AVEC ACTES A DIFFUSION RESTREINTE OU SANS ACTES

Lorsque plusieurs auteurs sont mentionnés dans les présentations orales qui suivent, le nom de l'orateur est souligné.

[37] Favretto-Cristini N., Cristini P., Broseta D., Khalid P. & Nichita D. (2007) Réflexions spéculaires ou non des ondes sismiques : outil d'analyse et de monitoring de stockage de CO2 ? *Rencontres Institut Français du Pétrole / Université de Pau*, Pau (France), 18 décembre 2007.

[38] Favretto-Cristini N. & Cristini P. (2007) Some reflections on reflectors and their effect on seismic wave propagation. 3^e *Réunion générale du GDR Ondes (CNRS)*, Pessac (France), 21-23 novembre 2007.

[39] Favretto-Cristini N. & Cristini P. (2007) Some reflections on reflectors and their effect on seismic wave propagation. *Acoustical Imaging Workshop*, Cargèse (France), 15-20 octobre 2007.

[40] Favretto-Cristini N., Cristini P. & de Bazelaire E. (2006) Reflections on the 3D amplitude of the seismic P-waves reflected from an interface. 1^{st} *Greek-French Workshop on Computational Aspects of Acoustic Propagation*, Heraklion (Crete), 20-21 septembre 2006.

[41] Makinde W., Favretto-Cristini N. & de Bazelaire E. (2004) Modélisation numérique de la diffusion des ondes sismiques par une surface rugueuse. *Réunion thématique "Propagation des ondes sismiques : modèles et applications" du GDR Ondes*, Paris (France), 24-25 mai 2003.

[42] Favretto-Cristini N. & de Bazelaire E. (2003) Amplitude bias caused by interface scattering. $1^{ère}$ *Réunion générale "Interférences d'ondes" du GDR Ondes*, Marseille (France), 08-10 décembre 2003.

[43] Favretto-Cristini N. & de Bazelaire E. (2003) Modélisation de la diffraction des ondes sismiques par des réseaux de cavités à l'interface entre deux milieux élastiques : problème multi-échelles en géophysique. *Réunion thématique du GDR Ondes*, Paris, 5-6 mai 2003.

[44] Favretto-Anrès N. (1998) Interaction ondes d'interface et diffusion. *Journée d'Etude sur les "Propriétés physiques des interfaces" à Elf Exploration Production*, Pau (France), 8-9 Janvier 1998.

[45] Favretto-Anrès N. (1995) Caractérisation des fonds marins à partir de mesures acoustiques des ondes d'interface. *Journée d'Etude sur la "Caractérisation acoustique des milieux plans stratifiés" à l'ICPI*, Lyon (France), 26 septembre 1995.

[46] Favretto-Anrès N. (1994) L'onde de Stoneley-Scholte à l'interface fluide parfait / solide viscoélastique. *Réunion GESPA*, Corte (France), 4-6 octobre 1994.

SEMINAIRES

Lorsque plusieurs auteurs sont mentionnés dans les présentations orales qui suivent, le nom de l'orateur est souligné.

[47] Favretto-Cristini N., Cristini P. & de Bazelaire E. (2006) Réflexions sur le calcul 3D de l'amplitude des ondes P réfléchies par une interface. *Séminaire du Département des Sciences de la Terre de l'Université de Pau et des Pays de l'Adour*, novembre 2006.

[48] Favretto-Cristini N. & Cristini P. (2006) Rôle des interfaces dans les milieux fracturés. *Journée d'étude TOTAL/Laboratoire MIGP*, Pau (France), 27 octobre 2006.

[49] Favretto-Cristini N., Cristini P. & Komatitsch D. (2005) Effet de la zone superficielle altérée et de la topographie sur la propagation des ondes sismiques. *Journée d'étude TOTAL/Laboratoire MIGP*, Pau (France), 3 novembre 2005.

[50] Favretto-Cristini N., Nivière B., Hervouët Y. & Komatitsch D. (2004) Détection des décollements et caractérisation de la déformation associée. *Journée d'étude TOTAL/Laboratoire MIGP*, Pau (France), 31 août 2004.
[51] Favretto-Cristini N. (2004) Diffusion des ondes par les interfaces et AVO/AVA : les acquis, les perspectives. *Séminaire TOTAL*, Pau (France), 6 janvier 2004.
[52] Favretto-Cristini N. (2003) Diffusion des ondes sismiques par des interfaces latéralement hétérogènes : cas des interfaces fracturées ou rugueuses. *Journée d'étude TOTAL/Laboratoire MIGP*, Pau (France), 21 octobre 2003.
[53] Favretto-Cristini N. (2001) Le rôle des ondes d'interface et des ondes diffractées dans le phénomène de diffusion d'amplitude. *Séminaire du Département des Sciences de la Terre de l'Université de Pau et des Pays de l'Adour*, décembre 2001.
[54] Favretto N. (1999) Quelques nouvelles réflexions sur le phénomène de diffusion d'interface. *Séminaire du Département des Sciences de la Terre de l'Université de Pau et des Pays de l'Adour*, mai 1999.
[55] Favretto-Anrès N. (1997) Propagation de l'onde de Stoneley à l'interface solide/solide avec des conditions de type collage - Applications en géophysique. *Séminaire du Département des Sciences de la Terre de l'Université de Pau et des Pays de l'Adour*, octobre 1997.
[56] Favretto-Anrès N. (1995) L'onde de Stoneley-Scholte à l'interface fluide parfait/solide viscoélastique - Théorie et expériences. *Séminaire du Laboratoire de Mécanique et d'Acoustique de Marseille*, novembre 1995.

RAPPORT D'ETUDES

[57] Favretto-Cristini N. & Cristini P. (2010) Projet ANR EMSAPCO2 : *Rapport final d'activités (2007-2010)* du Laboratoire de Mécanique & d'Acoustique, 69 pages, septembre 2010.
[58] Favretto N. (1999) Diffraction d'ondes élastiques par un réseau périodique de strip-cracks présent à une interface solide/solide. *Rapport fin de contrat CNRS n°151095400*, 44 pages. Directeur scientifique : Pr Hervé Perroud.
[59] Favretto-Anrès N. (1998) La diffusion aux interfaces : étude de la propagation des ondes aux interfaces non parfaitement soudées (partie II). *Rapport fin de contrat ADERA n°421530*, 41 pages. Directeur scientifique : Pr Hervé Perroud.
[60] Favretto-Anrès N. (1998) La diffusion aux interfaces : étude de la propagation des ondes aux interfaces non parfaitement soudées (partie I). *Rapport fin de contrat ADERA n°421530*, 80 pages. Directeur scientifique : Pr Hervé Perroud.
[61] Favretto-Anrès N. (1997) Utilisation des ondes de type Stoneley-Scholte et Love pour la caractérisation acoustique des sédiments marins. *Thèse de Doctorat de Mécanique de l'Université de la Méditerranée*, 206 pages, 1er janvier 1997. Directeur de thèse : Jean-Pierre Sessarego (UPR 7051 Laboratoire de Mécanique et d'Acoustique, Marseille).
[62] Favretto N. (1995) The Stoneley-Scholte wave : combination of three heterogeneous plane waves. Participation à la rédaction du *Rapport final du projet européen REBECCA* (Reflection from Bottom, Echo Classification and Characterization of Acoustical propagation) n°MAS2-CT91-0002, octobre 1995.
[63] Favretto N. (1993) Etude des ondes d'interface en vue de la caractérisation acoustique des sédiments marins. *Rapport de fin de stage de DEA de Mécanique de Marseill*e, filière Acoustique et Dynamique des Vibrations, option Acoustique Sous-Marine, Univ. Aix-Marseille II, 37 pages, novembre 1992-juin 1993. Directeur de stage : Jean-Pierre Sessarego.

Annexe D

Copie de publications

Une copie des articles suivants est placée ci-après :

En lien avec le Chapitre 2

Favretto-Cristini N., Cristini P. & de Bazelaire E. (2009) What is a seismic reflector like ? *Geophysics* 74(1), T13-T23.

Favretto-Cristini N., Cristini P. & de Bazelaire E. (2007) Influence of the Interface Fresnel zone on the reflected P-wave amplitude modelling. *Geophysical Journal International* 171, 841-846.

Favretto-Cristini N., Cristini P. & de Bazelaire E. (2008) On the influence of the Interface Fresnel zone for estimating media parameters from seismic Amplitude-versus-Angle curves. In *Theoretical and Computational Acoustics 07*, M. Taroudakis and P. Papadakis (eds), 139-148.

En lien avec le Chapitre 3

Makinde W., Favretto-Cristini N. & de Bazelaire E. (2005) Numerical modeling of interface scattering of seismic wavefield from a random rough interface in acoustic medium : comparison between 2D and 3D cases. *Geophysical Prospecting* 53(3), 373-397.

Favretto-Cristini N. & de Bazelaire E. (2003) PP amplitude bias caused by interface scattering : are diffracted waves guilty ? *Geophysical Prospecting* 51, 99-115.

Favretto-Cristini N. (2004) Wave scattering by a periodic array of in-plane cracks at the interface between dissimilar media. In *Monografias del Seminario Matematico Garcia de Galdeano* vol. 31, VIII Jornadas Zaragoza-Pau de Matemática Aplicada y Estadística, M.C. López de Silanes et al. (eds), 469-478.

En lien avec le Chapitre 4

Favretto-Cristini N., Komatitsch D., Carcione J.M. & Cavallini F. (2011) Elastic surface waves in crystals. Part 1 : Review of the physics. *Ultrasonics* 51, 653-660.

GEOPHYSICS, VOL. 74, NO. 1 (JANUARY-FEBRUARY 2009); P. T13–T23, 11 FIGS.
10.1190/1.3033216

What is a seismic reflector like?

Nathalie Favretto-Cristini[1], Paul Cristini[1], and Eric de Bazelaire[2]

ABSTRACT

The spatial region that is in the vicinity of an interface and actually affects the interface response, and hence the reflected wavefield, is of particular interest for the characterization of reflectors from a seismic viewpoint. This region is represented by a volume of integration of medium properties above and below the interface whose maximum lateral extent corresponds to the lateral extent of the interface Fresnel zone, and whose maximum vertical extent is equal to a thickness we evaluate approximately for subcritical incidence angles for a plane interface as well as for curved interfaces of anticline and syncline type. The maximum vertical extent might be larger than the seismic wavelengths for subcritical incidence angles close to the critical angle and for a strong impedance contrast at the interface. Although the part of the reflector volume lying below the interface and affecting traveltime measurements actually is smaller than described in previous studies, the whole part of the reflector volume that affects the amplitude of the reflected wavefield is larger than estimates in previous studies, which considered only the spatial region below the interface. For a syncline (respectively, an anticline), it is larger (respectively, smaller) than described for a plane interface. In addition to providing more physical insights into the wave reflection process, this study might have significant implications for seismic interpretation using amplitude-variation-with-angle methodologies.

INTRODUCTION

The basis of many seismic studies is ray theory (Červený, 2001). Nevertheless, as measured seismic data have a finite low-frequency content, it is accepted that seismic wave propagation is not limited to an infinitely narrow line called ray but is extended to a finite volume of space around the raypath (i.e., the first Fresnel volume) (Kravtsov and Orlov, 1990), which contributes to the received wavefield for each frequency. The first Fresnel volume (FV) and its intersection with an interface, called the interface Fresnel zone (IFZ), have received wide attention in past decades. These concepts are being developed continually, and they have found so many applications in seismology and seismic exploration that it is impossible here to review all the books and articles that consider them in relation to seismic wave propagation (Schleicher et al., 1997; Spetzler and Snieder, 2004; Zhou et al., 2005). Nevertheless, we will mention the works compiled in Červený (2001).

Červený and his coauthors have suggested two methods that include FV parameter calculations into the ray-tracing procedure in complex 2D and 3D structures. The first method, called Fresnel volume ray tracing (Červený and Soares, 1992), combines the paraxial ray approximation with dynamic ray tracing and is applicable only to zero-order waves (direct, reflected, and transmitted waves), whereas the second method, more accurate than the first, is based on network ray tracing (Kvasnička and Červený, 1994). Unfortunately, the second method can be applied only to waves arriving at receivers in first arrivals.

Kvasnička and Červený (1994, 1996a, 1996b) have derived analytic expressions for FVs of seismic body waves and for IFZ for simple structures with plane interfaces, offering deeper insight into the properties of FV and IFZ. It is interesting to note that FV boundaries with corresponding FZ also can be estimated by using the method of isochron rays (Iversen, 2004).

Of particular interest are the size of the IFZ and size of the volume of the reflector involved in reflection time measurements (Hagedoorn, 1954) because each can be related to horizontal and vertical resolutions of seismic methods (Sheriff, 1980; Lindsey, 1989). Until now, only the IFZ and penetration depth of the FV below the interface have been considered thus in studies. If seismic amplitudes at receivers must be evaluated, the interface reflectivity must be determined. It is well known that except for mathematical convenience, interfaces are not infinitely thin. The underlying question then is: Considering an isolated interface, how thick are the spatial regions, above and below the interface, that actually might affect the inter-

Manuscript received by the Editor 5 March 2008; revised manuscript received 21 July 2008; published online 29 December 2008.
[1]Formerly Université de Pau, Laboratoire de Modélisation et Imagerie en Géosciences de Pau (MIGP), CNRS, Pau, France; presently Centre National de la Recherche Scientifique, Laboratoire de Mécanique et d'Acoustique, Marseille, France. E-mail: favretto@lma.cnrs-mrers.fr; cristini@lma.cnrs-mrs.fr
[2]Deceased June 28, 2007

face response and hence the reflected wavefield measured at the receivers? In other words, what is a reflector like from a seismic viewpoint? That question is the focus of this paper.

As noted above, as most seismic wave propagation studies have kinematic objectives, only the IFZ and penetration depth of the FV below the interface have received special attention in recent years. They have been evaluated approximately by analytic expressions for the case of a plane homogeneous interface (i.e., a plane interface with no lateral change in its physical properties) (Kvasnička and Červený, 1996a) or by using network ray tracing (Kvasnička and Červený, 1994). Unfortunately, to our knowledge, the spatial region above the plane interface in the incidence medium, which also affects the interface response, has never been identified. In addition, very few works are devoted to computations of the IFZ at a curved interface. Moreover, most of these works are mainly concerned with the case of normal wave incidence onto the interface (Lindsey, 1989; Iversen, 2006).

We mention that Hubral and his coworkers found the projected FZ of a zero-offset reflection onto the subsurface reflector using a standard 3D common-midpoint (CMP) traveltime analysis, without knowing the reflector overburden (Hubral et al., 1993; Schleicher et al., 1997). We refer also to the work of Kvasnička and Červený (1994). Using network ray tracing, they performed FV and IFZ parameter calculations for the wave transmission process in simple 2D structures, such as a low-velocity body with a slightly curved shape embedded in a higher-velocity medium (Kvasnička and Červený, 1994). Contrary to the work of Hubral and his coworkers (Hubral et al., 1993; Schleicher et al. 1997), knowledge of the velocity model is required for computations. Kvasnička and Červený (1994) have concluded that the FV penetrates inside the low-velocity body with a penetration distance equal to the penetration distance for head waves.

Gelchinsky (1985) derived symmetrized invariant formulas for the computation of the IFZ and FV for media of complex structure (e.g., an inhomogeneous medium with curvilinear interfaces), the restriction being that the medium is considered locally homogeneous in the vicinity of the FZ center. The formulas for the IFZ were obtained with the help of the Kirchhoff approximation and expressions for the Fresnel size for a particular case, and on the basis of the reciprocity relation. Lindsey (1989) studied changes in the IFZ size for normal wave incidence when the reflector is either a syncline or an anticline, as compared with the IFZ size for a plane reflector. Unfortunately, all these formulas do not provide insights on the size of the volume of the curved reflector involved in reflection time and amplitude measurements. We propose to address this issue.

We extend Lindsey's study to the case of oblique wave incidence onto a spherically shaped interface of anticline or syncline type. We derive analytic expressions for the size of the IFZ. In addition, we estimate analytically the maximum vertical extension of the volume that actually contributes to seismic amplitude. This estimation is valid in the symmetry plane between the source and receiver and for subcritical incidence angles. The derived formulas are obtained by using the curvature transmission and reflection laws of Hubral and Krey (1980). The case of a plane interface being viewed as a special case of a spherically shaped interface, we derive the expression for the vertical extent of the effective reflection volume, valid in the symmetry plane between the source and receiver and for subcritical incidence angles. In addition, we propose an approximate analytic expression for penetration depth of the FV below the plane interface, which provides more accurate results than the analytic expressions given in Kvasnička and Červený (1996a).

The paper is organized in three sections. The first section provides overviews of the FV and IFZ concepts. The maximum lateral extent of the (curved or plane) reflector volume (i.e., the size of the IFZ) is determined as a function of the incidence angle, and as a function of the interface curvature for the two types of curved interface. In the second section, the size of the spatial regions above and below a (curved or plane) homogeneous interface, which actually affect the interface response and hence the reflected wavefield, is evaluated as a function of the incidence angle for subcritical incidence angles. The third section presents some illustrative results for a given medium configuration and for the three types of interface (e.g., plane, anticline, and syncline).

The influence of the wave incidence onto the interface, and the influence of the interface curvature, on the size of the reflector volume are investigated more particularly. The influence of the impedance contrast at a plane interface on the penetration depth of the FV is studied also. To check accuracy, the results are compared with analytically exact results and approximate results obtained by Kvasnička and Červený (1996a) for a given medium configuration. We find that, although the part of the reflector volume lying below the interface and affecting the traveltime measurements actually is smaller than described in previous studies, the whole part of the reflector volume, which affects the amplitude of the reflected wavefield, is larger than previously estimated. We also find that for the syncline, the part of the reflector volume that actually affects the reflected wavefield is larger than that described for a plane interface, whereas for an anticline it is smaller.

For the remainder of this paper, we assume that the interface of interest is isolated from all others. We mean that the distance between this interface and another interface is much larger than $V/2B$, where V is the medium velocity and B is the frequency bandwidth of the source. In addition, we consider only the P-P reflection.

MAXIMUM LATERAL EXTENT OF A REFLECTOR

We consider two homogeneous isotropic elastic half-spaces in welded contact at a curved interface. The spherically shaped interface, which can be of anticline or syncline type, is tangent at the point $M\,(0,0,z_M)$ to the plane $z = z_M$, which represents the plane interface of interest in this study. The xy-plane includes the point source S $(-x_S,0,0)$ and receiver R $(x_S,0,0)$. The vertical z-axis is directed downward. A spherical wave with a constant amplitude is generated by the source in the upper half-space. The spherical wave can be decomposed into an infinite sum of plane waves (PW) synchronous with each other at the time origin.

We consider the harmonic PW with frequency f, which propagates in the upper half-space with the velocity V_{P1} from S to R, after being reflected by the interface at the point M in a specular direction θ with respect to the normal to the interface (Figure 1). Let the traveltime of the specular reflected wave be t_{SMR}, which is the sum of the wave traveltime t_{SM} from the source S to the point M and the wave traveltime t_{MR} from the point M to the receiver R.

The set of all possible rays SM_iR with constant traveltime t_{SMR} defines the isochrone for the source-receiver pair (S,R) relative to the specular reflection SMR. This isochrone describes an ellipsoid of revolution tangent to the interface at M, and whose rotational axis passes through S and R, defined by

$$\frac{x^2}{\left(\frac{z_M}{\cos\theta}\right)^2} + \frac{y^2+z^2}{z_M^2} - 1 = 0. \quad (1)$$

This equation is valid whatever the curvature of the interface. The frequency-dependent spatial region that actually affects the reflected wavefield is known to be the Fresnel volume (FV) corresponding to the pair (S,R) and associated with the wave reflection at M.

By definition, the FV is formed by virtual diffraction points F so that the waves passing through these points interfere constructively with the specular reflected wave. This condition is fulfilled when the path-length difference is less than one-half of the wavelength $\lambda_1 = V_{P1}/f$ corresponding to the dominant frequency f of the narrow-band source signal (Kravtsov and Orlov, 1990)

$$|l_{SF} + l_{FR} - (l_{SM} + l_{MR})| \le \frac{\lambda_1}{2}, \quad (2)$$

or

$$|t_{SF} + t_{FR} - (t_{SM} + t_{MR})| \le \frac{1}{2f}, \quad (3)$$

the quantity l_{XY} denoting the distance between the point X and point Y, and t_{XY} denoting the traveltime from X to Y.

As is well known, the main contribution to the wavefield comes from the first FV as the rapid oscillatory responses of the higher-order FVs and Fresnel zones cancel out and give minor contributions to the wavefield (Born and Wolf, 1999). In our work, we restrict ourselves to the first FV, which is referred to simply as FV. The FV is represented by only the part of the volume bounded by two ellipsoids of revolution with foci at S and R, which are tangent to fictitious planes parallel to the plane $z = z_M$ and located at a distance $\lambda_1/4$ below and above the plane $z = z_M$ (Figure 1), which is situated above the interface of interest (e.g., plane, anticline, or syncline) in the upper half-space. The two ellipsoids of revolution are defined by

$$\frac{x^2}{\left(\frac{z_M}{\cos\theta} \pm \frac{\lambda_1}{4}\right)^2} + \frac{y^2+z^2}{\left(\frac{z_M}{\cos\theta} \pm \frac{\lambda_1}{4}\right)^2 - z_M^2\tan^2\theta} - 1 = 0. \quad (4)$$

In fact, as seismic wavefields are transient and large band, it is generally necessary to decompose the source signal into narrow-band signals for which monochromatic FV can be constructed for the prevailing frequency of the signal spectrum (Knapp, 1991).

The IFZ is defined as the extent of intersection of the FV by the interface, which here is spherically shaped. Unlike the case of a plane interface (Kvasnička and Červený, 1996a), the IFZ is not represented by an ellipse centered at the reflection point M when the source S and receiver R are situated at the same distance from the interface. Depending on whether the interface is of anticline or syncline type, the IFZ alters in shape appropriately, and its size might not be determined in the same way for both types. Following Hubral and Krey (1980), the radius of the interface curvature R_{int} is positive if the in-

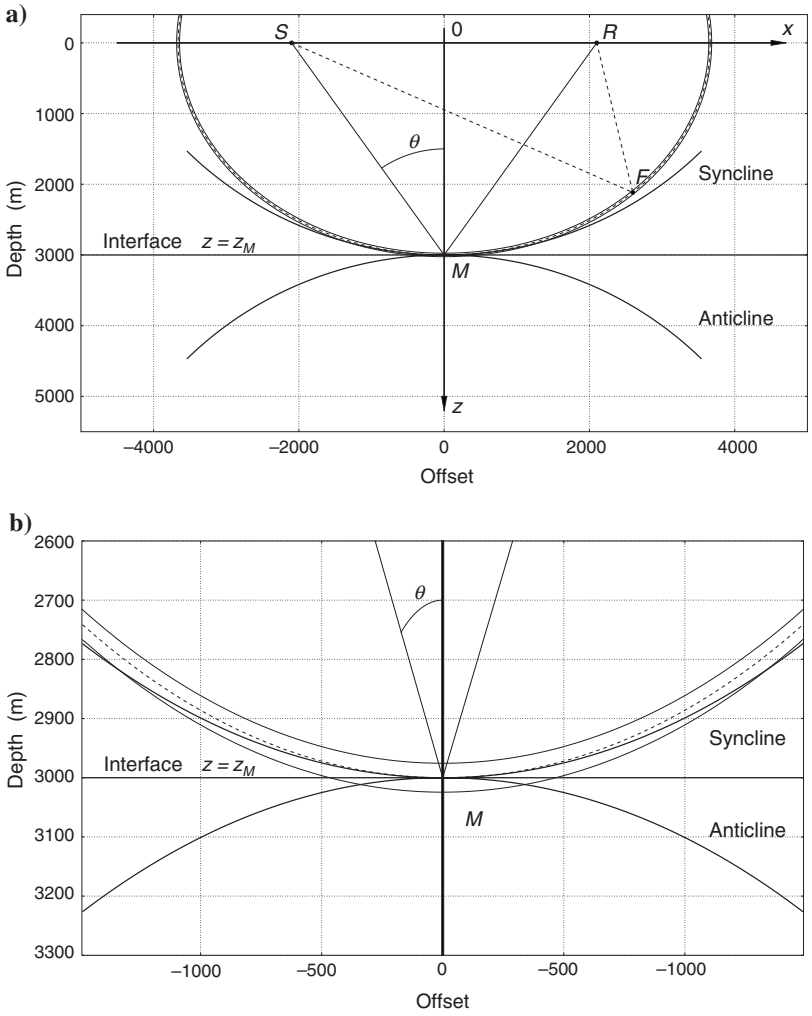

Figure 1. Representation, in the xz-plane, of the Fresnel volume involved in the wave reflection at the point M at a curved interface of anticline or syncline type under the incidence angle $\theta = 35°$. The source S and receiver R are situated at a distance $z_M = 3000$ m from the xy-plane tangent to the interface at the point M. The radius of the interface curvature is $R_{int} = \pm 5000$ m (positive for the anticline, negative for the syncline). Velocities of the upper and lower half-spaces are $V_{P1} = 2000$ m/s and $V_{P2} = 2800$ m/s, respectively, and the frequency $f = 25$ Hz. Seismic wavelengths in the upper and lower half-spaces then are $\lambda_1 = 80$ m and $\lambda_2 = 112$ m, respectively. The critical angle is equal to $\theta_C = 45.58°$. (a) The Fresnel volume is given by the volume between the ellipsoids of revolution with foci at S and R and located in the upper half-space (see the text for more details). (b) Focus on the Fresnel volume in the vicinity of the interfaces. The dashed line describes the isochron for the source-receiver pair (S,R) relative to the specular reflection SMR. The interface Fresnel zone, characterized by the extent of intersection of the Fresnel volume by the interfaces, is larger for the syncline than for the anticline.

terface appears convex to the incident wave. The radius R_{int} then is chosen positive for an anticline and negative for a syncline. This study extends the analysis by Lindsey (1989), who considered only the case of normal wave incidence onto the curved interface.

For Lindsey, the critical parameter that influences the size of the IFZ for a syncline is the ratio between the depth z_M of the reflection point M and radius of the interface curvature R_{int}. Note that the critical parameter actually is the ratio between the radius of curvature R_{iso} of the ellipsoid of revolution describing the isochrone for the pair (S,R) relative to the specular reflection SMR and radius of the interface curvature R_{int}, the radius R_{iso} being equal to the depth z_M for normal wave incidence. Depending on whether this ratio is less or larger than unity, the size of the IFZ is defined as the extent of intersection of the ellipsoid of revolution located at the distance $\lambda_1/4$ either above or below the plane $z = z_M$ by the syncline.

On the contrary, the size of the IFZ for an anticline is defined as the extent of intersection of the ellipsoid of revolution located at the distance $\lambda_1/4$ below the plane $z = z_M$ by the anticline, whatever the value of its radius of curvature R_{int}. For the sake of brevity, only the most relevant equations necessary for determining the size of the IFZ for an anticline are presented hereafter. Equations relative to the syncline can be derived easily from equations relative to the anticline by replacing the (positive) radius of the anticline curvature R_{int} by the (negative) radius of the syncline curvature R_{int}.

First we define the maximum lateral semiextent x_{max} of the IFZ following the x-axis in the xz-plane. In this plane, the anticline with the curvature center $C^+(0, z_M + R_{int})$ is represented by a circle defined by

$$x^2 + [z - (z_M + R_{int})]^2 = R_{int}^2. \tag{5}$$

Replacing the variable x by its expression obtained from the formulation of the ellipsoid of revolution, equation 4, and keeping only the sign + in the term $(z_M/\cos\theta \pm \lambda_1/4)^2$,

$$x^2 = a^2\left(1 - \frac{z^2}{b^2}\right), \tag{6}$$

where $a = z_M/\cos\theta + \lambda_1/4$ and $b = (a^2 - z_M^2\tan^2\theta)^{1/2}$, we obtain an equation of the second degree in the unknown z whose solutions z_1 and z_2 are

$$z_{1,2} = \frac{z_M + R_{int} \pm \Delta^{1/2}}{1 - \frac{a^2}{b^2}}, \tag{7}$$

where $\Delta = (z_M + R_{int})^2 - (1 - a^2/b^2)[a^2 + z_M(z_M + 2R_{int})]$ is always positive. Keeping only the solution z_1 or z_2 for which the inequality $1 - z^2/b^2 > 0$ is satisfied, and hence for which the variable x is positive, we deduce the maximum lateral semiextent x_{max} of the IFZ following the x-axis in the plane of incidence from equation 6 so that

$$x_{max} = a\left\{1 - \frac{z_{1,2}^2}{b^2}\right\}^{1/2}. \tag{8}$$

In the yz-plane, the ellipsoid of revolution located at the distance $\lambda_1/4$ below the plane $z = z_M$ is reduced to a circle defined by

$$y^2 + z^2 = b^2, \tag{9}$$

whereas the anticline is a circle defined by

$$y^2 + [z - (z_M + R_{int})]^2 = R_{int}^2. \tag{10}$$

The maximum lateral semiextent y_{max} of the IFZ following the y-axis in the yz-plane, i.e., in the direction perpendicular to the plane of incidence, then is given by the intersection of these two circles,

$$y_{max} = \left\{b^2 - \left[z_M + \frac{\lambda_1}{4}\left(\frac{z_M}{\cos\theta} + \frac{\lambda_1}{8}\right)(z_M + R_{int})^{-1}\right]^2\right\}^{1/2}, \tag{11}$$

where the quantity in the square root bracket is always positive.

The characteristics x_{max} and y_{max} of the IFZ at the surface of the anticline depend on the position of the source-receiver pair and on the incidence angle θ of the ray SM. The IFZ becomes larger in the incidence plane than in the transverse plane as the angle θ increases. Moreover, larger portions of the interface are involved for low-frequency than for high-frequency components of the wavefield. The characteristics x_{max} and y_{max} of the IFZ also depend on the radius of the interface curvature R_{int}. For the anticline, the IFZ becomes larger in the incidence plane than in the transverse plane as the radius of the interface curvature R_{int} increases. For sufficiently great radius R_{int}, the IFZ for the anticline is identical to the IFZ for the plane interface $z = z_M$. It is represented by an ellipse centered at the reflection point M whose in-plane semiaxis x_{max} and transverse semiaxis y_{max} are expressed as (Kvasnička and Červený, 1996a)

$$x_{max} = y_{max}\left[1 - \frac{z_M^2\tan^2\theta}{\left(\frac{z_M}{\cos\theta} + \frac{\lambda_1}{4}\right)^2}\right]^{-1/2}, \quad y_{max} = \left[\frac{\lambda_1}{2}\left(\frac{z_M}{\cos\theta} + \frac{\lambda_1}{8}\right)\right]^{1/2}. \tag{12}$$

Here, we must clarify some important points. Use is made in many papers of the classical representation of the FV, which is an ellipsoid of revolution with foci located at the receiver R and at the image source S″ situated symmetrically to the source S on the other side of the plane interface (Figure 2). This representation, mainly based on transmission considerations, is suitable to account for heterogeneities of the medium body located in the vicinity of the rays SM and MR, whereas the FV representation we use is more appropriate to account for heterogeneities of the interface, as it is connected strictly to the wave reflection process.

Moreover, unlike the classical one, this representation allows in a straightforward manner the definition of volumes above and below the interface, which characterize the reflector. The following section is focused on this definition. Note that the two FV representations are complementary and must be combined if wave propagation in media with heterogeneities in the medium body and at the interface is investigated.

MAXIMUM VERTICAL EXTENT OF A REFLECTOR

It is well known that the FV of the reflected wave is not limited by the interface, but penetrates across the interface in the lower half-space (Hagedoorn, 1954). The penetration depth can be evaluated approximately in an analytic way following traveltime measurements (Kvasnička and Červený, 1996a) or in a numerical way, using

network ray tracing (Kvasnička and Červený, 1994). We propose to derive analytically, in a straightforward manner, an approximate expression for the penetration depth of the FV across the curved interface, valid in the plane of symmetry between S and R and for subcritical incidence angles. This new expression provides more accurate results than those obtained by Kvasnička and Červený.

The curvature transmission law described in Hubral and Krey (1980, p. 43),

$$K_2 = K_1 \frac{V_{P2}}{V_{P1}} \left(\frac{\cos\theta}{\cos\theta'} \right)^2 + \frac{K_{int}}{\cos\theta'} \left(\frac{V_{P2}}{V_{P1}} \frac{\cos\theta}{\cos\theta'} - 1 \right), \quad (13)$$

connects the curvature K_2 of the transmitted wavefront to the curvature K_1 of the incident wavefront and to the interface curvature K_{int}. The transmission angle θ' is connected to the incidence angle θ through Snell's law, and V_{P2} denotes the velocity in the lower half-space. In the case of a curved interface, because the interface curvature K_{int} is different from zero, the curvature transmission law, equation 13, becomes in terms of radii of curvature R_2 and R_1 of the transmitted and incident wavefronts, respectively,

$$\frac{1}{R_2} = \frac{1}{R_1} \frac{V_{P2}}{V_{P1}} \left(\frac{\cos\theta}{\cos\theta'} \right)^2 + \frac{1}{R_{int}\cos\theta'} \left(\frac{V_{P2}}{V_{P1}} \frac{\cos\theta}{\cos\theta'} - 1 \right), \quad (14)$$

where R_{int} denotes the radius of the interface curvature.

By substituting the radii of curvature R_1 and R_2 for their respective expressions $z_M/\cos\theta$ and $z_{S'}/\cos\theta'$, we get the position $z_{S'}$ of the new fictitious source-receiver pair (S',R') with respect to the plane $z = z_M$, as a function of the incidence angle θ,

$$z_{S'} = \frac{z_M V_{P1} \cos^3\theta'}{V_{P2}\cos^3\theta + \frac{z_M}{R_{int}}(V_{P2}\cos\theta - V_{P1}\cos\theta')}. \quad (15)$$

The pair (S',R') can be viewed as an image of the pair (S,R) for the transmission process (Figure 3). That means that this fictitious source-receiver pair provides the same wavefront curvature as the pair (S,R). Unlike the real transmission process, which involves the upper and lower half-spaces, the wavefront relative to (S',R') propagates entirely in the lower half-space as if the upper half-space did not exist. This procedure is similar to the well-known procedure applied for the reflection process, which consists of replacing the pair (S,R) by its mirror image (S'',R'') (Figure 2).

As above, by considering the ellipsoid of revolution with foci S' and R' tangent to the plane $z = z_M$ at M (Figure 3),

$$\frac{x^2}{\left(\frac{z_{S'}}{\cos\theta'} \right)^2} + \frac{y^2 + z^2}{z_{S'}^2} - 1 = 0, \quad (16)$$

and the new ellipsoids that bound the FV associated with the reflection $S'MR'$,

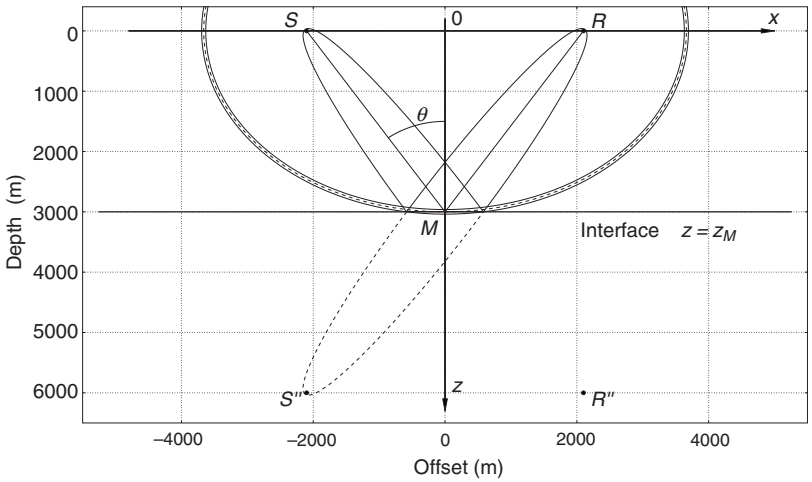

Figure 2. Representations, in the xz-plane, of the Fresnel volume involved in the wave reflection at the point M at the plane interface under the incidence angle $\theta = 35°$. The source S and receiver R are situated at a distance $z_M = 3000$ m from the interface. The classical representation of the Fresnel volume is based on the ellipsoid of revolution with foci located at R and at the mirror image S''. Another representation of the Fresnel volume associated with the reflection SMR is given by the volume located in the upper half-space between the ellipsoids of revolution with foci at S and R (see the text and Figure 1 for more details). See the legend of Figure 1 for medium properties.

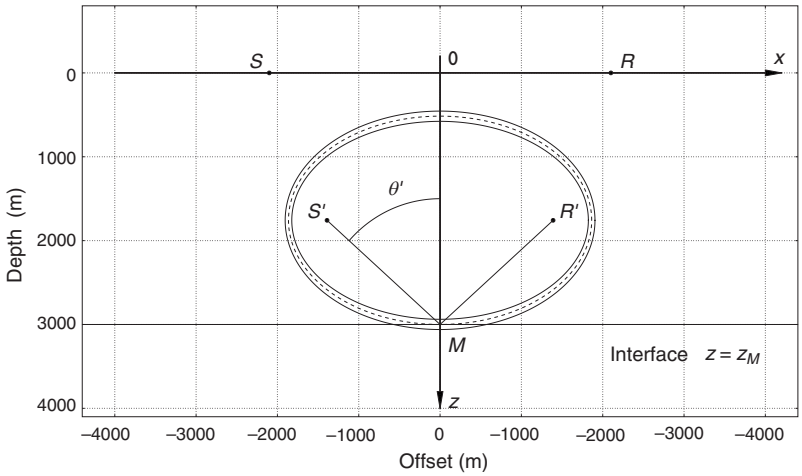

Figure 3. Representation, in the xz-plane, of the Fresnel volume involved in the fictitious wave reflection at the point M at a plane interface under the incidence angle θ'. The fictitious source-receiver pair (S',R') located at a distance $z_{S'}$ from the interface plane can be viewed as an image of the pair (S,R) for the transmission process. It provides the same wavefront curvature as (S,R) and propagates entirely in the lower half-space, as if the upper half-space did not exist. See the legend of Figure 1 for medium properties.

$$\frac{x^2}{\left(\frac{z_{S'}}{\cos\theta'} \pm \frac{\lambda_2}{4}\right)^2} + \frac{y^2 + z^2}{\left(\frac{z_{S'}}{\cos\theta'} \pm \frac{\lambda_2}{4}\right)^2 - z_{S'}^2 \tan^2\theta'} - 1 = 0, \quad (17)$$

it is straightforward to evaluate approximately the maximum penetration depth D_2, in the lower half-space, of the FV associated with the specular reflection *SMR*,

$$D_2 = \left[\left(\frac{z_{S'}}{\cos\theta'} \pm \frac{\lambda_2}{4}\right)^2 - z_{S'}^2 \tan^2\theta'\right]^{1/2} - z_{S'} = \left(z_{S'}^2 + \frac{\lambda_2 z_{S'}}{2\cos\theta'} + \frac{\lambda_2^2}{16}\right)^{1/2} - z_{S'}. \quad (18)$$

Because this expression is evaluated locally in the plane of symmetry between S and R and for subcritical incidence angles θ, it is valid whatever the radius of the interface curvature R_{int}. Nevertheless, the expression for the position $z_{S'}$ of the fictitious pair (S',R'), equation 15, differs following the radius of the interface curvature R_{int}. The penetration depth out of the plane of symmetry between S and R also can be evaluated in the same way from the envelope of the ellipsoids of revolution with foci S' and R' moving along caustics. Nevertheless, for postcritical incidence angles, we cannot define the penetration depth of the FV below the interface by using the curvature transmission law, because total reflection occurs.

Note that equation 18 provides only approximate evaluation of the actual penetration depth of the FV below the interface because the derivation based upon the curvature transmission law of Hubral and Krey (1980) does not take into account the fact that the incidence angle for the penetrating rays is not identical to the incidence angle of the central specular reflected ray. Expansion of equation 18 shows that for the values of the incidence angle θ close to zero, and then for great position $z_{S'}$, the first-order approximation to penetration depth D_2 with respect to $1/z_{S'}^2(\lambda_2 z_{S'}/2\cos\theta' + \lambda_2/8)$ corresponds to the approximation given by equation 38 in Kvasnička and Červený (1996a),

$$D_2 \simeq \frac{\lambda_2}{4\cos\theta'}. \quad (19)$$

Following the same reasoning, it seems clear that a region above the interface in the upper half-space also contributes to the interface response, and hence to the reflected wavefield. The maximum thickness D_1 of this region can be evaluated in the plane of symmetry between S and R and for subcritical incidence angles θ in the same way as above, the pair (S'',R'') being viewed as a mirror image of the pair (S,R) with respect to the plane $z = z_M$ (Figure 2),

$$D_1 = \left(z_{S''}^2 + \frac{\lambda_1 z_{S''}}{2\cos\theta} + \frac{\lambda_1^2}{16}\right)^{1/2} - z_{S''}. \quad (20)$$

We must determine the position $z_{S''}$ of the pair (S'',R''). The curvature reflection law in Hubral and Krey (1980, p. 43),

$$K_2 = K_1 + \frac{2K_{\text{int}}}{\cos\theta}, \quad (21)$$

becomes, in terms of radii of curvature R_2 and R_1,

$$\frac{1}{R_2} = \frac{1}{R_1} + \frac{2}{R_{\text{int}}\cos\theta}. \quad (22)$$

By substituting the radii of curvature R_1 and R_2 for their respective expressions $z_M/\cos\theta$ and $z_{S''}/\cos\theta$, we get the position $z_{S''}$ of the new fictitious source-receiver pair (S'',R'') with respect to the plane $z = z_M$, as a function of the incidence angle θ,

$$z_{S''} = \frac{z_M R_{\text{int}}\cos^2\theta}{2z_M + R_{\text{int}}\cos^2\theta}. \quad (23)$$

For the case of a plane interface, the radius of the interface curvature R_{int} tends to infinity, and the position $z_{S''}$ is equal to z_M. Unlike the penetration depth D_2, we can evaluate exactly the thickness D_1 for a plane interface, in the plane of symmetry between S and R, whatever the incidence angle θ, except for grazing angles. We also can evaluate exactly the distance D_1 out of the plane of symmetry in the same way as above because the caustics along which the foci S'' and R'' move are degenerate and then are reduced to points. Unlike the case of the plane interface, however, we no longer can evaluate exactly the thickness D_1 above a curved interface for subcritical incidence angles θ in the plane of symmetry between S and R, because the caustics along which the foci S'' and R'' move are no longer degenerate and thus are not reduced to points.

We can define now what a reflector is like from the seismic viewpoint. A reflector is a volume of integration of medium properties above and below the interface. This volume is represented by spatial regions with the maximum thicknesses D_1 and D_2 evaluated in the plane of symmetry between the source and receiver (Figure 4). Its maximum lateral extent corresponds to the lateral extent of the IFZ, and its maximum vertical extent corresponds to the thickness $D = D_1 + D_2$. In this work, we consider that the elastic media in contact are homogeneous and isotropic, which is an ideal case. The presence of heterogeneities or anisotropy in the media body might modify the size of the reflector volume, and more specifically the expres-

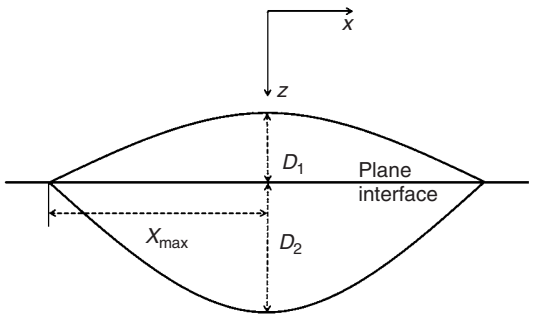

Figure 4. Schematic description of a seismic plane reflector in the xz-plane, i.e., the spatial region in the vicinity of the interface, which actually affects the interface response. The in-plane semiextent of the interface Fresnel zone is denoted by x_{max}. The distance D_1 is the maximum thickness of the region above the interface in the upper half-space, whereas the distance D_2 characterizes the penetration distance of the Fresnel volume (associated with the reflected wave *SMR*) below the interface in the lower half-space. These distances are evaluated in the plane of symmetry between the source and receiver and for subcritical incidence angles.

sions for the IFZ and thicknesses D_1 and D_2. It would be interesting to analyze the effect of anisotropy of the media on the size of the reflector volume. Our future contributions will focus on this topic.

RESULTS AND DISCUSSION

To illustrate the theoretical derivations, two cases of curved interfaces and one case of plane interface between elastic half-spaces are chosen. The source-receiver plane is located at a distance $z_M = 3000$ m from the plane tangent to the curved interfaces, which can be of anticline or syncline type. The radius of the interface curvature R_{int} is equal to ± 5000 m. It is positive for an anticline and negative for a syncline. The plane $z = z_M$ represents the plane interface of interest. The velocities of the upper and lower half-spaces are $V_{P1} = 2000$ m/s and $V_{P2} = 2800$ m/s, respectively. The frequency f being chosen is 25 Hz, and seismic wavelengths in the upper and lower half-spaces then are $\lambda_1 = 80$ m and $\lambda_2 = 112$ m, respectively. The critical angle is equal to $\theta_C = 45.58°$.

Figure 5 depicts the variation in size of the IFZ for an anticline and a syncline, as a function of the incidence angle θ, for the given value of the radius of the interface curvature R_{int}. The variation in size of the IFZ for a plane reflector also is shown for comparison. For $\theta = 0$ and for a given type of interface, the in-plane semiextent $x_{\max}$ and transverse semiextent $y_{\max}$ are equal. Following the type of interface, the IFZ then is represented by either a plane or a curved disk. With increasing θ, the IFZ becomes larger and larger in the incidence plane than in the transverse plane.

This feature is more pronounced for the syncline, the maximum size in the incidence plane being reached at a particular incidence angle θ, where the radius of the interface curvature R_{int} approaches the radius of curvature R_{iso} of the ellipsoid of revolution describing the isochrone for the source-receiver pair relative to the specular reflection *SMR*. This is shown more clearly in Figure 6, which depicts the variation in size of the IFZ for an anticline and a syncline, as a function of the radius of the interface curvature R_{int}, for a given incidence angle θ. When the radius R_{iso} is larger than the threshold value leading to the maximum size of the IFZ in the incidence plane, the in-plane semiextent $x_{\max}$ then decreases because the IFZ no longer is defined as the intersection of the ellipsoid of revolution located at the distance $\lambda_1/4$ below the plane $z = z_M$ by the syncline, but rather as the intersection of the ellipsoid located at the distance $\lambda_1/4$ above the plane $z = z_M$ by the syncline (Figure 1).

As suggested above, the critical parameter therefore is the ratio between the radius R_{iso} and radius R_{int}. We can show easily after straightforward calculations that for the syncline, the IFZ in the incidence plane is increased in size, as compared with that for a plane interface, approximately by the factor

$$F_S = \left(1 + \frac{z_M}{R_{\text{int}}} \frac{\beta^2}{\beta^2 - z_M^2 \tan^2\theta}\right)^{-1}, \tag{24}$$

with negative radius R_{int} and $\beta = z_M/\cos\theta \pm \lambda_1/4$, the sign + (respectively, −) corresponding to the choice of the ellipsoid of revolution located at the distance $\lambda_1/4$ below (respectively, above) the plane $z = z_M$.

For the anticline, the IFZ in the incidence plane is decreased in size, as compared with that for a plane interface, approximately by the factor

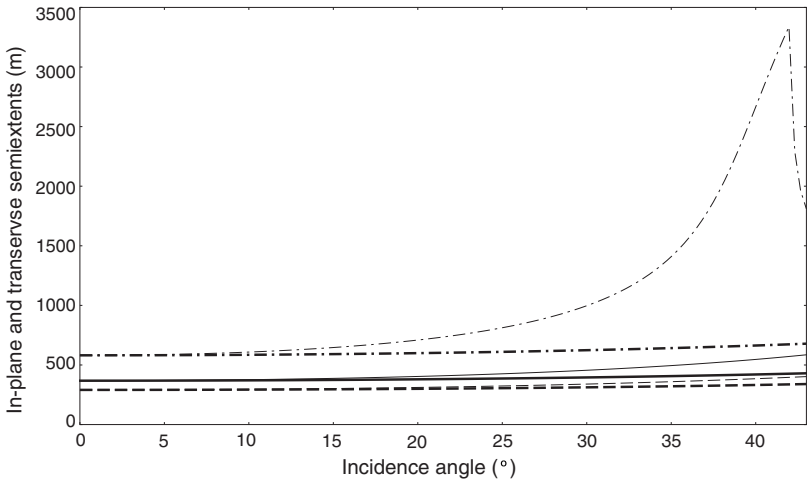

Figure 5. Variation in the size of the interface Fresnel zone at the surface of an anticline (dashed line) and a syncline (dash-dot line), as a function of the incidence angle θ, as compared with the results for a plane interface (solid line). Light curves are associated with the in-plane semiextent $x_{\max}$ (in the incidence plane); bold curves represent the variation in the transverse semiextent $y_{\max}$ (in the plane perpendicular to the incidence plane). See the legend of Figure 1 for medium properties.

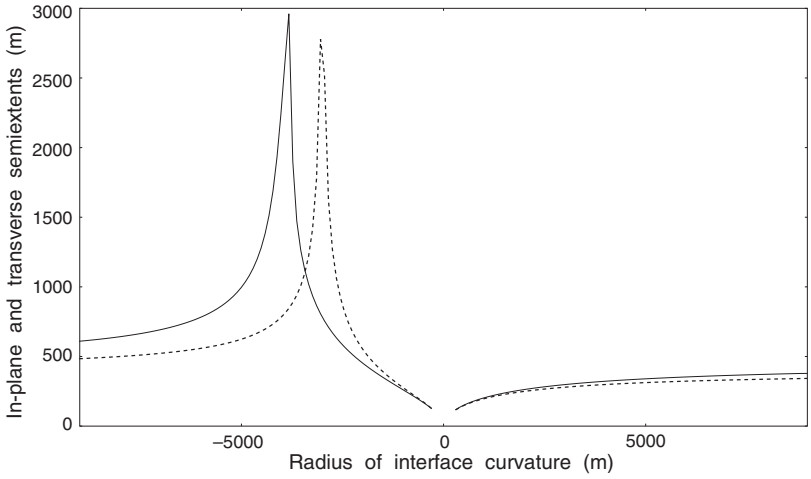

Figure 6. Variation in the in-plane semiextent $x_{\max}$ (solid lines) and in the transverse semiextent $y_{\max}$ (dashed lines) of the interface Fresnel zone at the surface of an anticline (positive radius of interface curvature) and a syncline (negative radius of interface curvature), as a function of the radius of interface curvature R_{int}. The incidence angle θ is equal to 30°. See the legend of Figure 1 for medium properties.

$$F_A = \left(1 + \frac{z_M}{R_{\text{int}}}\frac{a^2}{a^2 - z_M^2 \tan^2\theta}\right)^{-1}, \qquad (25)$$

with positive radius R_{int} and $a = z_M/\cos\theta + \lambda_1/4$. The factors F_S and F_A tend to those given in Lindsey (1989) when the wave incidence is normal to the interface.

Similar conclusions can be drawn for the variation in the maximum semiextent $y_{\max}$ of the IFZ in the transverse plane for the anticline and syncline. The critical parameter that influences the length $y_{\max}$ is the ratio between the radius of curvature R_{iso} of the ellipsoid of revolution describing the isochrone for the source-receiver pair relative to the specular reflection *SMR* in the transverse plane (i.e., the depth z_M of the reflection point M) and radius of the interface curvature R_{int}. For the anticline (respectively, the syncline), the IFZ in the transverse plane is decreased (respectively, increased) in size, as compared with that for a plane interface, approximately by the factor

$$F = \left(1 + \frac{z_M}{R_{\text{int}}}\right)^{-1}, \qquad (26)$$

with positive radius R_{int} for the anticline and negative radius R_{int} for the syncline. Note in Figure 6 that when the value of the radius of the interface curvature R_{int} tends to infinity, the size of the IFZ for a curved interface tends to that for a plane interface.

Figure 7 shows the variation in penetration depth D_2 as a function of the incidence angle θ, for a given value of the radius of the interface curvature R_{int} for the anticline and syncline, whereas Figure 8 presents the variation in penetration depth D_2 as a function of the incidence angle θ for a plane interface. To check the accuracy of our approximation, the approximate results provided by equation 18 were compared with the exact values (Appendix A) for the anticline and syncline. For $\theta = 0°$, the penetration depth D_2 equals the well-known value $\lambda_2/4$ (Kvasnička and Červený, 1996a), as for the plane interface (Figure 8).

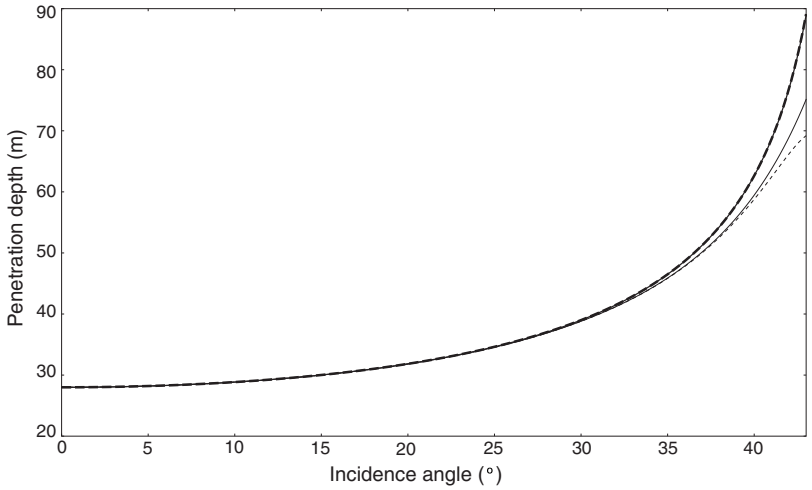

Figure 7. Variation in the penetration depth D_2 as a function of the incidence angle θ for an interface of anticline (light curves) or syncline (bold curves) type. Comparison of results provided by our approximation (dashed lines) with the exact solution (solid lines). See the legend of Figure 1 for medium properties.

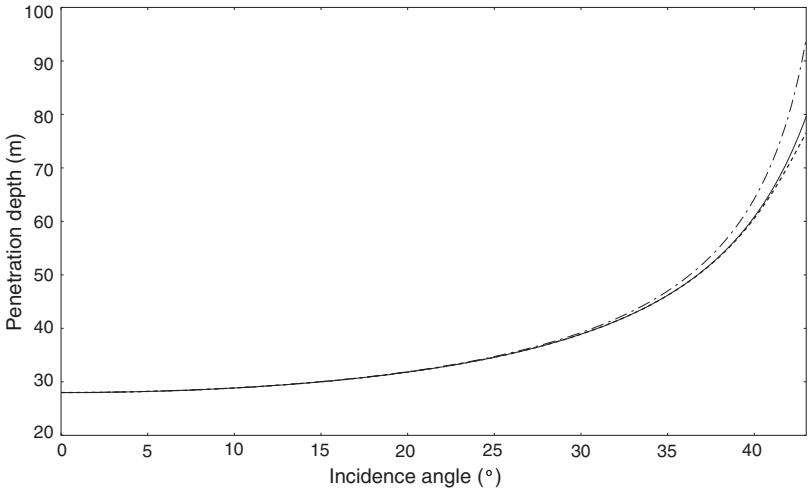

Figure 8. Variation in the penetration depth D_2 as a function of the incidence angle θ for a plane interface. Comparison of results provided by our approximation (dashed line) with exact solution (solid line) and results predicted by the approximation of Kvasnička and Červený (1996a) (dash-dot line).

Inspection of Figure 7 shows that the penetration depth D_2 increases with increasing subcritical angle θ, but it is always less than the seismic wavelength λ_2. For the syncline, it can be larger than the seismic wavelength λ_1 for subcritical incidence angles θ close to the critical angle $\theta_C = 45.58°$. Moreover, the values for the depth D_2 provided by our approximation deviate only slightly from the exact values for the syncline, the discrepancies being less than 0.01% up to the angle $\theta = 43°$, which is in the vicinity of the critical angle θ_C. For the anticline, however, the discrepancies do not exceed 0.01% up to the angle $\theta = 40°$ and 7.5% up to the angle $\theta = 43°$, our approximation underestimating the exact value for the penetration D_2.

Note that whatever the type of interface, the penetration depth D_2 has the same values for incidence angle θ lying between 0° and approximately 30°. For subcritical angles lying above 30°, the penetration depth D_2 for the syncline is, however, larger than that for the anticline. By comparing the curves obtained for the curved interfaces (Figure 7) and those obtained for the plane interface (Figure 8), we can note that the penetration depth D_2 for the syncline is increased in length, as compared with that for a plane interface, by approximately 16%, whereas the penetration depth D_2 for the anticline is decreased by approximately 10%.

Figure 8 shows the variations in the penetration depth D_2 as a function of the incidence angle θ provided by our approximation (equation 18), compared with the values obtained with the approximation of Kvasnička and Červený (1996a) (equation 19) and with the exact values (Appendix A). With increasing subcritical angle θ, the penetration depth D_2 increases, but it is always less than the seismic wavelength λ_2. Moreover, the values for D_2 provided by our approximation

deviate only slightly from the exact values. The discrepancies between them do not exceed 0.44% up to the angle $\theta = 40°$ and 4% up to the angle $\theta = 43°$, which is in the vicinity of the critical angle $\theta_C = 45.58°$.

On the contrary, the discrepancies between values for D_2 given by the approximation of Kvasnička and Červený (1996a) and the exact solution strongly increase with increasing angle θ, more particularly for angles above 30°. For $\theta = 43°$ the discrepancies exceed 23%. As a consequence, the part of a reflector below the interface, which actually affects the interface response and hence the reflected wavefield, is smaller than previous estimates. This conclusion has been found to come true whatever the medium configuration chosen. Nevertheless, for a given incidence angle θ the discrepancies between the values for D_2 provided by our approximation and those given by the approximation of Kvasnička and Červený (1996a) decrease with decreasing impedance contrast at the interface, as shown in Figure 9. For instance, for the impedance contrast equal to 1.2 and the incidence angle $\theta = 30°$, the discrepancy does not exceed 0.27%.

Figure 10 displays the variation in the thickness D_1 above the interface in the upper half-space, as a function of the incidence angle θ, for the given value of the radius of the interface curvature R_{int} for the anticline and syncline. To check the accuracy of our approximation, the approximate results provided by equation 20 were compared with the exact values (Appendix B). Approximate values for D_1 deviate only slightly from the exact values, the discrepancies between them lying below 0.05% up to the angle $\theta = 43°$.

Figure 10 also depicts the variation in the distance D_1, as a function of the incidence angle θ, for a plane interface. In this case, as mentioned above, the distance D_1 provided by equation 20 is evaluated exactly. Whatever the type of interface and for the normal wave incidence ($\theta = 0°$), the distance D_1 equals the value $\lambda_1/4$. The thickness D_1 increases with increasing incidence angles θ, but it is always less than the seismic wavelength λ_1 and penetration depth D_2. Moreover, the thickness D_1 is not much influenced by the interface curvature, the dicrepancies between the curves associated with the syncline and anticline being less than 1%.

In this work, we have identified the zone in the vicinity of a (plane or curved) interface that actually affects the interface reflectivity, and we have established the spatial limits of this effective reflector volume, which merits further investigation. Although these spatial limits might vary following the properties of the bulk media in contact resulting, for instance, from anisotropy or from the presence of heterogeneities, defining these limits for an ideal case (e.g., homogeneous and isotropic media in contact) enables us to fix ideas and provide a road map for future applications to real media.

In addition to providing more physical insights into the wave reflection process, our study could have significant implications for seismic interpretation using amplitude-variation-with-angle (AVA) methodologies. On the one hand, when amplitude measurements are considered, we must evaluate the interface reflectivity by considering the effective reflector volume that actually affects it, and by accounting for heterogeneities located within this volume. More specifically, we must select heterogeneities whose characteristic length, along with their spatial distribution within the reflector volume, might interact with properties of the incident wave, so as to derive a model of the effective behavior of the reflector volume.

A structural description of multiscaled heterogeneities located within the reflector volume must be considered, therefore, as a preliminary step toward the modeling of the interface response. Our future contributions will focus on this topic. However, we specify that in the absence of heterogeneity located within the reflector volume,

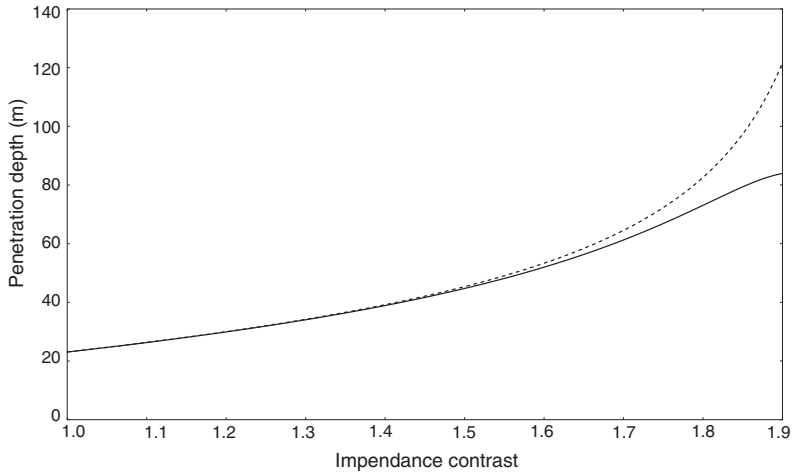

Figure 9. Variation in the penetration depth D_2 as a function of the impedance contrast at a plane interface for the incidence angle $\theta = 30°$. Comparison of results provided by our approximation (solid line) with results predicted by the approximation of Kvasnička and Červený (1996a) (dashed line).

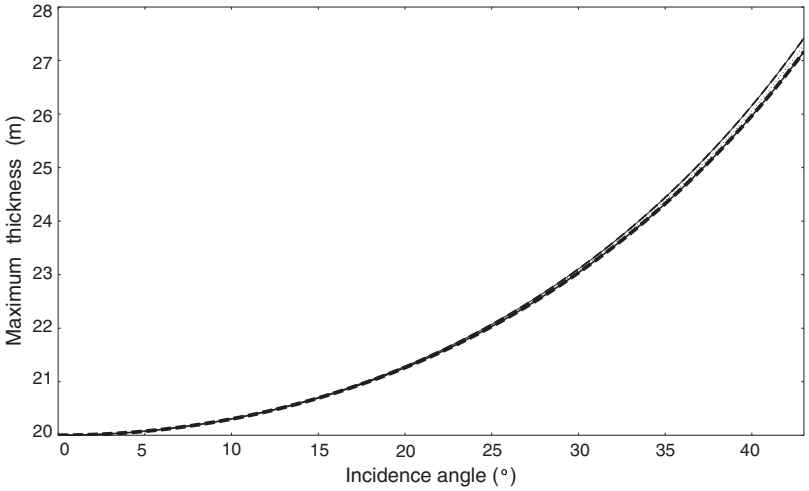

Figure 10. Variation in the maximum thickness D_1 as a function of the incidence angle θ for an interface of anticline (light curves) or syncline (bold curves) type and for a plane interface (dotted line). Comparison of results provided by our approximation (dashed line) with the exact solution (solid line). See the legend of Figure 1 for medium properties.

we must account for only the IFZ for modeling the interface response. In a previous work (Favretto-Cristini et al., 2007), we pointed out the consequences of ignoring the IFZ in forward modeling of seismic wave reflection. More specifically, for wide-angle AVA methodologies and near the critical incidence angle, the geometric spreading compensation no longer is sufficient to reduce the point-source amplitudes to plane-wave (PW) amplitudes predicted by Zoeppritz equations. The additional application of the IFZ concept to the PW theory is necessary to obtain the reflected P-wave amplitudes measured at receivers.

These results have significant implications for seismic interpretation using amplitudes: Assuming that the AVA curves corresponding to real measured data might be described well by the PW theory leads to biased estimations of the media properties, even in the ideal case of homogeneous isotropic media. Our present work is focused precisely on this particular aspect and will be reported later. On the other hand, when only traveltime measurements are considered, for instance for locating reflectors in the media, there is no need to define the region above the interface with the thickness D_1, because this region is already included in the classical representation of the FV, which is the ellipsoid of revolution with foci located at the receiver R and at the image source S'' (Figure 2). In this case, only the region below the interface with the thickness D_2 must be considered.

CONCLUSION

We have identified the zone in the vicinity of an interface that actually affects the interface reflectivity and hence the reflected wavefield. Our work extends previous studies to the case of the oblique wave incidence onto a plane interface, or onto a curved interface of anticline or syncline type, between two homogeneous and isotropic media. We have derived analytic expressions for evaluating approximately the spatial limits of the effective reflector volume.

A comparison with exact results has shown that our expressions provide more accurate results than those given in previous works. The effective reflector volume has its maximum lateral extent equal to the lateral extent of the interface Fresnel zone, and its maximum vertical extent equal to a thickness that might be larger than the seismic wavelength of the incident wave for great incidence angles close to the critical angle. Although the part of the reflector volume lying below the interface and affecting traveltime measurements actually is smaller than described in previous studies, the whole part of the reflector volume affecting the amplitude of the reflected wavefield is larger than previous estimates.

ACKNOWLEDGMENTS

The work reported here is the result of a fruitful collaboration during many years between us, Nathalie Favretto-Cristini and Paul Cristini, and our late friend Dr. Eric de Bazelaire. We consider ourselves extremely fortunate to have had the opportunity to work closely with a scientist of Dr. de Bazelaire's caliber.

We gratefully appreciate the careful reviews by J. P. Lindsey, B. Bednar, A. Stovas, and associate editor D. Draganov. We thank them for their valuable comments and suggestions to improve the manuscript. We also thank Jacques Blanco for his encouragement and enthusiasm for this work.

The work was supported in part by the Agence Nationale de la Recherche (ANR) under the EMSAPCO2 project.

APPENDIX A

EXACT DERIVATION OF THE PENETRATION DEPTH D_2 OF THE FRESNEL VOLUME FOR SUBCRITICAL INCIDENCE ANGLES

We consider the case of a spherically shaped interface of anticline type with the center of curvature C and radius of curvature R_{int}. As the source S and receiver R are located at the same distance from the plane tangent to the curved interface, the penetration zone of the FV is symmetrical, and its deepest point M' is located in the plane of symmetry between S and R (Figure A-1). The penetration distance D_2, which corresponds to the maximum distance D of the point M' from the reflection point M, can be determined mathematically by solving the optimization problem

$$D_2 = \max_{\alpha}\{D\}, \tag{A-1}$$

where

$$D = \left[\left(\frac{\lambda_1}{4} - l_{SA} + l_{SM}\right)^2\left(\frac{V_{P2}}{V_{P1}}\right)^2 - R_{\text{int}}^2\cos^2\alpha\right]^{1/2} + R_{\text{int}}(1 - \sin\alpha), \tag{A-2}$$

obtained from the definition of the Fresnel zone:

$$\frac{l_{SA}}{V_{P1}} + \frac{l_{AM'}}{V_{P2}} - \frac{l_{SM}}{V_{P1}} = \frac{1}{4f}, \tag{A-3}$$

where $l_{SA} = [(z_M \tan\theta + R_{\text{int}}\cos\alpha)^2 + (z_M + R_{\text{int}}(1 - \sin\alpha))^2]^{1/2}$, $l_{SM} = z_M/\cos\theta$, and $l_{AM'} = [R_{\text{int}}^2\cos^2\alpha + (D - R_{\text{int}}(1 - \sin\alpha))^2]^{1/2}$.

In the case of a plane interface, the penetration distance D_2 corresponds to the maximum distance D of M' from the interface plane $z = z_M$. As above, it can be determined mathematically by solving the optimization problem

$$D_2 = \max_{X}\{D\}, \tag{A-4}$$

where $X = l_{AM}$ and $D = [(\lambda_1/4 - l_{SA} + l_{SM})^2(V_{P2}/V_{P1})^2 - X^2]^{1/2}$,

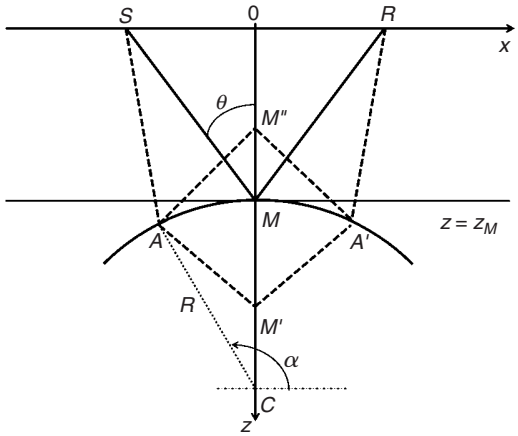

Figure A-1. Schematic description of the configuration for deriving the penetration depth D_2 of the Fresnel volume in the lower half-space and the thickness D_1 in the upper half-space for the case of a spherically shaped interface of anticline type with the center of curvature C and radius of curvature R_{int}.

obtained from the definition of the Fresnel zone with $l_{SA} = [(z_M \tan\theta - X)^2 + z_M^2]^{1/2}$ and $l_{AM'} = (X^2 + D^2)^{1/2}$.

APPENDIX B

EXACT DERIVATION OF THE MAXIMUM THICKNESS D_1 FOR SUBCRITICAL INCIDENCE ANGLES

Considering the configuration depicted in Figure A-1, the maximum thickness D_1, which corresponds to the maximum distance D' of the point M'' from the reflection point M, can be determined mathematically by solving the optimization problem

$$D_1 = \max_{\alpha}\{D'\}, \tag{B-1}$$

where

$$D' = \left[\left(\frac{\lambda_1}{4} - l_{SA} + l_{SM}\right)^2 - R_{\text{int}}^2\cos^2\alpha\right]^{1/2} - R_{\text{int}}(1 - \sin\alpha), \tag{B-2}$$

obtained from the definition of the FZ with $l_{AM''} = [R_{\text{int}}^2\cos^2\alpha + (D + R_{\text{int}}(1 - \sin\alpha))^2]^{1/2}$, the distances l_{SM} and l_{SA} being given in Appendix A.

REFERENCES

Born, M., and E. Wolf, 1999, Principles of optics, 7th exp. ed.: Cambridge University Press.

Červený, V., 2001, Seismic ray theory: Cambridge University Press.

Červený, V., and J. Soares, 1992, Fresnel volume ray tracing: Geophysics, **57**, 902–915.

Favretto-Cristini, N., P. Cristini, and E. de Bazelaire, 2007, Influence on the Interface Fresnel zone on the reflected P-wave amplitude modeling: Geophysical Journal International, **171**, 841–846.

Gelchinsky, B., 1985, The formulae for the calculation of the Fresnel zones or volumes: Journal of Geophysics, **57**, 33–41.

Hagedoorn, J. G., 1954, A process of seismic reflection interpretation: Geophysical Prospecting, **2**, 85–127.

Hubral, P., and T. Krey, 1980, Internal velocities from seismic reflection time measurements: SEG.

Hubral, P., J. Schleicher, M. Tygel, and C. Hanitzch, 1993, Determination of Fresnel zones from traveltime measurements: Geophysics, **58**, 703–712.

Iversen, E., 2004, The isochron ray in seismic modeling and imaging: Geophysics, **69**, 1053–1070.

———, 2006, Amplitude, Fresnel zone, and NMO velocity for PP and SS normal-incidence reflections: Geophysics, **71**, no. 2, W1–W14.

Knapp, R., 1991, Fresnel zones in the light of broadband data: Geophysics, **56**, 354–359.

Kravtsov, Y., and Y. Orlov, 1990, Geometrical optics of inhomogeneous media: Springer-Verlag, Springer Series on Wave Phenomena.

Kvasnička, M., and V. Červený, 1994, Fresnel volumes and Fresnel zones in complex laterally varying structures: Journal of Seismic Exploration, **3**, 215–230.

———, 1996a, Analytical expressions for Fresnel volumes and interface Fresnel zones of seismic body waves: Part 1 — Direct and unconverted reflected waves: Studia Geophysica et Geodetica, **40**, 136–155.

———, 1996b, Analytical expressions for Fresnel volumes and interface Fresnel zones of seismic body waves: Part 2 — Transmitted and converted waves. Head waves: Studia Geophysica et Geodetica, **40**, 381–397.

Lindsey, J., 1989, The Fresnel zone and its interpretative significance: The Leading Edge, **8**, 33–39.

Schleicher, J., P. Hubral, M. Tygel, and M. Jaya, 1997, Minimum apertures and Fresnel zones in migration and demigration: Geophysics, **62**, 183–194.

Sheriff, R., 1980, Nomogram for Fresnel-zone calculation: Geophysics, **45**, 968–972.

Spetzler, J., and R. Snieder, 2004, The Fresnel volume and transmitted waves: A tutorial: Geophysical Journal International, **69**, 653–663.

Zhou, Y., F. Dahlen, G. Nolet, and G. Laske, 2005, Finite-frequency effects in global surface-wave tomography: Geophysical Journal International, **163**, 1087–1111.

Geophys. J. Int. (2007) **171,** 841–846 doi: 10.1111/j.1365-246X.2007.03573.x

Influence of the Interface Fresnel zone on the reflected *P*-wave amplitude modelling

Nathalie Favretto-Cristini,[1] Paul Cristini[1] and Eric de Bazelaire[2]*

[1] *Laboratoire de Modélisation et Imagerie en Géosciences de Pau, Université de Pau, CNRS,* BP 1155*,* 64013 *Pau, France. E-mail: nathalie.favretto@univ-pau.fr*

[2] 11 *route du Bourg,* 64230 *Beyrie-en-Béarn, France*

Accepted 2007 July 27. Received 2007 May 13; in original form 2004 December 3

SUMMARY

The aim of the paper is to emphasize the importance of accounting for the Fresnel volume and for the Interface Fresnel zone (IFZ) for calculating the amplitude of the *P* wave emanating from a point source and recorded at a receiver after its specular reflection on a smooth homogeneous interface between elastic media. For this purpose, by considering the problem of interest as a problem of diffraction by the IFZ, that is, the physically relevant part of the interface which actually affects the reflected wavefield, we have developed a method which combines the Angular Spectrum Approach (ASA) with the IFZ concept to get the 3-D analytical solution. The variation in the reflected *P*-wave amplitude evaluated with the ASA, as a function of the incidence angle, is compared with the plane wave (PW) reflection coefficient and with the exact solution provided by the 3-D code OASES, for one solid/solid configuration and two dominant frequencies of the source. For subcritical incidence angles the geometrical spreading compensation is mostly quite sufficient to reduce the point-source amplitudes to the PW amplitudes. On the contrary, for specific regions of incidence angles for which the geometrical spreading compensation is not sufficient anymore, that is, near the critical region and in the post-critical domain, the ASA combined with the IFZ concept yields better results than the PW theory whatever the dominant frequency of the source, which suggests that the additional application of the IFZ concept is necessary to obtain the reflected *P*-wave amplitude. Nevertheless, as the ASA combined with the IFZ has been used only for evaluating the contribution of the reflected wavefield at the receiver, its predictions fail when the interference between the reflected wave and the head wave becomes predominant.

Key words: amplitude, Fresnel volume, Interface Fresnel zone, *P* wave, reflected wave, smooth interface.

INTRODUCTION

Since many decades geophysicians have developed various theoretical methods to fit the real seismic data, their ultimate goal being to invert them to retrieve the geometrical and physical characteristics of the Earth. Since the media heterogeneity can be highly complex, depending on the seismic frequency range of interest, using the exact form (in the time domain) of waves emanating from a point source and being reflected by interfaces (Aki & Richards 2002, chap. 6) can be a very difficult task for interpreting some seismic observations. Interpretation of such observations then always relies on approximations.

The basis of many seismic studies is the ray theory (Cerveny 2001). Under this approximation it is assumed that the high-frequency part of elastic energy propagates along infinitely narrow lines through space, called rays, which join the source and the receiver. Ray theory is then strictly valid only in the limit of a hypothetical infinite-frequency wave. As recorded data have a finite frequency content, it is accepted that seismic wave propagation is extended to a finite volume of space around the ray path, called the first Fresnel volume (Kravtsov & Orlov 1990), hereafter denoted FV. The wave properties are thus influenced not only by the media structure along the ray, but also by the media structure in the vicinity of the ray. This well-known limitation of ray theory has received broad attention in recent past years. The concept of FV (also known as physical ray, 3-D Fresnel zone, etc.) is continually being developed and has found so many applications in seismology and in seismic exploration, that it is impossible here to review all the books and articles which pay attention to it in seismic wave propagation. Nevertheless, we shall mention the works of Cerveny and his co-authors who have proposed two methods for including FV parameter calculations into the ray tracing procedure in complex

*Deceased on 2007, June 28th

2-D and 3-D structures. The first one, called the Fresnel volume ray tracing (Cerveny & Soares 1992), combines the paraxial ray approximation with the dynamic ray tracing and is only applicable to zero-order waves (direct, reflected and transmitted waves...), whereas the second method, more accurate than the previous one, is based on network ray tracing (Kvasnicka & Cerveny 1994). Contrary to the previous methods, the FVs can also be computed without knowledge of the velocity model of the media (Hubral *et al.* 1993). Note that analytical expressions for FVs of seismic body waves and for their intersection with interfaces, called the Interface Fresnel zones (IFZ), have been derived in Kvasnicka & Cerveny (1996a) and in Kvasnicka & Cerveny (1996b). Many works have shed new light on the role of the FVs in the seismic imaging of reflectors. They have shown that, besides being connected with the resolution of seismic methods (Sheriff 1980; Lindsey 1989; Knapp 1991), the FVs also play a role in the migration and demigration processes (Hubral *et al.* 1993; Schleicher *et al.* 1997). Moreover, FVs have been applied to inversion studies of seismic data (Yomogida 1992) and they have been incorporated into tomographic traveltime inversion schemes (Vasco & Majer 1993). Note also that in global seismology, sensitivity kernels have been developed for global tomography inversions to overcome the limitations of ray theory and to account for finite-frequency effects upon seismic wave propagation (Zhou *et al.* 2005). Sensitivity kernels (also known as Fréchet kernels) linearly relate velocity perturbations of the medium to changes in some seismic observables (traveltime, waveform, splitting intensity) of the band-limited waves (Marquering *et al.* 1999; Dahlen *et al.* 2000; Dahlen & Baig 2002; Favier & Chevrot 2003). FVs and sensitivity kernels are closely connected through the concept of constructive interferences of waves (Vasco *et al.* 1995; Spetzler & Snieder 2004).

The variability of the amplitudes of the reflected waves with the incidence angle is of great interest for many seismological applications, for instance to constrain localization of reflectors and media properties. Since the media heterogeneity can be highly complex in the typical seismic frequency range, and considering that both source and receivers are usually located far from the interfaces, the exact form of spherical waves generated by a point source is not convenient for interpreting complex seismic observations. A survey of the literature brings to light that most calculations are generally performed within the framework of monochromatic plane wave (PW) theory or finite-frequency theory without nevertheless taking into account the frequency-dependent spatial regions (i.e. FVs) in the vicinity of the ray. This is justified by the fact that for some typical configurations and for subcritical incidence angles, the geometrical spreading compensation is mostly quite sufficient to reduce the point-source amplitudes to the PW amplitudes. On the contrary, for critical and post-critical incidence angles this compensation is generally not sufficient anymore, and an additional processing should be considered. To the best of the authors' knowledge, a theoretical study of the FV and IFZ imprint on the reflected wave amplitudes for critical and post-critical angles has not been developed yet, despite the band-limited nature of seismic data. This is the purpose and scope of this work.

The paper is divided in two sections. Section 1 is mainly concerned with 3-D analytical derivations. After briefly introducing the FV and IFZ concepts, we describe the method we used for deriving the amplitude of the *P* wave emanating from a point source and recorded at a receiver after its reflection on a smooth interface between elastic media. As the problem under consideration can be viewed as a problem of diffraction by the IFZ, that is, the physically relevant part of the interface which actually affects the reflected wavefield, we applied the Angular Spectrum Approach (ASA) (Goodman 1996) to get the 3-D analytical solution. Section 2 investigates the role of the IFZ in the reflected wave propagation, more specially in the critical and post-critical regions. The variation in the reflected *P*-wave amplitude, as a function of the incidence angle, evaluated with the ASA is compared with the PW reflection coefficient, and with the exact solution obtained with the 3-D code OASES (http://acoustics.mit.edu/faculty/henrik/oases.html), for one solid/solid configuration and two dominant frequencies of the source.

1 3-D ANALYTICAL DERIVATIONS OF THE REFLECTED *P*-WAVE AMPLITUDE

1.1 Characteristics of the Interface Fresnel zone

We consider two homogeneous isotropic elastic media in welded contact at a plane interface characterized by the *xy*-plane, the vertical *z*-axis being directed downwards. The point source S($-x_S$, 0, $-z_S$) and the receiver R(x_S, 0, $-z_S$) are located at a distance z_S from the interface. The source generates in the upper medium a spherical wave with a constant amplitude. The spherical wave can be decomposed into an infinite sum of PW synchronous each other at the time origin. We consider the harmonic PW with frequency f which propagates in the upper medium with the velocity V_{P1} from S to R, after being reflected by the interface at the Cartesian coordinate origin M(0,0,0) in a specular direction θ with respect to the normal to the interface. Let the traveltime of the ray SMR be t_{SMR}.

The frequency-dependent spatial region in the vicinity of the ray SMR which actually affects the wavefield at the receiver R is known to be the FV corresponding to the source–receiver pair (S, R) and relative to the specular reflection SMR. By definition, the FV is formed by virtual points F which satisfy the following condition (Kravtsov & Orlov 1990):

$$|t\,(F,S)+t\,(F,R)-t\,(M,S)-t\,(M,R)| \leq \frac{1}{2\,f}, \tag{1}$$

or:

$$|l\,(F,S)+l\,(F,R)-l\,(M,S)-l\,(M,R)| \leq \frac{\lambda_1}{2}, \tag{2}$$

where $\lambda_1 = \frac{V_{P1}}{f}$ is the wavelength corresponding to the dominant frequency f of the narrow-band source signal. The quantity $t\,(X,Y)$ denotes the traveltime from the point X to the point Y, and $l\,(X,Y)$ the distance between X and Y. The boundary of the FV is then given by the following equation:

$$|l\,(F,S)+l\,(F,R)-l\,(M,S)-l\,(M,R)| = \frac{\lambda_1}{2}. \tag{3}$$

Here, it must be specified that, as seismic wavefields are transient and large-band, it is generally necessary to decompose the source signal into narrow-band signals for which monochromatic FV can be constructed for the prevailing frequency of the signal spectrum (Knapp 1991). The physical meaning of eq. (2), describing the FV concept, is quite obvious: the waves passing through the diffraction points F interfere constructively with the specular reflected wave when the path-length difference is less than one-half of the wavelength λ_1. As is well known, the main contribution to the wavefield comes from the first FV as the rapid oscillatory responses of the higher-order FVs and Fresnel zones cancel out and give minor contributions to the wavefield (Born & Wolf 1999). That is why in our work we restrict ourselves to the first FV which will be simply referred to as FV.

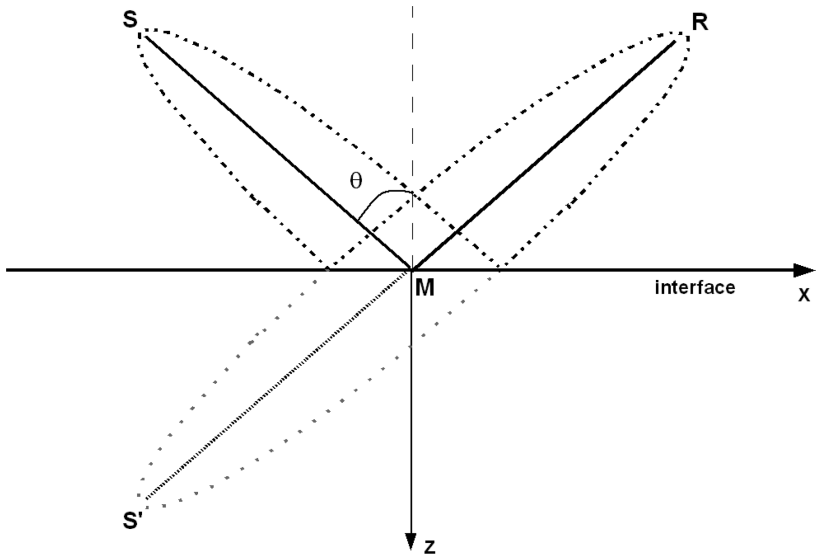

Figure 1. Representation in the *xz*-plane of the Fresnel volume involved in the wave reflection at the point M at a plane homogeneous interface, under the incidence angle θ. The source S and the receiver R are located at a distance z_S from the interface. The classical representation of the Fresnel volume is the ellipsoid of revolution with foci located at R and at the image source S' situated symmetrically to the point source S on the other side of interface. The Interface Fresnel zone is characterized by the intersection of the ellipsoid of revolution (Fresnel volume) with the interface plane.

The IFZ is defined as the cross-section of the FV by an interface which may not be perpendicular to the ray SMR. If the source S and the receiver R are situated at the same distance from the interface, the IFZ is represented by an ellipse centred at the reflection point M. The common way of determining the size of the IFZ is to consider the FV represented by the ellipsoid of revolution with foci at the receiver R and at the image source S' situated symmetrically to S on the other side of interface (Fig. 1). The boundary of this FV is then given by the following equation:

$$|l(F, S') + l(F, R) - l(M, S') - l(M, R)| = \frac{\lambda_1}{2}, \tag{4}$$

or in the Cartesian coordinates (x, y, z) after some straightforward calculations:

$$\frac{(x\ \sin\theta - z\ \cos\theta)^2}{\left(\frac{z_S}{\cos\theta} + \frac{\lambda_1}{4}\right)^2} + \frac{y^2 + (x\ \cos\theta + z\ \sin\theta)^2}{\frac{\lambda_1}{2}\ \left(\frac{z_S}{\cos\theta} + \frac{\lambda_1}{8}\right)} = 1. \tag{5}$$

The boundary of the IFZ is then obtained from the formulation of the ellipsoid of revolution, eq. (5), equating the variable z to zero:

$$\frac{x^2}{r^{\parallel 2}} + \frac{y^2}{r^{\perp 2}} = 1, \tag{6}$$

where the in-plane semi-axis $r^{\parallel}$, corresponding to the plane of incidence, and the transverse semi-axis $r^{\perp}$, corresponding to the direction perpendicular to the plane of incidence, of the IFZ are expressed as (Kvasnicka & Cerveny 1996a):

$$r^{\parallel} = \left[\frac{\lambda_1}{2}\ \left(\frac{z_S}{\cos\theta} + \frac{\lambda_1}{8}\right)\right]^{\frac{1}{2}} \left[1 - \frac{z_S^2 \tan^2\theta}{\left(\frac{z_S}{\cos\theta} + \frac{\lambda_1}{4}\right)^2}\right]^{-\frac{1}{2}},$$

$$r^{\perp} = \left[\frac{\lambda_1}{2}\ \left(\frac{z_S}{\cos\theta} + \frac{\lambda_1}{8}\right)\right]^{\frac{1}{2}}. \tag{7}$$

The characteristics of the IFZ depend on the position of the source–receiver pair, and also on the incidence angle of the ray SM. Moreover, larger portions of the interface (reflector) are involved for low-frequency than for high-frequency components of the wavefield. It is also well known that a perturbation of the medium actually affects the reflected wave when this perturbation is located inside the IFZ.

1.2 Analytical expression for the reflected *P*-wave amplitude

We consider the same previous configuration. Let the orthotropic source be located at the point S, far from the plane interface between two homogeneous isotropic elastic media. The spherical *P* wave emanating from the source propagates obliquely in the upper medium and strikes the interface. It is then reflected from the interface and finally recorded at the receiver located at the point *R*, far from the interface. Our objective is to calculate the amplitude of the reflected wavefield measured at the receiver, by accounting for the FV and the IFZ which physically contribute to the wave propagation process.

The problem under consideration can be viewed as a problem of diffraction by the physically relevant part of the interface (namely, the IFZ). We chose to apply the ASA (Goodman 1996) to get the 3-D analytical solution to this problem. The motivations of this choice are twofold. Provided the spherical wavefield is decomposed by Fourier analysis into a linear combination of elementary plane wavesurfaces, travelling in different directions away from the source, the effect of propagation over distance is simply a change of the relative phases of the various plane wavesurface components. Moreover, despite their apparent differences, the ASA and the first Rayleigh-Sommerfeld solution (Goodman 1996, chap. 3, p. 47) yield identical predictions of diffracted fields (Sherman 1967). The advantage of using the ASA then seems obvious: it permits straightforward derivations of the measured amplitude of the reflected wave at the point R. We refer to the book of Goodman (Goodman 1996, chap. 3, pp. 55–61) for a detailed treatment of the ASA.

When using the ASA, we have to remind that it is a technique for modelling the propagation of acoustic fields between parallel planes. Considering the case of the field reflection from an oblique interface then requires several steps including rotational transformation of

complex amplitudes in the Fourier domain. This step which is the most essential and significant operation in the problem of interest here causes various problems. The non-linearity of the rotational transformation has to be taken into account and a Jacobian must be introduced. The rotational transformation also causes numerical problems, more specifically the distortion of equidistant sampling grid of the field and a shift in the centre frequency in the resulting spectrum, which makes the standard Fast Fourier Transform (FFT) algorithm inapplicable. Efficient solutions to these problems can be found in (Matsushima *et al.* 2003). We refer to the paper of Matsushima and his collaborators for a detailed treatment of these solutions.

The procedure of the method we used to get the amplitude of the reflected wavefield measured at the receiver can be summarized as follows. At the interface $z = 0$, and more precisely within the IFZ, the amplitude U generated by the point source S and diffracted by the IFZ has a 2-D Fourier transform given by:

$$A\left(f_x, f_y, 0, \theta\right) = \int\int_{-\infty}^{+\infty} U\left(x, y, 0, \theta\right) \exp\left[-j2\pi\left(f_x x + f_y y\right)\right] \mathrm{d}x\,\mathrm{d}y \qquad (8)$$

where $U(x, y, 0, \theta) = \frac{e^{j\frac{2\pi f}{V_{P1}} R_M}}{R_M} H(x, y, \theta)$ with $R_M = \sqrt{x^2 + y^2 + z_I^2}$ and $z_I = z_S/\cos\theta$.

The function $H(x, y, \theta)$ represents the size of the IFZ which is a function of the incidence angle θ:

$$\begin{cases} H(x, y, \theta) = 1 & \text{if } (x, y) \in IFZ \\ H(x, y, \theta) = 0 & \text{if } (x, y) \notin IFZ \end{cases}$$

The term $A\left(f_x, f_y, 0, \theta\right)$ represents the plane wave decomposition of the incident wavefield, that is, the angular spectrum. The direction cosines of each plane wave associated with the frequencies (f_x, f_y) are given by (Goodman 1996):

$$\alpha = \lambda_1 f_x\,, \quad \beta = \lambda_1 f_y, \quad \gamma = \sqrt{1 - \alpha^2 - \beta^2}.$$

As the incident wavefield is reflected from the interface, the angular spectrum of the resulting wavefield is obtained by multiplying $A\left(f_x, f_y, 0, \theta\right)$ by the classical plane wave reflection coefficient $R\left(f_x, f_y, \theta\right)$ given by Zoeppritz equations (Aki & Richards 2002):

$$A_R(f_x, f_y, 0, \theta) = A(f_x, f_y, 0, \theta)\, R(f_x, f_y, \theta). \qquad (9)$$

The reflection coefficient takes into account the fact that the central ray is incident on the interface under the incidence angle θ. The angular spectrum $A_R(\tilde{f}_x, \tilde{f}_y, 0, \theta)$ is then calculated from $A_R(f_x, f_y, 0, \theta)$ for the interface plane rotated by θ clockwise about the origin M. This plane is perpendicular to the specularly reflected ray passing through the point M. At this step, we must multiply the angular spectrum $A_R(\tilde{f}_x, \tilde{f}_y, 0, \theta)$ by the Jacobian $J(\tilde{f}_x, \tilde{f}_y, \theta)$ resulting from the rotational transformation in order to get the correct energy of each plane wave component. The resulting angular spectrum in the rotated plane is:

$$\tilde{A}_R(\tilde{f}_x, \tilde{f}_y, 0, \theta) = A_R(\tilde{f}_x, \tilde{f}_y, 0, \theta)\, |J(\tilde{f}_x, \tilde{f}_y, \theta)|. \qquad (10)$$

We must also apply a method of interpolation to obtain an equidistant sampling grid of the spectrum, as suggested in (Matsushima *et al.* 2003). The angular spectrum $\tilde{A}_R(\tilde{f}_x, \tilde{f}_y, 0, \theta)$ is then propagated to the parallel plane passing through the receiver R. The resulting spectrum is expressed as:

$$\tilde{A}_R(\tilde{f}_x, \tilde{f}_y, -z_S, \theta) = \tilde{A}_R(\tilde{f}_x, \tilde{f}_y, 0, \theta) \exp\left[j\, 2\pi\gamma\, \frac{z_I}{\lambda_1}\right]. \qquad (11)$$

Table 1. Properties of the homogeneous, isotropic, and elastic media in contact. ρ, V_P and V_S denote, respectively, the density, P- and S-wave velocities for the upper (subscript 1 in the text) and lower media.

Properties	V_P (m s^{-1})	V_S (m s^{-1})	ρ (kg m^{-3})
Upper medium	4000	2000	2000
Lower medium	5200	2500	2400

By using inverse Fourier transform, we get the amplitude of the reflected wavefield:

$$U_R(\tilde{x}, \tilde{y}, -z_S, \theta) = \int\int_{-\infty}^{+\infty} \tilde{A}_R(\tilde{f}_x, \tilde{f}_y, -z_S, \theta) \exp[j2\pi(\tilde{f}_x\tilde{x} + \tilde{f}_y\tilde{y})]\mathrm{d}\tilde{x}\,\mathrm{d}\tilde{y}. \qquad (12)$$

Since the receiver is located at the centre of the plane, the amplitude of the reflected wavefield at the receiver is finally given by $U_R(0, 0, -z_S, \theta)$.

2 COMPARISON WITH THE EXACT SOLUTION AND WITH THE PLANE WAVE THEORY PREDICTION

The aim of this section is to evaluate the importance of using the band-limited data concept, based on the IFZ, in order to simulate the amplitudes of the reflected waves recorded at receivers. For this purpose, it is instructive to compare the variation in the amplitude obtained with our approximation (ASA combined with the IFZ concept), as a function of the incidence angle, with the amplitude predicted by a numerical code which provides the exact solution, and with the amplitude predicted by the classical PW theory [here, the Zoeppritz equations (Aki & Richards 2002)]. We used the 3-D code OASES (http://acoustics.mit.edu/faculty/henrik/oases.html) to compute accurately synthetic seismograms in media. OASES is a general purpose computer code for modelling seismo-acoustic propagation in horizontally stratified media using wavenumber integration in combination with the Direct Global Matrix solution technique (Schmidt & Jensen 1985; Schmidt & Tango 1986; Jensen *et al.* 1994). In seismology, the wavenumber integration methods are often referred to as reflectivity methods or discrete wavenumber methods (Fuchs & Muller 1971; Bouchon 1981; Kennett 1983; Olson *et al.* 1984; Muller 1985). This software has the great advantage of providing reference solutions for various types of sources (explosive source, vertical point force, etc.). In addition, upward and downward propagation of compressional and of shear waves can be easily separated. This 3-D code is widely used in the underwater acoustics community and has been thoroughly validated.

One case of interface between elastic media whose properties are reported in Table 1 has been chosen to illustrate the theoretical results. The interface is situated at a distance $z_S = 3000$ m from the source–receiver plane. For the 3-D code the amplitude of the source signal is chosen to be the Fourier transform of a Ricker wavelet with either the dominant frequency $f = 32$ Hz and the frequency bandwidth $B = 10$ Hz, or $f = 12$ Hz and $B = 6$ Hz.

Fig. 2 depicts the amplitude-versus-angle (AVA) curves provided by the exact solution and by our approximation for the frequencies $f = 32$ and 12 Hz, and the AVA curves provided by the PW theory which does not depend on frequency. A geometrical spreading compensation factor equal to $\frac{z_S}{\cos\theta}$ was applied to the predictions of our 3-D approximation and to the synthetic data provided by the 3-D code OASES, in order to be compared in a suitable way with the

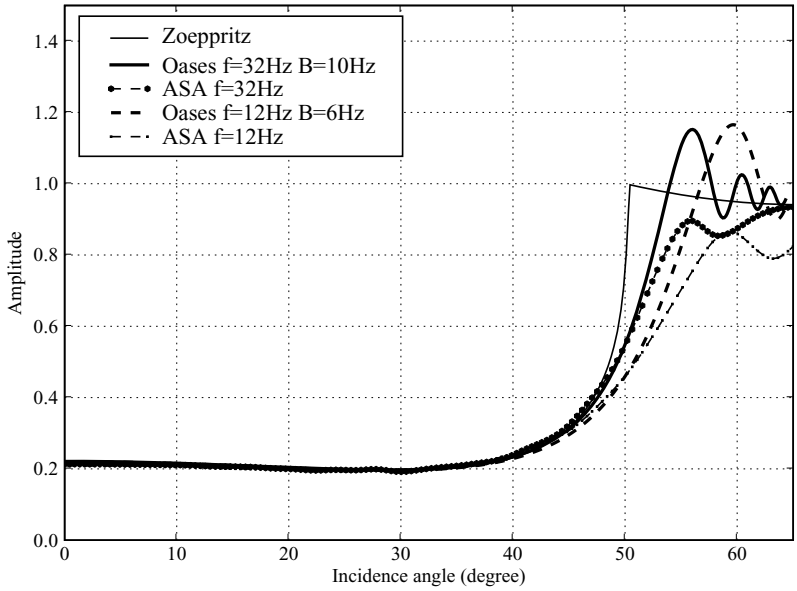

Figure 2. Variation of the amplitude of the P wave reflected from a plane interface, as a function of the incidence angle. Comparison between the plane wave reflection coefficient and the spreading-free amplitudes associated with the exact solutions and with the approximate solutions. The exact solutions were provided by the 3-D code OASES. The source signal was a Ricker wavelet with either the dominant frequency $f = 32$ Hz and the frequency bandwidth $B = 10$ Hz, or $f = 12$ Hz and $B = 6$ Hz. The approximate solutions were obtained by applying the Angular Spectrum Approach together with the Interface Fresnel Zone concept for $f = 32$ and 12 Hz.

PW predictions. Inspection of Fig. 2 shows that for small subcritical angles, AVA curves associated with the exact (OASES) solution and AVA curves associated with the PW theory are quite identical. The discrepancies between them do not exceed 1.4 per cent (for $f = 12$ Hz) and 1 per cent (for $f = 32$ Hz) up to $\theta = 40^\circ$. As the PW reflection coefficient varies smoothly with the incidence angle, the geometrical spreading compensation is sufficient to reduce the amplitude of the reflected wave generated by the point source to the reflected PW amplitude. The effect of the IFZ on the wave amplitude, is therefore, negligible for small incidence angles in the subcritical region. Between $\theta = 40^\circ$ and the critical angle $\theta_C = 50.28^\circ$, the PW reflection coefficient rapidly increases with the incidence angle, and the geometrical spreading compensation is not sufficient anymore. The discrepancies between the exact curves and the PW reflection coefficient increase monotonically with the incidence angle and exceed 105 per cent (for $f = 12$ Hz) and 70 per cent (for $f = 32$ Hz) for θ_C. Therefore, the additional application of the IFZ concept becomes necessary to get the reflected P-wave amplitude. Note that the discrepancies between the exact solution and the reflection coefficient also increase with decreasing frequencies. The PW theory does not yield reasonable results for low frequencies.

In Fig. 2 we can also note that near the critical angle, the predictions of our approximation which combines the ASA and the IFZ concept yields better results than the PW reflection coefficient, more particularly between $\theta = 40^\circ$ and θ_C. Whatever the frequency, the discrepancies between the ASA curves and the exact curves do not exceed 5 per cent up to $\theta = 52^\circ$ and are smaller than 1 per cent for $\theta_C = 50.28^\circ$. Nevertheless, with increasing incidence angle, the approximate solutions show increasing discrepancies in comparison with the corresponding exact solutions. The discrepancies reach the maximum value of 26 per cent for $\theta = 60^\circ$ and $f = 12$ Hz, and the maximum value of 22 per cent for $\theta = 56^\circ$ and $f = 32$ Hz. Beyond these angles they sharply decrease with increasing incidence angles. The explanation of the discrepancies between our approximate solutions and the exact ones may come from the fact that we calculated only the reflected wave amplitude, whereas the code OASES provides the amplitude of the interference between the reflected and the head wavefields. The contribution of each wavefield to the global amplitude at the receiver cannot be discriminated in the synthetic seismograms because both waves have the same traveltime for a specific range of incidence angles. In fact, it would be interesting to get the amplitude of the head wave by using the combination of the ASA with the IFZ concept associated with this particular wave, in order to determine the contribution of the reflected wave and the contribution of the head wave at the receiver, taking into account the phase shifts. This would enlighten on the complex physical process of wave interference with the reflected wave. Our present work is focused precisely on this particular aspect and will be reported later.

CONCLUSION

The aim of the paper was to discuss the influence of the IFZ for modelling the amplitude of the P wave emanating from a point source and recorded at a receiver after its specular reflection on a smooth interface between two elastic media. As the problem of interest can be viewed as a problem of diffraction by the IFZ, that is, the physically relevant part of the interface which actually affects the reflected wavefield, we have applied the ASA combined with the IFZ concept to get the 3-D analytical solution. The variation in the reflected P-wave amplitude obtained with the ASA, as a function of the incidence angle, has been compared for one solid/solid configuration and two frequencies of the source with the PW reflection coefficient and with the exact solution obtained with the 3-D code OASES. It results that for subcritical incidence angles the geometrical spreading compensation is mostly quite sufficient to reduce the point-source amplitudes to the PW amplitudes. On the contrary, near the critical region, the ASA combined with the IFZ

concept yields better results than the PW theory whatever the dominant frequency of the source. These results suggest that near and beyond the critical region the geometrical spreading compensation is not sufficient anymore, and that the additional application of the IFZ concept, therefore, becomes necessary to obtain the reflected *P*-wave amplitude. As in the paper our approximation is concerned only with the reflected wavefield, its predictions fail in the post-critical region when the interference between the reflected wave and the head wave becomes predominant. For a further validation of our method, we need to evaluate the contribution of the head wave at the receiver by taking into account its own IFZ, in order to combine it with the contribution of the reflected wavefield at the receiver. Our present work is focused precisely on this particular aspect and will be reported later.

ACKNOWLEDGMENTS

The manuscript has been significantly improved thanks to the relevant suggestions of anonymous reviewers and the editor. We appreciate the time and effort that they invested in our study and we gratefully acknowledge them.

The work reported here is the result of fruitful collaboration with our friend Dr Eric De Bazelaire during many years. We consider ourselves extremely fortunate to have had the opportunity to work at close quarters with a scientist of his calibre, and more specially to have stroken up a profound friendship with him.

REFERENCES

Aki, K. & Richards, P., 2002. *Quantitative Seismology*, 2nd edn, University Science Books, Sausalito, CA, USA.

Born, M. & Wolf, E., 1999. *Principles of Optics*, 7th expanded edn, Cambridge University Press, Cambridge, UK.

Bouchon, M., 1981. A simple method to calculate Green's functions for elastic layered media, *Bull. seism. Soc. Am.,* **71,** 959–971.

Cerveny, V., 2001. *Seismic Ray Theory*, Cambridge University Press, Cambridge, UK.

Cerveny, V. & Soares, J.E.P., 1992. Fresnel volume ray-tracing, *Geophysics,* **57,**(7), 902–915.

Dahlen, F.A. & Baig, A.M., 2002. Fréchet kernels for body wave amplitudes, *Geophys. J. Int.,* **150,** 440–466.

Dahlen, F.A., Hung, S.-H. & Nolet, G., 2000. Fréchet kernels for finite-frequency traveltimes-I. Theory, *Geophys. J. Int.,* **141,** 157–174.

Favier, N. & Chevrot, S., 2003. Sensitivity kernels for shear wave splitting in transverse isotropic media, *Geophys. J. Int.,* **153,** 213–228.

Fuchs, K. & Muller, G., 1971. Computation of synthetic seismograms with the reflectivity method and comparison of observations, *Geophys. J. R. astr. Soc.,* **23,** 417–433.

Goodman, J.W., 1996. *Introduction to Fourier Optics*, 2nd edn, MacGraw-Hill, New York, USA.

Hubral, P., Schleicher, J., Tygel, M. & Hanitzch, C., 1993. Determination of Fresnel zones from traveltime measurements, *Geophysics,* **58**(5), 703–712.

Jensen, F.B., Porter, M.B., Kuperman, W.A. & Schmidt, H., 1994. *Computational Ocean Acoustics*, American Institute of Physics, New York.

Kennett, B.L.N., 1983. *Seismic Wave Propagation in Stratified Media*, Cambridge University Press, Cambridge.

Knapp, R.W., 1991. Fresnel zones in the light of broadband data, *Geophysics,* **56**(3), 354–359.

Kravtsov, Yu.A. & Orlov, Yu.I., 1990. *Geometrical Optics of Inhomogeneous Media*, Springer Series on Wave Phenomena, Springer-Verlag, NY.

Kvasnicka, M. & Cerveny, V., 1994. Fresnel volumes and Fresnel zones in complex laterally varying structures, *J. Seism. Explor.,* **3,** 215–230.

Kvasnicka, M. & Cerveny, V., 1996a. Analytical expressions for Fresnel volumes and interface Fresnel zones of seismic body waves. Part 1: direct and unconverted reflected waves, *Stud. Geophys. Geod.,* **40,** 136–155.

Kvasnicka, M. & Cerveny, V., 1996b. Analytical expressions for Fresnel volumes and interface Fresnel zones of seismic body waves. Part 2: transmitted and converted waves. Head waves, *Stud. Geophys. Geod.,* **40,** 381–397.

Lindsey, J., 1989. The Fresnel zone and its interpretative significance, *The Leading Edge,* **8,**(10), 33–39.

Marquering, H., Dahlen, F.A. & Nolet, G., 1999. Three-dimensional sensitivity kernels for finite-frequency traveltimes: the banana-doughnut paradox, *Geophys. J. Int.,* **137,** 805–815.

Matsushima, K., Schimmel, H. & Wyrowski, F., 2003. Fast calculation method for optical diffraction on tilted planes by use of the angular spectrum of plane waves, *J. Opt. Soc. Am. A,* **20,**(9), 1755–1762.

Muller, G., 1985. The reflectivity method: a tutorial, *J. Geophys.,* **58,** 153–174.

Olson, A.H., Orcutt, J.A. & Fisher, G.A., 1984. The discrete wavenumber/finite element method for synthetic seismograms, *Geophys. J. R. astr. Soc.,* **77,** 412–460.

Schleicher, J., Hubral, P., Tygel, M. & Jaya, M.S., 1997. Minimum apertures and Fresnel zones in migration and demigration, *Geophysics,* **62,** 183–194.

Schmidt, H. & Jensen, F.B., 1985. A full wave solution for propagation in multilayered viscoelastic media with application to Gaussian beam reflection at fluid-solid interfaces, *J. Acoust. Soc. Am.,* **77,** 813–825.

Schmidt, H. & Tango, G., 1986. Efficient global matrix approach to the computation of synthetic seismograms, *Geophys. J. R. astr. Soc.,* **84,** 331–359.

Sheriff, R.E., 1980. Nomogram for Fresnel-zone calculation, *Geophysics,* **45,**(5), 968–972.

Sherman, G.C., 1967. Application of the convolution theorem to Rayleigh's integral formulas, *J. Opt. Soc. Am.,* **57,** 546–547.

Spetzler, J. & Snieder, R., 2004. The Fresnel volume and transmitted waves: a tutorial, *Geophys. J. Int.,* **69,**(3), 653–663.

Vasco, D.W. & Majer, E.L., 1993. Wavepath traveltime tomography, *Geophys. J. Int.,* **115,** 1055–1069.

Vasco, D.W., Peterson, J.E. Jr & Majer, E.L., 1995. Beyond ray tomography: wavepaths and Fresnel volumes, *Geophysics,* **60,**(6), 1790–1804.

Yomogida, K., 1992. Fresnel zone inversion for lateral heterogeneities in the earth, *Pure Appl. Geophys.,* **138,**(3), 391–406.

Zhou, Y., Dahlen, F.A., Nolet, G. & Laske, G., 2005. Finite-frequency effects in global surface-wave tomography, *Geophys. J. Int.,* **163,** 1087–1111.

Theoretical and Computational Acoustics '07
Michael Taroudakis and Panagiotis Papadakis (Editors)

ON THE INFLUENCE OF THE INTERFACE FRESNEL ZONE FOR ESTIMATING MEDIA PARAMETERS FROM SEISMIC AMPLITUDE-VERSUS-ANGLE CURVES

NATHALIE FAVRETTO-CRISTINI [1], PAUL CRISTINI [1] and ERIC DE BAZELAIRE [2,+]

[1] *Laboratoire de Modélisation et Imagerie en Géosciences (MIGP),CNRS, Université de Pau, BP 1155, 64013 Pau, France. Contact author: nathalie.favretto@univ-pau.fr*
[2] *11 route du Bourg, 64230 Beyrie-en-Béarn, France*
[+] *Deceased on 2007, June 28th*

Abstract

The band-limited property and the low-frequency content of the seismic data are rarely taken into account in wave reflection modeling. In this work we point out the consequences of ignoring such signal characteristics in both forward and inverse modeling of seismic wave reflection. The variation in the reflected P-wave amplitude as a function of the incidence angle, also known as AVA curve, obtained with the classical plane-wave (PW) theory, is compared with the exact solution provided by the 3D code OASES, and with our approximation which accounts for the spatial region which physically contributes to the wave reflection process, i.e. the Interface Fresnel zone. Our approximation provides much better data predictions than the PW theory, widely used in AVA studies in seismic exploration. Moreover, assuming that the AVA curves corresponding to real data may be well described by the PW theory leads to inaccurate estimations of the media properties. Our approximation may be therefore an attractive alternative to classical methods to extract information relative to bottom parameters from AVA signals.

Introduction

In seismic reflection surveys the waves generated by a point source propagate in the stratified Earth, and are recorded at the surface by the receivers, after being reflected by the interfaces. Classically in geophysical exploration, the so-called technique AVO (Amplitude Variation with Offset), respectively AVA (Amplitude Variation with Angle), uses the variability of the reflected P-wave amplitude with source-receiver distance, respectively with incidence angle, to constrain the reflector location and the media properties. Since the media heterogeneity can be highly complex in the seismic frequency range (typically, between 10 and 60 Hz), retrieving these characteristics is actually a difficult task. Solving such an inverse problem implies that one could find a set of media parameters which may fit the propagation measurements, and therefore that a theoretical model of wave propagation was first developed. A survey of the literature brings to light that most calculations are generally performed within the framework of monochromatic plane-wave (PW) theory [3]. The amplitude of the reflected P-waves is thus evaluated knowing the characteristics of the source and the PW reflection coefficient

at the interface, and considering the geometrical-spreading compensation. The angular dependence of reflection coefficients for plane waves impinging on a plane interface between two semi-infinite, homogeneous, isotropic, and elastic media is exactly described by the Zoeppritz equations [1]. Nevertheless, as the complexity of these equations defies physical insight and prevents from processing simple inversion techniques for estimating parameters of real media, useful linearized versions of the exact plane wave reflection coefficients [1] have been therefore commonly applied in AVO/AVA analyses [3]. These approximations, valid only for typical range of small incidence angles and for weak impedance contrast between media, have greatly facilitated physical understanding and parameter estimation, but are nowadays becoming obsolete with the computer power. The underlying assumptions of the PW theory, illustrated by the Zoeppritz equations, are the infinite frequency and the infinite bandwidth of the signals. However, the measured seismic data are band-limited signals and have a low frequency content. A question then arises: what is the effect of these signal characteristics on wave reflection modeling and on estimation of media properties? In the paper we focus on this question.

Besides the PW theory, the basis of many seismic studies is the ray theory. Under this approximation it is assumed that the high-frequency part of elastic energy propagates along infinitely narrow lines through space, called rays, which join the source and the receiver. Ray theory is then strictly valid only in the limit of a hypothetical infinite-frequency wave. As measured seismic data have a low frequency content, it is accepted that seismic wave propagation is extended to a finite volume of space around the ray path, called the 1^{st} Fresnel volume [10], which contributes to the received wavefield for each frequency. The 1^{st} Fresnel volume, hereafter denoted FV, and its intersection with a reflector, called the Interface Fresnel zone (IFZ), have received broad attention in recent past years. These concepts are continually being developed and have found so many applications in seismology and in seismic exploration that it is impossible here to review all the books and articles which pay attention to them in seismic wave propagation [14, 15, 17]. Nevertheless, we shall mention the works of Červený and his co-authors who have suggested two methods for including FV parameter calculations into the ray tracing procedure in complex 2D and 3D structures. The first one, called the Fresnel volume ray tracing, combines the paraxial ray approximation with the dynamic ray tracing, and is only applicable to zero-order waves (direct, reflected and transmitted waves...), whereas the second method, more accurate than the previous one, is based on network ray tracing [16]. They have also derived analytical expressions for FVs of seismic body waves and for IFZ for simple structures, which offers a deeper insight into the properties of FV and IFZ [11, 12]. Of particular interest are the size of the IFZ and the size of the volume of the reflector involved in reflection time measurements [7] because each one can be related to the horizontal and vertical resolutions of seismic methods [13]. Unfortunately, as Červený and co-authors' objectives were concerned essentially with kinematic ray tracing, the expressions they derived are incomplete. Until now, only the IFZ and the penetration depth of the FV below the reflector were considered in studies. Nevertheless, if the seismic amplitudes at receivers have to be evaluated, we must determine the interface reflectivity by accounting for the whole spatial region in the vicinity of the interface which affects it. In other words, we must account for the IFZ and for certain volumes below the interface in the transmission medium and above the interface in the incidence medium which define the reflector from the seismic viewpoint [5]. If there is no heterogeneity in the vicinity of the interface, only the IFZ must be considered for the computation of the interface reflectivity. On the other hand, if only traveltime measurements are considered, for instance, for locating the reflectors in the media, there is no need for defining the region above the interface, because this region is already included in the representation of the FV. In this case, only the region beyond the interface has to be considered. The consequences of ignor-

ing the IFZ in forward modeling of wave reflection process have been recently pointed out in [4], however, to the best of the authors' knowledge, the role of the IFZ in the inverse modeling has not been investigated yet. This is precisely the goal of our work. To focus specifically on the imprint of the IFZ, we consider a very simple elastic model, e.g. a smooth homogeneous interface between homogeneous, isotropic, and elastic media.

The paper is divided in two sections. Section 1 briefly recalls the concept of FV and IFZ. Section 2 investigates the role of the IFZ in both forward and inverse modeling of wave reflection. The variation in the reflected P-wave amplitude as a function of the incidence angle, evaluated with our approximation which combines the IFZ concept with the Angular Spectrum Approach (ASA) [6], is compared with the classical PW reflection coefficient, and with the exact solution obtained with the 3D code OASES (http://acoustics.mit.edu/faculty/henrik/oases.html). The influence of the classical PW theory framework which does not account for the IFZ, widely used for AVO/AVA studies, on the estimation of elastic media properties is also investigated by simple inversion processing. Finally, we discuss the implications of our approximation in the estimation of media properties.

1 General background: the concept of Fresnel volume and Interface Fresnel zone

We consider two homogeneous isotropic elastic media in welded contact at a plane interface located at a distance z_M from the xy-plane including the point source S ($-x_S$,0,0) and the receiver R (x_S,0,0). We assume that the interface is isolated from the other ones. We mean that the distance between this interface and another one is much greater than $\frac{V}{2B}$, where V is the medium velocity and B is the frequency bandwidth of the source. The source generates in the upper medium a spherical wave with a constant amplitude. The spherical wave can be decomposed into an infinite sum of PW synchronous each other at the time origin. We consider the harmonic PW with frequency f which propagates in the upper medium with the velocity V_{P1} from S to R, after being reflected by the interface at the point M(0,0,z_M) in a specular direction θ with respect to the normal to the interface (Fig. 1). Let the traveltime of the specular reflected wave be t_{SMR}.

The set of all possible rays SM_iR with constant traveltime t_{SMR} defines the isochrone for the source-receiver pair (S,R) relative to the specular reflection SMR. This isochrone describes an ellipsoid of revolution tangent to the interface at M, whose rotational axis passes through S and R. By definition, the FV corresponding to S and R and associated with the reflection at M is formed by virtual diffraction points F such that the waves passing through these points interfere constructively with the specular reflected wave. This condition is fulfilled when the path-length difference is less than one-half of the wavelength $\lambda_1 = \frac{V_{P1}}{f}$ corresponding to the dominant frequency f of the narrow-band source signal [10]:

$$|l(F,S)+l(F,R)-l(M,S)-l(M,R)| \leq \frac{\lambda_1}{2} \quad , \tag{1}$$

the quantity $l(X,Y)$ denoting the distance between the point X and the point Y. As is well-known, the main contribution to the wavefield comes from the 1^{st} FV as the rapid oscillatory responses of the higher-order FVs and Fresnel zones cancel out and give minor contributions to the wavefield [2]. In our work we restrict ourselves to the 1^{st} FV which is simply referred to as FV. The FV is represented by the volume situated above the interface in the upper medium and bounded by two ellipsoids of revolution, with foci at S and R, tangent to fictitious parallel

planes to the interface and located at a distance $\frac{\lambda_1}{4}$ below and above the interface (Fig. 1). The two ellipsoids of revolution are defined by:

$$\frac{x^2}{\left(\frac{z_M}{\cos\theta} \pm \frac{\lambda_1}{4}\right)^2} + \frac{y^2}{\left(\frac{z_M}{\cos\theta} \pm \frac{\lambda_1}{4}\right)^2 - z_M^2 \tan^2\theta} + \frac{z^2}{\left(\frac{z_M}{\cos\theta} \pm \frac{\lambda_1}{4}\right)^2 - z_M^2 \tan^2\theta} - 1 = 0 \quad . \quad (2)$$

Note that, as seismic wavefields are transient and large-band, it is generally necessary to decompose the source signal into narrow-band signals for which monochromatic FV can be constructed for the prevailing frequency of the signal spectrum [9].

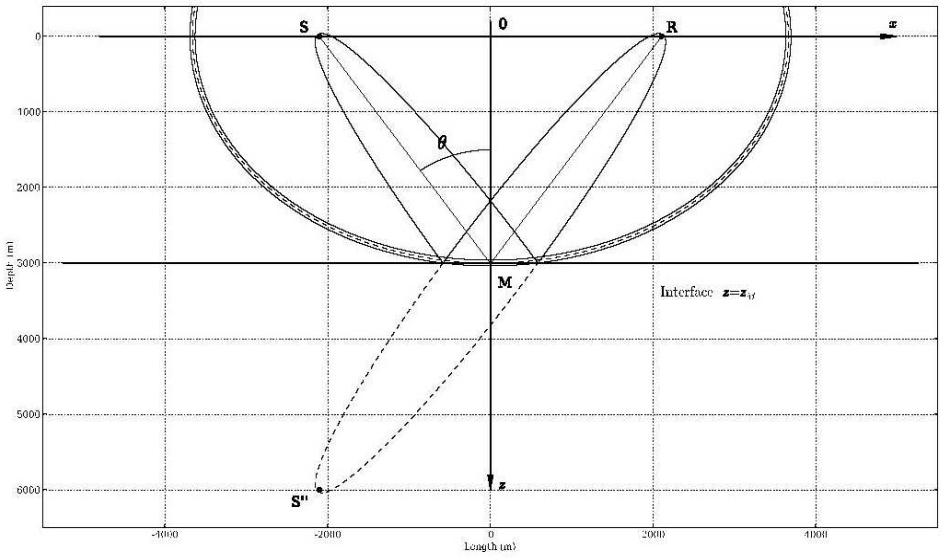

Fig. 1: Representations, in the xz-plane, of the Fresnel volume involved in the wave reflection at the point M at a plane interface, under the incidence angle $\theta = 35°$. The source S and the receiver R are situated at a distance 3000 m from the interface. The classical representation of the Fresnel volume is the ellipsoid of revolution with foci located at R and at the image source S''. Another representation of the Fresnel volume associated with the reflection SMR is given by the volume located in the incidence medium between the ellipsoids of revolution with foci at S and R (see the text for more details). The velocities in the upper and lower media are respectively $V_{P1} = 4000$ m/s and $V_{P2} = 5200$ m/s, and the frequency $f = 32$ Hz. The seismic wavelengths in the upper and lower media are respectively $\lambda_1 = 125$ m and $\lambda_2 = 162.5$ m. The critical angle is equal to $\theta_C = 50.28°$.

The IFZ is defined as the cross section of the FV by an interface which may not be perpendicular to the ray SM. If the source S and the receiver R are situated at the same distance from the interface, the IFZ is represented by an ellipse centered at the reflection point M, whose equation is obtained from the formulation of the ellipsoid of revolution, eq.2, keeping the sign + and replacing z by z_M. The in-plane semi-axis $r^{\parallel}$ and the transverse semi-axis $r^{\perp}$ of the IFZ are then expressed as [11]:

$$r^{\parallel} = r^{\perp}\left[1 - \frac{z_M^2 \tan^2\theta}{\left(\frac{z_M}{\cos\theta} + \frac{\lambda_1}{4}\right)^2}\right]^{-\frac{1}{2}} \quad , \; r^{\perp} = \left[\frac{\lambda_1}{2}\left(\frac{z_M}{\cos\theta} + \frac{\lambda_1}{8}\right)\right]^{\frac{1}{2}} \quad . \quad (3)$$

The characteristics of the IFZ depend on the positions of the source-receiver pair, and also on the incidence angle of the ray SM. Moreover, larger portions of the interface are involved for low-frequency than for high-frequency components of the wavefield, and also for great incidence angles θ rather than for small angles (Fig. 2). It is also well-known that a perturbation of the medium actually affects the reflected wave when this perturbation is located inside the IFZ.

As an aside, we should point out here that in many papers is used the classical representation of the FV which is an ellipsoid of revolution with foci located at R and at the mirror image S" of the source S (Fig. 1). This representation, mainly based on transmission considerations, is suitable for accounting for the heterogeneities of the medium body located in the vicinity of the ray, while the FV representation we use is more appropriate to account for the heterogeneities of the interface, as it is connected strictly to the wave reflection process. Moreover, unlike the classical one, this representation allows the definition of the volumes above and beyond the interface which characterize the reflector [5]. Note that the two representations are complementary and must be combined if the wave propagation in media with heterogeneities in the body and at the interfaces is investigated.

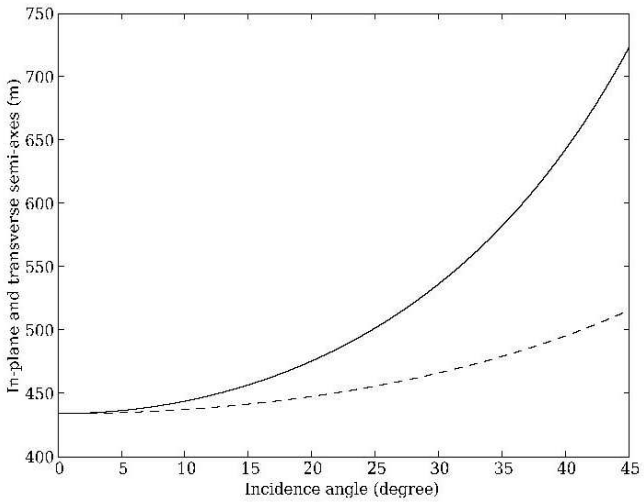

Fig. 2: Variation in the in-plane semi-axis $r^{\parallel}$ (—) and in the transverse semi-axis $r^{\perp}$ (- - -) of the Interface Fresnel zone as a function of the incidence angle θ. The medium configuration is identical to that described in Fig.1.

2 The role of the Interface Fresnel zone in wave propagation

The aim of this section is to investigate the role of the IFZ in the wave reflection process, and more specifically, to point out the consequences of ignoring the IFZ in both forward and inverse modeling of wave propagation.

2.1 Media, model and exact solution

Consider the same configuration as previously. One type of interface between elastic media has been chosen to illustrate the theoretical results. The upper medium has the density $\rho = 2000\,kg/m^3$, the P-wave velocity $V_P = 4000\,m/s$, and the S-wave velocity $V_S = 2000\,m/s$,

whereas the amount in the medium properties through the interface are $\triangle\rho = 400\,kg/m^3$, $\triangle V_P = 1200\,m/s$ and $\triangle V_S = 500\,m/s$. The interface is situated at a distance $z_M = 3000\,m$ from the source-receiver plane. The source spectrum is chosen to be the Fourier transform of a Ricker wavelet with the dominant frequency $f = 32\,Hz$ and the frequency bandwidth $B = 8\,Hz$.

The amplitude of the P-wave reflected from the part of interface which physically contributes to the wave propagation process, and measured at the receiver R, has to be calculated. As the problem under consideration can be viewed as a problem of diffraction by the IFZ, we chose to apply the Angular Spectrum Approach (ASA) [6] combined with the IFZ concept to get the 3D analytical solution to this problem. Using the ASA permits straightforward derivations of the measured amplitude of the reflected wave at the point R. We refer the reader to our previous publication [4] for a detailed description of the procedure. In addition, we used the 3D code OASES to compute accurately synthetic seismograms in media. OASES is a general purpose computer code for modeling seismo-acoustic propagation in horizontally stratified media using wavenumber integration in combination with the Direct Global Matrix solution technique [8]. This 3D code, widely used in the underwater acoustics community, has been thoroughly validated.

2.2 Contribution of the IFZ to the seismic amplitude

Our objective being to evaluate the importance of accounting for the IFZ for calculating the amplitude of the P-wave reflected from the interface, it is instructive to compare the variation in the amplitude obtained with our method, as a function of the incidence angle, with the amplitude predicted by the code OASES which provides the exact solution, and with the amplitude predicted by the classical PW theory (here, the Zoeppritz equations [1]). Fig. 3 depicts these amplitude-versus-angle (AVA) curves for the medium configuration described in Section 2.1.. A geometrical spreading compensation factor equal to $\frac{z_M}{\cos\theta}$ was applied to the predictions of our 3D approximation, and to the synthetic data provided by the 3D code OASES, in order to be compared in a suitable way with the PW predictions.

Inspection of Fig. 3 shows that for small subcritical angles, AVA curves associated with the exact solution and with the PW theory are quite identical. The discrepancies between them do not exceed 1% up to $\theta = 40°$. As the PW reflection coefficient varies smoothly with the incidence angle, the geometrical spreading compensation is sufficient to reduce the amplitude of the reflected wave generated by the point source to the reflected PW amplitude. The effect of the IFZ on the wave amplitude is negligible for small incidence angles in the subcritical region. Between $\theta = 40°$ and the critical angle $\theta_C = 50.28°$, the PW reflection coefficient rapidly increases with the incidence angle, and the geometrical spreading compensation is not sufficient anymore. The discrepancies between the exact curve and the PW reflection coefficient increase with the incidence angle and exceed 70% for θ_C. Therefore, the additional application of the IFZ concept becomes necessary to get the reflected P-wave amplitude. We should point out that as expected, the discrepancies between the exact solution and the PW reflection coefficient strongly increase with decreasing dominant frequency of the source signal [4].

Below and close to the critical angle, the predictions of our approximation better fit the exact solution than the PW reflection coefficient, more particularly between $\theta = 47°$ and θ_C. The discrepancies between the ASA curves and the exact curves do not exceed 5% up to $\theta = 52°$ and are smaller than 1% for θ_C. Nevertheless, with increasing incidence angle, the approximate solution shows increasing discrepancies, in comparison with the exact solution, reaching the maximum value of 22% for $\theta = 56°$. The explanation comes from the fact that we calculated only the reflected wave amplitude, whereas the code OASES provides the amplitude of

the interference between the reflected and the head wavefields. Unfortunately, the contribution of each wavefield to the global amplitude recorded at the receiver cannot be discriminated in the synthetic seismograms. For great postcritical angles, for which the signal relative to the head wave and the signal relative to the reflected wave can be separated in time, our approximation tends to the exact solutions. Our present work is focused on this topic and results will be reported later. Note that general conclusions drawn above which are concerned with the medium configuration described in Section 2.1. are in fact common to other models with lower or stronger impedance contrasts at the interface. We should also point out that, contrary to the PW solution, the predictions of our approximation fit reasonably well the exact solution in the vicinity of the critical angle, whatever the dominant frequency of the source signal [4].

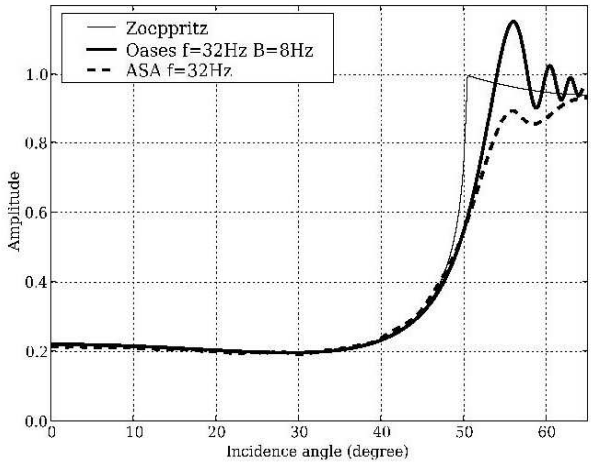

Fig. 3: Variation of the amplitude of the P-wave reflected from a plane interface, as a function of the incidence angle. Comparison between the plane-wave reflection coefficient and the spreading-free amplitudes associated with the exact solution and with the approximate solution. The exact solution is provided by the 3D code OASES, whereas the approximate solution is obtained by applying the Angular Spectrum Approach together with the Interface Fresnel Zone concept. (See text for the description of the medium configuration)

2.3 Estimation bias

Our objective is to evaluate quantitatively the error made on the estimation of the media properties when the IFZ is not taken into account in the inversion procedure. Consider that the real data measured by the receivers are represented in fact by the exact curve provided by the code OASES. The measured reflectivity implicitly accounts for the low-frequency content and the limited bandwidth of data. Nevertheless, one usually assumes that the real curves can be well described by the monochromatic PW theory, and inversion algorithms are therefore based upon the Zoeppritz equations. Which effect on parameter estimation has this assumption?

To answer to this question we developed a quite simple inversion procedure applied to the AVA curves. The properties ρ, V_P, and V_S, of the upper medium being considered as a priori informations, the estimation problem was reduced to the determination of the parameters $\Delta\rho$, ΔV_P, and ΔV_S (i.e. the amount in properties through the interface) which minimize in the least-square sense the cost function D expressing the distance between the real amplitude provided by OASES and the simulated ones represented by the Zoeppritz curve:

$$D = \frac{1}{N} \sum_{n=1}^{N} \left[(Ampl_{OASES})_n - (Ampl_{Zoeppritz})_n \right]^2 , \tag{4}$$

where the parameter N denotes the number of points of the sampled AVA curves. This number was chosen arbitrarily equal to 24. The initial estimates of the parameters $\Delta\rho$, ΔV_P, and ΔV_S, were chosen arbitrarily equal to $100\,kg/m^3$, $100\,m/s$, and $100\,m/s$, respectively. A number of algorithms exist for solving least-square minimization problems. As several parameters had to be recovered simultaneously, we chose the Simplex method. The inversion algorithm was first tested against the PW AVA curve which represented here the measured data. Whatever the initial estimates, the parameters $\Delta\rho$, ΔV_P, and ΔV_S, were identified with a high accuracy, the estimation errors calculated with respect to the real values given in Section 2.1. being below $10^{-4}\%$. We could then trust in the inversion procedure. The inversion algorithm was then tested against the AVA curves provided by the code OASES. This led to the estimations of the amount in the medium properties through the interface reported in Table 1, together with the estimation errors calculated with respect to the real values given in Section 2.1., for various ranges of incidence angles and for the dominant frequency $f = 32\,Hz$ and the source signal bandwidth $B = 8\,Hz$. Firstly, we can note that the media properties are identified with a reasonably good accuracy for typical range of incidence angles in classical AVA studies, e.g. for angles θ varying within the range $[0, 40°]$. The estimation errors are below 1%, except for the parameter $\Delta\rho$ for which the estimation error slightly exceeds 1%. These results which were expected come from the fact that for small incidence angles, the AVA curve provided by the PW theory fits well the exact one (Fig. 3). On the contrary, in the context of wide-angle AVA studies, e.g. for incidence angles θ varying within the range $[0, 55°]$ and containing here the critical angle, the AVA curve provided by the PW theory does not fit the exact one. As a consequence, except for $\Delta\rho$ for which the estimation error is about 4%, the parameters cannot be recovered with accuracy, the estimation errors lying above 14%. Note more particularly the very bad estimation of the parameter ΔV_S, for which the estimation error exceeds 70%. We guess that these estimation errors would increase with decreasing frequency, as the PW theory which has the underlying assumption of infinite-frequency wave propagation cannot fit the exact solution. These preliminary results show that accounting for the frequency content and the limited bandwidth of the source signal seems to be essential to constrain the estimation of media properties in the inversion process for wide-angle AVA studies.

We then tested the previous inversion procedure by considering that the simulated data were now provided by our approximation, i.e. by simply replacing the term $Ampl_{Zoeppritz}$ by the term $Ampl_{approx}$ in the expression 4 of the cost function D. This led to the estimations of the parameters $\Delta\rho$, ΔV_P, and ΔV_S reported in Table 1, together with the estimation errors calculated with respect to the real values given in Section 2.1., for incidence angles θ varying within the range $[0, 55°]$ and for the dominant frequency $f = 32\,Hz$ and the source signal bandwidth $B = 8\,Hz$. Except for $\Delta\rho$ for which the estimation error exceeds 25%, the parameters ΔV_P and ΔV_S are much better estimated than previously with the Zoeppritz formulation, the estimation errors lying below 9%. Note more particularly the good estimation of the parameter ΔV_S, for which the estimation error is below 4%. Considering these preliminary results provided by both forward and inverse modeling of wave reflection, and despite the lack of its high accuracy in the critical angle region, our approximation which accounts for the IFZ seems to be an attractive alternative to the above-mentioned classical methods to extract information relative to bottom parameters from AVO/AVA signals. Our paper emphasizes this feature rather than addressing the question of how to achieve it technically. Nevertheless, the inverse problem needs further investigations and future work will focus on this aspect.

Amount in medium properties	Zoeppritz				Approximation	
	$\theta \in [0, 40°]$		$\theta \in [0, 55°]$		$\theta \in [0, 55°]$	
	estimate	error	estimate	error	estimate	error
$\Delta\rho\ (kg/m^3)$	405.6	1.4 %	384.3	3.9 %	298.4	25.4 %
$\Delta V_P\ (m/s)$	1196.4	0.3 %	1027.2	14.4 %	1302.2	8.5 %
$\Delta V_S\ (m/s)$	497.3	0.5 %	134.4	73.1 %	519.4	3.9 %

Tab. 1: Estimation of media properties and estimation errors from exact AVA curves for the dominant frequency $f = 32\,Hz$ and the source signal bandwidth $B = 8\,Hz$. The critical angle is $\theta_C = 50.28°$. (See text for the description of the medium configuration)

Conclusion

The goal of the paper was to point out the consequences of ignoring the band-limited property and the low-frequency content of the seismic data in both forward and inverse modeling of wave reflection, as it is traditionnally done for typical AVA (Amplitude-versus-Angle) contexts in geophysical exploration. For this purpose, we have investigated more precisely the role of the Interface Fresnel zone, which physically contributes to the reflected wavefield, in the computation of the reflected P-wave amplitude measured at the receiver, and also in the estimation of media properties from AVA signals. First, AVA curve obtained with the classical plane-wave (PW) theory has been compared with the exact solution provided by the 3D code OASES, and with our approximation which accounts for the Interface Fresnel zone. Our approximation has provided much better data predictions than the PW theory traditionnally used in AVA studies. It has been then shown that assuming that the AVA curves corresponding to real data may be well described by the PW theory leads to inaccurate estimations of the media properties. It was finally suggested that our approximation might be therefore an attractive alternative to classical methods to extract information relative to bottom parameters from AVA signals.

Acknowledgments

The work reported here is the result of discussions and fruitful collaboration with our late friend Dr Eric de Bazelaire during many years. We consider ourselves extremely fortunate to have had the opportunity to work at close quarters with a scientist of his calibre. We also sincerely acknowledge the chairman of the session "Inverse problems in Acoustics", Dr E. Skarsoulis, as well as the audience, to have contributed to honour the memory of Eric who died four days before the beginning of the ICTCA07, by observing a minute's silence after the talk.

REFERENCES

[1] K. Aki and P.G. Richards. *Quantitative seismology*. University Science Books, second edition, 2002.

[2] M. Born and E. Wolf. *Principles of Optics*. Cambridge University Press, 7th expanded edition. edition, 1999.

[3] J.-P. Castagna. AVO-analysis, tutorial and review. In J.-P. Castagna and M.M. Backus, editors, *Offset-dependent reflectivity, theory and practice of AVO analysis*, volume 8 of *Investigations in Geophysics*, pages 3–36. SEG, 1993.

[4] N. Favretto-Cristini, P. Cristini, and E. de Bazelaire. Influence on the Interface Fresnel zone on the reflected P-wave amplitude modelling. *Geophysical Journal International*, 171:841–846, 2007.

[5] N. Favretto-Cristini, P. Cristini, and E. de Bazelaire. Some reflections on reflectors and wave amplitudes. *Acta Acustica*, 93:909–916, 2007.

[6] J.W. Goodman. *Introduction to Fourier Optics*. MacGraw-Hill, second edition, 1996.

[7] J. G. Hagedoorn. A process of seismic reflection interpretation. *Geophysical Prospecting*, 2:85–127, 1954.

[8] F.B. Jensen, M.B. Porter W.A. Kuperman, and H. Schmidt. *Computational Ocean Acoustics*. American Institute of Physics, New York, 1994.

[9] R.W. Knapp. Fresnel zones in the light of broadband data. *Geophysics*, 56(3):354–359, 1991.

[10] Yu.A. Kravtsov and Yu.I. Orlov. *Geometrical optics of inhomogeneous media*. Springer Series on Wave Phenomena. Springer-Verlag, NY., 1990.

[11] M. Kvasnička and V. Červený. Analytical expressions for Fresnel volumes and interface Fresnel zones of seismic body waves. Part 1: Direct and unconverted reflected waves. *Stud. Geophys. Geod.*, 40:136–155, 1996.

[12] M. Kvasnička and V. Červený. Analytical expressions for Fresnel volumes and interface Fresnel zones of seismic body waves. Part 2: Transmitted and converted waves. Head waves. *Stud. Geophys. Geod.*, 40:381–397, 1996.

[13] J.P. Lindsey. The Fresnel zone and its interpretative significance. *The Leading Edge*, 8(10):33–39, 1989.

[14] J. Schleicher, P. Hubral, M. Tygel, and M.S. Jaya. Minimum apertures and Fresnel zones in migration and demigration. *Geophysics*, 62:183–194, 1997.

[15] J. Spetzler and R. Snieder. The Fresnel volume and transmitted waves: a tutorial. *Geophys. J. Int.*, 69(3):653–663, 2004.

[16] V. Červený. *Seismic Ray Theory*. Cambridge University Press, Cambridge, UK, 2001.

[17] Y. Zhou, F.A. Dahlen, G. Nolet, and G. Laske. Finite-frequency effects in global surface-wave tomography. *Geophys. J. Int.*, 163:1087–1111, 2005.

Geophysical Prospecting, 2005, **53**, 373–397

Numerical modelling of interface scattering of seismic wavefield from a random rough interface in an acoustic medium: comparison between 2D and 3D cases

Wasiu Makinde,[1]* Nathalie Favretto-Cristini[1] and Eric de Bazelaire[2]

[1]*CNRS-FRE 2639, Imagerie Géophysique, Université de Pau et de Pays de l'Adour, BP 1155, 64013 Pau Cedex, and* [2]*11, Route du Bourg, 64230 Beyrie-en-Béarn, France*

Received June 2003, revision accepted May 2004

ABSTRACT

Seismic wavefield scattering from a statistically randomly rough interface in a multilayered piecewise homogeneous medium is studied in 3D. The influence of the surface roughness on the scattered wavefield is analysed numerically by using a finite-difference operator in the acoustic domain. Since interface scattering in the real practical sense is a 3D physical phenomenon, we show in this work that the scattering response of a randomly rough interface is not the same in 3D situations as in the 2D cases described in some earlier works. For a given interface roughness height in 3D, an interface roughness height at least three times greater is required to produce an equivalent phase scattering effect in 2D situations, for a given correlation length of the interface roughness scale. Based on observations from spectral analysis, we show that scattering results principally in de-phasing and frequency band-limiting of the incident wavefront, the frequency band-limiting properties being comparable to cases reported in the literature for absorption and thin-layer filtering. The interface scattering phenomenon should be critically considered when using amplitude and phase information from seismic signal during inversion processes.

INTRODUCTION

The amplitude and phase of seismic signal are two important parameters which are normally exploited during inversion processes in reflection seismology. In order to be able to use information from these parameters for inversion purposes, it is essential that the method for modelling the subsurface includes all the physical phenomena that affect these parameters. Interface scattering is one such important physical phenomenon almost overlooked in reflection seismology, despite its considerable impact on these parameters. It is well known that a scattering regime depends on the relationship between the wavelength and the scale of heterogeneity. In this work, we show that the effect of interface scattering becomes significant when the interface roughness height attains 1/5 of the wavelength of the incident wave ($\lambda/5$). This might result in errors which could at times be as much as 50% in the quantitative interpretation of the amplitude of reflected waves. Thus, all inversion methods using these parameters to recover the acoustic impedances or stratigraphy of the subsurface should take this important phenomenon into consideration.

Interface scattering of a seismic wavefield is associated with the spatial distributions of irregular geological contacts at the interface between layers of the stratified earth. It is well known that surface roughness is not an intrinsic property of a surface but depends on the properties of the wave that is being scattered (Ogilvy 1991). The scale of the interface roughness in relation to the wavelength of the incident wave is thus crucial in determining how energy is scattered from an interface. In optical and radar remote sensing, surfaces with roughness of the order of $\lambda/10$, where λ is the wavelength of the incident

*Now at: Total E&P Nigeria, Trans Amadi Industrial Layout, Port-Harcourt, Nigeria. E-mail: Wasiu.Makinde@total.com

wave on the surface, are generally considered smooth. The Rayleigh criterion (Ishimaru 1978) takes the limit or threshold for the smoothness of a surface to be $h < \lambda/8\cos\theta$, where h represents the surface height roughness (root-mean-square (rms) height) and θ is the angle of incidence. Consequently, if we assume a plane wave at normal incidence and use the $\lambda/10$ criterion, then for the seismic frequency bandwidth range ($10 \leq f \leq 60$ Hz) and the P-wave velocity range often encountered ($1500 \leq v \leq 5000$ m/s), surfaces with a roughness height less than the values in the range between 3 m and 50 m are considered smooth in seismic reflection surveys. Most geological surfaces are considered to be seismically 'smooth'. Nevertheless, many natural occurrences are exceptions to this limit and thus the effects of interface scattering must be taken into consideration in realistic earth models.

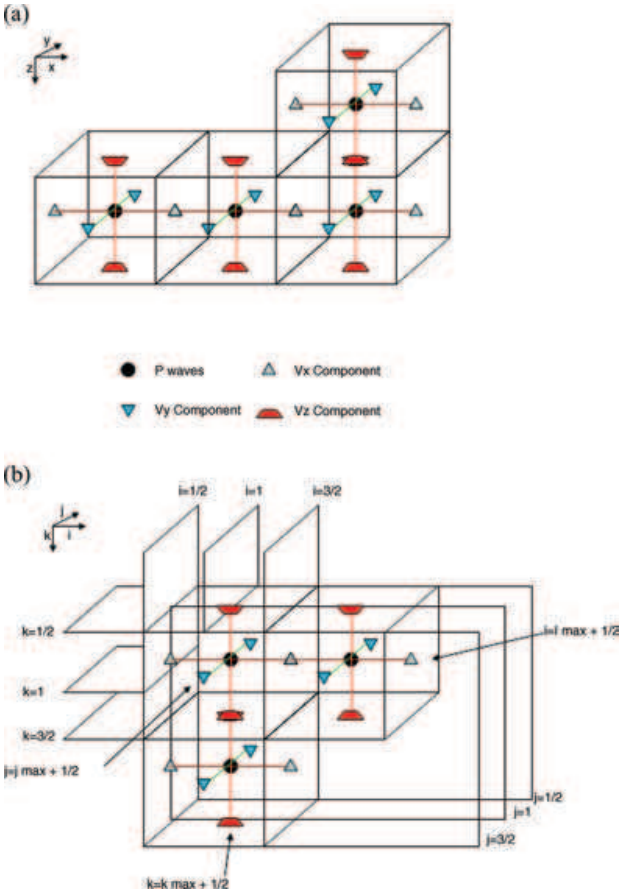

Figure 1 Grid sampling used in the discretization of the equations with the 3D mesh: (a) shows the cubic grids which constitute the 3D mesh; these can be shifted in one or many directions to obtain the staggered grid formalism of Virieux (1986). The blackened nodes are computed at time t while the other nodes are computed at times $t + \frac{1}{2}$; (b) shows the grid node indexing employed. The pressure nodes are represented in solid black in both cases.

Irregular interfaces could be created by the disruption of sedimentary layers as pre- or post-depositional deformation features. This can occur when a palaeo-relief is covered by a more recent sedimentary layer with velocities different from the adjacent layers, as is the case with angular unconformities. It also occurs in the case of certain mobile shale/sediment interfaces along shale domes and salt/sediment interfaces along salt domes and salt roofs below overhangs, often encountered in deltaic environments. Another important case worth mentioning is that of volcanic eruption (basalt). Highly rugose interfaces are the result of primary and secondary erosion processes, of jointing due to shrinkage during cooling, of vesicles due to degassing, of baking effects or of lava filling previous topography. Furthermore, consecutive deposition and erosion can amplify the relief up to a hectometre scale. These interfaces are encountered in both land and marine environments, and are known to constitute major imaging problems. The weathered zone is a well-known scatterer in land seismic data and it is known to be highly spatially irregular. Interface scattering could affect the phase and/or amplitude of the incident wavefield (Favretto-Cristini and de Bazelaire 2003), and is detrimental to the final seismic image when true/preserved amplitude imaging is being considered.

The extent to which interface roughness affects wave scattering behaviour has been the subject of studies in many fields, for example, electromagnetics, ground-penetrating radar, medicine, etc. However, the general understanding of scattering of seismic waves from highly irregular boundaries is limited because of theoretical and experimental difficulties (Schultz and Toksöz 1993). The theoretical difficulty arises from surface interactions, resulting in non-linear mathematical formulations and computationally intensive algorithms. Experimentally, the non-linearity manifests itself as multiple scattering. This multiple scattering is not easy to analyse in a simple fashion because scattered waves propagate along many complex paths. For these reasons, most earlier works have focused on detailed investigation of very specific interface structures, limited mostly to 2D cases and sometimes to 2.5D configurations. For example, Kawase (1988) used boundary elements to study the scattering of surface waves in a semicircular canyon. Bouchon, Campillo and Gaffet (1989) used discrete wavenumbers to investigate scattering of SH-waves between layers in 'synclines' and 'anticlines'. Axilrod and Ferguson (1990) studied SH-wave scattering from a sinusoidal grating using various discrete wavenumber techniques. Schultz and Toksöz (1991) used finite-differences and laboratory model-tank experiments to study the scattering from randomly distributed grooves. Schultz and Toksöz (1993)

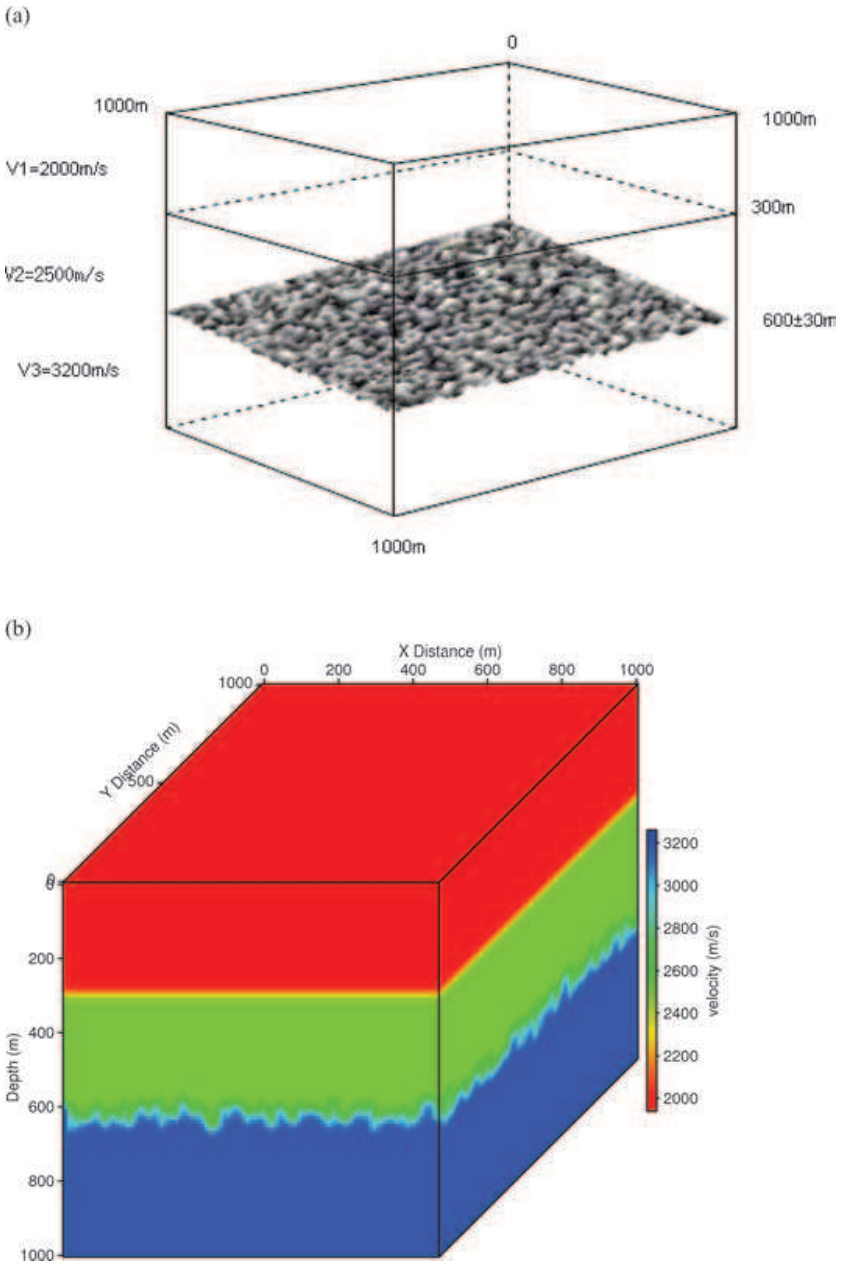

Figure 2 Simple three-layered earth model used for the numerical simulations in the 3D case: (a) is a skeletal representation of the model revealing the nature of the scattering interface in 3D; (b) shows a realization of the 3D model with surface rms height of 40 m.

also studied the enhanced backscattering of SH-waves from a highly irregular random interface to show that, in parallel with what is observed in optics, enhanced backscattering results directly from multiple scattering, and its character varies significantly as a function of impedance contrasts, incident angle and rms slope of the interface. Martini and Bean (2002) studied the effect of interface scattering from a fractal basalt environment and applied wave-equation datuming in an attempt to remove it.

Since the number of degrees of freedom required to model a 3D surface is proportional to the surface area, numerical simulation of a general 3D rough surface scattering problem is computationally expensive (Warnick and Chew 2001). This is the main reason why, in some earlier works, the simplification of translationally invariant surfaces is often used to reduce the computational cost. This, however, requires the use of earth models that are not geologically realistic. Translationally invariant surfaces (for example, corrugated surfaces where the

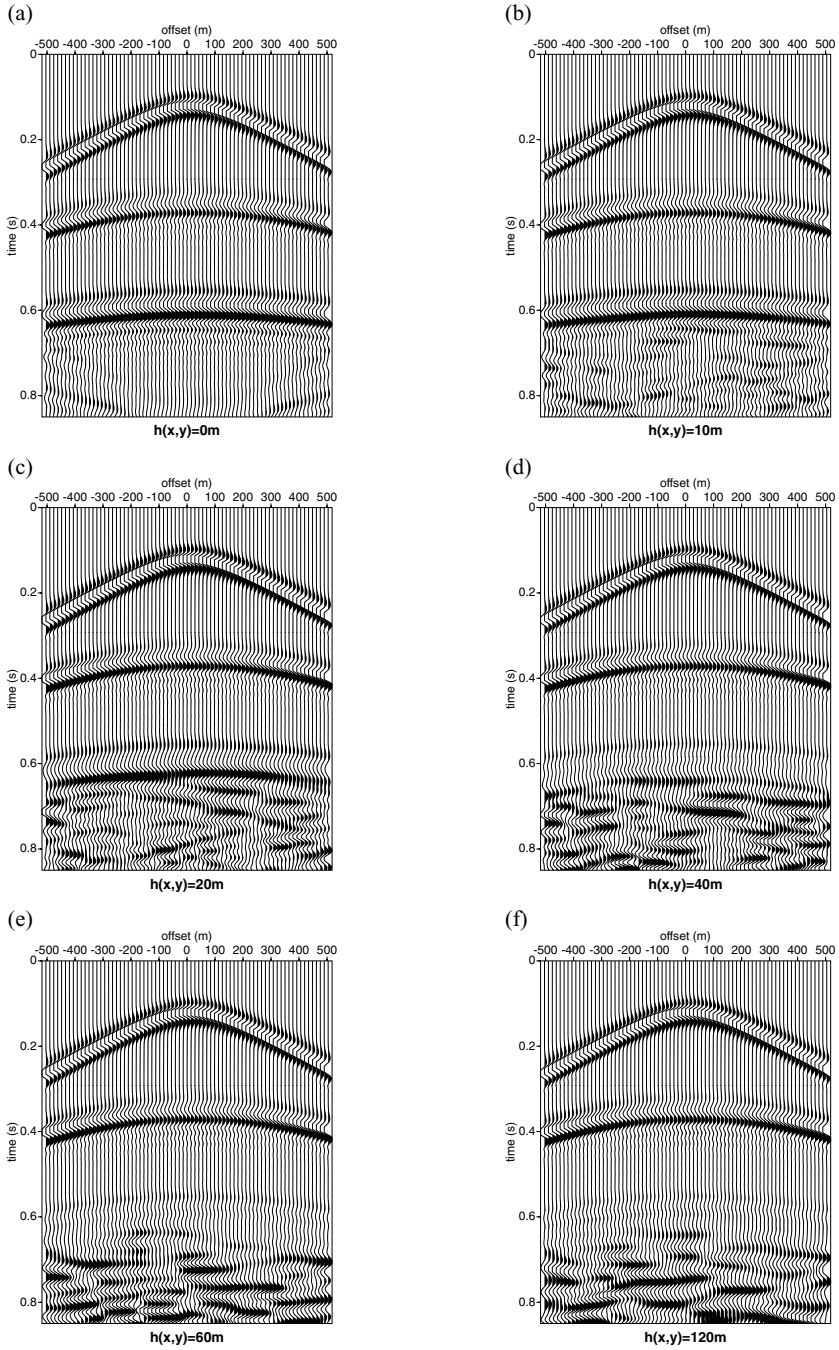

Figure 3 Receiver group data extracted from 3D data cube. The data refer to computations for different surface rms height values $h(x, y)$: (a) 0 m, (b) 10 m, (c) 20 m, (d) 40 m, (e) 60 m and (f) 120 m, for the 3D case. The computation with $h(x, y) = 0$ corresponds to the reference model (no phase scattering observed).

surface roughness varies only in one direction and is invariant in the other) do not occur in nature, and since interface scattering is a 3D phenomenon, the understanding of seismic wavefield scattering from a 3D random rough surface becomes crucial. We present a numerical study of the interface scattering of a seismic wavefield from a 3D random rough interface and compare the results with the corresponding 2D case. We employ a finite-difference operator in the acoustic domain to simulate wave propagation in a multilayered medium with a rough random interface, generated by perturbing a plane interface with a Gaussian random function. The effect of the surface height on the properties of the seismic wavefield scattered from the randomly rough interface is studied. This provides information on the way the interface scattering affects

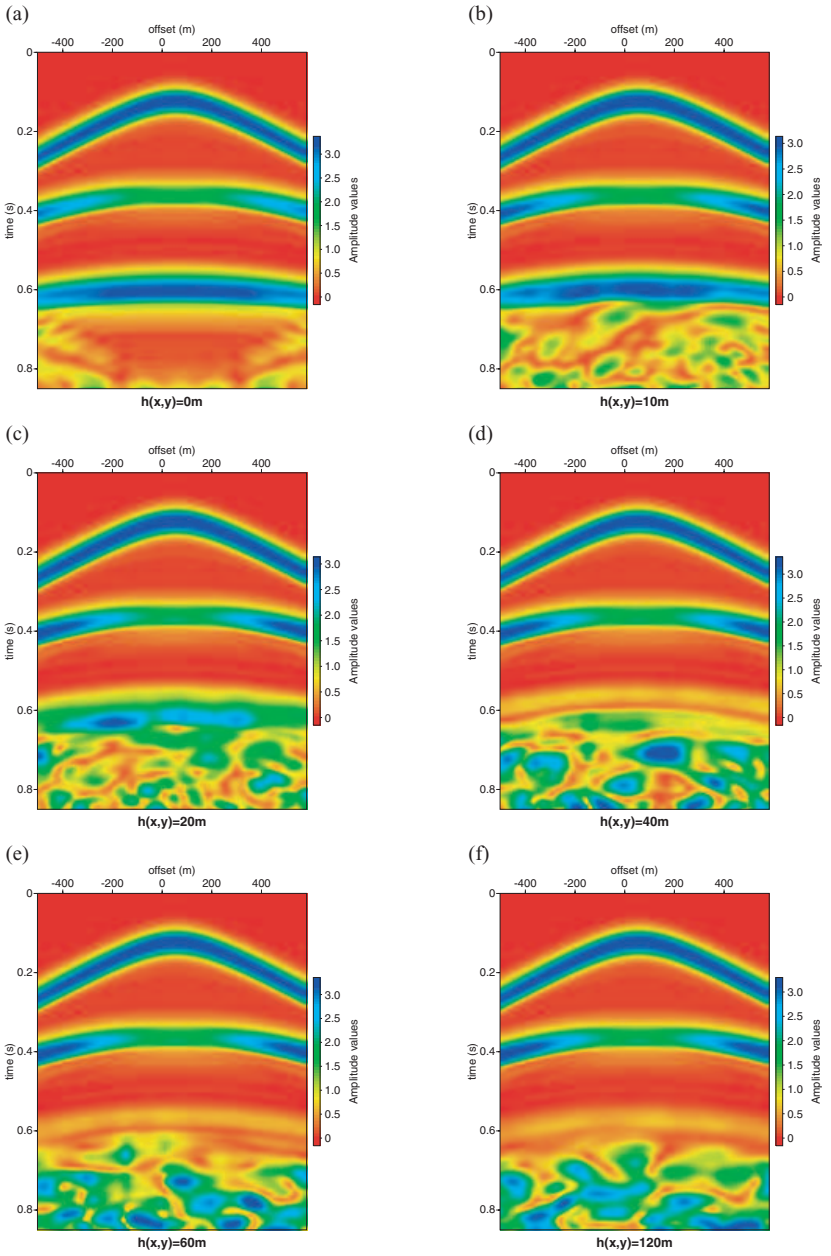

Figure 4 Instantaneous amplitude computed by the Hilbert transform method (envelope) on the synthetic data shown in Fig. 3.

the quality of the final seismic image. Comparative studies between the 2D and the 3D cases also show that the seismic response of random rough surfaces is not the same in 2D and 3D situations.

NUMERICAL ANALYSIS

Statistical description of the interface roughness

A rough interface is usually described in terms of its deviation from a 'smooth' reference surface. The shape and location of the reference surface are chosen according to the long-range behaviour of the surface. Essentially, two aspects of the nature of random rough surfaces are usually considered: the spread of the heights about the reference surface, and the variation of these heights along the surface. Statistical methods employed to describe rough surfaces are beyond the scope of this paper; however, a comprehensive list of descriptive methods and their significance can be found in Ogilvy (1991).

If the interface between two adjacent layers with different elastic/acoustic properties is statistically rough, we can

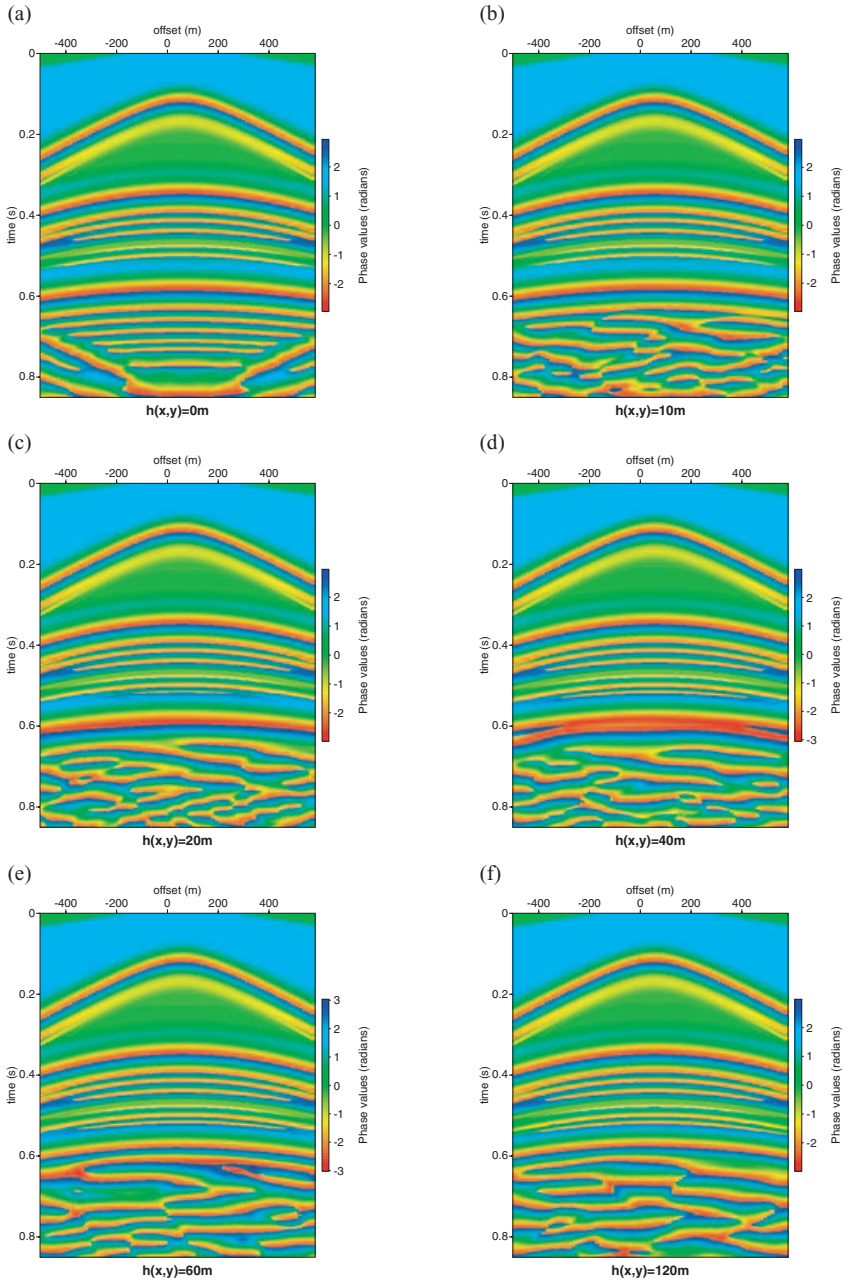

Figure 5 Phase spectrum computed for the data shown in Fig. 3.

describe such an interface by the relationship,

$$h = \xi(\mathbf{r}), \tag{1}$$

where h represents the depth in the model, $\mathbf{r}$ is a 2D vector lying in the $(x, y,0)$-plane, and $\xi(\mathbf{r})$ is, in our case, a Gaussian random function with zero mean and a correlation function given by

$$\left\langle \xi(\mathbf{r})\xi(\mathbf{r}') \right\rangle_s = C(\mathbf{r} - \mathbf{r}'). \tag{2}$$

The brackets $\langle \ldots . \rangle_s$ indicate averaging over the realization of the random function ξ. Although anisotropy occurs in nature in such a way that geological surfaces may possess surface azimuthal anisotropy, surfaces created by stochastic processes are usually stationary and statistically isotropic, having statistical characteristics independent of the azimuth. For the purpose of our analysis, we considered a statistically isotropic 3D random interface. Consequently, the correlation function distribution is independent of the azimuth along such a surface.

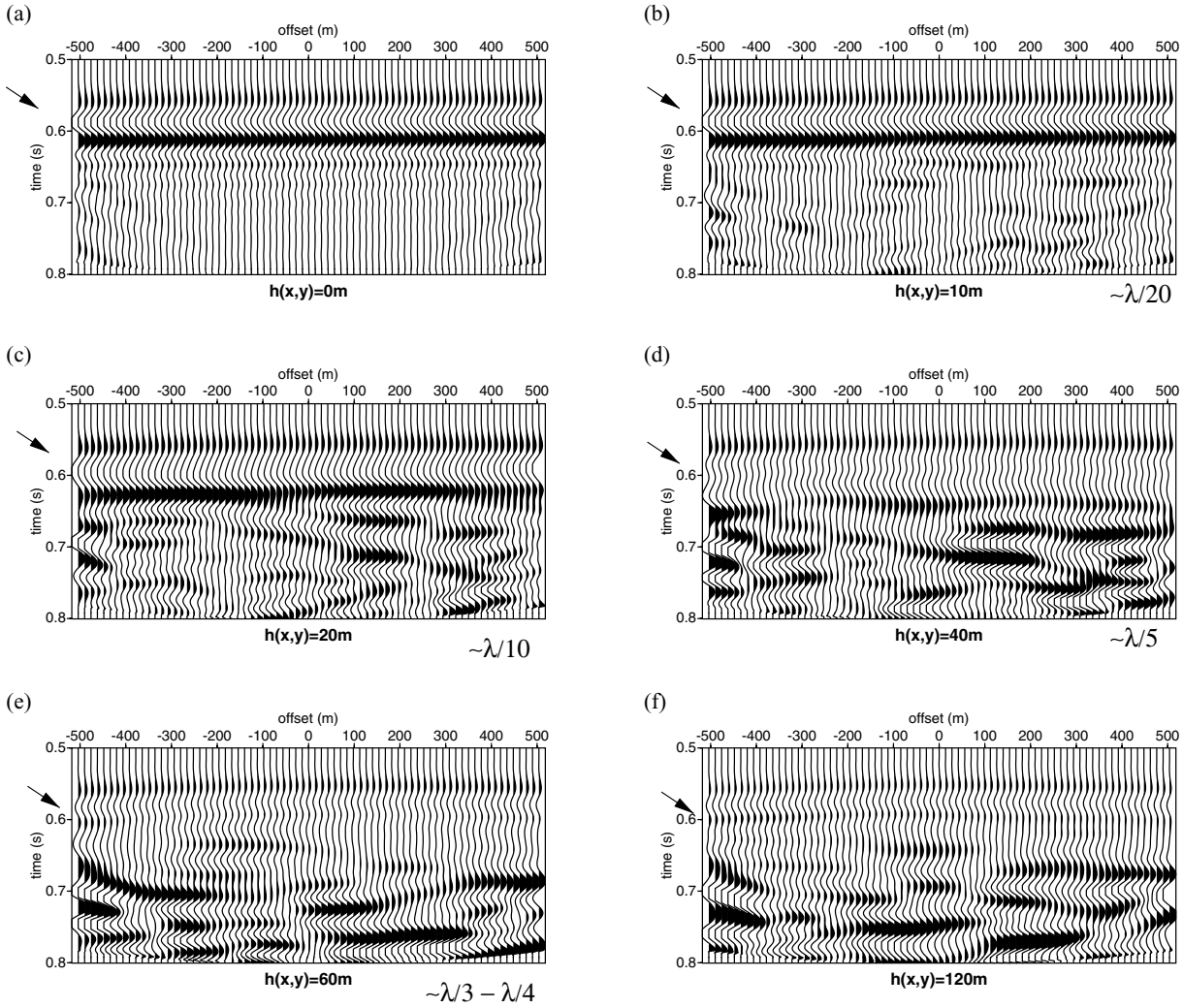

Figure 6 The seismic response of the second interface in the models after moveout correction to flatten the events for all offset ranges. This interface is a reflector for the reference model (a). It is a scattering interface in the other models: (b) $h(x, y) = 10$ m, (c) $h(x, y) = 20$ m, (d) $h(x, y) = 40$ m, (e) $h(x, y) = 60$ m, (f) $h(x, y) = 120$ m. The reflection appears at 0.6 s for the reference model (a). For increasing surface heights (b)–(f), the reflected event 'disappears' as the incident energy is gradually converted to scattered energy that is delayed on the section.

The roughness could take different values of the order of the wavelength of the propagating seismic signal in the medium above the scattering interface ($h/\lambda_c = 0.0, 0.048, 0.096, 0.192, 0.288$ and 0.576). Here, h is the rms height of the surface and λ_c is the central wavelength of the propagating seismic wave. A correlation length of 50 m was chosen to be independent of the azimuth on the surface.

Numerical scheme

We developed a 3D centred finite-difference numerical scheme in the acoustic domain based on the staggered grid formalism of Virieux (1986). This involved discretization of the hyperbolic system of the equations expressing the conservation of mass and hydrodynamics, by a first-order scheme at the nodes of a 3D mesh. This mesh was composed of cubic grids shifted by a half-mesh in one or many directions (Fig. 1a). Although the computational grids are cubic, the grid sampling was carefully chosen such that the interface distribution was well sampled in the three directions and was very much less than the correlation length of the interface distribution function. This procedure permits the computation of the pressure fields at the nodes at the centre of each cube in the grid, and the x-, y- and z-components of the velocity at nodes at the centre of each

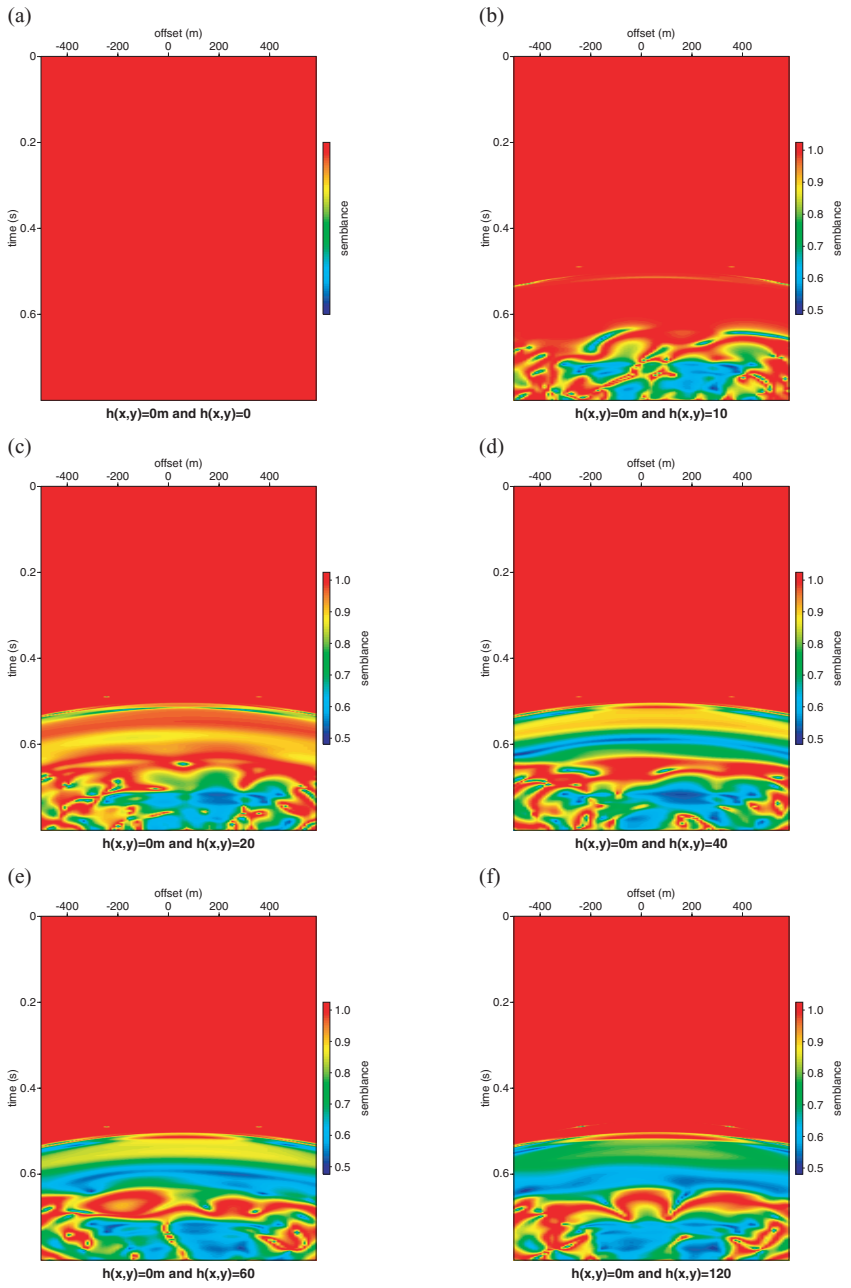

Figure 7 Computed semblance on the envelope between the reference model data and the data computed for the different surface height roughnesses of the 3D models. This gives a measure of the observed effect of phase scattering. (a) $h(x, y) = 0$ m versus $h(x, y) = 0$ m, (b) $h(x, y) = 0$ m versus $h(x, y) = 10$ m, (c) $h(x, y) = 0$ m versus $h(x, y) = 20$ m, (d) $h(x, y) = 0$ m versus $h(x, y) = 40$ m, (e) $h(x, y) = 0$ m versus $h(x, y) = 60$ m and (f) $h(x, y) = 0$ m versus $h(x, y) = 120$ m.

cube face. For the purpose of our analysis, we only considered the pressure field. To ensure the accuracy of the computed results, spurious reflections off the absorbing boundaries were avoided by padding the computational grid with an encasing spongy layer since these absorbing boundaries were only approximate.

The wave propagation in a 3D acoustic medium is governed by a system consisting of the equation of conservation of mass and the hydrodynamic equation. These equations can be written respectively as

$$\frac{\partial P}{\partial t}(x, y, z, t) - \rho(x, y, z, t)c^2(x, y, z, t)\mathrm{div}(\mathbf{v}(x, y, z, t)) = c^2(x, y, z)g(x, y, z, t) \tag{3}$$

and

$$\rho(x, y, z)\frac{\partial \mathbf{v}}{\partial t}(x, y, z, t) - \nabla P(x, y, z, t) = \mathbf{f}(x, y, z, t), \tag{4}$$

where P is a scalar function representing the pressure and $\mathbf{v}$ is the velocity vector in the medium at each point (x, y, z) in

Table 1 Spectral characteristics of the trace, obtained from the trace of the computed data for the 3D reference model

Parameters	Input signal	Interface 1	Interface 2
Frequency limits (Hz)	0–51	0–51	0–51
Carrier frequency (Hz)	20.23	20.90	20.00
Spectral eccentricity	0.300	0.272	0.271
Spectral bandwidth	44.65	44.32	44.54

Table 2 Spectral characteristics of the trace, extracted from the trace of the computed data of the 3D scattering model for a surface height of 40 m

Parameters	Input signal	Interface 1	Scattering interface
Frequency limits (Hz)	0–51	0–51	0–49
Carrier frequency (Hz)	20.42	20.05	22.60
Spectral eccentricity	0.293	0.300	0.183
Spectral bandwidth	44.48	44.83	42.19

space at each instant t of time, ρ is the density and c is the velocity of wave propagation at point $(x, y, z) \in \Re^3$. g and $\mathbf{f}$ represent, respectively, the source term and the external force field.

Considering that the medium is a closed system with no external force field, the system of equations (3) and (4) gives the following system of partial derivative equations:

$$\frac{\partial P}{\partial t} = c^2 \rho \mathrm{div}\mathbf{v} - c^2 g, \tag{5}$$

$$\frac{\partial v_x}{\partial t} = \frac{1}{\rho}\frac{\partial P}{\partial x}, \qquad \frac{\partial v_y}{\partial t} = \frac{1}{\rho}\frac{\partial P}{\partial y}, \qquad \frac{\partial v_z}{\partial t} = \frac{1}{\rho}\frac{\partial P}{\partial z}. \tag{6}$$

The above system of partial differential equations was discretized by employing the centred finite-difference scheme. If we take the spatial sampling in the three Cartesian coordinates (x, y, z) to be respectively Δx, Δy, Δz, and i, j, k, t to be the discretization indices on the x-, y-, z-axes and the time axis respectively, we can write the discretized equations as follows:

$$\begin{aligned} P^t_{i,j,k} = P^{t-1}_{i,j,k} + \Delta t (C^2 R)_{i,j,k} \Bigg\{ & \frac{1}{\Delta x}\left[U^{t-1/2}_{i+1/2,j,k} - U^{t-1/2}_{i-1/2,j,k}\right] \\ & + \frac{1}{\Delta y}\left[V^{t-1/2}_{i,j+1/2,k} - V^{t-1/2}_{i,j-1/2,k}\right] \\ & + \frac{1}{\Delta z}\left[W^{t-1/2}_{i,j,k+1/2} - W^{t-1/2}_{i,j,k+1/2}\right]\Bigg\} - \Delta t C^2_{i,j,k} G^{t-1/2}_{i,j,k}, \end{aligned} \tag{7}$$

where $P^t_{i,j,k}$ and $G^t_{i,j,k}$ represent the values of p and g, respectively, at the nodes $i\Delta x$, $j\Delta y$, $k\Delta z$ at instant t. $R_{i,j,k}$ and $C_{i,j,k}$ represent the values ρ and c respectively at the nodes $i\Delta x$, $j\Delta y$, $k\Delta z$, while $U^{t-1/2}_{i-1/2,j,k}$, $V^{t-1/2}_{i,j-1/2,k}$, $W^{t-1/2}_{i,j,k+1/2}$ represent the values of v_x, v_y and v_z respectively at the grid nodes and are time-indexed. Figure 1(b) shows examples of grid sampling and grid node indexing employed for the discretization of the equations.

The upper surface of the model was taken to be a zero-displacement surface (homogeneous Dirichlet-type boundary condition), while an absorbing condition was implemented at the other edges. The scattering interface (also the internal interfaces) was not treated with explicit boundary conditions because they are expressed in a homogeneous formulation (Kelly *et al.* 1976). They were represented as changes in velocity and density (acoustic parameters) as these quantities are expressed in a heterogeneous formulation. The problem of multiple scattering was thus implicitly addressed.

To verify the accuracy of the solution produced by the numerical scheme, we benchmarked the computation on a reference model with three horizontal plane interfaces. The traveltimes and amplitudes computed were compared with those calculated theoretically and were found to agree exactly. Since this model also serves as the reference model for the interface scattering analysis, we chose the acoustic parameters to be identical to those of the models used for the scattering studies.

Description of the 3D and 2D models

The models used for this study are simple piecewise stratified cubes consisting of three layers (Figs 2a, b) of dimensions 1000 m × 1000 m × 1000 m with interval velocities of 2000 m/s, 2500 m/s and 3200 m/s. The scattering interface was located at the base of the second layer with a velocity of 2500 m/s. The rms height of the scattering surface had values 0 m, 10 m, 20 m, 40 m, 60 m and 120 m for the simulations. An explosive source characterized by a first-order Ricker wavelet was used as the input signal. Considering a seismic signal of central frequency 12 Hz and a velocity 2500 m/s, the central wavelength in the medium above the scattering interface was about 208 m. Thus the scattering model with surface rms height of 20 m corresponds to the limit of the $\lambda/10$ criterion. The surface correlation length of 50 m was chosen with the height distribution totally independent of azimuth, thus attaining a statistically isotropic surface.

The scattering surface was generated with a random function creating a point distribution that has a Gaussian probability distribution function with zero mean. The Gaussian distribution was preferred rather than other types of

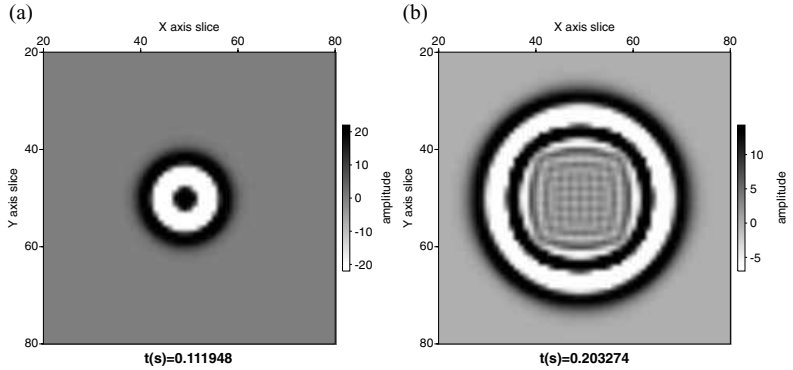

Figure 8 Snapshots of wave propagation in the 3D medium below the source at the (x, y, 0)-plane at different time-steps for the model with a surface height of 40 m. The reflection from the first interface (smooth) is at about 0.4 s (d).

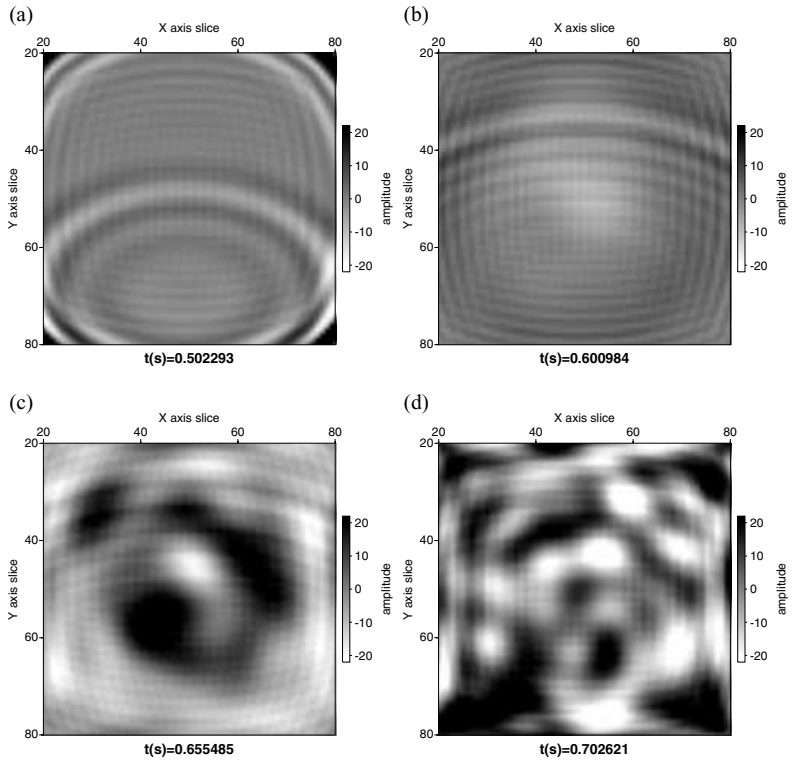

Figure 9 Snapshots of wave propagation in the 3D medium below the source. Note the phase change as the wavefield reaches the scattering interface between 0.6 and 0.7 s (c) and (d).

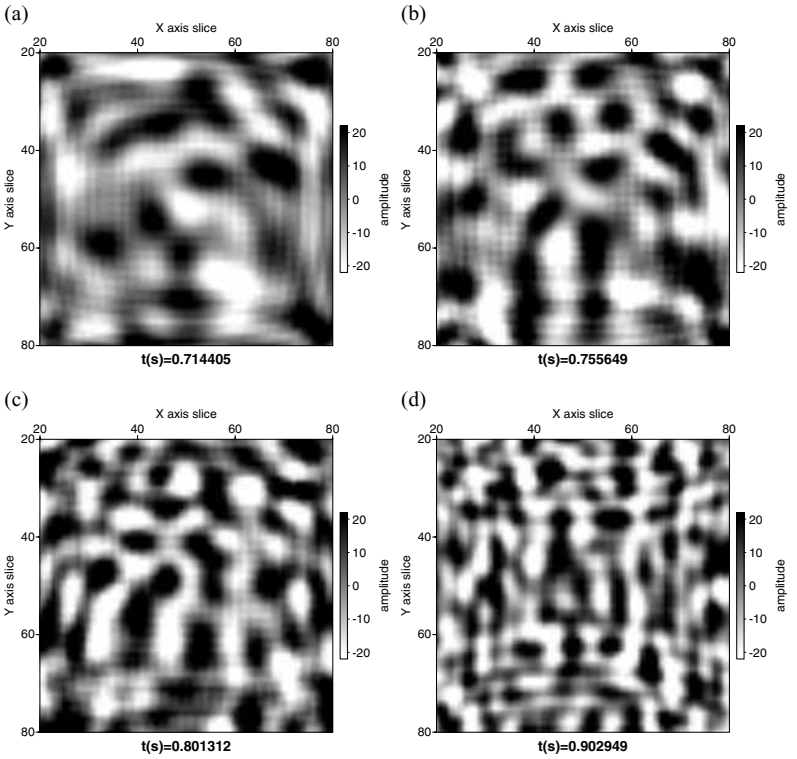

Figure 10 Snapshots of wave propagation in the 3D medium. Note that the response becomes more random after the scattering interface.

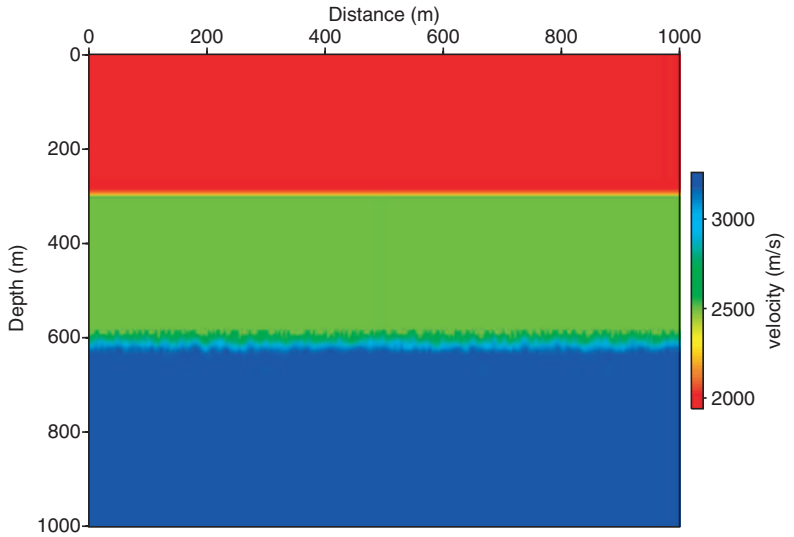

Figure 11 An example of a 2D model with a surface height of 40 m. This represents a slice in the $(x, y, 0)$-plane of the 3D model having the same surface height.

probability distribution (exponential for example) because most natural stochastic processes are better described with a Gaussian distribution. Moreover, the determination and computation of the related statistical parameters for Gaussian functions is relatively simple. Gaussian random deviates could be generated by performing a Box–Muller transform operation on uniform deviates (Box and Muller 1958). The probability distribution of such a distribution is given by

$$\Pi(h)\mathrm{d}(h) = \frac{1}{\sqrt{2\pi}} \exp\left(-\frac{h^2}{2\sigma^2}\right) \mathrm{d}h, \tag{8}$$

where $h = h(x, y)$ is the surface height distribution function. This implies that the number of points below and above the reference plane are equal. In such a case, the surface height

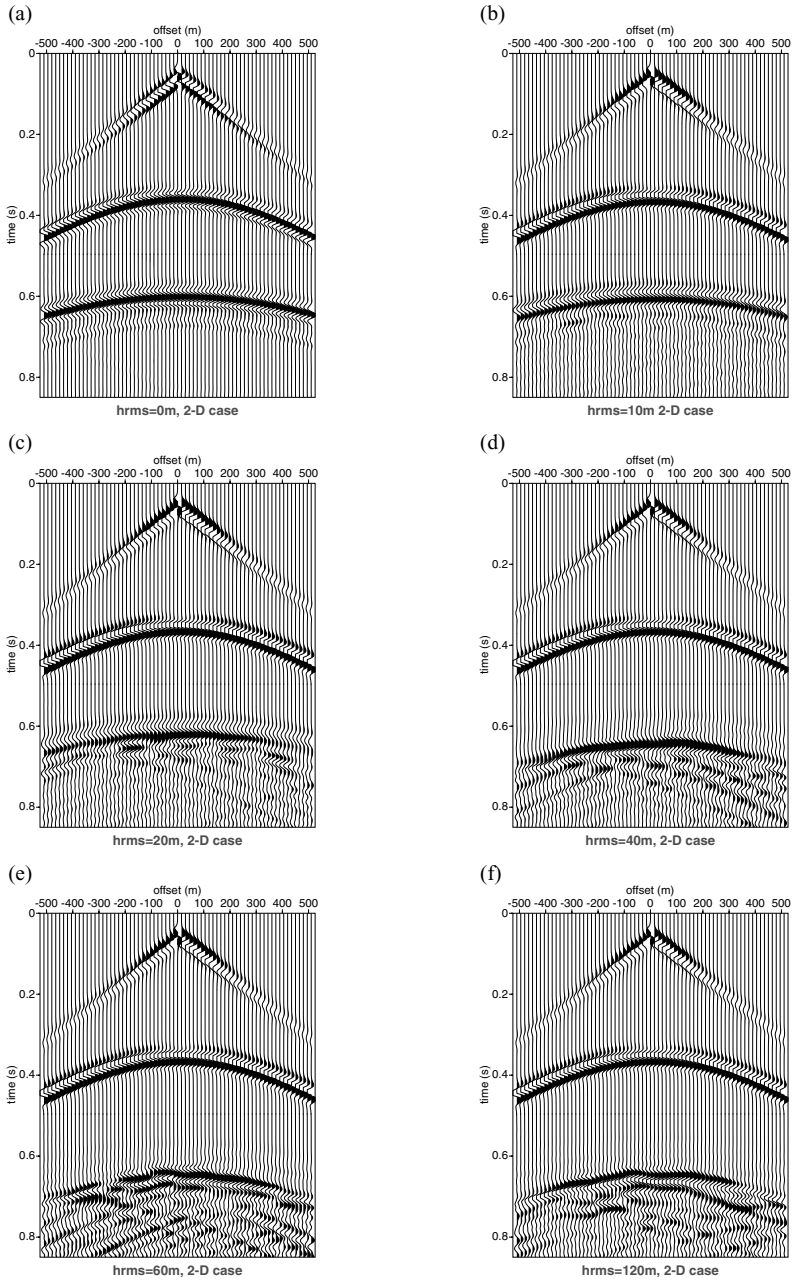

Figure 12 Simulations on 2D models with different rms heights. Simulations were realized for surface rms heights of (a) 0 m, (b) 10 m, (c) 20 m, (d) 40 m, (e) 60 m and (f) 120 m.

function satisfies the relationship,

$$\langle h \rangle_{\mathrm{s}} = \int_{-\infty}^{\infty} h \Pi(h) \mathrm{d}h = 0, \tag{9}$$

such that the rms height of the distribution equals the standard deviation and is given by

$$\sigma^2 = \sqrt{\langle h^2 \rangle_{\mathrm{s}}}, \tag{10}$$

where σ^2 is the variance. The correlation function of such a distribution is given by

$$C(\mathbf{r}) = \frac{\langle h(r) h(r+\mathbf{r}) \rangle_{\mathrm{s}}}{\sigma^2} = \exp\left(\frac{\mathbf{r}^2}{l_0}\right), \tag{11}$$

where l_0 is the correlation length of the distribution, r is a scattering point away from the surface, $\mathbf{r}$ is the vector separating two points and h is the surface height function. The variance determines the height variation of the interface while the

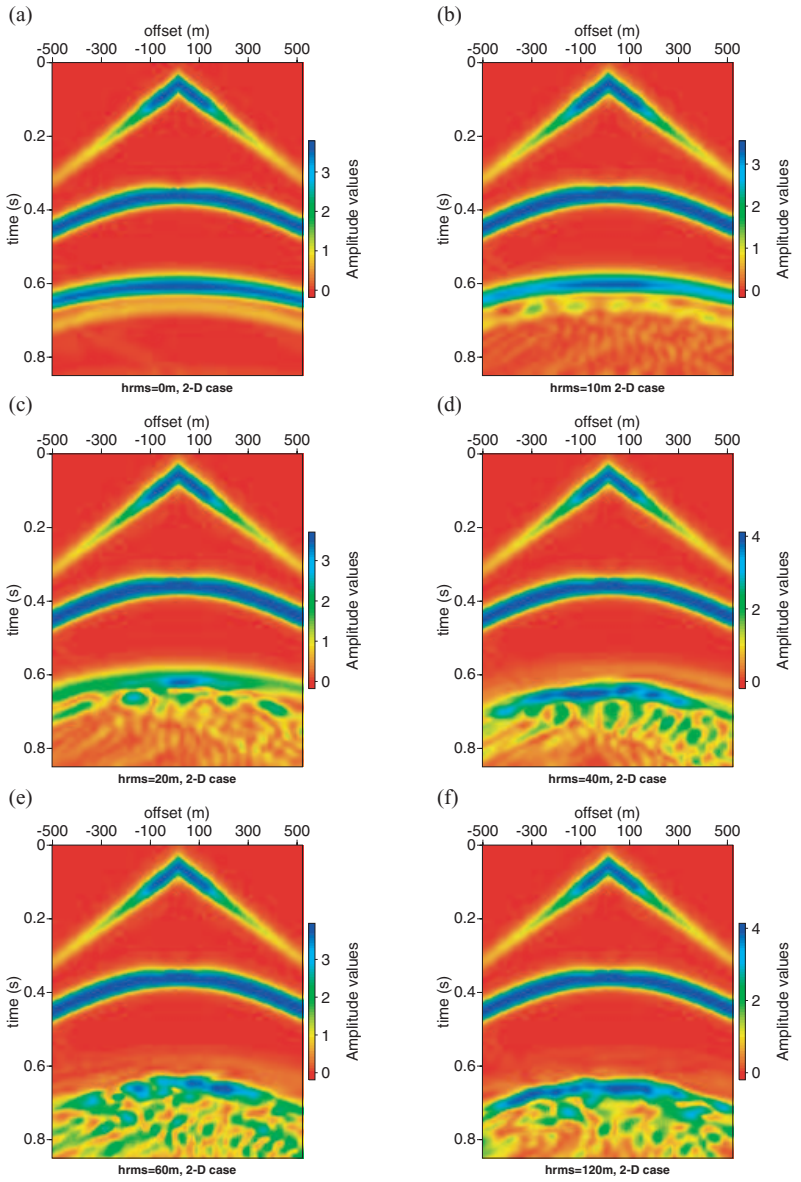

Figure 13 Instantaneous amplitude (envelope) computed with the Hilbert transform on the synthetic data from the 2D simulations of Fig. 12.

correlation length determines the maximum spatial frequency, or the lowest spatial wavelength in the surface distribution. The spatial spectrum of the interface function is the Fourier transform of the autocovariance function (non-normalized autocorrelation function) given by

$$\Psi(\mathbf{k}) = \frac{\sigma^2}{2\pi} \int C(\mathbf{r}) e^{i\mathbf{k}\mathbf{r}} d\mathbf{r}, \qquad (12)$$

where $\mathbf{k}$ is a unit vector in the z-direction.

For each simulation, we placed a network of receivers at the surface of the model. Since a homogeneous Dirichlet-type boundary was implemented at the upper surface of the model, a buried source at depth 60 m positioned at the centre was used. This accounts for the time delay observed on the computed data. The receiver spacing in the x- and y-directions was 15 m, thus giving a network of 66 × 66 traces in both x- and y-directions for a 1 km^2 acquisition. The total simulation time was 0.8 s. This configuration records the total field in the stratified medium.

For comparative studies, we also realized equivalent 2D models which correspond to slices at the middle of the 3D models (in the $(x,0,z)$-plane) with rms heights of the surface of

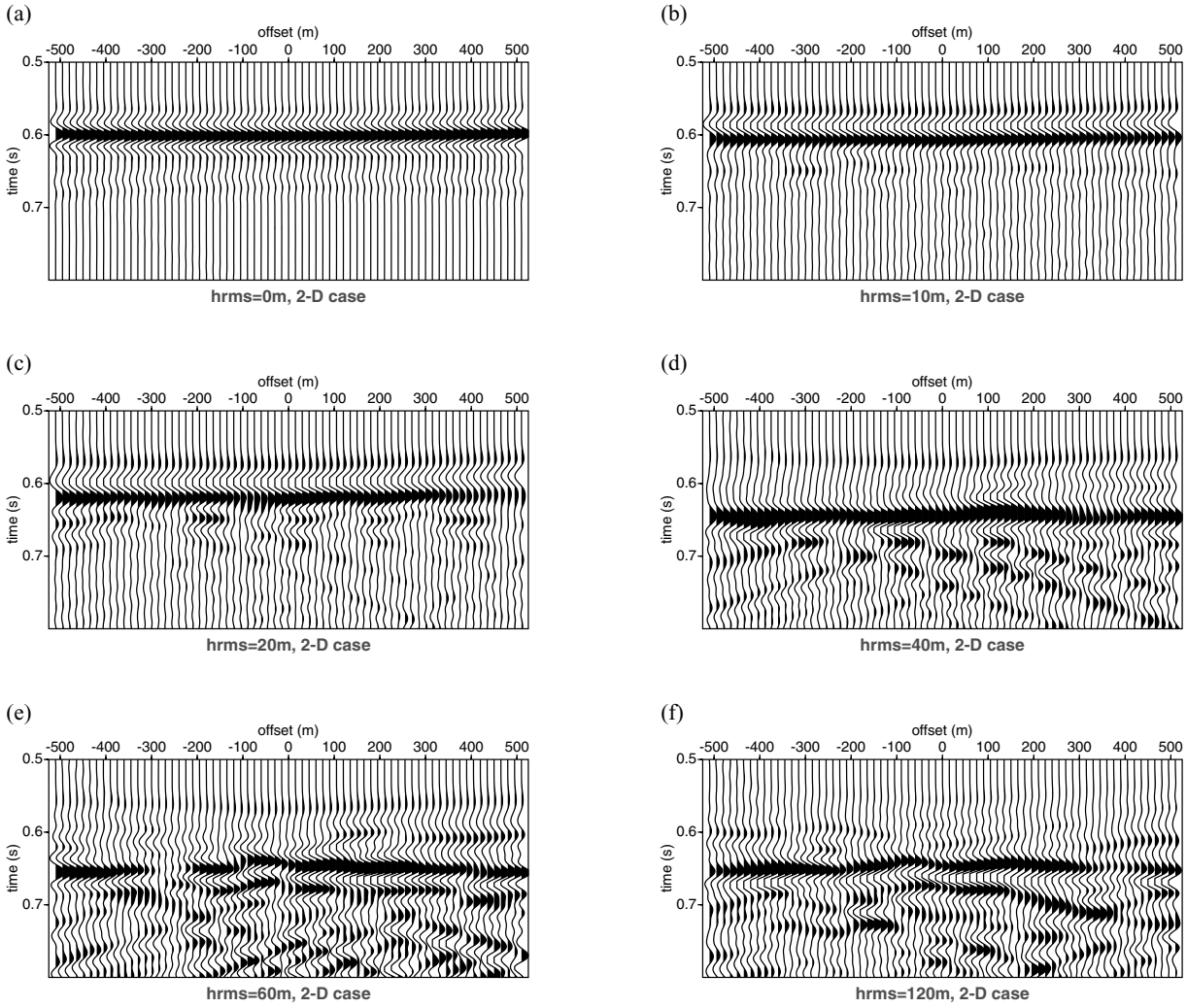

Figure 14 As Fig. 6 but for 2D simulations. Note the continuity of the events for all computed data and the relatively weak phase scattering compared with the 3D case.

0 m, 20 m, 40 m, 60 m and 120 m. These models were used for comparisons between the 2D and 3D situations for phase scattering studies.

NUMERICAL RESULTS AND DISCUSSION

In this section, we present the results of the numerical simulations on the 3D and 2D models, which are the solutions to the forward scattering problem. Firstly, we analyse the results of the 3D simulations. We then compare the 3D case with the 2D case and finally calibrate the 2D results with the 3D results. In our discussion, we refer to the effect of the interface scattering phenomenon of seismic signal on the phase of the signal as phase scattering or de-phasing. Analysis of the results of the 3D simulations is carried out on the extracted central group of the computed 3D data cube. This is a slice in the (x, t)-plane of the data cube. Since the 3D rugose interface employed for the simulations is statistically isotropic, significant discrepancies are not expected in the results of the computed data with respect to azimuth.

3D case

Figures 3(a–f) obtained from the extracted receiver groups from the centre of the simulated data cube (a slice in the (x, t)-plane) represent the simulated pressure field in the 3D medium where either no scattering interface (a), considered as the reference model, or a scattering interface with surface height of

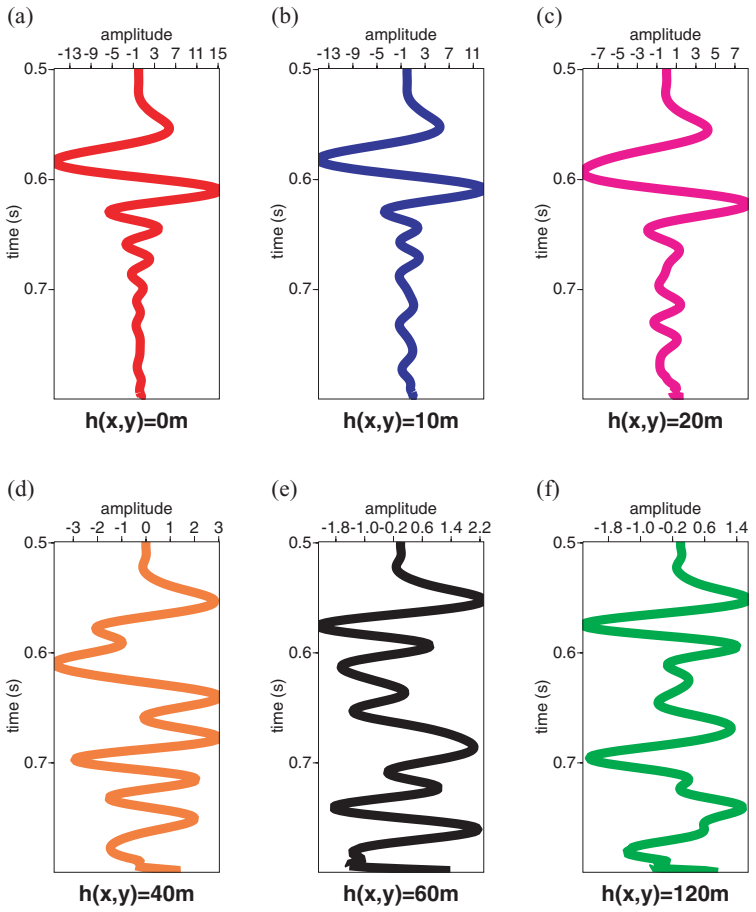

Figure 15 Stacked traces of the 3D data of Fig. 6.

(b) 10 m, (c) 20 m, (d) 40 m, (e) 60 m or (f) 120 m occurs. For the reference model $h(x, y) = 0$ m, the direct arrival and the response of the two plane interfaces are clearly discernible at zero-offset times of about 0.1 s, 0.4 s and 0.6 s, respectively. Parasitic corner reflections arising from corners of boundaries can be seen, with a very weak amplitude. These, however, do not fundamentally affect the results as they are less than 5% of the amplitude and within the acceptable limit. Comparison of Fig. 3(a) (the reference model) with Figs 3(b–f) shows that the rough interface creates a spatially random de-phasing of the incident wavefield and that the de-phasing increases as the surface height distribution function, $h(x, y)$, increases from 10 m to 120 m. The principal effect of the interaction between the random rough surface and the incident wavefield is the transformation of a part of the incident energy into random noise which is delayed on the section and forms the random, incoherent part below 0.6 s. This results from the spatial convolution of the incident wavefield with the random function describing the surface height distribution. According to the Fourier theorem, if the function $h(x, y)$ describing the interface distribution is random, then the scattering pattern of the wavefield can also be described as a random distribution (de Coulon 1996). In general, the phase dependence or the effects of a signal can be nullified by computing the envelope (instantaneous amplitude) of the analytic signal by the Hilbert transform of such a signal. This permits a better visualization of the de-phasing effect on the computed data. Figure 4 shows the computed envelope of the data for the reference model and the models with surface heights from 10 m to 120 m, while Fig. 5 shows the computed phase spectra. The de-phasing is clearly evident on these plots, especially looking closely at the response of the scattering interface. The phase scattering increases with increasing surface height for a given correlation length. The computed phase spectra of the data also corroborate this observation (Fig. 5). Even for a surface height of $h(x, y) = 20$ m, which corresponds to the threshold limit of $\lambda/10$, the phase scattering can already be seen and the observed de-phasing is not negligible (Figs 3c and 4c).

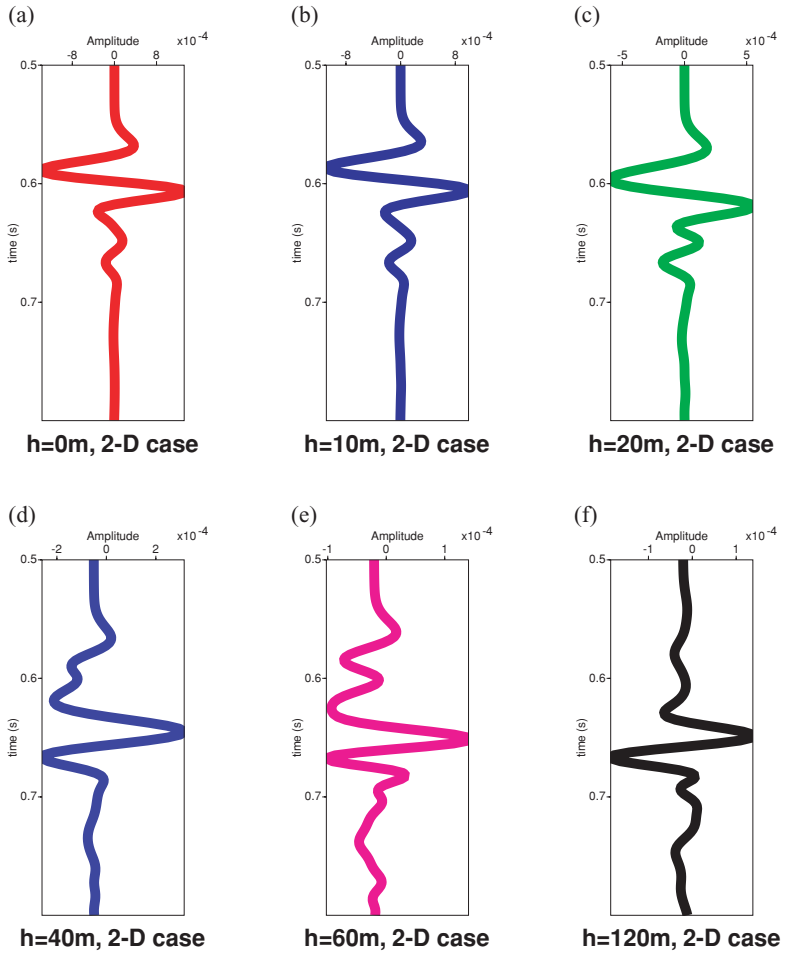

Figure 16 Stacked traces of the 2D data of Fig. 14. Note that the phase scattering is less pronounced.

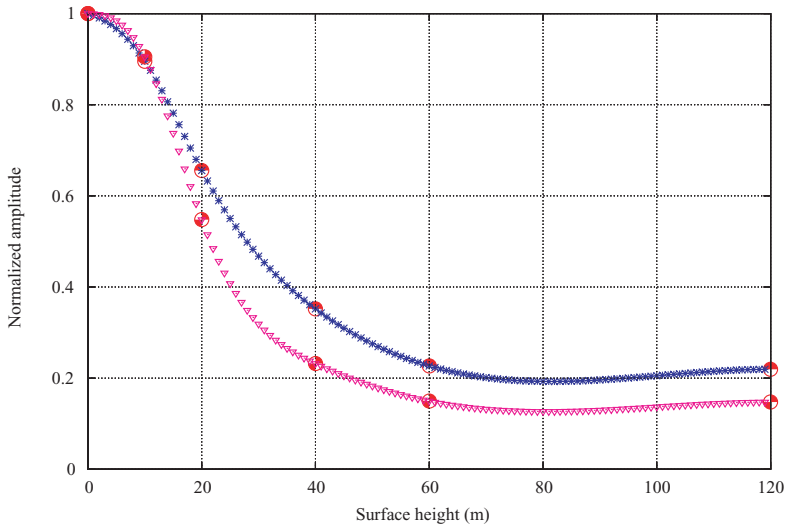

Figure 17 Normalized amplitude as a function of surface height for the synthetic data computed on the 3D (purple) and the 2D (blue) models with different surface heights. The amplitude reduces from unity to a minimum between surface heights of 40 m and 60 m, corresponding to $\lambda/5$ and $\lambda/4$, respectively.

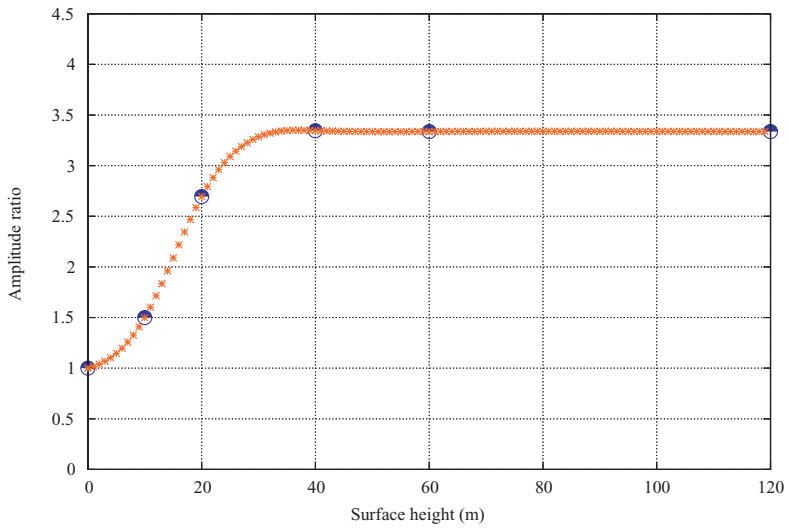

Figure 18 Ratio of the normalized amplitude of 3D and 2D data as a function of surface height. The amplitude increases from unity to about 3.4 and then remains constant.

To demonstrate the de-phasing effect qualitatively, we concentrate on the seismic response from the second interface. This interface is a perfect reflector in the reference model and a scattering reflector in the other models. A moveout correction was then applied to flatten the events for all the offset range for this interface, using exact velocity information (Fig. 6). The reflection from this interface occurs at about 0.6 s two-way traveltime (TWT) for the reference model (Fig. 6a). Figures 6(b–f) show the results for the models with surface rms heights of 10 m, 20 m, 40 m, 60 m and 120 m, respectively. The simulation on the model with a surface rms height of 10 m was carried out to show the phase evolution between the reference model, $h(x, y) = 0$, and the model with a surface height of 20 m which corresponds in our case to the Rayleigh threshold limit for a smooth interface. It was, however, observed that over all the offset range, the phase scattering is totally negligible and that there is no time delay on the recorded signal for this height. This, however, is not true as the surface height function increases from 20 m to 120 m (Figs 6c–f). For this range of the surface height function, the reflection gradually disappears from 0.6 s TWT for increasing surface height, as the incident seismic energy is converted to the scattered energy that appears at a delayed time on the section. As the surface height function increases, the phase scattering becomes more pronounced.

To facilitate the comparison of the de-phasing effect with the reference model in the 3D situation, we computed the semblance panels on the envelopes between the reference model and each set of computed data for the different surface heights. The semblance coefficient on the envelope can give a measure of similarity or semblance between two panels. If the envelopes of two given panels are respectively E_1 and E_2, the semblance on the envelopes can then be defined by the following equation:

$$S = \frac{(E_1 + E_2)^2}{2\left(E_1^2 + E_2^2\right)}. \tag{13}$$

This quantity lies between 0.5 and 1.0. A value of 0.5 means that there is no similarity between the two quantities being compared, while a value of 1.0 means equality of the compared quantities. Figure 7(a) shows the semblance on the envelope of the reference model and itself. On this figure the semblance coefficient is 1.0 as expected. Figures 7(b–f) show the semblance on the envelope of the reference model and the other models with surface heights of 10 m, 0–20 m, 0–40 m, 0–60 m and 0–120 m, respectively. The upper part of each figure has a semblance of unity as this part, comprising the direct arrival and the response of the first interface, is identical for the reference model and all the scattering models. The lower part from 0.6 s TWT, which is a measure of the scattered energy for each model compared with the reference model, has different semblance values. This corroborates the earlier observations of increasing phase scattering with increasing surface rms height which is not negligible for $\lambda/10$ (i.e. for $h(x, y) = 20$ m). Further results of the spectral analysis for the reference and the scattering models are summarized in Tables 1 and 2, respectively. These results show that the spectral bandwidth of the signal is generally reduced after scattering and that the spectral eccentricity of the signal is significantly affected. Spectral eccentricity is defined as the degree of symmetry or skewness of the amplitude spectrum of a signal. For example, zero-phased

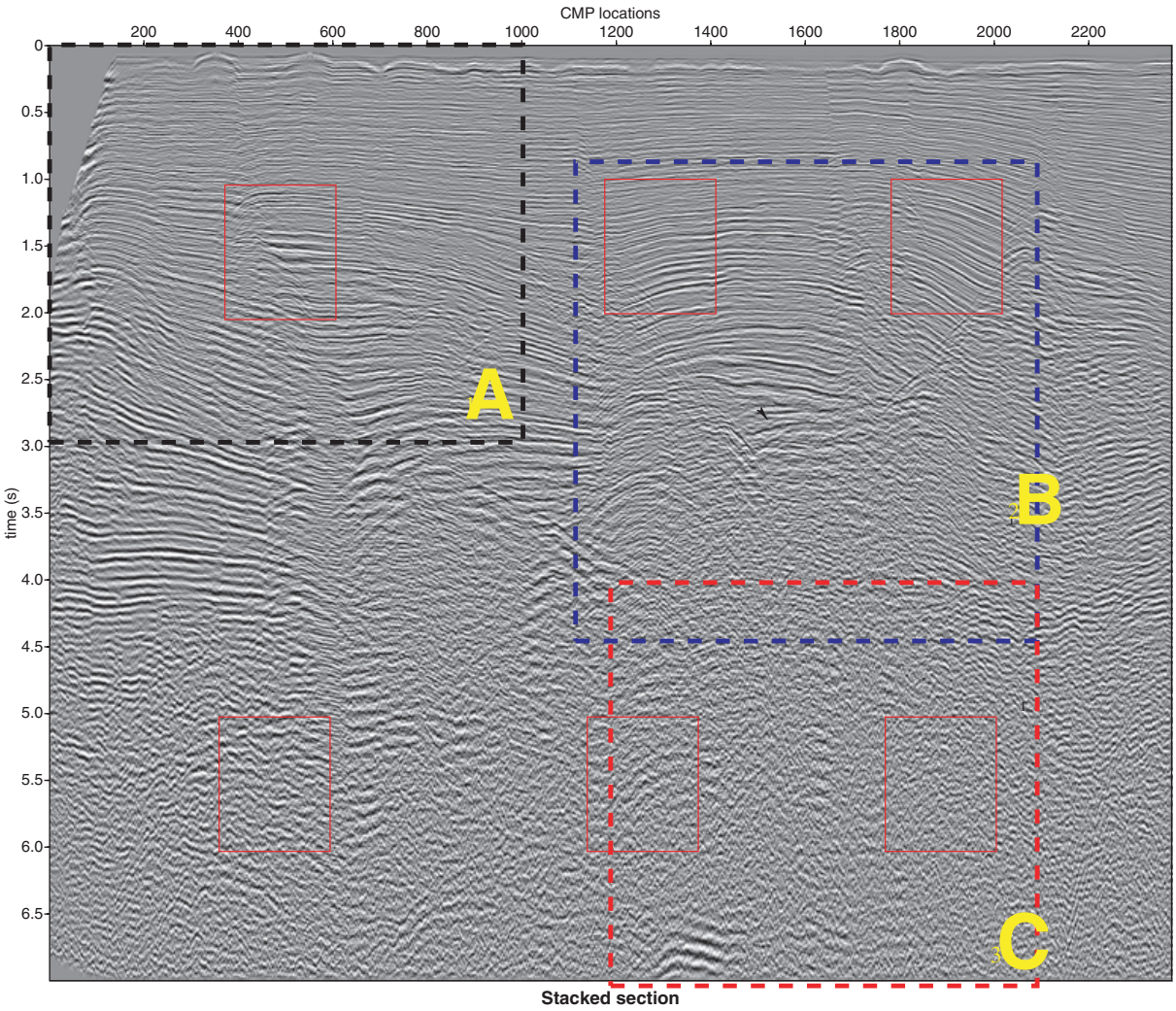

Figure 19 Real data example from offshore Niger Delta, off the West African coast. On this stacked section, the zones in the dotted boxes are explained in the text. The red boxes show the time windows used for the spectral analysis.

signal has a symmetrical amplitude spectrum and thus zero spectral eccentricity.

Figures 8 , 9 and 10 show snapshots of the wave propagating in the 3D medium at various time-steps in the (x, y)-plane below the source for the model with a surface height of 40 m. The wavefield is then described at different times before and after passing through each interface in the 3D medium. Propagating through the first interface which is a smooth surface, the wavefront remains spherical and in-phase and hence its slice is circular (Fig. 8d). On reaching the scattering interface, the wavefront loses its sphericity and its phase becomes affected (Fig. 9c). Passing through the scattering interface, the wavefront sphericity is completely lost and the phase now becomes random (Fig. 10). One part of the incident energy is strongly backscattered while the other part is transmitted through the scattering interface. The transmitted scattered wave will become further scattered in the upgoing direction, leading to further loss of phase information. The backscattered energy is usually stronger than the transmitted scattered energy, with respect to the reflection. The ratio of the transmitted to the scattered energy is a few percent; however, the ratio of the backscattered to the reflected energy is of the order of 1. Consequently, a scattering effect will occur on a stacked section and neglecting it will lead to significant errors in the quantitative interpretation of the reflection amplitude.

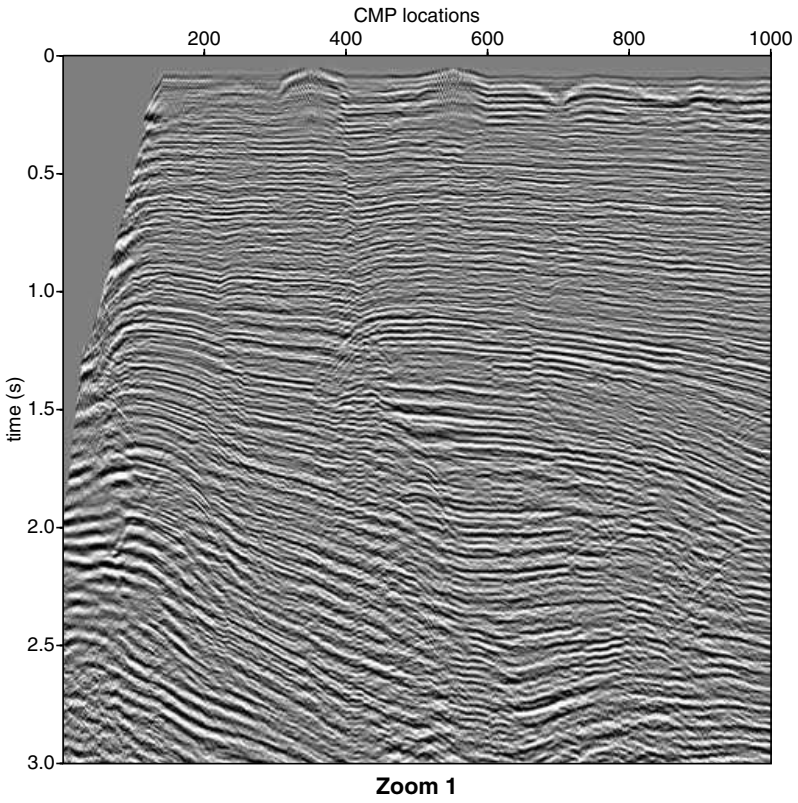

Figure 20 Zoom of zone A (black dotted box in Fig. 19). Note the good signal-to-noise ratio and the good phase fidelity of this part of the image above the scattering interface.

2D case

The equivalent 2D models used for the 2D simulations were slices of the 3D models in the (x, 0, z)-plane. The acoustic properties are thus identical to those of the 3D models. Taking the slice of the 3D model in any azimuthal direction would not affect the result as the surface distribution is independent of azimuth. Figure 11 shows such a model for a surface height of 40 m. A line source was used, resulting in circular wavefront propagation as opposed to a point source that generates spherical wavefronts for the 3D simulations. Figures 12 and 13 represent the computed data and their computed envelopes, respectively, while Fig. 14 describes the response of the second interface after moveout correction with exact velocity information. The conclusions concerning the results from the 2D simulations are identical to the results obtained for the 3D simulations: i.e. the phase scattering effect increases with increasing surface height function.

2D versus 3D

Simulations run on the equivalent 2D models show that the phase scattering effect observed is not the same as that in the 3D case. This can be better observed in Figs 6 and 14, which represent the response of the scattering interfaces in both scenarios. On the one hand, Fig. 6, which depicts simulations on the 3D models with surface rms heights of 0 m, 10 m, 20 m, 40 m, 60 m and 120 m, shows, with increase in surface height, a faster attenuation of the primary arrival at 0.6 s TWT, more pronounced scattered energy, as is evident from the generated random noise, and a more significant delay of the coda waves, as shown by the arrows on the figures. On the other hand, Fig. 14, which represents the results of the 2D simulations for the same surface height range as that of the 3D case, shows a less pronounced attenuation of the event at 0.6 s, less random noise and a continuation of the phase of the event. As an example, this event completely loses its continuity at a surface height of 40 m for the 3D case, whereas continuity is observed for the same event up to a surface height of 120 m for the 2D case.

Calibration of the scattered amplitude

In order to compare the effect of the 3D and 2D rough interfaces on the seismic section, we need to calibrate the amplitude of the events in the two cases. For this procedure, only the seismic response of the scattering surface is necessary for

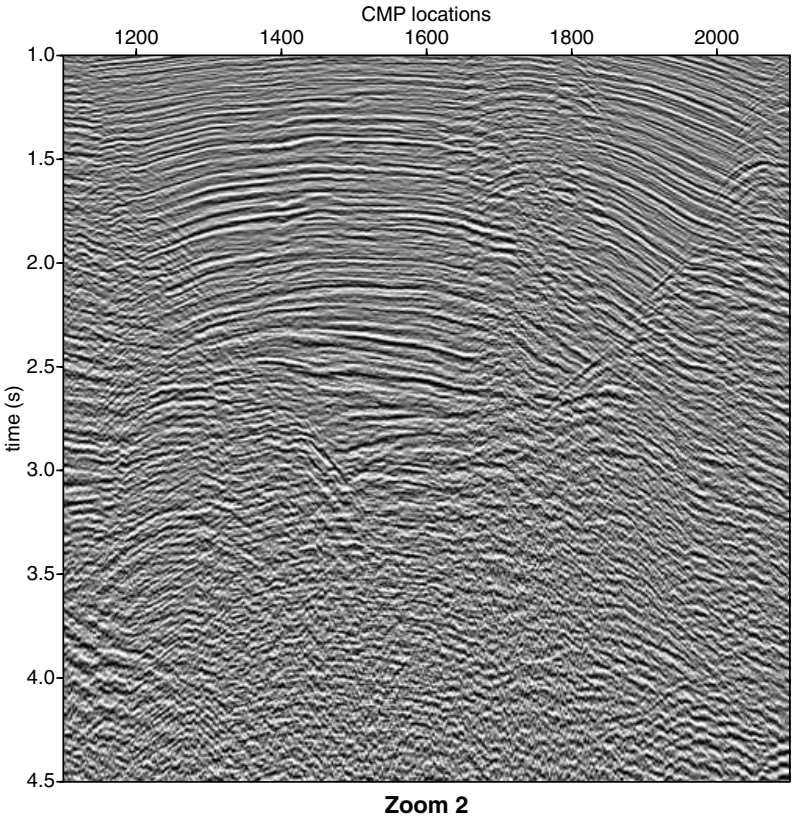

Figure 21 Zoom of zone B (blue dotted box in Fig. 19). Transition at the scattering interface.

the computations, as the direct arrival and the response of the first interface are the same for the reference and scattering models, as shown on the semblance calculation (Fig. 7). These extracted responses within a sufficient time window (Figs 6 and 14) were corrected for geometrical spreading after the moveout correction, with exact velocity information. The geometrically corrected data are stacked to obtain a single trace for each simulation. The stacked traces for the 3D and 2D simulations, shown respectively in Figs 15 and 16, corroborate the earlier observations that the phase scattering is stronger in the 3D case than in the 2D case. This is evident from the more pronounced coda waves and time delay of the interface response in the 3D case. The maximum amplitude on the envelope of the analytic signal of each stacked trace was determined and plotted as a function of the surface height (Fig. 17) after normalization with the amplitude of the reference trace for both cases. The curve associated with the normalized amplitude exhibits a Gaussian shape with decreasing values starting from 1.0, corresponding to the normalized amplitude with respect to the reference model, and reaching a minimum between surface heights of 40 m and 60 m, which correspond approximatively to $\lambda/5$ and $\lambda/4$, respectively. This attenuation is, however, stronger in the 3D case than in the 2D case. The Gaussian shape of the curve is related to the statistics of the surface distribution function. The ratio of the normalized 3D to 2D amplitudes was also computed and plotted versus the surface height function (Fig. 18). This curve shows the increase in the 3D/2D normalized amplitude ratio from unity for the reference model to a maximum of 3.4 at a surface height of 40 m; the ratio of the amplitudes then becomes constant with increasing surface height.

Consequently, for a given interface roughness height in the 3D situation, an interface roughness height of at least three times higher is required to produce an equivalent scattering effect in the 2D situation for a given correlation length of the surface distribution. This interesting result has to be kept in mind when 2D simulations of wave propagation in media with rough interfaces are realized.

Real data example

In this section, we briefly introduce the interface scattering phenomenon encountered in real situations and its effect on the final seismic image quality. Figure 19 illustrates

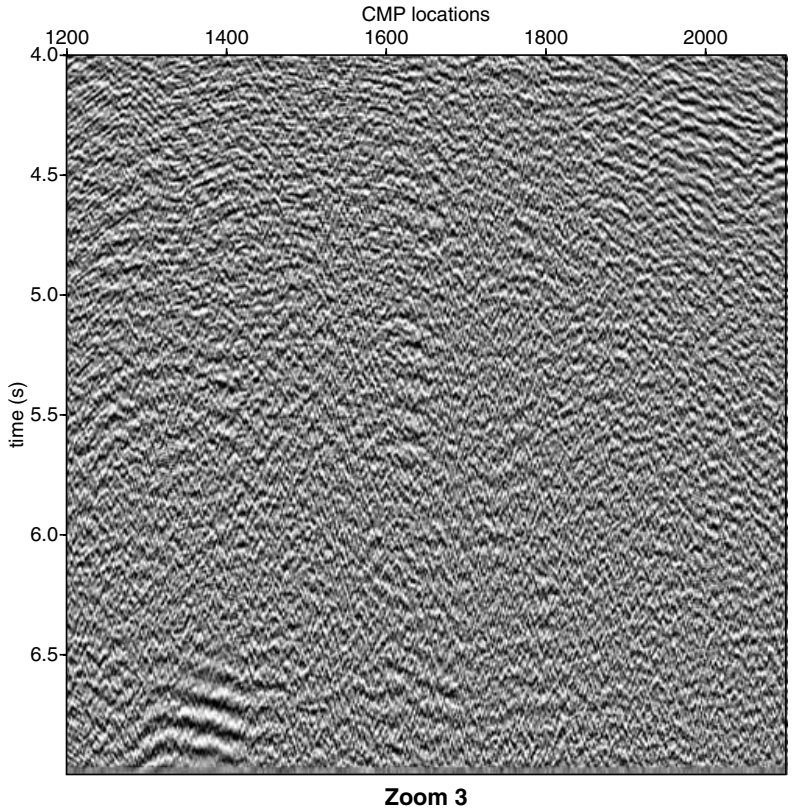

Figure 22 Zoom of zone C (red dotted box in Fig. 19). Note the poor phase fidelity as the events become random below the scattering interface.

Table 3 Spectral characteristics of the CMP time window for CMP range 400–600

Parameters	CMP 400–600 upper	CMP 400–600 lower
Frequency limits (Hz)	6.61–69.87	5.74–48.76
Carrier frequency (Hz)	38.57	26.93
Spectral eccentricity	-1.06×10^{-2}	1.49×10^{-2}
Spectral bandwidth	63.26	43.03
Signal-to-noise ratio (dB)	17.01	2.07

Table 4 Spectral characteristics of the CMP time window for CMP range 1200–1400

Parameters	CMP 1200–1400 upper	CMP 1200–1400 lower
Frequency limits (Hz)	6.60–77.11	5.70–52.36
Carrier frequency (Hz)	42.07	29.67
Spectral eccentricity	-6.13×10^{-3}	-2.75×10^{-2}
Spectral bandwidth	70.51	46.65
Signal-to-noise ratio (dB)	18.76	−1.59

a real seismic section from the offshore Niger Delta, off the West African coast. This section was obtained in a part of the region where gravity sliding and shale tectonics dominate the structural styles. The interaction of the undercompacted, overpressured, mobile shale-bodies with encasing sand-bodies results in the creation of highly rugose interfaces between the sand- and shale-bodies. Three zones can be identified in Fig. 19, shown by the dotted boxes: the upper short time zone (A), characterized by a good signal-to-noise ratio and good phase fidelity (Fig. 20); a transitional zone (B), which also describes the limit of the rugose surface as corroborated from well data (Fig. 21); and the lower part (C) below the rugose interface, which is generally characterized by very poor signal-to-noise ratio (Fig. 22). A signal-to-noise-ratio interface scattering effect dominates below the transition. It randomizes the phase of the signal and converts part of the incident seismic energy into random noise, which eventually masks the reflections from the underlying reflectors. Spectral analysis was carried out at three different CMP time windows each spanning 200 CMPs along the stacked section. Different time windows were used at locations above and below the sand/shale interface. The signal-to-noise ratio within these windows was also evaluated. Tables 3, 4 and 5 summarize the results of the spectral analysis for the CMP time windows. The frequency

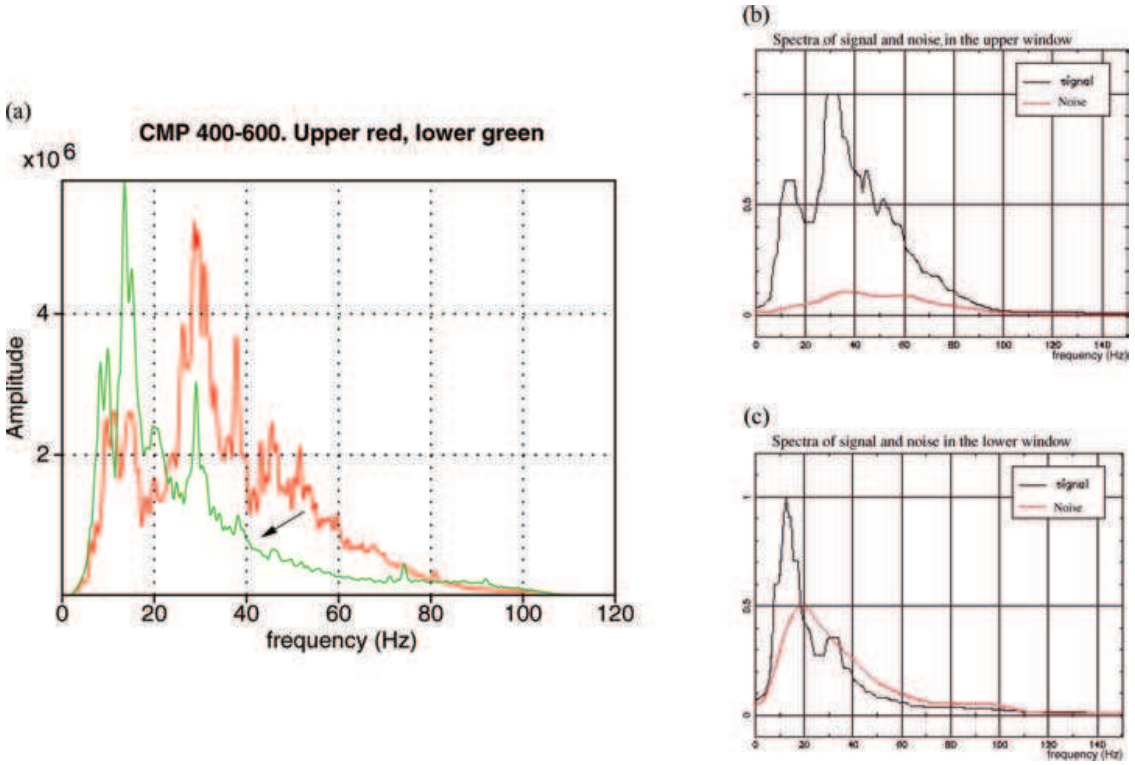

Figure 23 Spectral analysis of the real data: (a) spectra of the upper (red) and the lower (green) windows of CMP range 400–600 shown in Fig. 19. Note the reduction in the high-frequency content across the scattering interface; (b) spectra of the signal (black) and noise (red) in the upper window and (c) in the lower window. Note the considerable increase in the noise in the lower window.

Table 5 Spectral characteristics of the CMP time window for CMP range 1800–2000

Parameters	CMP 1800–2000 upper	CMP 1800–2000 lower
Frequency limits (Hz)	6.56–76.30	5.74–53.73
Carrier frequency (Hz)	42.53	31.82
Spectral eccentricity	-3.13×10^{-2}	-8.73×10^{-2}
Spectral bandwidth	69.73	47.98
Signal-to-noise ratio (dB)	19.95	−3.79

bandwidth was reduced from 63 Hz to 43 Hz for CMP range 400–600, from 71 Hz to 47 Hz for CMP range 1200–1400 and from 70 Hz to 48 Hz for CMP range 1800–2000, representing a reduction of between 40 and 48%. The lower frequencies in the frequency range do not change significantly between the time windows for each CMP range, whereas the higher frequencies are reduced, denoting the attenuation of the high frequencies as the wave passes through the scattering interface. These time windows are shown as red boxes in Fig. 19. The results of the spectral analysis are illustrated graphically in Figs 23 , 24 and 25 for CMPs 400–600, 1200–1400 and 1800–2000, respectively. These figures show the computed spectra of the upper time window (above the interface) and the lower time window (below the interface), together with the spectra of the signal and the noise. Noise is defined as the part of the signal that is not laterally correlated. The determination of this non-laterally correlated signal can be obtained by aligning the traces and determining the maxima of their intercorrelations. The average of the intercorrelation gives the signal while the average of the autocorrelation will give the signal and noise. The noise can then be obtained by subtracting the average of the intercorrelations from that of the autocorrelations. In general, the signal-to-noise ratio is drastically reduced between the time windows for all the CMP time windows as shown in Tables 3 , 4 and 5. High-frequency attenuation of seismic waves has earlier been identified and attributed to propagation effects, for example, due to absorption and thin-layer filtering (O'Doherty and Anstey 1971). It has also been shown to be progressive and global in such a case. In the case of a rugose interface, the observed attenuation is local and severe, occurring

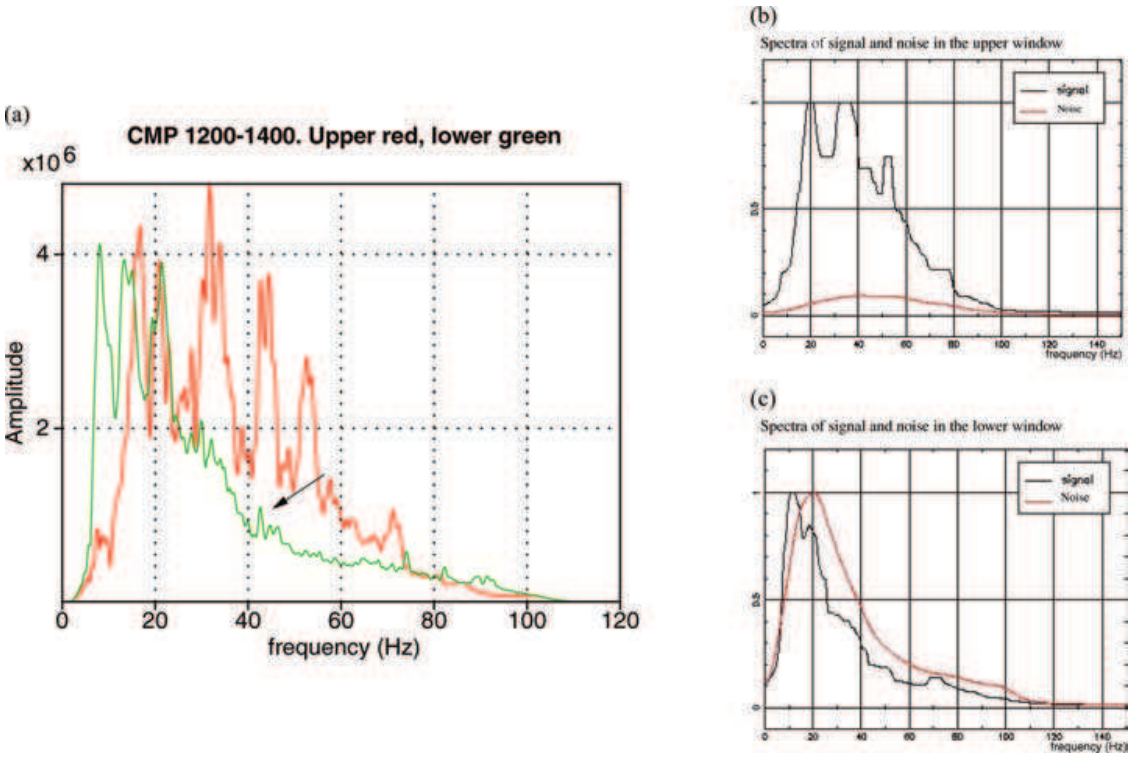

Figure 24 Spectral analysis of the real data: (a) spectra of the upper (red) and the lower (green) windows of CMP range 1200–1400 shown in Fig. 19; (b) spectra of the signal (black) and noise (red) in the upper window and (c) in the lower window. Note the total contamination of the signal by the noise in the lower window.

when the wavefield passes through the interface. This could be attributed to the multiple scattering effect, a mechanism by which the wavefield loses its high-frequency content as it is multiply scattered by the surface. Wavelengths shorter than or within the range of the surface height are mostly affected. Preservation of the lower and upper limits of the frequency spectrum (high and low frequency contents) is necessary for distinguishing the details on a seismic image. The loss of high-frequency content thus results in the loss of fine detail on a seismic image.

CONCLUSION

The main objective of this work was to investigate the effect of the interface scattering phenomenon on the seismic wavefield. Many previous studies carried out on different aspects of the problem have been restricted to 2D or 2.5D situations. Because interface scattering is a 3D phenomenon, we study the wave scattering from a randomly rough interface in a 3D configuration.

Using a finite-difference scheme in a 3D acoustic domain, we have described the effect of a random rough interface on the incident wavefield. In particular, we have shown that the interface scattering phenomenon results in the conversion of a part of the incident energy into scattered energy which is manifested as random noise, generally delayed after the reflected energy. We have also demonstrated that this effect increases with increasing surface height and becomes significant when the surface height attains 1/5 to 1/4 of the wavelength of the incident wave for a given correlation length. This phase scattering results from the spatial convolution of the incident wavefield with the function describing the surface height distribution. Consequently, the interface scattering response is not the same in 2D situations as in 3D situations; it is stronger in 3D. We have shown that surface heights that are approximately three times higher in the 2D case than in the 3D case are required to produce an almost equivalent scattering dephasing effect of the wavefield in the 2D and 3D situations. Consequently, the restriction of studies to 2D or 2.5D configurations results in the use of models that are not geologically

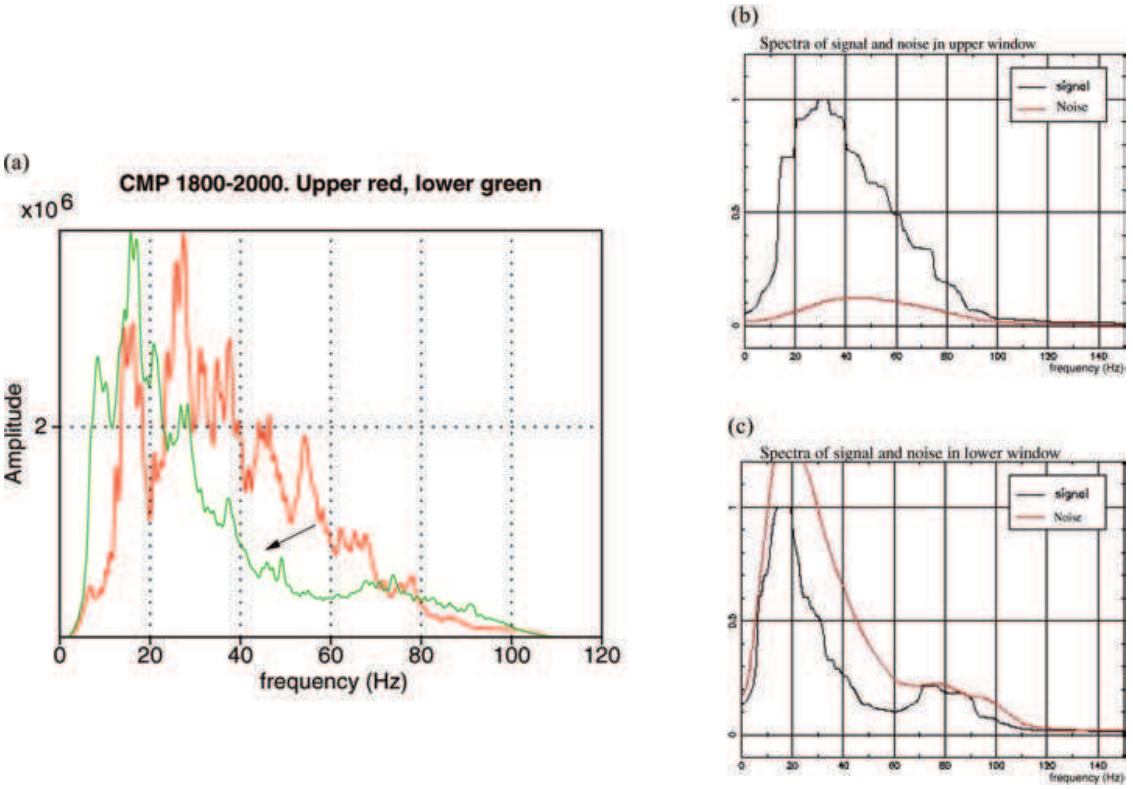

Figure 25 Spectral analysis of the real data: (a) spectra of the upper (red) and the lower (green) windows of CMP range 1800–2000 shown in Fig. 19; (b) spectra of the signal (black) and noise (red) in the upper window and (c) in the lower window. Note the total contamination of the signal by the noise in the lower window.

realistic and in an inappropriate modelling of the interface scattering phenomenon.

On real data, we have shown that seismic events resulting from interface scattering generally lose their high-frequency content due to multiple scattering, and hence contain more lower frequencies than reflected events. Finally, we have shown that the ratio of the backscattered energy to the reflected energy is high, which implies that an interface scattering effect will always be present on a stacked section in complex regions where rugose interfaces are present. Interface scattering of seismic wavefields occurs in nature in the presence of rugose interfaces with surface roughness heights of the order of the incident wavelength (order of metres). Its effect on the final seismic image is not always negligible in 3D as is often assumed, even when the surface heights are of the order of 1/10 of the incident wavefield. Consequently, this phenomenon should be critically considered when using phase information for inversion purposes, especially in geological settings where rugose surfaces are present. The interface scattering effect will be present on stacked sections but the dephasing will be proportional to the scattering surface height.

ACKNOWLEDGEMENTS

The research leading to this work was financed by Total Nigeria (EPNL), a subsidiary of the Total Group and the French Government. We are grateful to Dominique Rousset and Dimitri Komamtitsch of the University of Pau for fruitful discussions concerning the development of the 3D finite-difference code, especially on issues relating to absorbing boundaries. We thank Dr F. Martini and an anonymous reviewer for constructive criticism which helped in improving this paper.

REFERENCES

Axilrod H.D. and Ferguson J.F. 1990. SH-wave scattering from a sinusoidal grating: An evaluation of four discrete wave number

techniques. *Bulletin of the Seismological Society of America* **80,** 644–655.

Bouchon M., Campillo M. and Gaffet S. 1989. A boundary integral-equation discrete wavenumber representation method to study wave propagation in multilayered media having irregular interface. *Geophysics* **54,** 1134–1140.

Box G.E.P. and Muller M.E. 1958. A note on the generation of normal deviates. *Annals of Mathematical Statistics* **28,** 601–611.

de Coulon F. 1996. *Theorie et Traitement des Signaux*. Presses Polytechniques et Universitaires Romandes, Lausanne. ISBN 2040157786.

Favretto-Cristini N. and de Bazelaire E. 2003. PP-amplitude bias caused by interface scattering: Are diffracted waves guilty? *Geophysical Prospecting* **51,** 99–115.

Ishimaru A. 1978. *Wave Propagation and Scattering in Random Media*, Vol. 2. Academic Press. ISBN 0123747023.

Kawase H. 1988. Time domain response of a semi-circular canyon for incident SV, P and Rayleigh waves calculated by the discrete wavenumber boundary element method. *Bulletin of the Seismological Society of America* **78,** 1415–1437.

Kelly K.R., Ward R.W., Treitel S. and Alford R.M. 1976. Synthetic seismograms: A finite difference approach. *Geophysics* **41,** 2–27.

Martini F. and Bean C.J. 2002. Application of pre-stack wave equation datuming to remove interface scattering in sub-basalt imaging. *First Break* **20,** 395–403.

O'Doherty R.F. and Anstey N.A. 1971. Reflections on amplitudes. *Geophysical Prospecting* **19,** 430–458.

Ogilvy J.A. 1991. *Theory of Wave Scattering from Random Rough Surfaces*. Institute of Physics Publishing. ISBN 0750300639.

Schultz A.C. and Toksöz M.N. 1991. Seismic wave scattering from a randomly grooved interface: ultrasonic modeling and finite difference calculation. American Geophysical Union, Fall Meeting, Expanded Abstracts, S21A-03,8Z.

Schultz A.C. and Toksöz M.N. 1993. Enhanced backscattering of seismic waves from a highly irregular, random interface: SH case. *Geophysical Journal International* **144,** 91–102.

Virieux J. 1986. P-SV wave propagation in heterogeneous media: velocity stress finite difference method. *Geophysics* **51,** 889–901.

Warnick K.F. and Chew W.C. 2001. Numerical simulation methods for rough surface scattering. In: *Waves in Random Media II*. Institute of Physics Publishing. ISSN 09597174.

Geophysical Prospecting, 2003, **51**, 99–115

PP amplitude bias caused by interface scattering: are diffracted waves guilty?

Nathalie Favretto-Cristini[1]* and Eric de Bazelaire[1,2]

[1]*Centre National de la Recherche Scientifique, Laboratoire d'Imagerie Géophysique UMR 5831, Université de Pau et des Pays de l'Adour, BP 1155-64013 Pau Cedex, and* [2]*TotalFinaElf, CSTJF, Avenue Larribau, 64018 Pau Cedex, France*

Received November 2000, revision accepted November 2002

ABSTRACT

This paper is concerned with the problem of interpretation of anomalous seismic amplitudes, induced by the amplitude-scattering phenomenon. This phenomenon occurs in the vicinity of a crack distribution at the interface between elastic layers. The purpose of this work is to obtain a better understanding of the physics of this distinctive phenomenon, in order to interpret correctly the amplitudes of the reflected events. By analogy with studies in optics and in acoustics, we suggest that diffraction is widely involved in the amplitude-scattering phenomenon. Analytical evaluation of the amount of energy carried by the reflected and the diffracted waves shows that neglecting diffraction in numerical models leads to local underestimation of the amplitude of waves reflected at interfaces with gas-filled crack distribution.

INTRODUCTION

One of the open issues for the geophysical community is amplitude-preserved imaging. Many geophysicists are interested in a better understanding and exploitation of true amplitudes in depth migration and amplitude versus offset (AVO) studies, in order to improve the estimation of the physical properties of geological structures (Tygel 2001). They concentrate mainly on the computation of the correct weight functions that are required in the Kirchhoff migration formalism. We address the issue of true amplitudes of seismic events, in certain geological contexts, from another viewpoint. Does elastic modelling really take into account all the physical mechanisms arising in media? If not, what are the effects of neglecting some physical phenomena?

The paper addresses the problem of interpretation of anomalous seismic amplitudes. The problem under consideration is shown in Figs 1 and 2.

Figure 1(a) illustrates a real data set recorded in the Niger Delta, while Fig. 1(b) represents data obtained by conventional, pure reflection modelling. Details of the velocities V_P and V_S and the density are known from several wells where gas was detected. In Fig. 1(a), some distinctive events arise at certain stratigraphic surfaces (transgressive and downward-shift surfaces), and only on the left of the fault. These real events have anomalous amplitudes compared with the corresponding impedance contrasts recorded in wells. The observed amplitudes are higher than expected from the reflection coefficient (Fig. 1b).

Figure 2 illustrates a walkaway imaging with wave arrivals at polarization angles of 0° to 90° with respect to a vertical well. Only the energy associated with P-waves has been represented in this figure. P–S wave conversions and very weak amplitudes of the reflected P-waves are noted essentially in two red areas in Fig. 2. These areas are water-saturated zones. The anomalous amplitudes of the P-waves in these areas can be compared with those of the P-waves transmitted through the saturated zones, with traveltimes of around 3.0 and 3.5 s.

In short, the real amplitudes of the reflected events are stronger (respectively, weaker) than expected when gas (respectively, liquid) was detected at some erosional surfaces in wells. Neither conventional, pure reflection modelling nor any modelling based on homogenization of the interface properties (Baik and Thompson 1984; Angel and Achenbach 1985; Nihei, Myer and Cook 1995; Liu, Hudson and Pointer

*E-mail: nathalie.favretto@univ-pau.fr

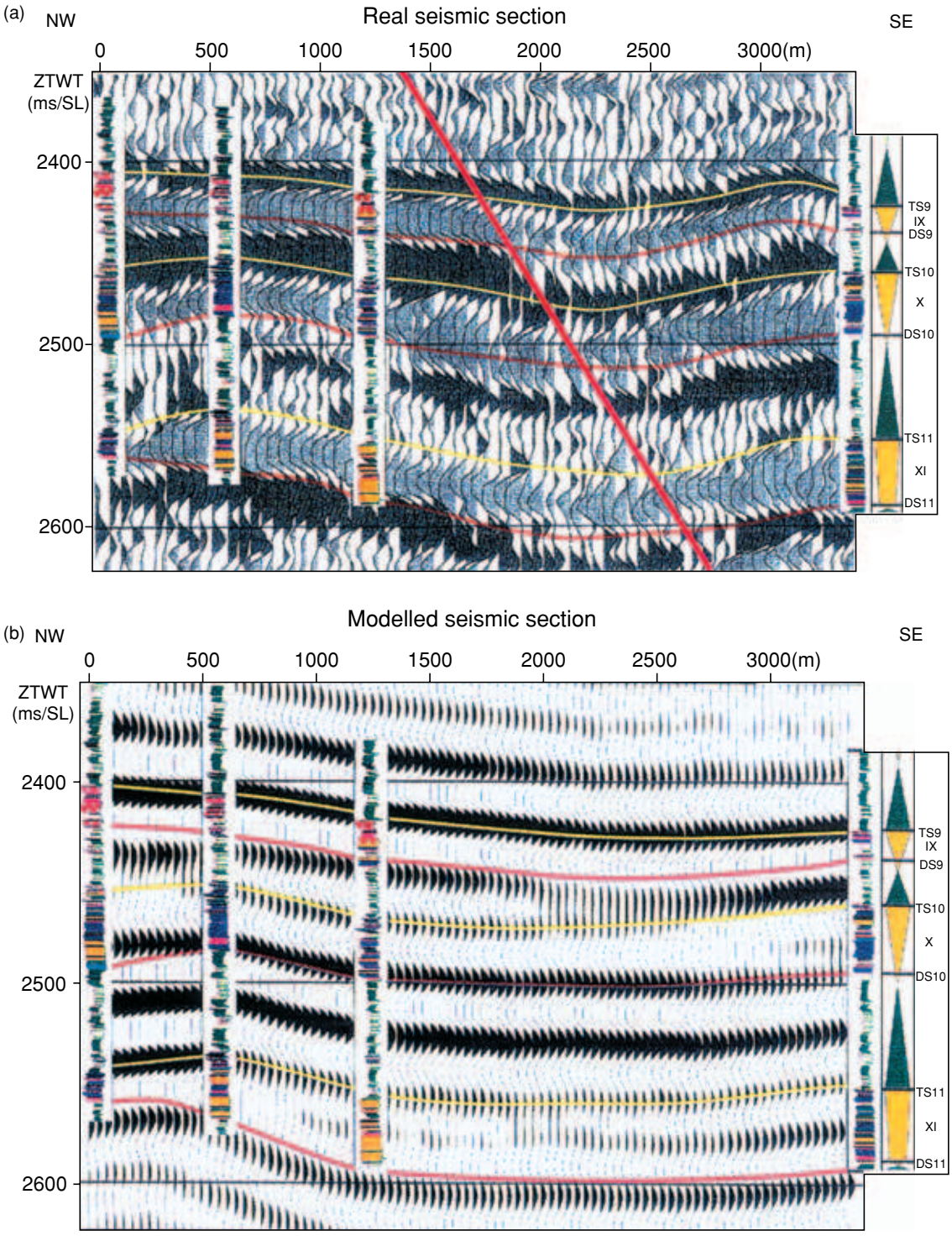

Figure 1 (a) An illustration of the 'gas amplitude-scattering' phenomenon on a real data set recorded in the Niger Delta. (b) Comparison with data obtained by pure reflection modelling. The log data are interpreted in terms of facies. The straight line represents a fault. (After Schulbaum 1996.)

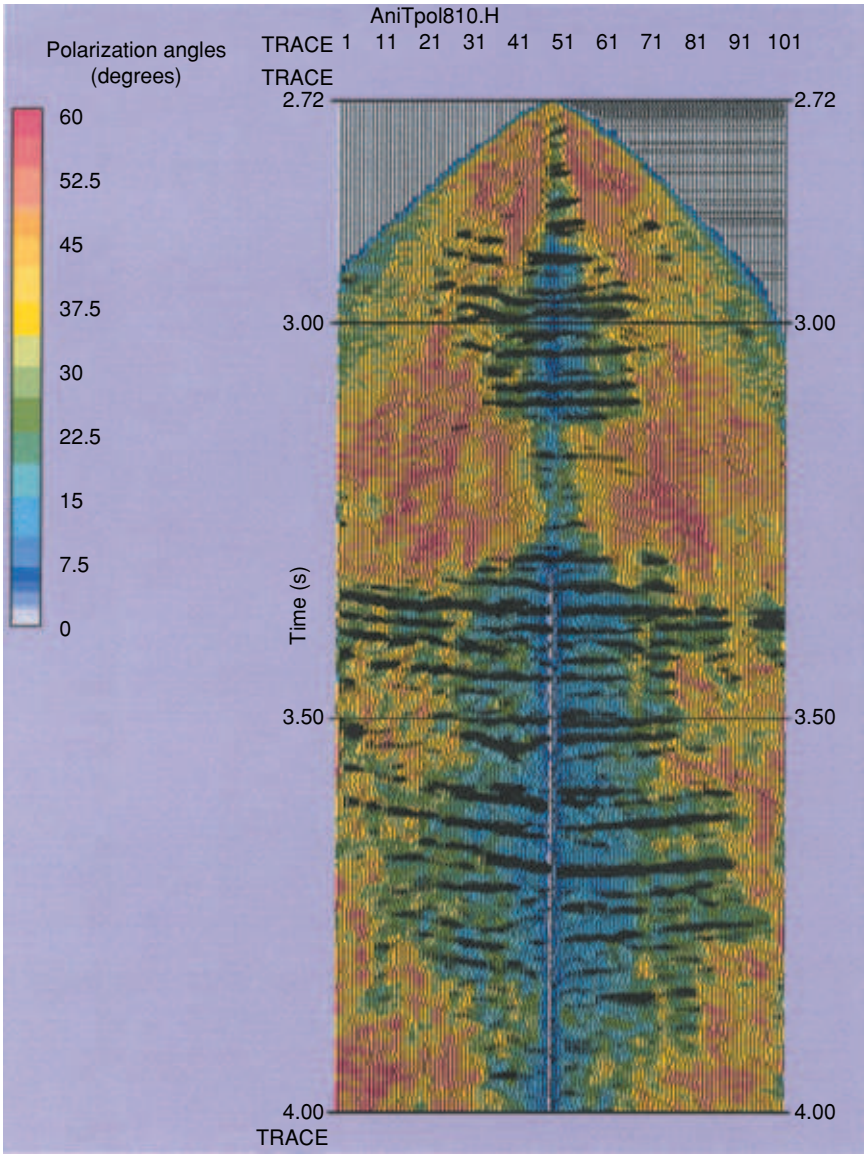

Figure 2 An illustration of the 'liquid amplitude-scattering' phenomenon on a walkaway imaging and polarization. Only the P-wave energy is represented. Blue areas represent P–P wave propagation, while red ones represent P–S wave conversions. (After J. Blanco 2000, pers. comm.)

2000; Myer 2000) could simulate these anomalous amplitudes. A phenomenon, different from pure reflection, was then neglected in such classical numerical models. We argue that the amplitude-scattering (AS) phenomenon is widely involved in such anomalous amplitudes. The aim of the paper is to show that neglecting such a distinctive phenomenon may lead to erroneous interpretation of real data in some cases, in particular when locating reflectors and inverting amplitudes.

The paper begins with a discussion of the AS phenomenon. What is it? Why can it not be modelled by classical numerical schemes? What are the physical mechanisms responsible for it? The second section briefly describes a way of modelling the AS phenomenon. Some numerical illustrations of the influence of the AS phenomenon on reflected events are also presented.

1 THE AMPLITUDE-SCATTERING (AS) PHENOMENON

In Fig. 1(a), events with anomalous amplitudes occur at certain stratigraphic surfaces. These surfaces result essentially from tectonics and/or erosion processes. These erosional surfaces are generally characterized by a spatial distribution of irregular geological contacts between layers. The cracks thus created at interfaces are filled with gas, liquid or solid. They

affect wave propagation, in particular elastic wave reflection, by creating interface scattering. At this point, we have to explain the meaning of the term 'interface scattering'. We consider interface scattering as scattering induced by a spatial distribution of irregular contacts between layers. Usually, both the phase and the amplitude of the incident wave may be altered by interface scattering on passing through the interface. In the special case when the amplitude but not the phase of the incident wavefront is altered, we speak of amplitude scattering, by analogy with optics (see Born and Wolf 1999, p. 447). If the phase but not the amplitude is altered, we speak of phase scattering. A well-known phase scatterer in land seismics is the weathered zone. More generally, interface roughnesses are phase scatterers whose effect on reflected signals has been studied extensively (Ogilvy 1991). Here, we are interested in the amplitude scattering induced by lateral heterogeneities at interfaces. We want to analyse the effects of a crack distribution at an interface on the amplitude of reflected signals. By analogy with studies in optics, in acoustics and in non-destructive testing (NDT) of materials, the spatial distribution of gas-, liquid- or solid-filled cracks may be viewed as diffraction gratings (Born and Wolf 1999). We consider that amplitude scattering results from the coherent or incoherent interference of the diffractions caused by each crack. Figures 1 and 2 clearly show that the effect of amplitude scattering on the amplitudes of reflected signals depends on the crack filling. We attempt to explain the physics behind these observations.

1.1 May interface waves (IW) be guilty?

The distribution of the welded contact areas and cracks between layers of a stratified earth can act as 'a comb transducer' (Viktorov 1967; Biryukov *et al.* 1995). The comb transducer is commonly used for excitation and detection of surface waves (Fig. 3). An incident P-wave, generated by an ultrasonic transducer, strikes the interface between the solid comb and the solid material. The P-wave is transformed into a surface wave (SW) at the end of the comb. The SW propagates at the free solid surface, and it is then coherently recombined by another comb into a P-wave. This P-wave is detected by another ultrasonic transducer. The incident wavelength determines the size of the active crack distribution.

We believe that such a physical mechanism can occur in the stratified earth, provided there is interaction between the incident wavelength and the spatial wavelength of the crack distribution. In future work, we will analyse in more detail the interference between the P-wave, resulting from the recombination of the SW by the crack distribution, and the bulk P-waves reflected at the interface.

1.2 May diffracted waves (DW) be guilty?

In order to understand better and to quantify the AS effects on seismic measurements, we consider a simple 2D propagation model, where the diffraction phenomena are clearly visible. Figure 4 depicts the 2D situation of two homogeneous elastic, isotropic half-spaces separated by a horizontal interface along which a periodic distribution of cracks exists. We refer to the lower medium as solid B and to the upper medium as solid A. We let K and Λ denote the spatial wavenumber and period of the crack distribution, with $K = 2\pi/\Lambda$. Figure 4 also indicates the distance between cracks, denoted by 2w. The quantity, $\Delta = K\mathrm{w} = \pi(2\mathrm{w}/\Lambda)$, will be seen in the later derivations to be a useful parameter of the configuration.

We next consider an incident plane P-wave, characterized by wavelength λ_{inc} and time frequency ω, that propagates in solid B and strikes the interface below the incidence angle θ_{inc} with respect to the surface normal. The corresponding unit propagation vector is denoted $\mathbf{u}_{\mathrm{inc}} = (\sin\theta_{\mathrm{inc}}, \cos\theta_{\mathrm{inc}})$.

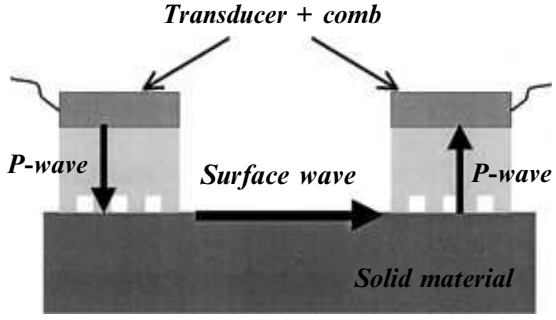

Figure 3 Excitation and detection of surface waves using comb transducers in acoustics and in NDT.

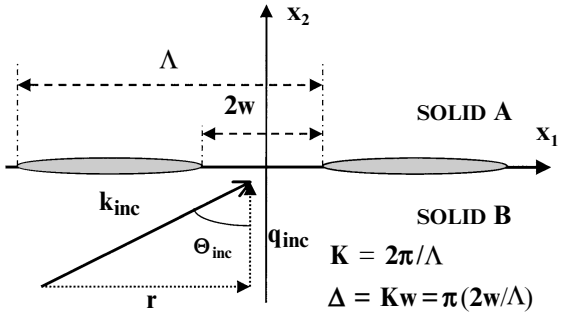

Figure 4 Periodic crack distribution at the boundary between Plexiglass® and Duraluminum® solids.

Finally, the wave vector of the incident wave is denoted $\mathbf{k}_{inc} = \boldsymbol{\omega}/\mathbf{s}_{inc} = (p_{inc}, q_{inc})$. Note that $\mathbf{s}_{inc} = (1/V_P)\mathbf{u}_{inc}$ is the slowness vector of the incident wave, where V_P is the P-wave velocity of the lower half-space (solid B). Finally, we assume that the incident horizontal wavenumber p_{inc} satisfies the condition $p_{inc} = r$, with $0 < r < K$.

After striking the cracked interface, the incident plane wave excites many diffracted waves that propagate in different directions. Diffractions with diffraction order $n = 0$ correspond to specular P–P and P–S reflections and transmissions. Diffractions with diffraction order $n \neq 0$ correspond to non-specular reflections and transmissions, whose existence is due only to the presence of the crack distribution at the interface (see e.g. Waterman 1975; Danicki 1999). Diffraction is simply a generalization of reflection/transmission phenomena. As stated above, our aim is to understand better and to quantify the impact of the excited non-specular reflected and transmitted waves, compared with their specular counterparts, which are the only ones considered in seismic interpretations.

In the next section, we briefly indicate the wave propagation description from which the energy of the relevant reflected, transmitted and diffracted waves can be computed. However, in order to design the modelling parameters that are best suited to our needs, it is instructive to consider what is to be expected.

When $\Lambda \geq \lambda_{inc}$, where λ_{inc} denotes the incident wavelength and Λ denotes the spatial wavelength of the crack distribution, many diffracted waves in both media are propagative. For that reason, we consider the case $\Lambda = \lambda_{inc}$ as one of our modelling situations. The case $\Lambda \ll \lambda_{inc}$ is the usual assumption in most theories and in that situation, diffracted waves in both media are usually evanescent and, consequently, are neglected in models. However, when the properties of media in contact are very different, and under certain conditions on the ratio Λ/λ_{inc}, diffracted waves can be propagative. To check whether this is actually the case, we consider, as our second modelling example, the condition $\Lambda = (1/3)\lambda_{inc}$. The results can be illustrated graphically by means of wavevector diagrams, i.e. slowness diagrams drawn for the frequency $f = V_{Pinc}/\lambda_{inc}$ in Fig. 5. In such diagrams, the direction of wave propagation and the relationships between the angles of incidence, reflection and refraction are straightforward (see Crandall 1970; Fokkema 1980; Helbig 1994, p. 372).

The elastic parameters of the two half-spaces in Fig. 4 were chosen to be those of Plexiglass® (lower medium) and Duraluminum® (upper medium). The reason for the above choice is that these media will be used in future experiments under actual laboratory conditions. It should be noted that the properties of Plexiglass® and Duraluminum® are quite similar to those of chalk and granite.

Wavevector diagrams of the two examples under consideration, in which only propagative waves are represented, are shown in Fig. 5. In Fig. 5(a), the case $\Lambda = \lambda_{inc}$ is represented, while Fig. 5(b) depicts the corresponding diagram when $\Lambda = (1/3)\lambda_{inc}$. Note in both cases the four slowness circles

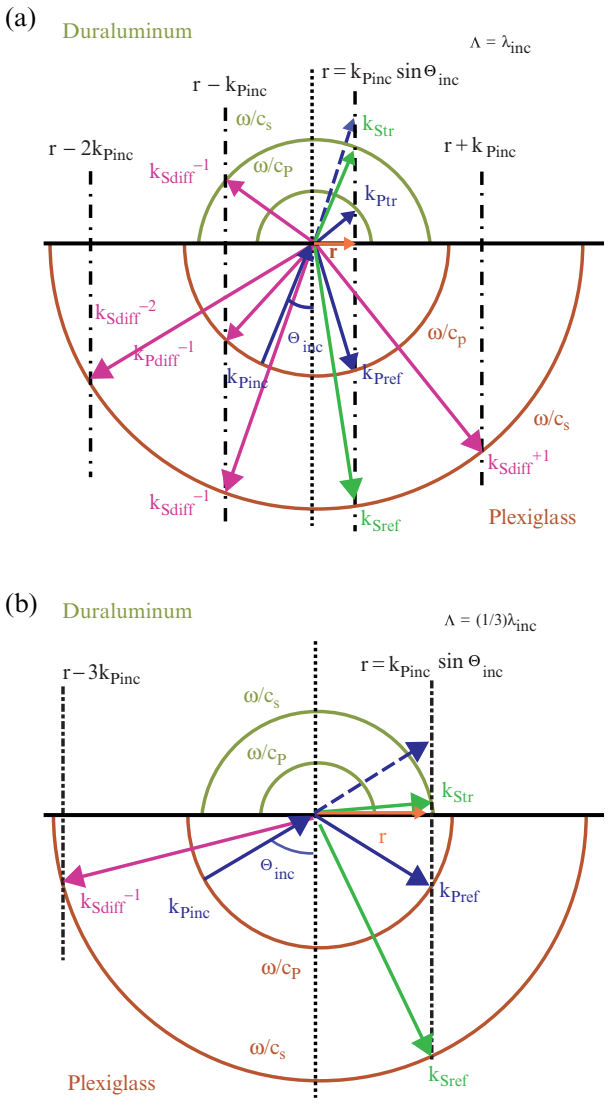

Figure 5 Wavevector diagrams illustrating diffraction (of order 0 and −1) of a P-wave incident on the Plexiglass®/Duraluminum® interface, for the cases (a) $\Lambda = \lambda_{inc}$ and (b) $\Lambda = (1/3)\lambda_{inc}$, Λ being the spatial wavelength of the gap distribution and λ_{inc} the incident P-wavelength. $\mathbf{k}$ is the wave vector. Only propagative waves are represented. The characteristics of the media are assumed to be: $V_P = 2670$ m/s and $V_S = 1120$ m/s (Plexiglass®), $V_P = 6440$ m/s and $V_S = 3170$ m/s (Duraluminum®).

for the given frequency f with radius $\omega/V_{P,S}$, where $V_{P,S}$ is the P- or S-wave velocity and $\omega = f/2\pi$ is the angular frequency. Following Brillouin and Parodi (1956), the wave vectors, $\mathbf{k}_{Pdiff}$ and $\mathbf{k}_{Sdiff}$, of the diffracted P- and S-waves are fixed by the requirement that their horizontal components, p_{Pdiff} and p_{Sdiff}, satisfy the condition $p_{Pdiff} = p_{Sdiff} = r + nK$, where n is an integer that characterizes the so-called diffraction order. The value $n = 0$ corresponds to the specular reflected and transmitted waves. Note that for $\Lambda < (1/3)\lambda_{inc}$, in the Plexiglass®/Duraluminum® configuration, only evanescent waves propagate at the interface, as the modulus of the horizontal components p_{Pdiff} and p_{Sdiff} of the wave vectors is such that $p_{P,Sdiff} = r \pm nK > k_{P,S}$.

1.3 The physical mechanisms involved in the AS phenomenon

As shown above, diffracted waves can arise from the crack distribution at the interface, provided there is interaction between the incident wavelength and the spatial wavelength of the crack distribution. In accordance with the energy conservation law, the energy carried by diffracted waves is not distributed to the other waves, in particular to the specular reflected P-waves. Neglecting diffraction phenomena, which is the case of interest here, leads to an incorrect energy balance, giving rise to an inaccurate estimation of the amplitudes of seismic reflections. As a consequence, the amplitudes of the specular reflected P-waves are generally overestimated in those numerical models that do not take into account the crack distribution at the interfaces. This is also true for the methods based on homogenization of the interface properties (Baik and Thompson 1984).

However, this result must be elaborated further, so as to take into account the situation in which the crack filling is either liquid or gas. The explanation is that the reflection coefficients in numerical models are calculated using only the impedances of the media in contact, without taking into account the crack distribution that produces diffraction effects. We consider such reflection coefficients as our reference reflection coefficients. The real reflection coefficient, 'measured' *in situ*, involves the effect of cracks. The real reflection coefficient is essentially a function of the impedance contrast between the crack filling and the first medium illuminated by the wave. The implicit condition is that the cracks are saturated. Consider first the case of water-saturated media in contact. The cracks at the interface are generally water-filled. The impedances of media and cracks are then quite similar. Replacing only the impedance of the medium into which waves are transmitted by the impedance of the crack filling does not modify the real reflection coefficient. Consequently, the amplitudes of the specular reflected P-waves are still overestimated in numerical models. Consider now the case of media in contact with gas-filled cracks. The impedances of media and cracks are very different, and the real reflection coefficient is greatly modified by this strong impedance contrast. The energy loss of the specular reflected P-waves, due to the presence of the diffracted waves, is then much weaker than the strong increase in the reflection coefficient. In this case, the amplitudes of the specular reflected P-waves may be underestimated in numerical models, as is shown in Fig. 1.

2 MODELLING OF THE AS PHENOMENON

It is clear that one of the key problems encountered in the modelling of the AS phenomenon is the difficulty in considering the crack distribution at interfaces in numerical schemes. Another difficulty is that of describing its effect on the wave propagation in the vicinity of the interface between layers. Previously, we suggested that the diffracted waves arising from the crack distribution were widely involved in the AS phenomenon. How can we model the diffraction effects? How can we quantify the diffracted and the specular reflected energies? How can we model the impact that the AS phenomenon has on seismic images? We propose to answer these questions by modelling the AS phenomenon in the simple 2D situation described in the previous section. As the present paper is concerned mainly with the interpretation of the modelling results and the relationship they have with conventional seismic interpretation, the analytical formulation of the wave-propagation problem will be presented briefly in the Appendix. Here, we give only the most relevant equations that are necessary for the calculations.

2.1 Numerical results

We are interested in the partitioning of the incident energy among the specular and non-specular reflected and transmitted waves in the solids A and B (see Fig. 4). The energy balance can be evaluated by determining the elastic Poynting vector, i.e. the time-averaged energy flux Π in the direction of $\boldsymbol{x}$, for each diffraction order n (Auld 1990):

$$\left\langle \mathbf{\Pi}_n^{A,B} \cdot \mathbf{x} \right\rangle = -\frac{1}{2} \Re\left(\mathbf{T}_n^{A,B^*} \cdot \left(j\omega \mathbf{U}_n^{A,B} \right) \cdot \mathbf{x} \right), \quad (1)$$

where the displacement vector $\mathbf{U}_n^{A,B}$ and the traction force vector $\mathbf{T}_n^{A,B}$ characterize the nth diffracted wavefield at the

interface (see Appendix), and the asterisk denotes complex-conjugate quantities. Usually, only the component Π_2 of Π along the $\mathbf{x_2}$-axis is considered in theoretical studies, as Π_2 is equal to zero for inhomogeneous waves that carry energy along the interfaces. However, rigorous characterization of the near-field wave propagation requires the evaluation of both components, Π_1 and Π_2, of the elastic Poynting vector. Here, we calculate only the component Π_2 associated with the specular ($n=0$) and non-specular ($n=-1$) reflected and transmitted P- and S-waves in each medium. With the help of (1) and (A4) (see Appendix), we find for $n=0$ (Danicki 1999):

$$\Pi_{\mathrm{P,S}}^{\mathrm{A,B}} = \frac{\rho_{\mathrm{A,B}}\omega^3}{2}\,\Re\left(\left|C_{\mathrm{P,S}}^{\mathrm{A,B}}\right|^2 q_{\mathrm{P,S}}^{\mathrm{A,B}}\right), \tag{2}$$

where the variables $C_{\mathrm{P,S}}^{\mathrm{A,B}}$ are expressed as a function of the traction force vector components

$$\begin{bmatrix} C_{\mathrm{P}}^{\mathrm{A}} \\ C_{\mathrm{S}}^{\mathrm{A}} \end{bmatrix} = \frac{\mathrm{j}}{\mu_{\mathrm{A}} D_{\mathrm{A}}} \begin{bmatrix} 2p_n(q_{\mathrm{s}}^{\mathrm{A}})_n & k_{\mathrm{s}}^{\mathrm{A}^2} - 2p_n^2 \\ -(k_{\mathrm{s}}^{\mathrm{A}^2} - 2p_n^2) & 2p_n(q_{\mathrm{P}}^{\mathrm{A}})_n \end{bmatrix} \begin{bmatrix} (T_n^{\mathrm{A}})_1 \\ (T_n^{\mathrm{A}})_2 \end{bmatrix}$$
$$\begin{bmatrix} C_{\mathrm{P}}^{\mathrm{B}} \\ C_{\mathrm{S}}^{\mathrm{B}} \end{bmatrix} = \frac{\mathrm{j}}{\mu_{\mathrm{B}} D_{\mathrm{B}}} \begin{bmatrix} 2p_n(q_{\mathrm{s}}^{\mathrm{B}})_n & -(k_{\mathrm{s}}^{\mathrm{B}^2} - 2p_n^2) \\ k_{\mathrm{s}}^{\mathrm{B}^2} - 2p_n^2 & 2p_n(q_{\mathrm{P}}^{\mathrm{B}})_n \end{bmatrix} \begin{bmatrix} (T_n^{\mathrm{B}})_1 \\ (T_n^{\mathrm{B}})_2 \end{bmatrix}. \tag{3}$$

The energy conservation law implies that

$$\sum_n \left\langle \mathbf{\Pi}_n^{\mathrm{A,B}} \cdot \mathbf{x_2} \right\rangle = \left\langle \mathbf{\Pi}_{\mathrm{inc}} \cdot \mathbf{x_2} \right\rangle, \tag{4}$$

that is, for $n=0$:

$$\left\langle \mathbf{\Pi}_{\mathrm{inc}} \cdot \mathbf{x_2} \right\rangle = \Pi_{\mathrm{P}}^{\mathrm{A}} + \Pi_{\mathrm{S}}^{\mathrm{A}} + \Pi_{\mathrm{P}}^{\mathrm{B}} + \Pi_{\mathrm{S}}^{\mathrm{B}}, \tag{5}$$

and for $n \neq 0$ (here, $n=-1$)

$$\left\langle \mathbf{\Pi}_{\mathrm{inc}} \cdot \mathbf{x_2} \right\rangle = \left(\Pi_{\mathrm{P}}^{\mathrm{A}} + \Pi_{\mathrm{S}}^{\mathrm{A}} + \Pi_{\mathrm{P}}^{\mathrm{B}} + \Pi_{\mathrm{S}}^{\mathrm{B}}\right) + \left(\Pi_{\mathrm{Pdiff}}^{\mathrm{A}} + \Pi_{\mathrm{Sdiff}}^{\mathrm{A}} + \Pi_{\mathrm{Pdiff}}^{\mathrm{B}} + \Pi_{\mathrm{Sdiff}}^{\mathrm{B}}\right). \tag{6}$$

Π_{inc} is the time-averaged energy flux associated with the incident wave.

Figures 6, 7, 8 and 9 illustrate the changes in the calculated ratio of the energy scattered by the P- and S-waves in the Plexiglass® and Duraluminum® solids to the incident energy, i.e. $\langle \mathbf{\Pi}_{\mathrm{P,S}}^{\mathrm{A,B}} \cdot \mathbf{x_2} \rangle / \langle \mathbf{\Pi}_{\mathrm{inc}} \cdot \mathbf{x_2} \rangle$ for $n=0$ and $\langle \mathbf{\Pi}_{\mathrm{P,Sdiff}}^{\mathrm{A,B}} \cdot \mathbf{x_2} \rangle / \langle \mathbf{\Pi}_{\mathrm{inc}} \cdot \mathbf{x_2} \rangle$ for $n=-1$, as a function of the incidence angle Θ_{inc}. The influence of the ratio $2\mathrm{w}/\Lambda$ (see Fig. 4) on the energy scattered is also shown. The ratio $2\mathrm{w}/\Lambda = 0.01$ represents the case in which the interface is almost completely disbonded, and the ratio $2\mathrm{w}/\Lambda = 0.99$ represents the case of a quasi-perfectly welded interface, hereafter referred to as the reference case. The incident P-wavelength λ_{inc} in Plexiglass® is greater than the spatial wavelength Λ of the crack distribution at the interface ($\Lambda = (1/3)\lambda_{\mathrm{inc}}$).

In Figs 6, 7, 8 and 9, we can observe the different critical angles corresponding to the refraction, along the interface, of the P- and S-waves in Duraluminum®:

$\Theta_{\mathrm{PDural}} = \arcsin(V_{\mathrm{PPlexi}}/V_{\mathrm{PDural}}) = 25^\circ$,
$\Theta_{\mathrm{SDural}} = \arcsin(V_{\mathrm{PPlexi}}/V_{\mathrm{SDural}}) = 57^\circ$.

For $\Lambda = (1/3)\lambda_{\mathrm{inc}}$, the diffracted S-wave of order -1 is propagative for the incident angles $\Theta_{\mathrm{inc}} > 38^\circ$. For $\Theta_{\mathrm{inc}} < 38^\circ$, the sum of the reflected and transmitted energy must be unity. This is not perfectly true in Figs 6(a), 7(a), 8(a) and 9(a), because the number of space harmonics retained in the field expansion (see Appendix), that determines the accuracy of the amplitude of the individual diffracted orders, was intentionally taken small, for simplicity of calculation. Above 38°, the diffracted energy must be taken into account in the energy balance. In Fig. 6(a), a Rayleigh wave that propagates at the free surface of the Duraluminum® material is generated at the incident angle $\Theta_{\mathrm{inc}} = 64^\circ$. This result appears consistent with the assumption of Section 1.1, that the crack distribution at the interface acts as a 'comb transducer'. The most important and new result, illustrated in Figs 6, 7 and 8, is the evaluation of the amount of energy associated with the diffracted wave. For the case of the quasi-disbonded interface, i.e. for $2\mathrm{w}/\Lambda = 0.01$ and for $2\mathrm{w}/\Lambda = 0.5$, the amount of energy is on average about 15% (Figs 6b and 7b). This amount decreases with increasing ratios, $2\mathrm{w}/\Lambda = 0.75$ and $2\mathrm{w}/\Lambda = 0.99$. For the reference case, the amount of energy is equal to zero, as no diffracted wave is generated (Fig. 9b). These results confirm the statement that neglecting the crack distribution at the interface, and the diffracted waves arising from this diffraction grating, leads to overestimation of the amplitude of the reflected events. In the case of the quasi-disbonded interface, i.e. for $2\mathrm{w}/\Lambda = 0.01$, the amplitude of the reflected P-wave is higher than its counterpart in the reference case, as the incident P-wave is fully reflected by the interface (Fig. 6a).

It should be noted that the curve describing the variation of the reflected P-wave energy for the incident angle $\Theta_{\mathrm{inc}} < 25^\circ$ is similar to that obtained in classical amplitude versus angle (AVA) images. For a weak impedance contrast between materials, the critical angle is generally about 70°.

2.2 Modelling of seismic images

The purpose of this section is to illustrate the consequences of the previous theoretical results on seismic images.

Figures 10, 11, 12 and 13 show the modelling of the reflected P-wave AVO in the Plexiglass®/Duraluminum® configuration. Figures 10(a), 11(a), 12(a) and 13(a) represent the

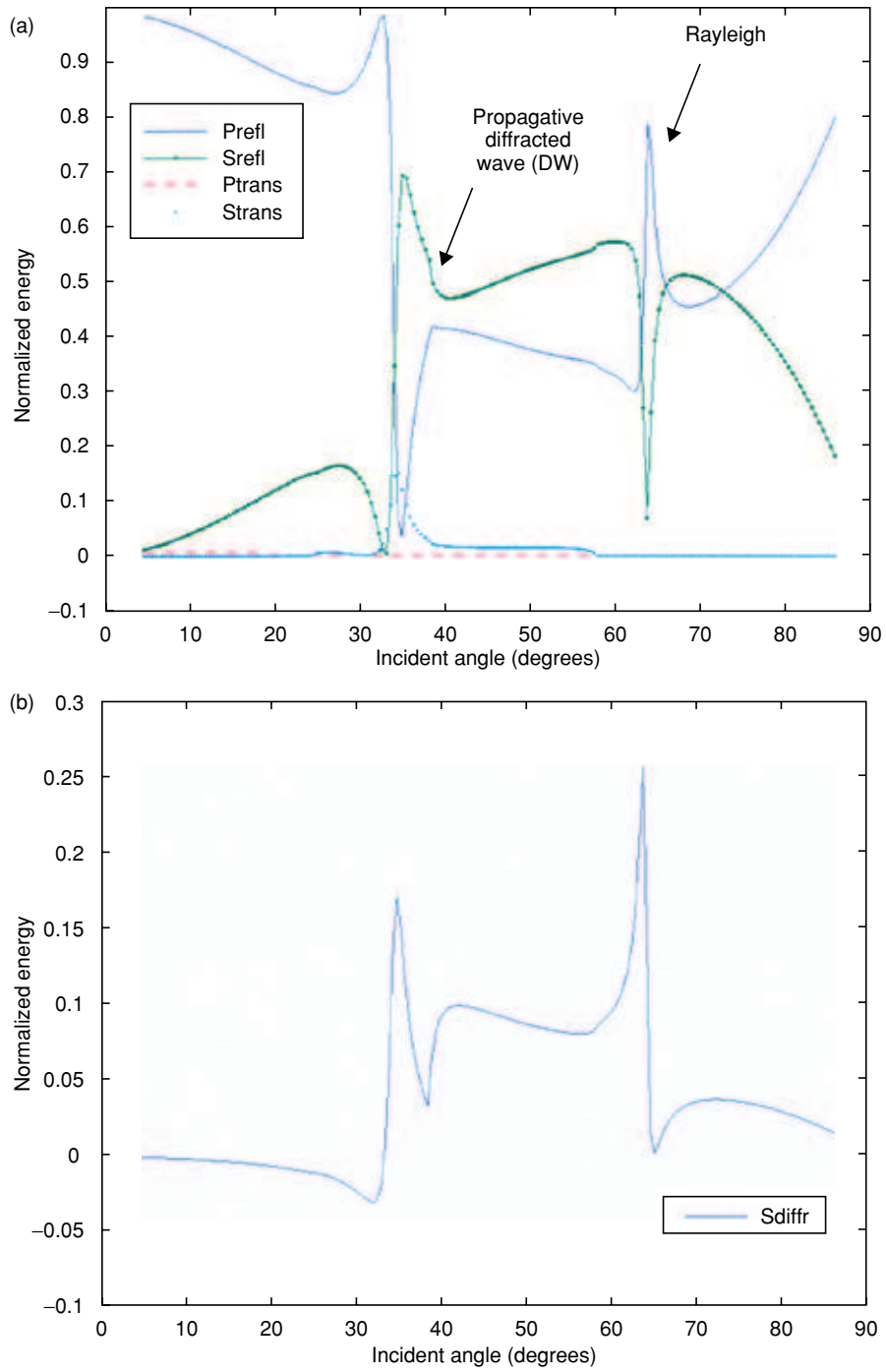

Figure 6 Energy of (a) the reflected and transmitted P- and S-waves, and (b) the diffracted S-wave as a function of the incident angle Θ_{inc}, in the Plexiglass®/Duraluminum® configuration. The characteristics of the gap distribution at the interface are: $\Lambda = (1/3)\lambda_{inc}$ and $2w/\Lambda = 0.01$.

AVO in 3D and Figs 10(b), 11(b), 12(b) and 13(b) represent the synthetic seismograms. The amplitude is calculated, for different crack distribution properties, from the theoretical analysis described in the previous section, by considering the CMP gather in a horizontal layer of thickness 1000 m and with P-wave velocity of 2670 m/s. The source signal (second-order Ricker) is modulated in AVO by the square root of the P-wave energy calculated analytically. The CMP gather is

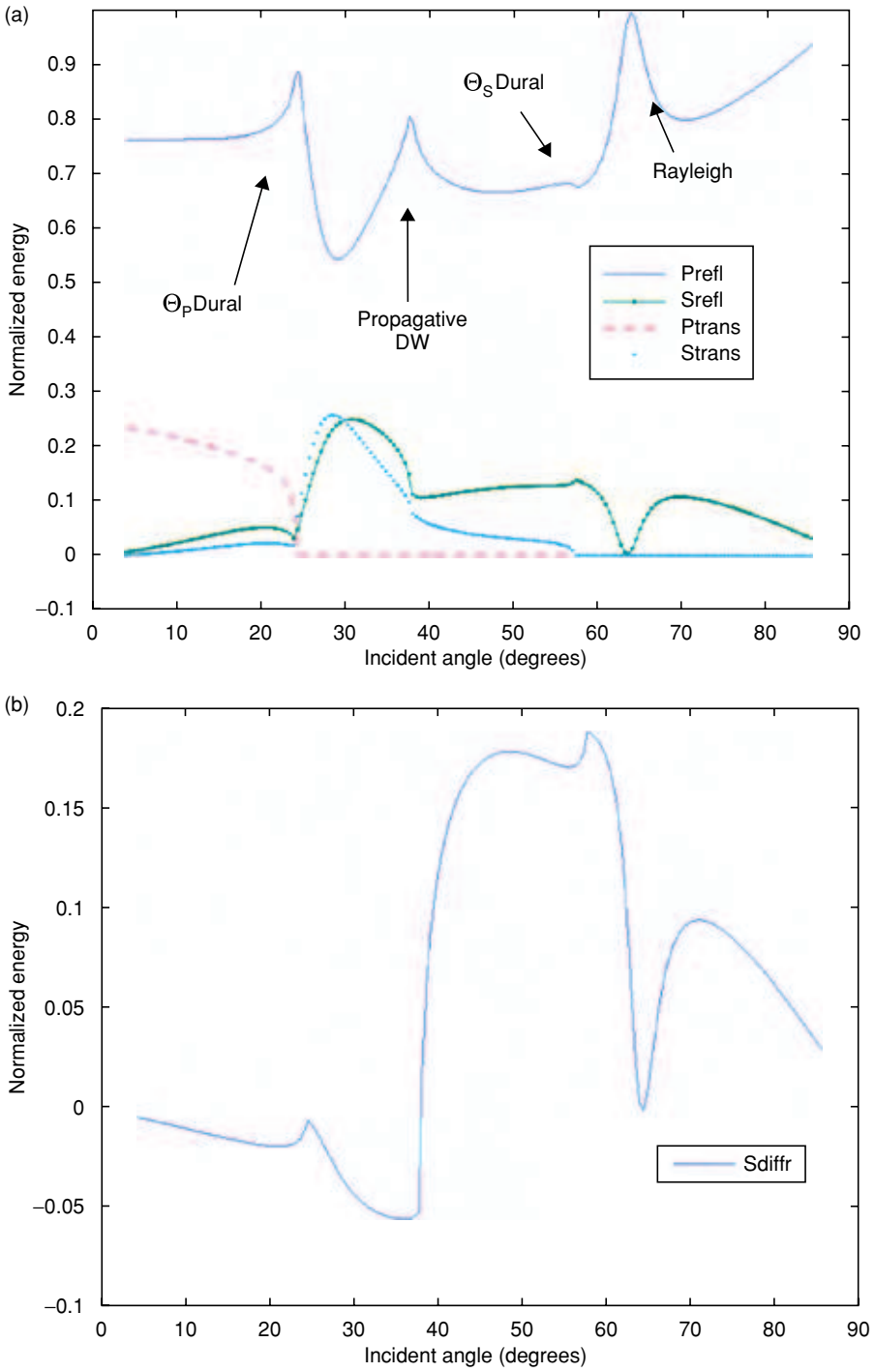

Figure 7 As Fig. 6 with the characteristic $2w/\Lambda = 0.5$.

assumed to have been processed with dynamic correction and geometrical amplitude compensation. As previously, Fig. 10 corresponds to the almost completely disbonded interface and Fig. 13 to the welded interface (reference image).

First, compare the traces corresponding to a small aperture (i.e. $0 < \Theta_{inc} < 38°$). The reflected P-wave stacking energy increases with decreasing ratio $2w/\Lambda$, which agrees with the usual theoretical considerations. For these small offsets, a theory

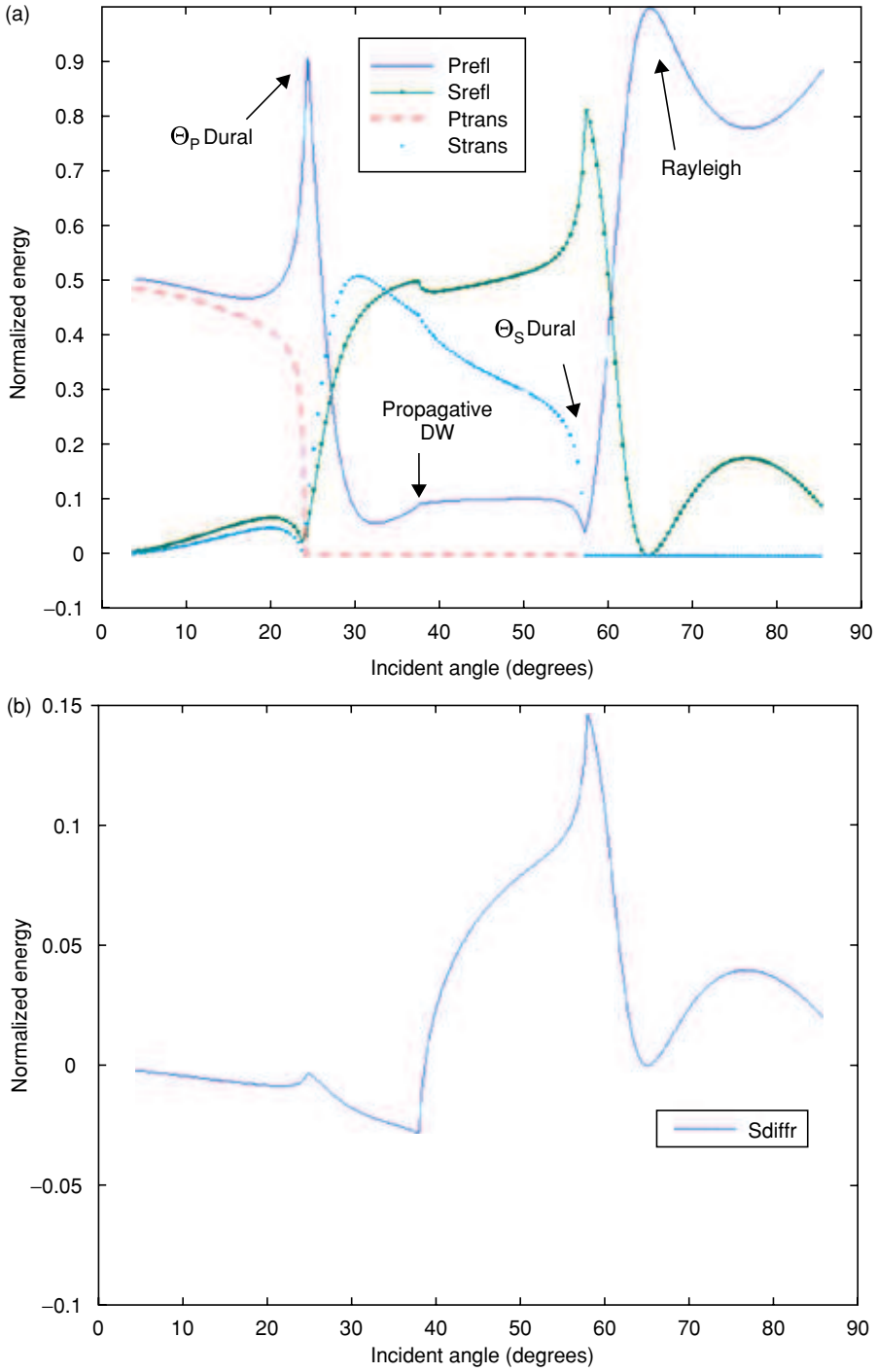

Figure 8 As Fig. 6 with the characteristic $2w/\Lambda = 0.75$.

based on homogenization of the interface properties can describe very well the behaviour of the real physical mechanisms, as no diffraction phenomena are involved. By contrast, for a greater aperture (say, $0 < \Theta_{inc} < 60^\circ$), diffraction phenomena are involved in the far traces ($38^\circ < \Theta_{inc} < 60^\circ$), and homogenization of the interface properties can no longer be applied. In this case, classical numerical models that do not take diffraction phenomena into account underestimate the amplitude of

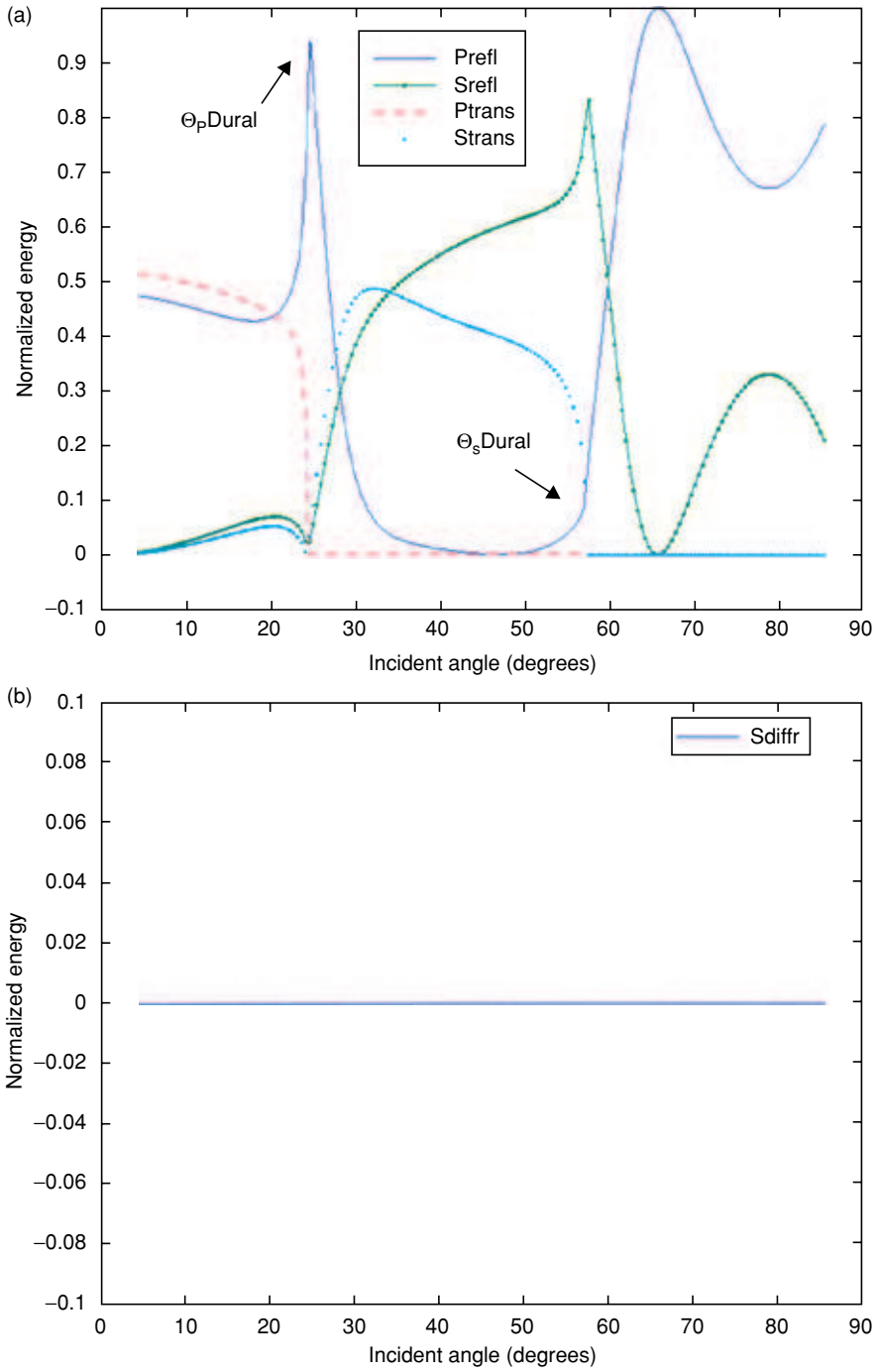

Figure 9 As Fig. 6 with the characteristic $2w/\Lambda = 0.99$.

the reflected P-wave, as is suggested by comparison of the traces in Figs 10(b) and 13(b). These results appear consistent with the discussion in Section 1.3 and with Fig. 1. Finally, let us examine the amount of the reflected P-wave energy in the far traces ($38^\circ < \Theta_{inc} < 60^\circ$) in Figs 10(b)–13(b). The amount of energy initially increases with decreasing ratio $2w/\Lambda$, reaching a maximum value for $2w/\Lambda = 0.5$; it then decreases with decreasing ratio $2w/\Lambda$. At the moment we do not have a full explanation for these striking characteristics, also observed in Figs 6(a)–9(a). They will be analysed in future work.

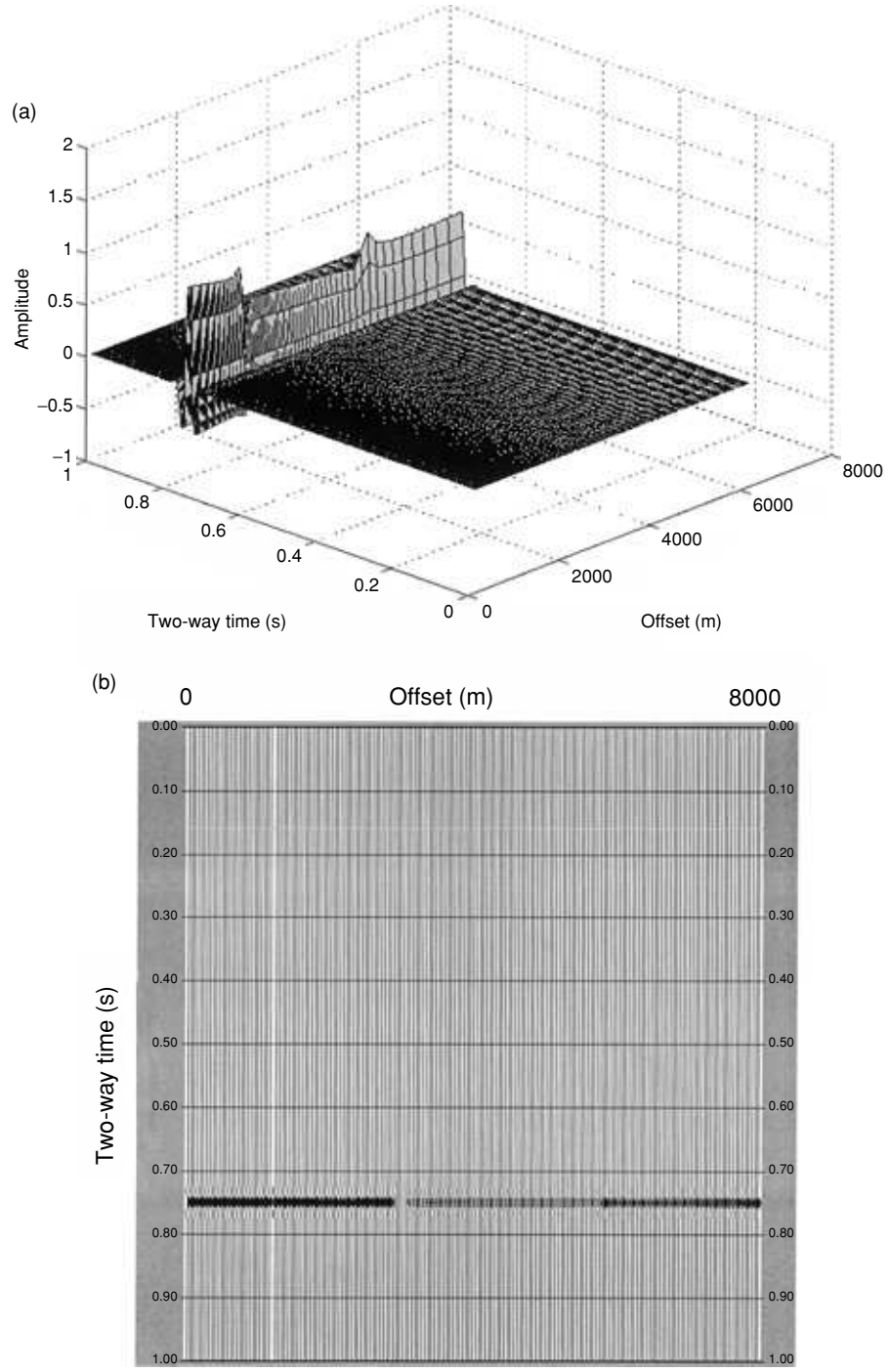

Figure 10 Modelling of the reflected P-wave AVO in the Plexiglass®/Duraluminum® configuration. (a) AVO in 3D; (b) synthetic seismograms. The characteristics of the gap distribution at the interface are: $\Lambda = (1/3)\lambda_{inc}$ and $2w/\Lambda = 0.01$.

CONCLUSION

This study was concerned with the problem of interpretation of anomalous seismic amplitudes induced by the amplitude-scattering (AS) phenomenon. This phenomenon, which alters the amplitude of the incident wavefronts, results from coherent and incoherent interference of diffractions caused by each element of a crack distribution at the interface between elastic layers.

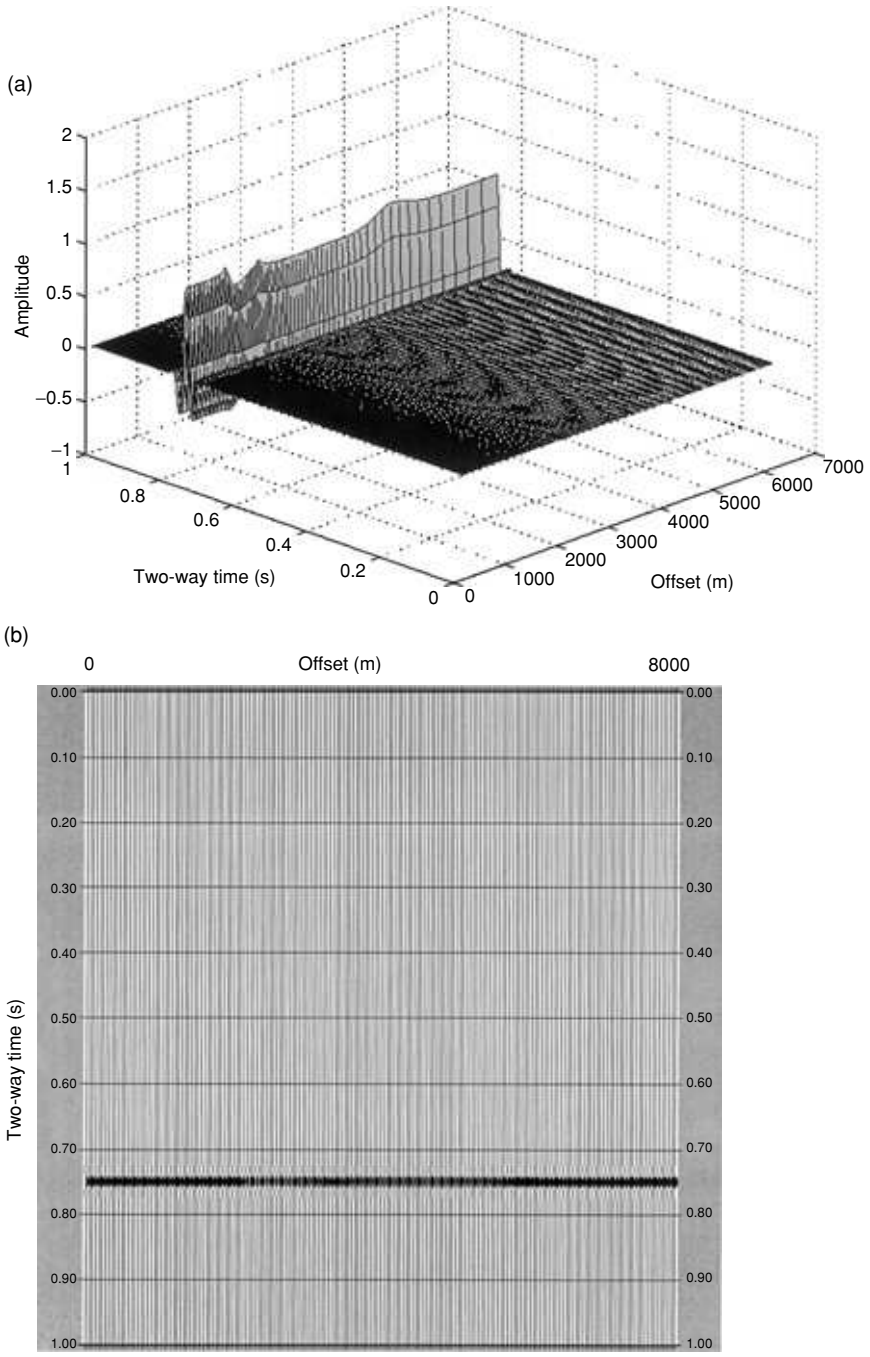

Figure 11 As Fig. 10 with the characteristic $2w/\Lambda = 0.5$.

Analysis of real seismic data has suggested that the effect of AS on the amplitudes of reflected signals depends on the crack filling (gas or liquid). The aim of the paper was to obtain a better understanding of the physics behind these observations.

Analogy with studies in optics, in non-destructive testing and in acoustics has suggested that diffraction phenomena arising from the crack distribution are widely involved in the anomalous amplitudes of reflected events. Analytical evaluation of the amount of energy carried by the reflected and the diffracted waves has shown that neglecting diffraction phenomena leads to local underestimation of the amplitude of waves reflected at interfaces with gas-filled cracks.

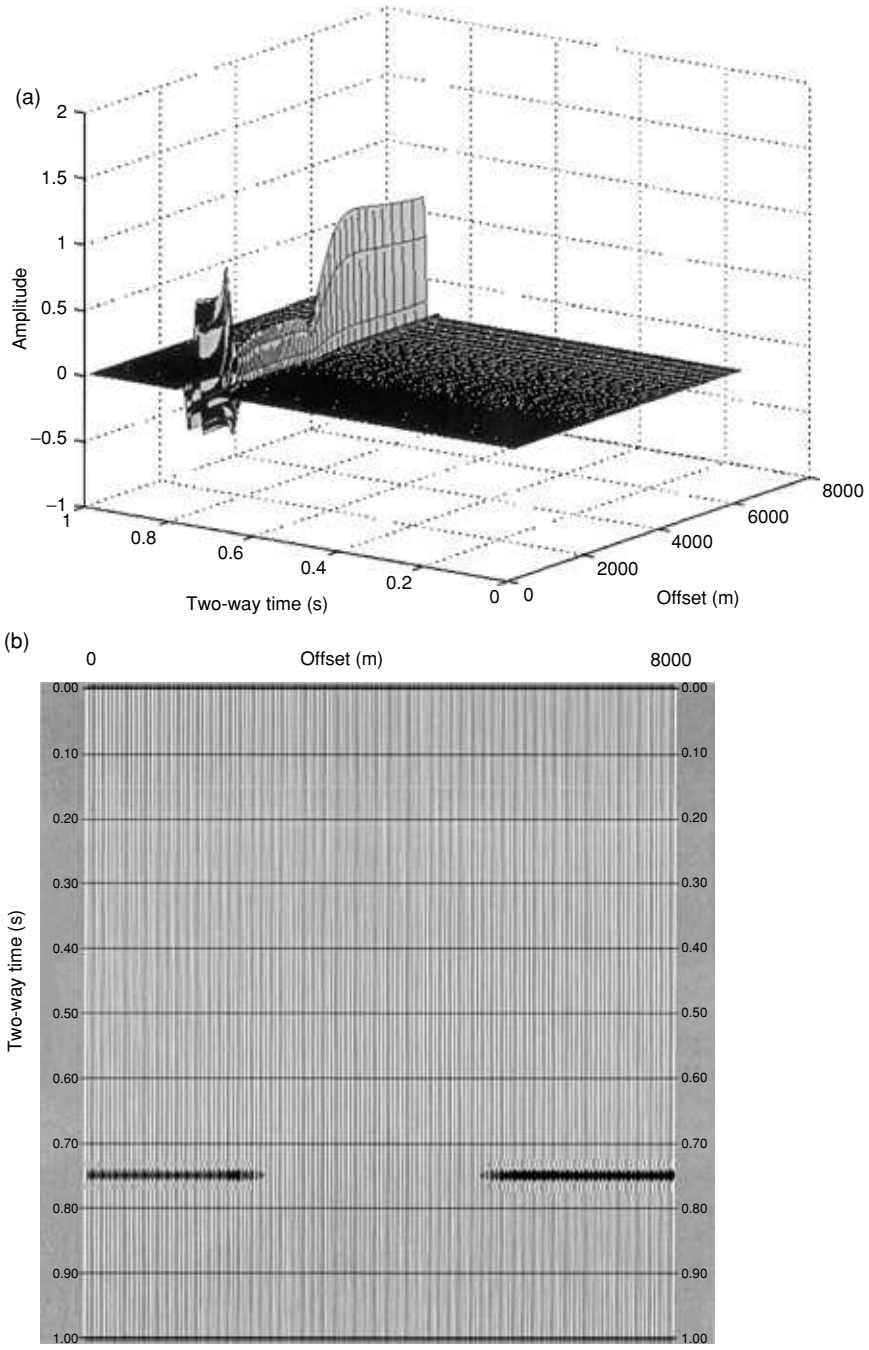

Figure 12 As Fig. 10 with the characteristic $2w/\Lambda = 0.75$.

Consequently, classical numerical modelling of seismic data that do not take into account diffraction phenomena cannot simulate correctly the real data amplitudes.

The influence of the AS phenomenon on seismic waves reflected at interfaces with liquid-filled cracks will be analysed in a forthcoming paper.

ACKNOWLEDGEMENTS

Martin Tygel showed much interest in this study. We thank him for his pertinent remarks and review that helped us to clarify many important points. Thanks to Hervé Perroud for reviewing an earlier version of the manuscript

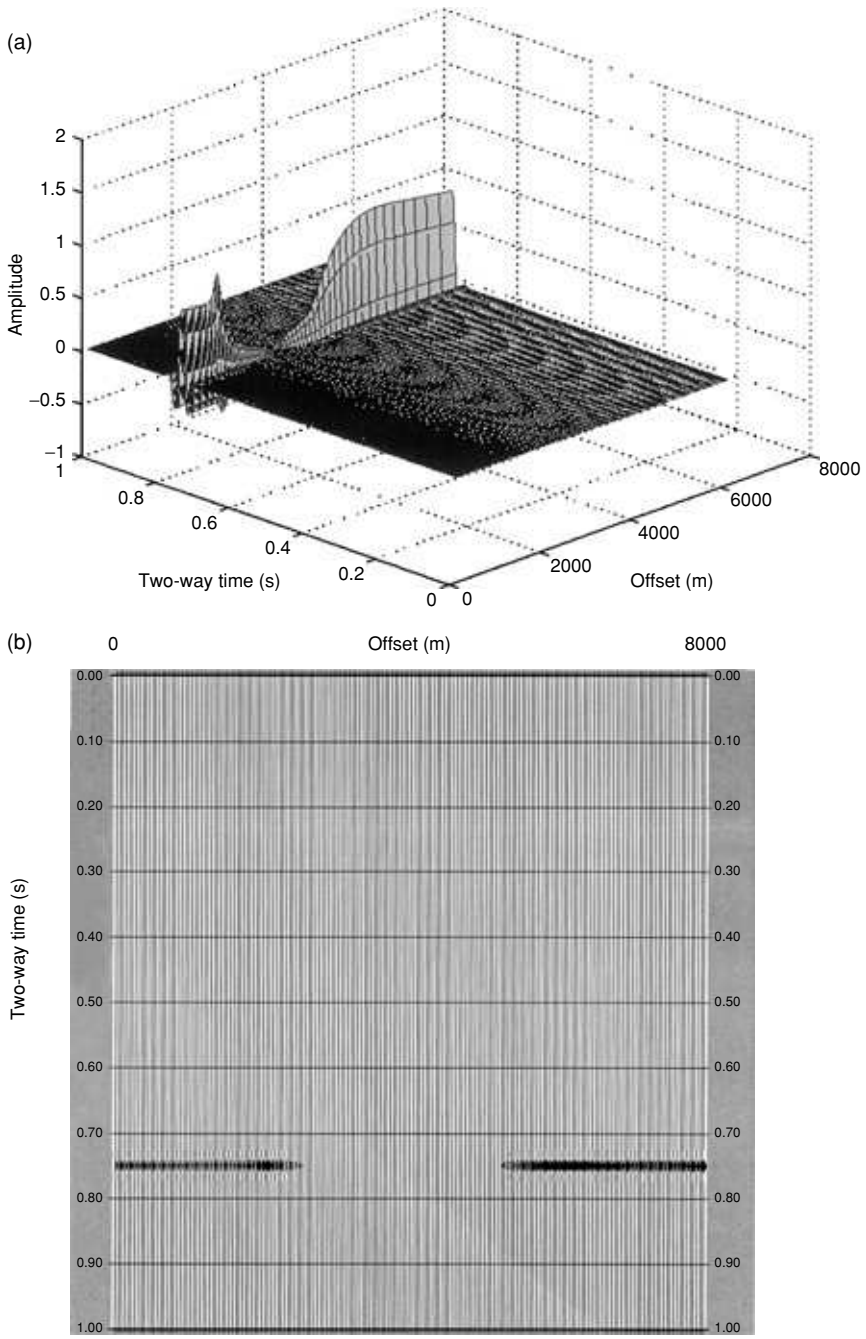

Figure 13 As Fig. 10 with the characteristic $2w/\Lambda = 0.99$.

and to Evgeny Landa for his encouragement. We are also grateful to Jacques Blanco and Laurent Schulbaum for providing the real seismic sections, and to Jean Magendie and Didier Rappin for providing the synthetic seismograms.

REFERENCES

Angel Y.C. and Achenbach J.D. 1985. Reflection of ultrasonic waves by an array of cracks. In: *Review of Progress in Quantitative Nondestructive Evaluation 4A* (eds D.O. Thompson and D.E. Chimenti), pp. 83–89. Plenum Press.

Auld B.A. 1990. *Acoustic Fields and Waves in Solids*, 2nd edn, two volumes. Krieger Publishing Co.

Baik J.-M. and Thompson R.B. 1984. Ultrasonic scattering from imperfect interfaces: a quasi-static model. *Journal of Nondestructive Evaluation* **4**(3/4), 177–196.

Biryukov S.V., Gulyaev Yu.V., Krylov V.V. and Plessky V.P. 1995. *Surface Acoustic Waves in Inhomogeneous Media* (eds L.M. Brekhovskikh *et al.*). Springer-Verlag, Inc.

Born M. and Wolf E. 1999. *Principles of Optics*, 7th expanded edn. Cambridge University Press.

Brillouin L. and Parodi M. 1956. *Propagation des Ondes dans les Milieux Périodiques*. Masson et Cie, Paris.

Crandall S.H. 1970. On the use of slowness diagrams to represent wave reflections. *Journal of the Acoustical Society of America* **47**, 1338–1342.

Danicki E. 1999. Resonant phenomena in bulk wave scattering by in-plane cracks. *Journal of the Acoustical Society of America* **105**, 84–92.

Fokkema J.T. 1980. Reflection and transmission of elastic waves by the spatially periodic interface between two solids (theory of the integral-equation method). *Wave Motion* **2**, 375–393.

Helbig K. 1994. *Foundations of Anisotropy for Exploration Seismics. Handbook of Geophysical Exploration, Section 1: Seismic Exploration*, **Vol. 22** (eds K. Helbig and S. Treitel). Pergamon Press, Inc.

Liu E., Hudson J.A. and Pointer T. 2000. Equivalent medium representation of fractured rock. *Journal of Geophysical Research* **105** (B2), 2981–3000.

Myer L.R. 2000. Fracture as a collection of cracks. *International Journal of Rock Mechanics and Minerals Science* **37**, 231–242.

Nihei K.T., Myer L.R. and Cook N.G.W. 1995. Numerical simulation of elastic wave propagation in granular rock with the boundary integral equation method. *Journal of the Acoustical Society of America* **97**, 1423–1434.

Ogilvy J.A. 1991. *Theory of Wave Scattering from Random Rough Surfaces*. Hilger.

Schulbaum L. 1996. *Traduction des surfaces stratigraphiques et des géométries deltaïques lors du passage de l'échelle puits à l'échelle sismique*. PhD thesis, Henri Poincaré Nancy I University.

Tygel M. (ed.) 2001. Special issue: Seismic true amplitudes. *Journal of Seismic Exploration* **10**.

Viktorov I.A. 1967. *Rayleigh and Lamb Waves* (ed. W.P. Mason). Plenum Press.

Waterman P.C. 1975. Scattering by periodic surfaces. *Journal of the Acoustical Society of America* **57**, 791–802.

APPENDIX

We derive expressions for the diffracted wavefield induced by a crack distribution at the interface between two different solids. These expressions are necessary for the evaluation of the amount of energy carried by each diffracted wave (see Section 2.1).

As described in Section 1.2, we consider a time-harmonic plane P-wave propagating in the solid B, at an angle Θ_{inc} with respect to the normal to the solid B/solid A interface, towards the solid A (Fig. 4). The associated incident displacement vector $\mathbf{U}_{inc}$ in the solid B can be written as

$$\mathbf{U}_{inc}(x_1, x_2; t) = \mathbf{u}_{inc}(x_1, x_2) \exp(-\mathrm{j}q_{inc}x_2) \exp(-\mathrm{j}p_{inc}x_1) \exp(\mathrm{j}\omega t),$$

where $\mathbf{u}_{inc} = (\sin\boldsymbol{\Theta}_{inc}, \cos\boldsymbol{\Theta}_{inc})$ is the unit propagation vector of the incident P-wave, $\mathbf{k}_{inc} = (p_{inc}, q_{inc}) = \mathbf{k}_P^B$ is the incident P-wavenumber and ω is the angular frequency.

At the interface, the full wavefield (displacement $\mathbf{U}_{tot}^{A,B}$ and stress $\mathbf{T}_{tot}^{A,B}$) in each medium, governed by known equations of motion, is expressed in the form:

In the solid A:

$$\begin{cases} \mathbf{U}_{tot}^{A} = \mathbf{U}_{diff}^{A} \\ \mathbf{T}_{tot}^{A} = \mathbf{T}_{diff}^{A} \end{cases}, \tag{A1}$$

and in the solid B:

$$\begin{cases} \mathbf{U}_{tot}^{B} = \mathbf{U}_{inc} + \mathbf{U}_{diff}^{B} \\ \mathbf{T}_{tot}^{B} = \mathbf{T}_{inc} + \mathbf{T}_{diff}^{B} \end{cases}. \tag{A2}$$

$\mathbf{U}_{diff}^{A,B}$ and $\mathbf{T}_{diff}^{A,B}$ characterize the diffracted fields in the solids A and B. At the interface, they are formulated as an infinite series of Bloch waves, as required by Floquet's theorem (see Waterman 1975; Auld 1990, vol. 2, p. 119):

$$\begin{bmatrix} \mathbf{T}_{diff}^{A,B} \\ \mathbf{U}_{diff}^{A,B} \end{bmatrix} = \sum_{n=-\infty}^{+\infty} \begin{bmatrix} \mathbf{T}_{n}^{A,B} \\ \mathbf{U}_{n}^{A,B} \end{bmatrix} \exp(-\mathrm{j}p_n x_1) \exp(\mathrm{j}\omega t), \tag{A3}$$

where $p_n = p_{inc} + nK$ is the Bloch wavenumber, n is the diffraction order and $K = 2\pi/\Lambda$ is the spatial wavenumber of the crack distribution defined from the spatial wavelength Λ. The diffracted fields represent the specular ($n = 0$) and non-specular ($n \neq 0$) reflected and transmitted fields. The wavefield in each medium is a superposition of the diffracted P- and S-waves components, with the general form,

$$\exp(-\mathrm{j}p_n x_1) \exp\left(\pm \mathrm{j}\left(q_{P,S}^{A,B}\right)_n x_2\right) \exp(\mathrm{j}\omega t),$$

where

$$\left(q_{P,S}^{A,B}\right)_n = \left(k_{P,S}^{A,B^2} - p_n^2\right)^{1/2} = -\mathrm{j}\left(p_n^2 - k_{P,S}^{A,B^2}\right)^{1/2}$$

with P- and S-wavenumbers $k_{P,S}^{A,B}$.

At the interface, the coefficients $\mathbf{U}_n^{A,B}$ and $\mathbf{T}_n^{A,B}$ of the infinite series, and the incident displacement $\mathbf{U}_{inc}$ and traction-force $\mathbf{T}_{inc}$ vectors (Auld 1990), are related by

$$\mathbf{U}_n^{A,B} = \overline{\overline{\mathbf{G}_n^{A,B}}}\, \mathbf{T}_n^{A,B}, \quad \mathbf{U}_{inc} = \overline{\overline{\mathbf{G}'_{inc}}}\, \mathbf{T}_{inc}, \tag{A4}$$

where the matrices $\overline{\overline{\mathbf{G}_n^{A,B}}}$ and $\overline{\overline{\mathbf{G}'_{inc}}}$ are defined from the known equations of motion.

The full wavefields ($\mathbf{U}_{\text{tot}}^{\text{A,B}}$ and $\mathbf{T}_{\text{tot}}^{\text{A,B}}$) must satisfy different boundary conditions at the interface:
on cracks

$$\mathbf{T}_{\text{tot}}^{\text{A}} = \mathbf{T}_{\text{tot}}^{\text{B}} = \mathbf{0}, \tag{A5a}$$

between cracks

$$\begin{cases} \Delta\mathbf{U} = \mathbf{U}_{\text{diff}}^{\text{A}} - \mathbf{U}_{\text{diff}}^{\text{B}} = \mathbf{0} \\ \mathbf{T}_{\text{tot}}^{\text{A}} = \mathbf{T}_{\text{tot}}^{\text{B}} \end{cases}, \tag{A5b}$$

where the function $\Delta\mathbf{U}$ denotes the particle displacement discontinuity at the interface. These boundary conditions cannot be exploited in a trivial way to analyse the wave diffraction problem. An efficient way of solving such a problem can be found in Danicki (1999). The paper presents a method of analysis of the generation of surface waves by comb transducers. This work is concerned with a crack distribution embedded in an isotropic elastic body. As the objectives of our work are different, we need to derive equations for the case of two different elastic media in contact. We then adapted the original work to our configuration. Referring the reader for details to the original paper (Danicki 1999), we give only the most relevant equations that are necessary for our work. Danicki (1999) assumed a finite series expansion for $\mathbf{T}_n^{\text{A}}$ in the form,

$$\mathbf{T}_n^{\text{A}} = \sum_{m=N_1}^{N_2+1} \mathbf{t}_{nm}^{\text{A}} P_{n-m}(\cos\Delta), \tag{A6}$$

in which P_n denotes Legendre functions of the first kind, and the variable $\Delta = K\text{w}$ describes the relative width of perfect contact between cracks (Fig. 4). Some interesting properties of Legendre functions allow the diffracted fields to satisfy the boundary conditions and the square-root singularities at the crack edges.

After some long but straightforward calculations (see Danicki 1999), analysis of the wave diffraction by periodic systems of in-plane cracks can be achieved by solving the system of $(N_2 - N_1 + 2)$ equations in $(N_2 - N_1 + 2)$ unknowns $\mathbf{t}_{nm}^{\text{A}}$, resulting from the boundary conditions (A5):

$$\begin{cases} \sum_{m=N_1}^{N_2+1} \left(S_{n-m}\,\overline{\overline{\mathbf{g}_\infty^n}} - \overline{\overline{\mathbf{g}_n}}\right)\mathbf{t}_{nm}^{\text{A}}\, P_{n-m}(\cos\Delta) = -\overline{\overline{\dot{\mathbf{g}}_{\text{inc}}}}\,\mathbf{T}_{\text{inc}}\,\delta_{n0} \\ \qquad\qquad\qquad\qquad\qquad\qquad\qquad\qquad\qquad\qquad \text{for } n \in [N_1, N_2], \\ \sum_{m=N_1}^{N_2+1} (-1)^m \overline{\overline{\mathbf{g}_\infty^{n=0}}}\,\mathbf{t}_{nm}^{\text{A}}\, P_{-m-r/k}(-\cos\Delta) = \mathbf{0} \end{cases}$$

where

$$S_v = \begin{vmatrix} 1 (v \geq 0) \\ -1 (v < 0) \end{vmatrix} \text{ and } \overline{\overline{\dot{\mathbf{g}}_{\text{inc}}}} = -\text{j}p_{\text{inc}}\left(\overline{\overline{\mathbf{G}'_{\text{inc}}}} + {}^{\text{t}}\overline{\overline{\mathbf{G}'_{\text{inc}}}}\right).$$

The matrix $\overline{\overline{\mathbf{g}_\infty^n}}$ is the asymptotic limit of the matrix $\overline{\overline{\mathbf{g}_n}} = -\text{j}p_n(\overline{\overline{\mathbf{G}_n^{\text{A}}}} - \overline{\overline{\mathbf{G}_n^{\text{B}}}})$, i.e.

$$\lim_{|p_n|\to\infty} \overline{\overline{\mathbf{g}_n(p_n)}} = S_{p_n}\,\overline{\overline{\mathbf{g}_\infty^n}}. \tag{A7}$$

For an interface between two elastic media with different properties, $\overline{\overline{\mathbf{g}_\infty^n}}$ is different from the matrix $\overline{\overline{\mathbf{g}_\infty}}$, reported in Danicki (1999) and determined for an interface between identical media. In the case of two different media, it is defined by

$$\overline{\overline{\mathbf{g}_\infty^n}} = \frac{1}{2\omega^2}\begin{bmatrix} X & Y \\ -Y & X \end{bmatrix},$$

where

$$X = \text{j}\left(Z_{\text{A}} k_{\text{S}}^{\text{A}^2} + Z_{\text{B}} k_{\text{S}}^{\text{B}^2}\right),\ Y = S_{p_n}\left(Z_{\text{A}} k_{\text{P}}^{\text{A}^2} - Z_{\text{B}} k_{\text{P}}^{\text{B}^2}\right),$$

$$Z_{\text{A,B}} = \frac{k_{\text{S}}^{\text{A,B}^2}}{\rho_{\text{A,B}}\left(k_{\text{S}}^{\text{A,B}^2} - k_{\text{P}}^{\text{A,B}^2}\right)},$$

$\rho_{\text{A,B}}$ denoting the density of the solids A and B.

The summation limits $m = N_1$ and $m = N_2 + 1$ of the finite series of the system are defined by considering the degree of accuracy that is chosen for the approximation (A7) of $\overline{\overline{\mathbf{g}_n}}$. In the present study, we considered $N_1 = -1$ and $N_2 = 0$. Knowing $\mathbf{T}_{\text{inc}}$, $\mathbf{U}_n^{\text{A,B}}$ and $\mathbf{T}_n^{\text{A,B}}$ are then recovered from the solutions $\mathbf{t}_{nm}^{\text{A}}$ and the relationships (A1)–(A6).

WAVE SCATTERING BY A PERIODIC ARRAY OF IN-PLANE CRACKS AT THE INTERFACE BETWEEN DISSIMILAR MEDIA

Nathalie Favretto-Cristini

Abstract. We investigate analytically the behaviour of time-harmonic elastic waves in the neighbourhood of a plane interface between dissimilar elastic media, where a periodic array of in-plane cracks exists. Waves incident on such a boundary excite a lot of propagating and evanescent scattered waves, and the incident energy is subjected to a complicated process of redistribution. The aim of the work is to quantify the amount of incident wave energy partitioned among the propagating scattered waves. The scattered fields are expressed in terms of Fourier series with coefficients depending on Legendre functions. Energies associated with the scattered waves are evaluated as a function of the incidence angle, and results are presented for three different distributions of the cracks at the interface. We show that the amount of the reflected wave energy and the amount of the diffracted wave energy increase with increasing percentage of cracks at the interface. We also suggest that, contrary to the case of an interface between identical media, the energy conservation law cannot be applied in the work presented here since phenomena associated with interface wave scattering are not taken into account.

§1. Introduction

Intensive studies have addressed the problem of elastic wave scattering by a periodic array of cracks because of its conceptual and practical importance in non destructive testing of materials, for example. Angel and Achenbach [1] have presented an exact analysis of the reflection of elastic waves by a planar array of periodically spaced cracks of equal lengths. By the use of Fourier series techniques, the mixed-boundary value problem for a typical strip is reduced to a singular integral equation of the 1st kind for the dislocation density across the crack faces. The equation is then solved numerically. The exact results are, however, rather complicated. The applicability of an approximate solution to the exact problem was investigated in numerous papers (see ref. [2] and the excellent review given there), in which the array of cracks are generally replaced by a layer of massless springs. The interface stiffnesses are chosen so that the spring layer produces the same static displacements as the array of cracks, when the elastic medium is subjected to distant uniform tension. Angel and Achenbach [3] have considered this quasi-static model as a low-frequency limit of the exact solution. In this case, only one specular reflected wave has to be taken into account at some distance from the plane of cracks. However, as the ratio of incident wavelength-to-array period decreases, the quasi-static

model becomes invalid, since more and more propagating reflected waves which travel into off-specular directions are generated by the secondary sources (i.e., cracks) at the interface.

Recently, Danicki has studied this problem from a very particular point of view [4, 5]. To solve the problem of wave scattering by a periodic array of cracks, the BIS method [6] has been applied. The method exploits some properties of Fourier series with coefficients expressed by Legendre functions. Three features make the use of Legendre functions particularly well-suited for modeling elastic wave fields by a periodic array of cracks. First, the series are periodic, as required by Floquet's theorem. Moreover, the identities concerning Legendre functions satisfy implicitly the mixed-boundary conditions. Finally, they also exhibit square-root singularity, in correspondence with the singularity of the wavefields at the crack edges. The solution to the wave-scattering problem can thus be obtained efficiently in an analytical way.

In the present paper, using the fundamentals of the BIS method, we investigate the complicated process of redistribution of the incident energy (associated either with a compressional wave, called a P-wave, or with a transverse wave, called a S-wave), as a function of the incidence angle, among the propagating scattered waves in the vicinity of a solid/solid interface with air (or gas)-filled cracks. For the sake of brevity, the influence of the characteristics of the crack array and the influence of the properties of the incident wave are shown. Numerical results, presented here for applications of geophysical interest [7], viz. the interface between chalk and granite, concern only the incident P-wave.

§2. Description of the configuration and formulation of the problem

We investigate the scattering of time-harmonic elastic waves by a periodic array of cracks at the boundary between two dissimilar media. The media are assumed to be homogeneous, isotropic, and perfectly elastic half-spaces, with mass density ρ, P-wave velocity C_P and S-wave velocity C_S. We refer to the upper medium ($x_2 < 0$) as solid B and to the lower medium ($x_2 > 0$) as solid A. The cracks lie in the plane $x_2 = 0$ and extend to infinity in the direction perpendicular to the $(\mathbf{x_1} - \mathbf{x_2})$ plane. The excitation being assumed to be independent of the $\mathbf{x_3}$-direction, the problem is a two-dimensional one. The period of the crack array is Λ; $K = \frac{2\pi}{\Lambda}$ denotes the spatial wavenumber. The regions of perfect bonding between the elastic half-spaces are $2w$ wide.

We consider a time-harmonic plane wave, characterized by the wavelength λ_{inc}, and angular frequency ω, that propagates in the solid B and hits the interface under the incidence angle α_{inc}, with respect to the normal to the interface. The associated incident particle displacement vector $\mathbf{U_{inc}}$ in the solid B can be written as:

$$\mathbf{U_{inc}}(x_1, x_2; t) = \mathbf{u_{inc}}(x_1, x_2) \exp(-jq_{inc}x_2) \exp(-jp_{inc}x_1) \exp(j\omega t) \tag{1}$$

where $\mathbf{u_{inc}} = (\sin\alpha_{inc}, \cos\alpha_{inc})$ is the unit propagation vector of the incident P-wave, or $\mathbf{u_{inc}} = (\cos\alpha_{inc}, -\sin\alpha_{inc})$ is the unit propagation vector of the incident S-wave, and $\mathbf{k_{inc}} = (p_{inc}, q_{inc}) = \mathbf{k^B_{P,S}}$ the incident P- or S-wavevector. The amplitude of the incident displacement vector is assumed to be unity. At the interface, the incident displacement vector $\mathbf{U_{inc}}$ and the traction-force vector $\mathbf{T_{inc}}$ are related by:

$$\mathbf{U_{inc}} = \overline{\mathbf{G'_{inc}}}\, \mathbf{T_{inc}} \tag{2}$$

where the matrix $\overline{\mathbf{G'_{inc}}}$, given below, is defined from the known equations of motion [8], in which absence of body forces is assumed:

$$T_{ij,j} + \rho\omega^2 U_i = 0 \tag{3}$$

$_{,j}$ denotes partial differentiation with respect to x_j.

After hitting the cracked interface, the incident wave excites a lot of diffracted waves that propagate in different directions. At the interface, the full wavefield (particle displacement vector $\mathbf{U^{A,B}_{tot}}$and traction-force vector $\mathbf{T^{A,B}_{tot}}$) in each medium, governed by equations of motion 3, is expressed in the form:

$$\left\{ \begin{array}{l} \mathbf{U^A_{tot}} = \mathbf{U^A_{diff}} \\ \mathbf{T^A_{tot}} = \mathbf{T^A_{diff}} \end{array} \right. \quad \text{and} \quad \left\{ \begin{array}{l} \mathbf{U^B_{tot}} = \mathbf{U_{inc}} + \mathbf{U^B_{diff}} \\ \mathbf{T^B_{tot}} = \mathbf{T_{inc}} + \mathbf{T^B_{diff}} \end{array} \right.$$

$\mathbf{U^{A,B}_{diff}}$and $\mathbf{T^{A,B}_{diff}}$ characterize the diffracted fields in the solids A and B. At the interface, they are formulated as an infinite series of Bloch waves, as required by Floquet's theorem [8]:

$$\left[\begin{array}{c} \mathbf{U^{A,B}_{diff}} \\ \mathbf{T^{A,B}_{diff}} \end{array} \right] = \sum_{n=-\infty}^{+\infty} \left[\begin{array}{c} \mathbf{U^{A,B}_{n}} \\ \mathbf{T^{A,B}_{n}} \end{array} \right] \exp\left(-jp_n x_1\right) \exp\left(j\omega t\right) \tag{4}$$

where $p_n = p_{inc} + nK \quad (0 < p_{inc} < K)$ is the Bloch wavenumber and n the diffraction order. The zeroth-diffracted waves correspond to classical reflections and transmissions, while the n^{th}-diffracted waves (with n different from zero) correspond to off-specular reflections and transmissions induced by the secondary sources at the interface (i.e., by the periodic array of cracks). p_{inc} is the horizontal wavenumber common to all waves of diffraction order zero. The scattered far-field consists of a superposition of a finite number of propagating P- and S-wave components, with the general form $\exp\left(-jp_n x_1\right) \exp\left(\pm j \left(q^{A,B}_{P,S}\right)_n x_2\right) \exp\left(j\omega t\right)$. In order to satisfy the radiation conditions by the wavefield in the half-spaces, the values of $\left(q^{A,B}_{P,S}\right)_n$ are chosen following the rule $\left(q^{A,B}_{P,S}\right)_n = \left[\left(k^{A,B}_{P,S}\right)^2 - p_n^2\right]^{\frac{1}{2}} = -j\left[p_n^2 - \left(k^{A,B}_{P,S}\right)^2\right]^{\frac{1}{2}}$, with P- and S-wavenumbers $k^{A,B}_{P,S}$.

We consider the coefficients $\mathbf{U^{A,B}_{n}}$and $\mathbf{T^{A,B}_{n}}$ of eq.4 as the fundamental quantities to be determined. At the interface, these coefficients are related by:

$$\mathbf{U^{A,B}_{n}} = \overline{\mathbf{G^{A,B}_{n}}}\, \mathbf{T^{A,B}_{n}} \tag{5}$$

where the matrices $\overline{\mathbf{G^{A,B}_{n}}}$ are defined from the equations of motion 3:

$$\overline{\mathbf{G^A_n}} = \frac{j}{\mu_A D_A} \left[\begin{array}{cc} \left(k_S^A\right)^2 \left(q_S^A\right)_n & p_n \left(\left(k_S^A\right)^2 - 2p_n^2 - 2\left(q_P^A\right)_n \left(q_S^A\right)_n\right) \\ -p_n \left(\left(k_S^A\right)^2 - 2p_n^2 - 2\left(q_P^A\right)_n \left(q_S^A\right)_n\right) & \left(k_S^A\right)^2 \left(q_P^A\right)_n \end{array} \right]$$

$$\overline{\mathbf{G^B_n}} = -{}^t\overline{\mathbf{G'_n}}$$

$\mu_A = \rho_A \left(C_S^A\right)^2$ is the Lame coefficient of solid A, and $D_A = \left[\left(k_S^A\right)^2 - 2p_n^2\right]^2 + 4p_n^2 \left(q_P^A\right)_n \left(q_S^A\right)_n$ is the known characteristic equation of the Rayleigh wave propagating at the free surface of

solid A [8]. ${}^t\overline{\mathbf{G}'_{\mathbf{n}}}$ is transposed to $\overline{\mathbf{G}'_{\mathbf{n}}}$. $\overline{\mathbf{G}'_{\mathbf{n}}}$, and also $\overline{\mathbf{G}'_{\mathbf{inc}}}$, is similar to $\overline{\mathbf{G}^{\mathbf{A}}_{\mathbf{n}}}$ calculated using the properties of solid B.

In this paper, we investigate wave scattering by a periodic array of thin air-filled cracks at the boundary between two welded elastic half-spaces. The resulting mixed-boundary conditions, satisfied by the full-wavefields at $x_2 = 0$, are thus:

$$\left\{ \begin{array}{c} \mathbf{T}^{\mathbf{A}}_{\mathbf{tot}} = \mathbf{T}^{\mathbf{B}}_{\mathbf{tot}} \\ \Delta\mathbf{U} = \mathbf{U}^{\mathbf{A}}_{\mathbf{tot}} - \mathbf{U}^{\mathbf{B}}_{\mathbf{tot}} = \mathbf{0} \end{array} \right. \text{ between cracks,} \tag{6}$$

$$\mathbf{T}^{\mathbf{A}}_{\mathbf{tot}} = \mathbf{T}^{\mathbf{B}}_{\mathbf{tot}} = \mathbf{0} \text{ on cracks,} \tag{7}$$

where the function $\Delta\mathbf{U}$ denotes the particle displacement discontinuity at the interface. In order to simplify these expressions, we introduce the auxiliary function $\mathbf{V}\,(x_1)$ [4]:

$$\mathbf{V}\,(x_1) = \frac{\partial}{\partial x_1}\,\left(\Delta\mathbf{U}\,(x_1)\right) = \sum_{n=-\infty}^{+\infty} \mathbf{V_n}\,\exp\left(-jp_n x_1\right)\,\exp\left(j\omega t\right)$$

where

$$\begin{array}{c} \mathbf{V_n} = \overline{\mathbf{g_n}}\,\mathbf{T}^{\mathbf{A}}_{\mathbf{n}} - \overline{\mathbf{g_{inc}}}\,\mathbf{T_{inc}}\delta_{n0} \\ \left\{ \begin{array}{c} \overline{\mathbf{g_n}} = -jp_n\,\left[\overline{\mathbf{G}^{\mathbf{A}}_{\mathbf{n}}} + {}^t\,\overline{\mathbf{G}'_{\mathbf{n}}}\right] \\ \overline{\mathbf{g_{inc}}} = -jp_{inc}\,\left[\overline{\mathbf{G}'_{\mathbf{inc}}} + {}^t\,\overline{\mathbf{G}'_{\mathbf{inc}}}\right] \end{array} \right. \end{array} \tag{8}$$

It has to be noted that the function $\mathbf{V}\,(x_1)$ determines $\Delta\mathbf{U}\,(x_1)$ within a constant. The boundary conditions 6 and 7 can then be reformulated, just for one period of the crack array, as:

$$\text{between cracks, i.e. } \forall x_1 \;|\; |x_1| < w, \; \left\{ \begin{array}{c} \mathbf{V}\,(x_1) = \mathbf{0} \\ \Delta\mathbf{U}\,(x_1 = 0) = \mathbf{0} \end{array} \right. \tag{9}$$

$$\text{on cracks, i.e. } \forall x_1 \;|\; \left\{ \begin{array}{c} -\Lambda + w < x_1 < -w \\ w < x_1 < \Lambda - w \end{array} \right. , \; \mathbf{T}^{\mathbf{A}}_{\mathbf{tot}} = \mathbf{0} \tag{10}$$

§3. Reformulation of the problem and solution

An efficient way of solving such a problem can be found in [4]. Nevertheless, as the objectives of our work are completely different from those described in the paper, we need to derive equations for the case of a periodic array of cracks at the interface between two different elastic media. We then adapted the original work to our configuration. Refering the reader for details to the original paper [4], we write down only the most relevant equations that are necessary for the comprehension of our work.

Refering to some interesting properties of the Legendre functions P_ν of the 1^{st}-kind and degree ν involved in Fourier series [6, 9], we note that the periodicity of the problem, the exhibition of the square-root singularities at the crack edges, and the boundary conditions 10 and 9 are automatically satisfied if the functions $\mathbf{V_n}$ and $\mathbf{T}^{\mathbf{A}}_{\mathbf{n}}$ are searched in the general form:

$$\mathbf{T_n^A} = \sum_{m=M_1}^{M_2} \mathbf{t_m}\, P_{n-m}\left(\cos\Delta\right) \tag{11}$$

$$\mathbf{V_n} = \sum_{m=M_1}^{M_2} S_{n-m}\, \mathbf{v_m}\, P_{n-m}\left(\cos\Delta\right) \tag{12}$$

where $S_\nu = \left| \begin{array}{ll} 1 & (\nu \geq 0) \\ -1 & (\nu < 0) \end{array} \right.$ $(\nu \in \mathbb{Z})$. The variable $\Delta = K\, w = \pi\, \frac{2w}{\Lambda}$ describes the relative width of perfect contact between cracks. The summation limits M_1 and M_2 over m are supposed to be large but finite.

Substitution of $\mathbf{T_n^A}$ and $\mathbf{V_n}$ in 8 by their representation 11 and 12 leads to:

$$\forall n \in \left]-\infty,\ +\infty\right[,\quad \sum_{m=M_1}^{M_2} S_{n-m}\, \mathbf{v_m} P_{n-m}\left(\cos\Delta\right) = \overline{g_n} \sum_{m=M_1}^{M_2} \mathbf{t_m} P_{n-m}\left(\cos\Delta\right) - \overline{\mathbf{g_{inc}}}\, \mathbf{T_{inc}} \delta_{n0} \tag{13}$$

In order to reduce the number of unknowns in the problem, a relation between $\mathbf{v_m}$ and $\mathbf{t_m}$ is established from 13 following the same rule as that explained in [4]:

$$\left\{ \begin{array}{ll} \forall n \geqslant 0,\ \forall m \in [M_1,\, M_2] & \mathbf{v_m} = \overline{\mathbf{g}_\infty}\, \mathbf{t_m} \\ \forall n < 0,\ \forall m \in [M_1,\, M_2] & \mathbf{v_m} = {}^t\overline{\mathbf{g}_\infty}\, \mathbf{t_m} \end{array} \right. \tag{14}$$

where $\overline{\mathbf{g}_\infty}$ and ${}^t\overline{\mathbf{g}_\infty}$ are the asymptotic limits of the matrix $\overline{\mathbf{g_n}}$, such that:

$$\left\{ \begin{array}{ll} \forall n \in \left]-\infty,\ N_1\right[\ ,\ p_n < -p_\infty, & \lim\limits_{n\to-\infty} \overline{\mathbf{g_n}}\left(p_n\right) = S_{p_n}\, {}^t\overline{\mathbf{g}_\infty} \\ \forall n \in \left]N_2,\ +\infty\right[\ ,\ p_n > p_\infty, & \lim\limits_{n\to+\infty} \overline{\mathbf{g_n}}\left(p_n\right) = S_{p_n}\overline{\mathbf{g}_\infty} \end{array} \right. \tag{15}$$

with

$$\overline{\mathbf{g}_\infty} = \frac{1}{2\omega^2} \left[\begin{array}{ll} j\left(X_A \left(k_S^A\right)^2 + X_B \left(k_S^B\right)^2\right) & \left(X_A \left(k_P^A\right)^2 - X_B \left(k_P^B\right)^2\right) \\ -\left(X_A \left(k_P^A\right)^2 - X_B \left(k_P^B\right)^2\right) & j\left(X_A \left(k_S^A\right)^2 + X_B \left(k_S^B\right)^2\right) \end{array} \right]$$

and $X_{A,B} = \dfrac{\left(k_S^{A,B}\right)^2}{\rho_{A,B}\left(\left(k_S^{A,B}\right)^2 - \left(k_P^{A,B}\right)^2\right)}$. $N_1 < 0$, $N_2 > 0$, and p_∞ are sufficiently large.

For an interface between two elastic media with different properties, we can note that the asymptotic limits of $\overline{\mathbf{g_n}}$ are quite different from the asymptotic limit determined for an interface between identical media and reported in [4]. From the approximation 14, it follows that 13 can be rewritten only in terms of the unknowns $\mathbf{t_m}$ ($\mathbf{T_{inc}}$ being known from 2):

$$\begin{array}{l} \forall n \in [N_1,\, 0[\,,\ \displaystyle\sum_{m=M_1}^{M_2} \left(S_{n-m}\, {}^t\overline{\mathbf{g}_\infty} - \overline{\mathbf{g_n}}\right) \mathbf{t_m}\, P_{n-m}\left(\cos\Delta\right) = \mathbf{0} \\ \forall n \in [0,\, N_2]\,,\ \displaystyle\sum_{m=M_1}^{M_2} \left(S_{n-m}\, \overline{\mathbf{g}_\infty} - \overline{\mathbf{g_n}}\right) \mathbf{t_m}\, P_{n-m}\left(\cos\Delta\right) = -\overline{\mathbf{g_{inc}}}\, \mathbf{T_{inc}} \delta_{n0} \end{array} \tag{16}$$

Eqs.16 express implicitly the boundary condition 10 and the first relation of the boundary condition 9. After some algebric manipulations, the second relation of the boundary condition 9 can be written for $r \neq 0$ and n fixed arbitrarily (here, n=0), with help of Dougall's expansion [9] and eq.14, in the form:

$$\sum_{m=M_1}^{M_2} (-1)^m \ \overline{\mathbf{g}_\infty}\ \mathbf{t_m}\ P_{-m-\frac{p_{inc}}{K}}\left(-\cos\Delta\right) = \mathbf{0} \tag{17}$$

Further analysis shows that the summation limits M_1 and M_2 over m can be defined as (see discussion in [4] and in the references given there): $M_1 = N_1 \leq 0$ and $M_2 = N_2 + 1 > 0$.

Solving the scattering problem and recovering the diffracted wavefields in media then require to find a nontrivial solution to the linear system of $[N_2 - N_1 + 2]$ equations (i.e. eqs.16 and 17) on $[N_2 - N_1 + 2]$ unknowns (i.e. $\mathbf{t_m}$). The summation limits N_1 and N_2 over n are dependent on the degree of accuracy that is judiciously chosen for the approximations 15 of the matrix $\overline{\mathbf{g_n}}$, and also on the physical behaviour of the cracked interface. In particular, all the propagating diffraction orders must be taken into account.

§4. Evaluation of the scattered energy

Since we are mainly interested in the redistribution of the incident wave energy among the propagating diffracted waves, we introduce the time-averaged energy flux $\mathbf{\Pi}$ in the $\mathbf{x_2}$-direction for each diffraction order n and for the incident wave [8]:

$$\begin{array}{l} \left(\mathbf{\Pi_n^{A,B}}\right)_{x_2} = -\frac{1}{2}\,\Re\left[\left(\mathbf{T_n^{A,B}}\right)_{21}\,\left(j\omega\,\left(\mathbf{U_n^{A,B}}\right)_1\right)^* + \left(\mathbf{T_n^{A,B}}\right)_{22}\,\left(j\omega\,\left(\mathbf{U_n^{A,B}}\right)_2\right)^*\right] \\ \left(\mathbf{\Pi_{P,Sinc}}\right)_{x_2} = -\frac{1}{2}\,\Re\left[\left(\mathbf{T_{P,Sinc}}\right)_{21}\,\left(j\omega\,U_1^{P,Sinc}\right)^* + \left(\mathbf{T_{P,Sinc}}\right)_{22}\,\left(j\omega\,U_2^{P,Sinc}\right)^*\right] \end{array} \tag{18}$$

where the asterisk denotes complex-conjugate quantities and $\Re\left(x\right)$ the real part of x. The displacement vector $\mathbf{U_n^{A,B}}$ and the traction force vector $\mathbf{T_n^{A,B}}$ are defined from the solution to the system of equations described in the previous section and from eq.5, while $\mathbf{U_{P,Sinc}}$ and $\mathbf{T_{P,Sinc}}$ are expressed from eqs 1 and 2. On the strength of eqs 18 and 5, the energy associated with the propagating nth-diffracted P- and S-waves can be defined in the vicinity of the cracked interface by:

$$\left(\mathbf{\Pi_{P,S}^{A,B}}\right)_{x_2}^n = \frac{1}{2}\,\rho_{A,B}\,\omega^3\,\Re\left[\left|\left(F_{P,S}^{A,B}\right)_n\right|^2\,\left(q_{P,S}^{A,B}\right)_n\right]$$

where the variables $\left(F_{P,S}^{A,B}\right)_n$ are expressed as a function of the traction force vector components [7]:

$$\begin{array}{l} \left[\begin{array}{c} \left(F_P^A\right)_n \\ \left(F_S^A\right)_n \end{array}\right] = \dfrac{j}{\mu_A\,D_n^A}\left[\begin{array}{cc} 2p_n\,\left(q_S^A\right)_n & \left(k_S^A\right)^2 - 2p_n^2 \\ -\left[\left(k_S^A\right)^2 - 2p_n^2\right] & 2p_n\,\left(q_P^A\right)_n \end{array}\right]\left[\begin{array}{c} \left(T_n^A\right)_{21} \\ \left(T_n^A\right)_{22} \end{array}\right] \\ \left[\begin{array}{c} \left(F_P^B\right)_n \\ \left(F_S^B\right)_n \end{array}\right] = \dfrac{j}{\mu_B\,D_n^B}\left[\begin{array}{cc} 2p_n\,\left(q_S^B\right)_n & -\left[\left(k_S^B\right)^2 - 2p_n^2\right] \\ \left(k_S^B\right)^2 - 2p_n^2 & 2p_n\,\left(q_P^B\right)_n \end{array}\right]\left[\begin{array}{c} \left(T_n^B\right)_{21} \\ \left(T_n^B\right)_{22} \end{array}\right] \end{array}$$

Since both media are lossless, we suppose that the energy flux interferences between the different diffraction orders can be neglected [10], and that the diffracted and incident fields then satisfy the following energy conservation law:

$$1 + \frac{\sum_n \left(\mathbf{\Pi_n^B}\right)_{x_2}}{\left(\mathbf{\Pi_{P,Sinc}}\right)_{x_2}} - \frac{\sum_n \left(\mathbf{\Pi_n^A}\right)_{x_2}}{\left(\mathbf{\Pi_{P,Sinc}}\right)_{x_2}} = 0 \tag{19}$$

where all summations are to be carried out over the collection of the pertaining propagating orders.

Figure 1 illustrates the changes in the ratio $\left|\frac{\left(\mathbf{\Pi_{P,S}^{A,B}}\right)^n_{x_2}}{\left(\mathbf{\Pi_{P,Sinc}}\right)_{x_2}}\right|$, associated with the different diffraction orders in the chalk and granite materials, as a function of the incidence angle α_{inc} associated only with the incident P-wave. The properties of the materials are: $\rho_B = 1180\, kg/m^3$, $C_{PB} = 2670\, m/s$, and $C_{SB} = 1120\, m/s$ for chalk, $\rho_A = 2700\, kg/m^3$, $C_{PA} = 6440\, m/s$, and $C_{SA} = 3170\, m/s$ for granite. The computations were carried out for three different crack distributions at the interface: 1% of cracks (i.e. $2w/\Lambda = 0.99$) which represents the case of a quasi-perfectly welded interface; 50% of cracks (i.e. $2w/\Lambda = 0.5$); 75% of cracks (i.e. $2w/\Lambda = 0.25$). The incident P-wavelength λ_{inc} in chalk was chosen to be greater than the spatial wavelength Λ of the crack distribution at the interface ($\Lambda = \frac{1}{3}\,\lambda_{inc}$). In this case, only one diffracted S-wave of order -1 is propagative in chalk, and only for the incidence angles α_{inc} greater than 38. The critical incident angle, at which the P-wave (respectively, S-wave) transmitted in granite becomes an inhomogeneous wave whose amplitude decays exponentially with distance away from the interface, is $\alpha_{inc} = 24.5$ deg. (respectively, $\alpha_{inc} = 57.4$ deg.). For solving the scattering problem, we chose the summation limits N_1 and N_2 over n such that $N_1 = -10$ and $N_2 = 10$ (all the propagating orders are taken into account in the calculations and the relations 15 are well satisfied). Figure 1 shows that the amount of S-diffracted energy, and also the amount of P-reflected energy, increase with increasing percentage of cracks at the interface. Consequently, neglecting the diffracted waves arising from the crack array at the interface leads to local underestimation of the actual amplitude of the reflected P-waves.

The most striking result is illustrated in Figure 2 which represents the computation of the first member of eq.19 as a function of the incidence angle α_{inc}. We can note that the energy conservation law is not satisfied for the different crack distributions (except for the case of 1% of cracks which is not shown here for the sake of brevity), contrary to the case of an interface between identical media [4]. One explanation to this striking result could be that the energy flux interferences cannot be neglected in such a configuration because, although the media in contact are elastic, the interface is laterally heterogeneous and not uniformly welded. Another explanation could be provided by analogy with studies in Non Destructive testing or in Acoustics. The spatial distribution of the welded contact areas and cracks at the interface can be viewed as a comb transducer which is commonly used for excitation and detection of surface waves. A part of the incident P-wave energy can be transferred to an interface wave (IW) which propagates along the interface between dissimilar elastic media. The IW can then be scattered by the crack distribution and recombined coherently into P-waves propagating in the bulk media. The part of the energy associated to the SW transferred to the bulk waves must then be taken into account in the energy conservation law 19, which will be done in future works.

§5. Conclusion

In the present paper, we have investigated the behaviour of time-harmonic elastic waves in the neighbourhood of a plane interface between dissimilar elastic media, where a periodic array of in-plane air-filled cracks exists. The aim of the work was to quantify the amount of incident wave energy distributed among the propagating scattered waves. The wave-scattering problem was formulated making use of the fundamentals of the theory recently developed by Danicki. Although in essence his method remains valid, the periodic array of cracks at the boundary between dissimilar media needed reformulation of the problem. The scattered fields were expressed in terms of Fourier series with coefficients depending on Legendre functions. Energies associated with the scattered waves of zeroth- and minus-first-diffraction order have been evaluated as a function of the incidence angle and for different crack distributions at the interface. We have shown that the amount of P-reflected energy (associated with zeroth-diffraction order) and the amount of S-reflected energy (associated with minus-first-diffraction order) increase with increasing percentage of cracks at the interface. As a result, neglecting the crack array leads to local underestimation of the actual amplitude of the reflected P-waves. We also suggest that, contrary to the case of an interface between identical media, the energy conservation law cannot be applied in this work since phenomena associated with interface wave scattering are not taken into account.

References

[1] Y.C. Angel and J.D. Achenbach, Reflection and transmission of elastic waves by a periodic array of cracks: oblique incidence, Wave motion 7, 375-397 (1985).

[2] S.I. Rokhlin and Y.J. Wang, Analysis of boundary conditions for elastic wave interaction with an interface between two solids, Journal of the Acoustical Society of America 89(2), 503-515 (1991).

[3] Y.C. Angel and J.D. Achenbach, Reflection of ultrasonic waves by an array of microcracks, in Review of Progress in Quantitative Non Destructive Evaluation, ed. By D.O. Thompson and D.E. Chimenti, Plenum Press NY, vol. 4A, 83-89 (1985).

[4] E.J. Danicki, Resonant phenomena in bulk-wave scattering by in-plane periodic cracks, Journal of the Acoustical Society of America 105(1), 84-92 (1999).

[5] E.J. Danicki, Scattering by periodic cracks and theory of comb transducers, Wave Motion 35, 355-370 (2002).

[6] E.J. Danicki, B. Langli and K. Blotekjaer, Spectral theory of EM scattering by periodic strips, IEEE Transactions on Antennas Propagation AP-43, 97-104 (1995).

[7] N. Favretto-Cristini and E. de Bazelaire, PP amplitude bias caused by interface scattering: are diffracted waves guilty?, Geophysical Prospecting 51, 99-115 (2003).

[8] B.A. Auld, Acoustic fields and waves in solids, 2nd edition, volumes 1 and 2, Krieger Publishing Company, Florida (1990).

[9] A. Erdélyi, W. Magnus, F. Oberhettinger and F.G. Tricomi, Higher transcendental functions, volume 1, chapter 3, Mc Graw-Hill NY (1953).

[10] J.M. Carcione, Wave fields in real media: wave propagation in anisotropic, anelastic and porous media, Seismic Exploration volume 31, Pergamon (2001).

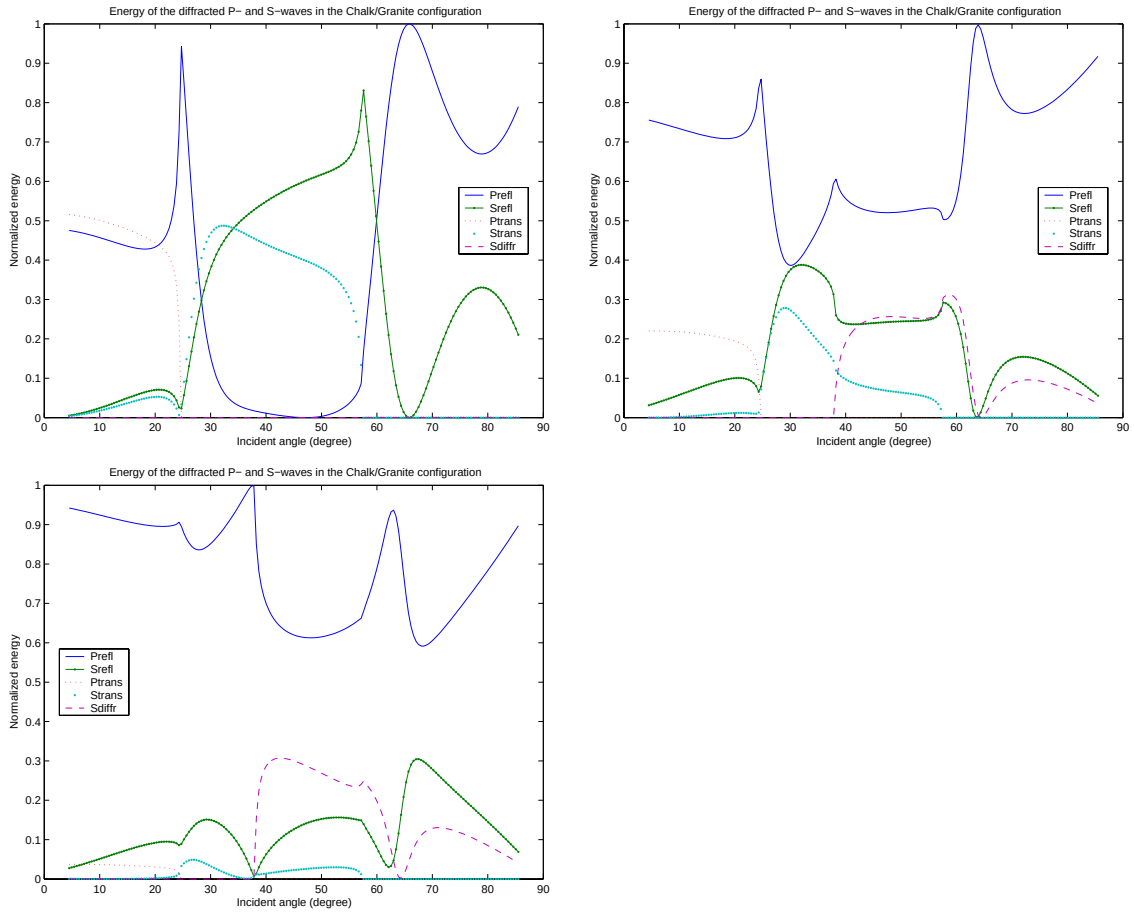

Figure 1: Energy associated with the different diffraction orders in the chalk and granite materials as a function of the incidence angle and for different crack distributions at the interface (1% of cracks (top left), 50% of cracks (top right), 75% of cracks (bottom left)).

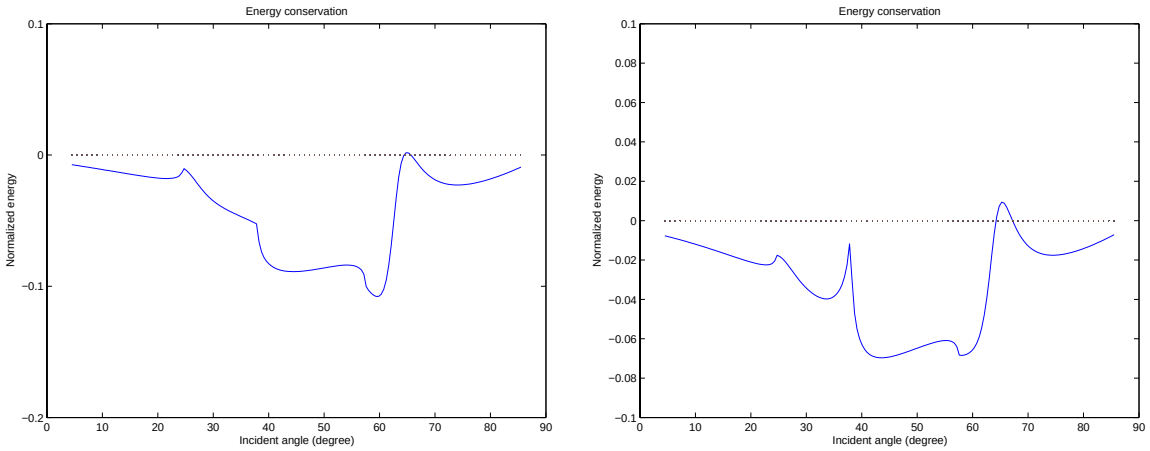

Figure 2: Computation of the first member of eq.19 as a function of the incidence angle and for two crack distributions at the interface chalk/granite (50% of cracks (left), 75% of cracks (right)).

Nathalie Favretto-Cristini
Centre National de la Recherche Scientifique
Laboratoire d'Imagerie Géophysique (FRE 2639)
Université de Pau et des Pays de l'Adour
BP 1155, 64013 Pau Cedex, France
nathalie.favretto@univ-pau.fr

Ultrasonics 51 (2011) 653–660

Contents lists available at ScienceDirect

Ultrasonics

journal homepage: www.elsevier.com/locate/ultras

Elastic surface waves in crystals. Part 1: Review of the physics

Nathalie Favretto-Cristini [a,*], Dimitri Komatitsch [b,1], José M. Carcione [c], Fabio Cavallini [c]

[a] Laboratoire de Mécanique et d'Acoustique (UPR 7051), CNRS, 31 chemin Joseph Aiguier, 13402 Marseille Cedex 20, France
[b] Géosciences Environnement Toulouse (UMR 5563), UR 154 CNRS Université Paul Sabatier, Observatoire Midi-Pyrénées, 14 Avenue Édouard Belin, 31400 Toulouse, France
[c] Istituto Nazionale di Oceanografia e di Geofisica Sperimentale, Borgo Grotta Gigante 42c, 34010 Sgonico, Trieste, Italy

ARTICLE INFO

Article history:
Received 13 December 2010
Received in revised form 18 February 2011
Accepted 24 February 2011
Available online 1 March 2011

Keywords:
Surface waves
Anisotropy

ABSTRACT

We present a review of wave propagation at the surface of anisotropic media (crystal symmetries). The physics for media of cubic and hexagonal symmetries has been extensively studied based on analytical and semi-analytical methods. However, some controversies regarding surfaces waves and the use of different notations for the same modes require a review of the research done and a clarification of the terminology. In a companion paper we obtain the full-wave solution for the wave propagation at the surface of media with arbitrary symmetry (including cubic and hexagonal symmetries) using two spectral numerical modeling algorithms.

Contents

1. Introduction

The problem of surface wave (also called surface acoustic wave – SAW) propagation in anisotropic media has been studied for many decades. It is of interest in acoustics of materials, e.g., nondestructive testing of materials, where the anisotropic elastic properties of thin coatings or media containing subsurface cracks may be evaluated from measurements of the characteristics of laser-generated SAW [1–6], in exploration geophysics [7–9], and in seismology [10–13].

A homogeneous isotropic elastic half-space can accommodate three types of bulk waves: the P, SV and SH waves, whose polarization vector is either parallel (for the P-wave) or perpendicular (for the two S-waves) to the slowness vector. The polarization of the S-waves with respect to the free surface of the half-space is either vertical (for the SV-wave) or horizontal (for the SH wave). Only the P-wave and the SV-wave may be coupled at the flat free

* Corresponding author.
E-mail addresses: favretto@lma.cnrs-mrs.fr (N. Favretto-Cristini), dimitri.komatitsch@get.obs-mip.fr (D. Komatitsch), jcarcione@inogs.it (J.M. Carcione), fcavallini@inogs.it (F. Cavallini).
URL: http://www.univ-pau.fr/dkomati1 (D. Komatitsch).
[1] Also at Institut Universitaire de France, 103 boulevard Saint-Michel, 75005 Paris, France. Formerly at Université de Pau et des Pays de l'Adour, CNRS and INRIA, Laboratoire de Modélisation et d'Imagerie en Géosciences (UMR 5212) and IPRA, Avenue de l'Université, 64013 Pau Cedex, France.

0041-624X/$ - see front matter © 2011 Elsevier B.V. All rights reserved.
doi:10.1016/j.ultras.2011.02.007

surface of homogeneous isotropic elastic solids. A Rayleigh-type SAW resulting from the linear combination of the inhomogeneous P- and S-waves then travels along the free boundary of an isotropic half-space. It propagates without dispersion with a constant velocity close to the S-wave velocity of the medium [14,15]. The energy carried by this SAW, whose polarization is elliptical in the sagittal plane, is concentrated in a one-wavelength-thick waveguide just below the free surface [16]. A point source radiates, in addition to the P, S and Rayleigh wavefronts, an S head wave that connects the P and S-waves [17,18].

In the presence of anisotropy, wave propagation presents substantial differences compared to the isotropic case. The polarization vector of the three bulk waves is not necessarily parallel nor normal to the slowness vector. Except for specific propagation directions, the "quasi" P- and the two "quasi" S-waves may be coupled at the boundary of the elastic half-space and, contrary to the isotropic case, the SAW in anisotropic media may then result from the linear combination of three or two inhomogeneous bulk waves, or even from only one inhomogeneous bulk wave. The anisotropic behavior of the medium therefore considerably modifies the existence and the structure of the SAW that propagates at the free surface of the medium. The most striking change is that an anisotropic half-space, contrary to the isotropic case, can accommodate various supersonic SAWs (i.e., SAWs with at least one homogeneous bulk wave component), as will be shown below. Moreover, the properties of the SAW are mainly constrained by the orientation of the free surface and by the direction of propagation.

Anisotropy therefore induces considerable difficulties in analytically and explicitly studying wave propagation. Attempts to derive explicit secular equations have been reported in [19–27], but most of the methods used are only applicable to specific anisotropic media with a high level of symmetry and may have spurious roots that must be carefully analyzed and suppressed. Few problems in elastodynamics have a closed-form analytical solution and some can be investigated with semi-analytical methods, but often one cannot be sure if these methods give reliable solutions. Being able to accurately simulate wave propagation numerically is therefore essential in a wide range of fields, including ultrasonics, earthquake seismology and seismic prospecting where the systems generally possess anisotropic properties, described, in their most general form, by 21 elastic coefficients and by the mass density of the material.

In the following sections we review many aspects of harmonic and transient wave propagation in anisotropic media. In a companion paper [28] we use two full-wave numerical methods to solve the problem without any approximation regarding the type of symmetry nor the orientation of the free surface.

2. Harmonic fields

A survey of the extensive literature shows that most theoretical and experimental studies on SAW propagation in anisotropic solids have been conducted in the frequency domain, which allows a deeper understanding of the physical phenomena involved. Unfortunately the various surface waves are often given different names in different articles for the same kind of waves. In Appendix A we therefore review the different surface waves that can be present in anisotropic media, and the results obtained in previous works.

To our knowledge, SAWs in an anisotropic half-space were first studied by Sveklo [29], Stoneley [30], Gold [31], Deresiewicz and Mindlin [32], and Synge [33], followed by Gazis et al. [34], Buchwald [35] and Buchwald and Davies [36]. After deriving a complex secular equation and solving it by discarding some valid solutions, such as those associated with the *generalized Rayleigh wave* for instance (see more comments in Burridge [37] and Musgrave [38]), most of the authors concluded incorrectly that SAWs could travel either only in discrete directions, or in some well-defined regions, along symmetry planes of certain cubic materials. Later, Lim and Farnell [39] made extensive numerical computations and could not find the previously reported range of "forbidden" directions of SAW propagation along symmetry as well as non-symmetry planes of various crystals. This result was also confirmed by the thorough mathematical analysis of the complex secular equation presented in Burridge [37]. Moreover, Lim and Farnell [39,40] studied numerically the range of existence and the behavior of the various waves that can propagate at the free surface of cubic crystals. By analyzing the roots of the secular equation in the complex plane, they deduced the velocity, attenuation, displacement, and energy flow of the large variety of "surface waves" for any direction of propagation at the (001), (110), and (111) planes of cubic media. The review of Farnell [41] is an excellent concise survey of harmonic propagation of SAWs at the free surface of cubic media.

These results obtained based on computer studies have been strengthened by theoretical foundations making use of the so-called "sextic" formalism. This approach, now known as the Stroh formalism, stems from the analogy between elastic fields created by uniformly moving line dislocations and surface-wave propagation, initially recognized by Stroh [42], and subsequently extended by many researchers, including Barnett, Lothe and their collaborators [43–45]. By expressing the equation of motion and the stress–strain law as a linear system of six first-order ordinary differential equations with respect to the six-dimensional polarization–traction vector, the sextic state-vector formalism reformulates the SAW problem into a standard eigenvalue problem [46,47]. The six eigenvectors represent six inhomogeneous waves. The three eigenvectors that are associated with physical solutions are directly related to the waves whose linear combination results in SAW solutions (see Barnett [48] for a concise description of the Stroh formalism for steady waves). Under the framework of the Stroh formalism, the criteria for the existence of the different kinds of waves that can propagate at the free surface of an anisotropic elastic half-space have been thoroughly discussed in many articles, and general theorems have been established.

Limiting bulk waves (LBW) are waves propagating along the surface of an anisotropic half-space with threshold velocities, namely the so-called limiting velocities. These waves exist for any crystallographic orientation, and their velocity can easily be determined geometrically from the analysis of the cross-section of the slowness surfaces of the three bulk waves at the sagittal plane. The successive limiting velocities are given by the tangential contact between the slowness branches and the normal to the free surface. The limiting velocities are therefore the lowest velocities for bulk wave propagation and the LBWs carry energy along the surface [49]. In an isotropic medium the velocity of the slowest LBW is just the S-wave velocity. The velocity V_{lim} of the slowest LBW plays a key role in the general theory of SAW propagation in anisotropic media, as it constitutes the transition between the subsonic region, where wave velocities V are smaller than V_{lim} and the eigenvalues of the SAW problem are three pairs of complex conjugates, and the supersonic region where wave velocities V are higher than V_{lim}. At the limit V_{lim}, called the first transonic state [48], one of the conjugate pairs coalesces into one degenerate eigenvalue that in the supersonic region splits into a pair of different real eigenvalues.

The *exceptional limiting bulk waves* (EBW), also improperly called the *exceptional bulk waves* (see Appendix A), also play a central role, as will be shown below. Such waves are in fact particular LBWs whose polarization vector always lies in the plane that bounds the anisotropic medium, and which satisfy the boundary conditions at the surface of the anisotropic half-space. In that

sense, they are similar to the so-called *surface skimming bulk wave* in isotropic half-spaces [48,50,51], the SH wave being a particular example of such a surface skimming bulk wave, and then a particular case of EBW. Nevertheless, contrary to the isotropic case, EBWs can be either quasi-S-waves or quasi-P-waves, and they are truly "exceptional" in the sense that they occur only for isolated directions of propagation on certain orientations of the crystal surface. For very simple cases such as high symmetry configurations (e.g., the [100] or [110] directions on the (001) surface of a cubic crystal), they are just an SH type.

In anisotropic media there is a large variety of SAWs that can be either subsonic or supersonic, contrary to the isotropic case. Two types of classifications have been proposed. The first is based on the degeneracies in the Stroh formalism [52–55], while the second is formulated in terms of the number of inhomogeneous (and homogeneous) bulk waves involved in the construction of the SAW solution. In the more general case when the free surface is not a symmetry plane of the anisotropic material, the SAW consists of a linear combination of three inhomogeneous waves. Yet, following the behavior of the roots of the characteristic equation and the value of the coefficients of the linear combination, the SAW can be composed of three, two, or even simply one inhomogeneous wave, contrary to the isotropic case. The SAWs are thus classified into three types: three-component, two-component, and one-component SAW. For instance, for some specific directions of propagation, such as symmetry planes, one bulk wave is not coupled with the two others, and only two of the three bulk waves are therefore involved in the construction of the SAW. As an example, one can mention the subsonic two-component SAW, which cannot be polarized parallel to the free boundary plane in stable anisotropic linear elastic half-spaces [56]. It has been proven that there exists at most one such "pure" SAW solution in the subsonic domain for a given geometry of propagation. As for the isotropic case, the pure SAW results from a linear combination of only two inhomogeneous bulk waves whose amplitude decays exponentially and monotonically away from the surface. This subsonic two-component Rayleigh wave (RW) exists, provided an EBW does not exist, otherwise a subsonic two-component generalized RW (see Appendix A), whose amplitude decays exponentially but with oscillations away from the surface, may or may not arise [45,46,57,58].

A SAW undamped in the direction of propagation is intrinsically a subsonic phenomenon. Nevertheless, contrary to the isotropic case, pure undamped two-component SAWs can propagate with supersonic velocity for some specific directions of propagation on the free surface of materials of various degrees of symmetry. The *symmetrical supersonic surface waves* (symmetrical SSW) (see Appendix A) are the first kind of two-component waves that can exist in the supersonic region. They can occur in so-called α-configurations [59–62], in which the so-called reference plane $\mathfrak{R}$, spanned by the normal $\hat{\mathbf{n}}$ to the surface and the propagation direction $\hat{\mathbf{m}}$, coincides with a plane of material symmetry [63]. For instance for cubic materials the symmetrical SSW can only exist on the (001) and (110) planes [64]. For high-symmetry directions, such as the [110] direction on the (001) plane of a cubic crystal, such a wave is simply a supersonic SAW of generalized-Rayleigh type. A pure undamped (two-component) generalized Rayleigh wave may propagate with supersonic velocity for isolated cases usually corresponding to high-symmetry directions of propagation in which an EBW exists [41]. This wave, which can be considered as secluded from the subsonic branch of the SAW, is in fact a starting point for the branch of a *leaky SAW* [65–67].

For off-symmetry directions, the elastodynamics equations of motion having both inhomogeneous and homogeneous wave solutions, the (three-component) leaky SAW radiates its energy towards the bulk of the anisotropic medium (see Appendix A), as the leaky Rayleigh waves do at specific liquid–solid interfaces [68]. The velocity of the leaky SAW and the magnitude of its attenuation along the direction of propagation strongly depend on the perturbation of the orientation from the symmetry direction [69], but for many cases the radiation of energy is small enough that the leaky SAWs are easily observable in experimental conditions [70,71]. As the orientation of the direction of propagation approaches high-symmetry directions, the contribution of the bulk homogeneous wave in the construction of the SAW may however vanish, together with the damping of the leaky SAW in the direction of propagation, and the (three-component) leaky SAW turns into a generalized RW. The leaky SAW can originate either from a (two-component) generalized RW (as is the case for the (001) plane of copper [41]), or from an EBW [72] by a resonance phenomenon [73,74] (as is the case for the (111) plane of copper [41]). Note that solutions of leaky-SAW type occur neither in isotropic media, nor in weakly anisotropic media (see Farnell [41], p. 164). Along the leaky SAW branch there may exist other isolated points where the contribution of the bulk homogeneous wave in the construction of the SAW may vanish, together with the damping of the leaky SAW [75,76], leaving a pure undamped two-component (non-symmetrical) supersonic SAW. This wave can be considered as secluded from the branch of the subsonic SAW, and it is then called the *secluded supersonic surface wave* (secluded SSW [77–79]) (see Appendix A).

The existence and the properties of SAW in anisotropic media are mainly constrained by the orientation of the free surface and by the direction of propagation. This fact is well illustrated by the secluded (non symmetrical) SSW. Indeed, this wave cannot propagate in the α-configuration [63,67,76]. Nevertheless, this kind of wave may propagate when the free boundary of the anisotropic half-space is a symmetry plane (the so-called β-configuration [63]), or when the plane perpendicular to the reference plane and to the direction of wave propagation is a symmetry plane (the so-called γ-configuration [63,67,76]). The secluded SSW generally exists for a direction for which there is also a subsonic RW [77]. This is precisely the case, for instance, for the (001) plane of cubic crystals [67]. Its occurrence has been investigated in a more general case by Maznev and Every [79] for a germanium crystal. It has been found to exist for a one-dimensional subspace, within the three-dimensional space of SAW geometries (i.e. surface orientations and propagation directions).

Contrary to the subsonic domain, a *one-component SAW* (see Appendix A), consisting of one inhomogeneous wave that satisfies the boundary condition at the surface of the anisotropic half-space, can exist in the supersonic region in an arbitrarily anisotropic crystal under certain conditions depending on the value of the elastic coefficients of the medium [60,80]. General existence theorems for such waves that do not exist in isotropic materials have also been established for anisotropic media with symmetry in many studies. No one-component SAW generally exists in α-, β-, or γ-configurations [60,81,82], except for particular triclinic materials [80] and for some orthorhombic and some transversely-isotropic (TI) materials [83]. More specifically, a one-component SAW cannot travel in stable TI media whose symmetry axis coincides with the direction of propagation [81,84]. It has also been shown that no one-component SAW can exist in stable cubic materials [81,84].

In the subsonic region, a kind of SAW arises in the neighborhood of the directions of propagation that permit the existence of an EBW [49] and therefore, following the condition for the existence of RW established by Barnett and Lothe [44], in the neighborhood of orientations for which a subsonic RW cannot propagate [85]. The so-called *quasi-bulk surface wave* (QBSW) (see Appendix A) can be viewed as a continuous transition from the RW towards the EBW, through non-pure SAW with particle displacements not occurring in the sagittal plane and energy flux not being collinear with the

propagation vector. Near the symmetry directions where an EBW can propagate, the SAW is transformed into a QBSW with a depth of penetration that increases for decreasing angles of deviation from the symmetry directions. The penetration of the wave into the crystal may become so large that the term "surface wave" can be misleading. In fact, the QBSW results from the (very) small contribution of two inhomogeneous waves and the predominant contribution of one wave whose characteristics differ slightly from those of the EBW. The properties of the QBSW, which are thus strongly related to the associated EBW, have been studied for crystals of hexagonal [85] and arbitrary [86] symmetries. In particular the phase velocity of the QBSW is found to be slightly smaller than the associated limiting velocity of the bulk waves.

Many authors have emphasized the close connection between the space of simple reflection and the space of degeneracy in the Stroh eigenvalue problem and in SAW problems [41,53,69,76,78,83,87,88].

3. Transient propagation

Whereas harmonic wave propagation at the free surface of anisotropic media has been widely investigated, research on transient wave propagation is rather scarce. The so-called Lamb's problem [89] is the study of the response of an elastic half-space to an impulsive line or point load at its surface. The fundamental solution for a homogeneous isotropic elastic material, both in the frequency and in the time domains, is classical [89,90]. Unfortunately, anisotropy introduces considerable difficulty in generalizing this solution. A convenient way of deriving the displacement Green's functions of anisotropic materials is to use integral transform techniques, and more specifically mixed Fourier–Laplace transforms. Several researchers have used the Cagniard-de Hoop (CdH) method [91–93] to reduce the Fourier–Laplace transforms to a single integral over a contour in a complex plane that must be determined. Kraut [94] first applied this method to study the 2D Lamb's problem for a line source of normal stress lying on the free surface of a TI medium (a beryl crystal) normal to the axis of symmetry. Burridge [95] extended the technique to the most general class of anisotropic solids and to a surface of arbitrary orientation loaded by an impulsive line traction. Only numerical results were presented for the surface displacement at the (111) plane of cubic copper, and the RW and leaky SAW were identified. The case of a point source, applied at the surface of TI solids with its normal coinciding with the axis of symmetry, has been treated in a similar way by Ryan [96]. In contrast with the 2D problem, the 3D Lamb's problem does not admit an explicit solution for the surface displacements. They are then found in terms of single finite integrals that must be evaluated numerically. In Payton [97], 2D and 3D problems of transient wave propagation in TI half-spaces that admit an explicit representation of the displacement field are studied. In particular, the epicenter motion of the surface due to a buried point source located on the symmetry axis, and the epicentral-axis motion caused by a normal point load suddenly applied on the surface, are explicitly evaluated based on residue calculations in the complex plane. They are also shown to be related by the Betti–Rayleigh theorem. More recently, Deschamps and his co-authors used the CdH technique to calculate the interior and the surface responses of a general cubic half-space to line and point loadings [98–101]. By analyzing the CdH contours and the singular points in the complex plane, they observed physical phenomena such as wavefront focusing for both the RW and the EBW as well as the diffraction caused by the cusps and the possible generation of the leaky SAW. Numerical calculations of only the normal component of the displacement (used in laboratory laser experiments) have been performed for a half-space belonging to the cubic class of symmetry. For instance, results for the (100) surface of a copper crystal and several directions of observation are shown in Bescond and Deschamps [100,101].

As for the anisotropic case the CdH technique requires the analysis of complicated branch-cut integrals in the complex plane, it is considered too cumbersome to be numerically handled and therefore alternative methods have been proposed. One of them, first developed by Willis [102] and then used by Wang and Achenbach [103–106], uses Fourier and Radon transforms. It is based on a direct construction of the solution to the 3D Lamb's problem for general anisotropic solids by a superposition of time-transient plane waves. It allows one to obtain integral expressions defined in a finite domain that corresponds to the projection of the slowness surface to the surface of the solid. Unfortunately, their calculations have not emphasized the cuspidal structure in the Rayleigh wavefront, as well as the existence of the leaky SAW. In a similar way, Tewary and Fortunko [107] derived an expression for the 3D waveforms due to a delta-function pulse on the free surface of tetragonal solids, convenient for numerical computations as it requires only a 1D numerical integration. Another alternative method to the CdH technique is based on Fourier transforms of the equations of motion and boundary conditions, with respect to the time and the spatial coordinates parallel to the surface. The surface displacement response of an anisotropic half-space to sudden loading at a point on the surface is then reduced to a 1D integral for numerical evaluation [108]. The method used by Every and his collaborators can cope with Rayleigh poles and leaky SAW resonances, as shown by the good agreement between the calculated surface displacement responses to a point loading for several directions on the (001)-oriented surface of copper crystal and measured surface waveforms [109]. More precisely, multiple RW arrivals resulting from the folding of the SAW ray surface associated with sharp peaks in the SAW amplitude expressing caustics in the SAW intensity, and then the so-called "phonon focusing effect" [110–115], have been predicted and observed experimentally, as well as leaky SAW resonance and singularities in bulk wave arrival associated with the presence of EBW. In the case of a general anisotropic half-space subjected to an impulsive line load, Maznev and Every [116] derived results similar to those reported by Burridge [95] by using Fourier transforms. They illustrated the role of SAW, leaky SAW and bulk waves in the calculated surface response for the (111)-oriented surface of silicon. The studies providing the dynamic displacement response of the (001)-, (110)-, and (111)-oriented surface of copper crystal, developed by [5,100,101,109], will be used as a reference in our numerical study reported in a companion paper.

4. Conclusions

We provided a review of harmonic and transient elastic wave propagation in anisotropic media with particular emphasis on surface-wave propagation in crystals, minerals and metals. This review clarifies the terminology used for the surface waves. In a companion paper we propose two spectral numerical modeling algorithms to obtain the full-wave solution for the wave propagation at the surface of media with arbitrary symmetry.

Acknowledgements

The authors thank Alexander Shuvalov and Arthur G. Every for fruitful discussion, and an anonymous reviewer for suggesting additional references.

This material is based in part upon research supported by European FP6 Marie Curie International Reintegration Grant MIRG-CT-2005-017461.

Appendix A. Waves propagating at the free surface of an anisotropic half-space

SAWs propagating along the free surface of an anisotropic elastic half-space result from the linear combination of three bulk waves, which are generally damped with depth. The associated displacement field $\mathbf{u}(\mathbf{r},t)$ can be written as:

$$\mathbf{u}(\mathbf{r},t) = \sum_{n=1}^{3} C_n \mathbf{A}_n \exp[ik(\mathbf{m}\cdot\mathbf{r} + p_n \mathbf{n}\cdot\mathbf{r} - Vt)] \quad \text{(A.a)}$$

where $\mathbf{r}$ is the space vector and t the time variable. The coefficients C_n of the linear combination for the three bulk waves are determined from the boundary conditions at the free surface and can be real- or complex-valued. They characterize the wave amplitude up to an arbitrary infinitesimal factor, while the vectors $\mathbf{A}_n$ denote their polarization. The wavenumber k, associated with the phase velocity V, is the projection of the wave vector $\mathbf{k}$ of the SAW on the direction of propagation $\mathbf{m}$ at the free surface of the anisotropic half-space. Vector $\mathbf{n}$ denotes the normal to the surface of the medium. Parameters $p_n = \mathbf{k}\cdot\mathbf{n}/\mathbf{k}\cdot\mathbf{m}$ are complex-valued in the subsonic region, while in the supersonic region at least one p_n lies on the real axis of the complex plane and is associated with a bulk wave. Depending on the values of C_n and p_n, the SAW consists of one, two, or three-components. There is a large variety of SAWs that can propagate at the free surface of anisotropic materials, therefore let us review them here.

A.1. Exceptional (limiting) bulk wave (EBW)

Strictly speaking, the exceptional bulk waves (EBW) [46,117] are bulk waves that satisfy the boundary conditions at the free surface of the anisotropic medium, and whose polarization vector always lies in the plane that bounds the medium [118]. Unlike the limiting bulk waves (LBW), these waves are in fact eigensolutions for the SAW problem. In most articles the term EBW is however improperly used for the particular EBW that propagates with the limiting velocity $V_{\lim}$, instead of the term "exceptional limiting bulk waves", although the exceptional limiting bulk waves are in fact a subset of the broader class of EBW. The exceptional limiting bulk waves then combine the properties of the EBW (namely, polarization parallel to the free surface of the medium, and boundary conditions satisfied at the free surface) with those of the limiting bulk waves (namely, propagation at the limiting velocity, and energy flux parallel to the crystal surface [45]). Hereafter and in the article, the exceptional limiting bulk waves are denoted by EBW. Though propagating along the surface, unlike SAWs the EBWs do not decrease in amplitude as the distance from the surface increases. Their presence is a general feature of general anisotropic crystals, and it is not limited to media with high symmetry only [118–121]. The EBWs are quite similar to the so-called surface skimming bulk waves in isotropic solids [48,50,51], SH waves being a particular case of such surface skimming bulk waves. Nevertheless, unlike these waves, EBWs are not limited to definite kinds of bulk waves [48]: they can be quasi-P or quasi-S-waves, provided that their polarization vector lies in the plane that bounds the medium. While quasi-S EBWs exist in all crystals, only few anisotropic media permit the propagation of quasi-P EBWs [51]. Moreover, EBWs satisfy the boundary conditions at the surface of the anisotropic half-space only for specific directions.

EBWs are also termed "improper SAWs", "bulk surface waves" [45], or even "surface skimming bulk waves" [48,50,109,122]. The term "lateral waves" is also used [4] and should be understood as "grazing rays". The EBW should not be mistaken for head waves.

Composite EBWs [57] that are a superposition of two or three EBWs can exist for certain types of transonic states, according to the classification established by Chadwick and Smith [46] (see Barnett [48] for a detailed discussion). Nevertheless, the EBW of the first kind described in Chadwick and Smith [46] and that is not composite is in fact the usual EBW defined in SAW theory.

A.2. Rayleigh wave (RW)

For an arbitrary free boundary surface and an arbitrary direction of propagation, the Rayleigh wave consists of a linear combination of three phase-matched evanescent waves whose amplitude decays exponentially and monotonically away from the surface. The RW is thus intrinsically a subsonic phenomenon. It then propagates undamped at the free surface of an elastic half-space with a subsonic velocity V_R that is slightly smaller than the limiting velocity $V_{\lim}$. The motion of the RW describes an ellipse that is generally tilted with respect to the sagittal plane. However, for symmetry directions, only two of the three waves are involved in the RW construction and the corresponding motion describing an ellipse occurs in the sagittal plane, as in the isotropic case. The energy carried by the RW is generally concentrated in a roughly one-wavelength-thick waveguide below the free surface for high-symmetry directions, but it can penetrate deeper in the bulk of the anisotropic medium for out-of-symmetry directions. The RW never coexists with an EBW propagating in the same direction, as in the isotropic case.

Because its properties are similar to those of a RW propagating at the free surface of an isotropic elastic medium, the RW is also called an "ordinary RW" [123], a "pure SAW" or "pure RW", or a "proper SAW" [44].

A.3. Generalized rayleigh wave (generalized RW)

The generalized Rayleigh wave is a kind of Rayleigh wave that can propagate with either a subsonic or supersonic velocity. It does not exist in isotropic media. Unlike the RW, it consists of two-components whose amplitude is non-monotonically damped towards the bulk of the anisotropic medium, but with an oscillatory trend [123,124]. The period of the oscillations of the amplitude as well as the penetration distance in the bulk of the medium and the velocity of the generalized RW depend on the so-called anisotropy parameter of the material. For instance, for the (0 0 1) plane of a cubic medium this parameter is characterized either by [125] $A = 2c_{44}/(c_{11} - c_{12})$, or by [123] $\eta = 1/A$, where c_{11}, c_{44}, and c_{12} are the three independent elastic coefficients of the anisotropic medium. It has been shown that the period of the oscillations decreases with increasing values of the anisotropy parameter [125] A, or decreasing values of parameter [123] η. Moreover, the velocity of the generalized RW decreases with decreasing values of parameter η. Approximate expressions for the phase velocity and the oscillation damping have been established for cubic media with $\eta < 1/4$ in Royer and Dieulesaint [125]. Usually, the generalized RW propagates undamped in the direction of propagation with a subsonic velocity and its polarization is elliptical in the sagittal plane. Nevertheless, the generalized RW can also be a two-component supersonic wave for isolated cases corresponding usually to high-symmetry directions of propagation [41]. In this case, it generally belongs to the branch of a leaky SAW [65,76]. Contrary to the RW, the generalized RW may coexist with an EBW propagating in the same direction.

The RW and the generalized RW cannot coexist. For instance, for cubic materials and depending on the anisotropy parameter η, the RW that propagates along symmetry directions on high-symmetry boundary surfaces can be either ordinary or generalized. Kosevich et al. [123,124,126] have analyzed the conditions under which the transition from an ordinary RW to a generalized RW takes place in cubic crystals for various values of the anisotropy

parameter η. Their work strengthens the numerical study of Gazis et al. [34]. The transition occurs at a particular value ($\eta = \eta_0 \simeq 1$) for which there is degeneracy of the roots of the characteristic equation for the bulk vibrations. The region $\eta < \eta_0$ corresponds to the existence of the generalized RW, while the region $\eta > \eta_0$ corresponds to the existence of the ordinary RW. It has been shown [124] that the non-convexity of the cross-section of the slowness surface of the bulk shear wave, polarized in the sagittal plane, is a sufficient but not a necessary condition for the existence of a generalized RW. In highly anisotropic crystals (i.e., for instance with $\eta \ll 1$), one of the two components involved in the construction of the generalized RW can become dominant, have an almost linear polarization normal to the free surface, and can penetrate into the crystals to a depth significantly greater than the wavelength. The generalized RW can thus possess the properties of both the bulk wave and the pure RW, whose penetration depth is about the wavelength. Such a wave is called the deeply penetrating RW (DPRW) and has been thoroughly investigated by Kosevich et al. [126] in the case of wave propagation along the [100] direction on the (001) plane of a cubic crystal. However, the DPRW can propagate in crystals characterized by a strong anisotropy of the velocity of bulk shear waves polarized in other sagittal planes as well [124].

The generalized RW is also sometimes called "Rayleigh wave" by Lothe and his collaborators, which may be confusing.

A.4. Quasi-bulk surface wave (QBSW)

The quasi-bulk (surface) wave arises in the neighborhood of the direction of propagation at which an EBW exists. The criterion for the existence (respectively, absence) of the QBSW in the neighborhood of symmetry orientations is then the absence (respectively, existence) of subsonic RWs propagating in the symmetry direction [85]. At small deviation from this symmetry direction, the bulk wave associated with the EBW is dominant in the construction of a three-component SAW and the three partial wave combination as a whole is referred to as a QBSW. In fact, the QBSW can be considered as a gradual change of the SAW into the EBW. Its polarization vector tilts towards the free surface of the anisotropic half-space. Furthermore, the smaller the angle of deviation from the symmetry orientation, the less damped the wave is into the medium, i.e., the wave penetrates deeper.

This is the reason why the QBSW is also called "quasi-bulk Rayleigh wave" [86], or "deeply penetrating Rayleigh wave" [5], which may lead to confusions with the terminology used by Kosevich and his collaborators to describe the behavior of RW in crystals with strong anisotropy [126].

A.5. Leaky surface acoustic wave (leaky SAW)

The leaky wave is a solution to the boundary-value problem in the form of a linear combination of two inhomogeneous waves and one bulk wave that radiates energy into the anisotropic medium. The leaky SAW is inherently a supersonic phenomenon, and its velocity lies between the first and second limiting velocities. This wave propagates damped in the direction of propagation. Nevertheless, as for many cases the radiation of energy is small enough, the leaky SAW can easily be observable in experimental conditions [70,71]. Its properties are quite similar to those of a leaky SAW propagating at the interface between an ideal fluid and an isotropic elastic medium [68,127]. Note that this kind of wave does not exist in an isotropic half-space. Approximate expressions for its velocity and the magnitude of its attenuation along the direction of propagation are given without any assumption on the symmetry of the crystal in [69]. The leaky SAW can be caused by a generalized RW or by an EBW [69,72,75].

The leaky SAW is also called "pseudo SAW" [85], or "supersonic wave".

A.6. Secluded supersonic surface wave (secluded SSW)

The secluded supersonic surface wave exists at the so-called pure points where the damping of the leaky wave in the direction of propagation vanishes together with the coefficient of the linear combination associated with the bulk wave. This results in a two-component (non-symmetrical) supersonic surface wave that generally exists for a specific direction along which a subsonic Rayleigh wave can also propagate [77–79]. It can be seen as due to confluence between the space of simple reflection and the leaky SAW branch [67,76,83,128].

The secluded SSW is also called "non-symmetrical supersonic wave" [79].

A.7. One-component surface acoustic wave (one-component SAW)

Mathematically, it is represented by degeneracy in the Stroh eigenvalue problem [60]. The one-component surface wave consists of only one inhomogeneous wave and is necessarily supersonic. There are three versions of the one-component SAW [83]. Two are polarized in the plane of the boundary of the anisotropic half-space [60,80]. The third is a supersonic generalized one-component surface wave similar to the generalized Rayleigh wave studied in Kosevich et al. [123]. No one-component SAW exists for either isotropic elastic materials, or crystals of cubic symmetry [81,84]. This kind of wave can occur under certain conditions for particular triclinic media [80] as well as for some particular TI media [81,83,84]. The one-component SAW can be seen as due to confluence between the space of degeneracy and a two-component secluded SSW [83].

A.8. Symmetrical surface waves (symmetrical SAW)

Symmetrical surface waves are necessarily two-component SAWs that can occur in both the subsonic and the supersonic regions when the sagittal plane in which they are polarized is a plane of symmetry of the material [59,60,66]. They form a continuous branch extending from the subsonic region into the supersonic region and occurring in materials of monoclinic, orthorhombic and cubic symmetry [61,62]. For high-symmetry directions on symmetry planes, such waves are typically of RW or generalized-RW type.

References

[1] B. Castagnéde, Y. Berthelot, Photoacoustic interactions by modulation and laser impact: applications in mechanics and physics of anisotropic solids, Journal d'Acoustique 5 (1992) 417–453.
[2] J.F. Chai, T.T. Wu, Determination of anisotropic elastic constants using laser-generated surface waves, Journal of the Acoustical Society of America 95 (1994) 3232–3241.
[3] D.C. Hurley, V.K. Tewary, A.J. Richards, Surface acoustic wave methods to determine the anisotropic elastic properties of thin films, Measurement Science Technology 12 (2001) 1486–1494.
[4] A.G. Every, Measurement of the near-surface elastic properties of solids and thin supported films, Measurement Science Technology 13 (2002) R21–R39.
[5] A.G. Every, M. Deschamps, Principal surface wave velocities in the point focus acoustic materials signature $V(z)$ of an anisotropic solid, Ultrasonics 41 (2003) 581–591.
[6] K. van Wijk, D. Komatitsch, J.A. Scales, J. Tromp, Analysis of strong scattering at the micro-scale, Journal of the Acoustical Society of America 115 (3) (2004) 1006–1011, doi:10.1121/1.1647480.
[7] J.M. Carcione, Domain decomposition for wave propagation problems, Journal of Scientific Computing 6 (4) (1991) 453–472.
[8] S. Hestholm, B. Ruud, 2D finite-difference elastic wave modelling including surface topography, Geophysical Prospecting 42 (1994) 371–390.
[9] E. Tessmer, D. Kosloff, 3-D elastic modeling with surface topography by a Chebyshev spectral method, Geophysics 59 (3) (1994) 464–473.

[10] M.D. Trifunac, Surface motion of a semi-cylindrical alluvial valley for incident plane *SH* waves, Bulletin of the Seismological Society of America 61 (1971) 1755–1770.
[11] M. Bouchon, Effect of topography on surface motion, Bulletin of the Seismological Society of America 63 (1973) 615–632.
[12] S. Crampin, D.B. Taylor, The propagation of surface waves in anisotropic media, Geophysical Journal International 25 (1–3) (1977) 71–87.
[13] S.J. Lee, H.W. Chen, Q. Liu, D. Komatitsch, B.S. Huang, J. Tromp, Three-dimensional simulations of seismic wave propagation in the Taipei basin with realistic topography based upon the spectral-element method, Bulletin of the Seismological Society of America 98 (1) (2008) 253–264, doi:10.1785/0120070033.
[14] L. Knopoff, On Rayleigh wave velocities, Bulletin of the Seismological Society of America 42 (1952) 307–308.
[15] L. Landau, E. Lifchitz, Théorie de l'élasticité (Theory of Elasticity), second ed., Mir, Moscow, Russia, 1953.
[16] I.A. Viktorov, Rayleigh and Lamb Waves: Physical Theory and Applications, Plenum Press, New-York, USA, 1967.
[17] W.L. Pilant, Elastic Waves in the Earth, Developments in Solid Earth Geophysics Series, vol. 11, Elsevier Scientific Publishing Company, Amsterdam, The Netherlands, 1979.
[18] J.M. Carcione, Modeling anelastic singular surface waves in the earth, Geophysics 57 (6) (1992) 781–792.
[19] P.K. Currie, The secular equation for Rayleigh waves on elastic crystals, Quarterly Journal of Mechanics and Applied Mathematics 32 (1979) 163–173.
[20] D.B. Taylor, P.K. Currie, The secular equation for Rayleigh waves on elastic crystals. II Corrections and additions, Quarterly Journal of Mechanics and Applied Mathematics 34 (1981) 231–234.
[21] M. Destrade, The explicit secular equation for surface acoustic waves in monoclinic elastic crystals, Journal of the Acoustical Society of America 109 (4) (2001) 1398–1402.
[22] M. Destrade, Surface waves in orthotropic incompressible materials, Journal of the Acoustical Society of America 110 (2) (2001) 837–840.
[23] M. Destrade, Rayleigh waves in symmetry planes of crystals: explicit secular equations and some explicit wave speeds, Mechanics of Materials 35 (2003) 931–939.
[24] T. Ting, Explicit secular equations for surface waves in monoclinic materials with the symmetry plane $x1 = 0$, $x2 = 0$ or $x3 = 0$, Proceedings of the Royal Entomological Society of London Series A – General Entomology 458 (2002) 1017–1031.
[25] T.C.T. Ting, Explicit secular equations for surface waves in an anisotropic elastic half-space from Rayleigh to today, in: R. Goldstein, G. Maugin (Eds.), Surface Waves in Anisotropic and Laminated Bodies and Defects Detection, Kluwer Academic Publishers, Dordrecht, The Netherlands, 2004, pp. 95–116.
[26] T.C.T. Ting, The polarization vector and secular equation for surface waves in anisotropic elastic half-space, International Journal of Solids and Structures 41 (2004) 2065–2083.
[27] A. Mielke, Y.B. Fu, Uniqueness of the surface-wave speed: a proof that is independent of the Stroh formalism, Mathematics and Mechanics of Solids 9 (2004) 5–15.
[28] D. Komatitsch, J.M. Carcione, F. Cavallini, N. Favretto-Cristini, Elastic surface waves in crystals – Part 2: Cross-check of two full-wave numerical modeling methods, Ultrasonics, submitted for publication.
[29] V.A. Sveklo, Plane waves and Rayleigh waves in anisotropic media, Doklady Akademii Nauk SSSR 59 (1948) 871–874.
[30] R. Stoneley, The propagation of surface elastic waves in a cubic crystal, Proceedings of the Royal Society of London, United Kingdom A232 (1955) 447–458.
[31] L. Gold, Rayleigh wave propagation on anisotropic (cubic) media, Physical Review 104 (6) (1956) 1532–1536.
[32] H. Deresiewicz, R.D. Mindlin, Waves on the surface of a crystal, Journal of Applied Physics 28 (6) (1957) 669–671.
[33] J.L. Synge, Elastic waves in anisotropic media, Journal of Mathematical Physics 35 (1957) 323–335.
[34] D.C. Gazis, R. Herman, R.F. Wallis, Surface elastic waves in cubic crystals, Physical Review 119 (2) (1960) 533–544.
[35] V.T. Buchwald, Rayleigh waves in anisotropic media, Quarterly Journal of Mechanics and Applied Mathematics 14 (4) (1961) 461–468.
[36] V.T. Buchwald, A. Davis, Surface waves in elastic media with cubic symmetry, Quarterly Journal of Mechanics and Applied Mathematics 16 (1963) 283–293.
[37] R. Burridge, The directions in which Rayleigh waves may be propagated on crystals, Quarterly Journal of Mechanics and Applied Mathematics 23 (2) (1970) 217–224.
[38] M. Musgrave, Crystal Acoustics – Introduction to the Study of Elastic Waves and Vibrations in Crystals, Holden-Day, San Francisco, USA, 1970.
[39] T.C. Lim, G.W. Farnell, Search for forbidden directions of elastic surface wave propagation in anisotropic crystals, Journal of Applied Physics 39 (9) (1968) 4319–4325.
[40] T.C. Lim, G.W. Farnell, Character of pseudo-surface waves on anisotropic crystals, Journal of the Acoustical Society of America 45 (4) (1969) 845–851.
[41] G.W. Farnell, Properties of elastic surface waves, in: W.P. Mason, R.N. Thurston (Eds.), Physical Acoustics, vol. 6, Academic Press, New-York, USA, 1970, pp. 109–166 (Chapter 3).
[42] A.N. Stroh, Steady-state problems in anisotropic elasticity, Journal of Mathematical Physics 41 (1962) 77–103.
[43] D.M. Barnett, J. Lothe, K. Nishioka, R.J. Asaro, Elastic surface waves in anisotropic crystals: a simplified method for calculating Rayleigh velocities using dislocation theory, Journal of Physics F: Metal Physics 3 (1973) 1083–1096.
[44] D.M. Barnett, J. Lothe, Consideration of the existence of surface wave (Rayleigh wave) solutions in anisotropic elastic crystals, Journal of Physics F: Metal Physics 4 (1974) 671–686.
[45] J. Lothe, D.M. Barnett, On the existence of surface-wave solutions for anisotropic elastic half-spaces with free surface, Journal of Applied Physics 47 (1976) 428–433.
[46] P. Chadwick, G.D. Smith, Foundations of the theory of surface waves in anisotropic elastic materials, in: C.S. Yih (Ed.), Advances in Applied Mechanics, vol. 17, Academic Press, New-York, USA, 1977, pp. 303–376.
[47] T.C.T. Ting, Anisotropic Elasticity: Theory and Applications, Oxford University Press, United Kingdom, 1996.
[48] D.M. Barnett, Bulk, surface, and interfacial waves in anisotropic linear elastic solids, International Journal of Solids and Structures 37 (2000) 45–54.
[49] V.I. Alshits, J. Lothe, Surface waves in hexagonal crystals, Soviet Physics Crystallography 23 (1978) 509–515.
[50] S.V. Biryukov, Y.V. Gulyaev, V.V. Krylov, V.P. Plessky, Surface Acoustic Waves in Inhomogeneous Media, Springer Series on Wave Phenomena, vol. 20, Springer-Verlag, Berlin, Germany, 1995.
[51] N.F. Naumenko, Application of exceptional wave theory to materials used in surface acoustic wave devices, Journal of Applied Physics 79 (12) (1996) 8936–8943.
[52] T.C.T. Ting, D.M. Barnett, Classifications of surface waves in anisotropic elastic materials, Wave Motion 26 (1997) 207–218.
[53] L. Wang, Space of degeneracy in the Stroh eigensystem and surface waves in transversely isotropic elastic media, Wave Motion 40 (2004) 173–190.
[54] L. Wang, Extraordinary degeneracy and space of degeneracy in transversely isotropic elastic media, Wave Motion 45 (2008) 264–277.
[55] J. Lothe, V. Alshits, Surface waves, limiting waves and exceptional waves: David barnett's role in the development of the theory, Mathematics and Mechanics of Solids 14 (2009) 16–37.
[56] D.M. Barnett, On the non-existence of subsonic boundary-polarized two-component free surface waves, Physica Scripta T44 (1992) 98–103.
[57] D.M. Barnett, J. Lothe, Free surface (Rayleigh) waves in anisotropic elastic halfspaces: the surface impedance method, Proceedings of the Royal Society of London, United Kingdom A402 (1985) 135–152.
[58] T. Ting, Explicit conditions for the existence of exceptional body waves and subsonic waves in anisotropic elastic solids, Wave Motion 46 (2009) 323–335.
[59] P. Chadwick, The behaviour of elastic surface waves polarized in a plane of material symmetry. I. General analysis, Proceedings of the Royal Society of London, United Kingdom A430 (1990) 213–240.
[60] D.M. Barnett, P. Chadwick, J. Lothe, The behaviour of elastic surface waves polarized in a plane of material symmetry. I. Addendum, Proceedings of the Royal Society of London, United Kingdom A433 (1991) 699–710.
[61] P. Chadwick, N.J. Wilson, The behaviour of elastic surface waves polarized in a plane of material symmetry. II. Monoclinic media, Proceedings of the Royal Society of London, United Kingdom A438 (1992) 207–223.
[62] P. Chadwick, N.J. Wilson, The behaviour of elastic surface waves polarized in a plane of material symmetry. III. Orthorhombic and cubic media, Proceedings of the Royal Society of London, United Kingdom A438 (1992) 225–247.
[63] P. Chadwick, Wave propagation in transversely isotropic elastic media. II. Surface waves, Proceedings of the Royal Society of London, United Kingdom A422 (1989) 67–101.
[64] D.M. Barnett, S.D. Gavazza, J. Lothe, Slip waves along the interface between two anisotropic elastic half-spaces in sliding contact, Proceedings of the Royal Society of London, United Kingdom A415 (1988) 389–419.
[65] K.A. Ingebrigtsen, A. Tonning, Elastic surface waves in crystals, Physical Review 184 (3) (1969) 942–951.
[66] L. Wang, Existence of symmetric surface waves and their relation with leaky surface waves in cubic materials, Physica Scripta T44 (1992) 128–132.
[67] L. Wang, J. Lothe, Simple reflection in anisotropic elastic media and its relation to exceptional waves and supersonic surface waves: (II) examples, Wave Motion 16 (1992) 101–112.
[68] J.M. Carcione, H.B. Helle, On the physics and simulation of wave propagation at the ocean bottom, Geophysics 69 (2004) 825–839.
[69] A.N. Darinskii, On the theory of leaky waves in crystals, Wave Motion 25 (1997) 35–49.
[70] H. Engan, K.A. Ingebrigtsen, A. Tonning, Elastic surface waves in alpha-quartz: observation of leaky surface waves, Applied Physics Letters 10 (1967) 311–313.
[71] F.R. Rollins Jr., T.C. Lim, G.W. Farnell, Ultrasonic reflectivity and surface wave phenomena on surfaces of copper single crystals, Applied Physics Letters 12 (7) (1968) 236–238.
[72] A.N. Darinskii, V.I. Alshits, J. Lothe, Simple reflection and leaky waves in the vicinity of a line of exceptional bulk waves, Wave Motion 30 (1999) 253–274.
[73] A.N. Darinskii, Leaky waves and the elastic wave resonance reflection on a crystal-thin solid layer interface. II Leaky waves given rise to by exceptional bulk waves, Journal of the Acoustical Society of America 103 (1998) 1845–1854.
[74] A.N. Darinskii, M. Weihnacht, Acoustic waves in bounded anisotropic media: theorems, estimations, and computations, IEEE Transactions on Ultrasonics, Ferroelectrics, and Frequency Control 52 (5) (2005) 792–801.

[75] G.W. Farnell, Review of pseudo-surface waves, in: Proceedings of the Surface Waves in Solids and Layered Structures (ISSWAS86) International Symposium, vol. 3, Novosibirsk, Russia, 1986, pp. 7–20.
[76] L. Wang, J. Lothe, Simple reflection in anisotropic elastic media and its relation to exceptional waves and supersonic surface waves (I) general theoretical considerations, Wave Motion 16 (1992) 89–99.
[77] S.A. Gundersen, L. Wang, J. Lothe, Secluded supersonic elastic surface waves, Wave Motion 14 (1991) 129–143.
[78] J. Lothe, L. Wang, Self-orthogonal sextic formalism for anisotropic elastic media: spaces of simple reflection and two-component surface waves, Wave Motion 21 (1995) 163–181.
[79] A.A. Maznev, A.G. Every, Secluded supersonic surface waves in germanium, Physics Letters A197 (1995) 423–427.
[80] D.M. Barnett, P. Chadwick, The existence of one-component surface waves and exceptional transonic states of types 2, 4 and E1 in anisotropic elastic media, in: J.J. Wu, T.C.T. Ting, D.M. Barnett (Eds.), Modern Theory of Anisotropic Elasticity and Applications, SIAM, Philadelphia, USA, 1991, pp. 199–214.
[81] P. Chadwick, Some remarks on the existence of one-component surface waves in elastic materials with symmetry, Physica Scripta T44 (1992) 94–97.
[82] T.C.T. Ting, The motion of one-component surface waves, Journal of the Mechanics and Physics of Solids 40 (7) (1992) 1637–1650.
[83] L. Wang, S.A. Gundersen, Existence of one-component surface waves in anisotropic elastic media, Physica Scripta 47 (1993) 394–404.
[84] A.N. Norris, One-component surface waves in materials with symmetry, Journal of the Mechanics and Physics of Solids 40 (7) (1992) 1569–1582.
[85] J. Lothe, V.I. Alshits, Existence criterion for quasi-bulk surface waves, Soviet Physics Crystallography 22 (1977) 519–525.
[86] A.N. Darinskii, Quasi-bulk Rayleigh waves in semi-infinite media of arbitrary anisotropy, Wave Motion 27 (1998) 79–93.
[87] V.I. Alshits, J. Lothe, Comments on the relation between surface wave theory and the theory of reflection, Wave Motion 3 (1981) 297–310.
[88] V.I. Alshits, J. Lothe, Some basic properties of bulk elastic waves in anisotropic media, Wave Motion 40 (2004) 297–313.
[89] H. Lamb, On the propagation of tremors over the surface of an elastic solid, Philosophical Transactions of the Royal Society of London Series A – Mathematical and Physical Sciences 203 (1904) 1–42.
[90] J.D. Achenbach, Wave Propagation in Elastic Solids, North-Holland, Amsterdam, The Netherlands, 1973.
[91] L. Cagniard, Réflexion et Réfraction des Ondes Sismiques Progressives, Gauthiers-Villars, Paris, 1939.
[92] A.T. de Hoop, A modification of Cagniard's method for solving seismic pulse problems, Applied Science Research B8 (1960) 349–356.
[93] J.H.M.T. van der Hijden, Propagation of Transient Elastic Waves in Stratified Anisotropic Media, North-Holland, Amsterdam, The Netherlands, 1987.
[94] E.A. Kraut, Advances in the theory of anisotropic elastic wave propagation, Reviews of Geophysics 1 (3) (1963) 401–448.
[95] R. Burridge, Lamb's problem for an anisotropic half-space, Quarterly Journal of Mechanics and Applied Mathematics 24 (1) (1971) 81–98.
[96] R.L. Ryan, Pulse propagation in a transversely isotropic half-space, Journal of Sound and Vibration 14 (4) (1971) 511–524.
[97] R.G. Payton, Elastic Wave Propagation in Transversely Isotropic Media, Martinus Nijhoff, The Hague, The Netherlands, 1983.
[98] A. Mourad, M. Deschamps, Lamb's problem for an anisotropic half-space studied by the Cagniard-de Hoop method, Journal of the Acoustical Society of America 97 (5) (1995) 3194–3197.
[99] A. Mourad, M. Deschamps, B. Castagnéde, Acoustic waves generated by a transient line source in an anisotropic half-space, Acustica – Acta Acustica 82 (1996) 839–851.
[100] C. Bescond, M. Deschamps, Dynamical surface response of a semi-infinite anisotropic elastic medium to an impulsive force, Journal of the Acoustical Society of America 103 (1) (1998) 114–124.
[101] C. Bescond, M. Deschamps, Erratum to dynamical surface response of a semi-infinite anisotropic elastic medium to an impulsive force, Journal of the Acoustical Society of America 104 (1) (1998) 599.
[102] J.R. Willis, Self-similar problems in elastodynamics, Philosophical Transactions of the Royal Society of London, United Kingdom Series A 274 (1973) 435–491.
[103] C.Y. Wang, J.D. Achenbach, A new method to obtain 3D Green's functions for anisotropic solids, Wave Motion 18 (1993) 273–289.
[104] C.Y. Wang, J.D. Achenbach, Elastodynamic fundamental solutions for anisotropic solids, Geophysical Journal International 118 (1994) 384–392.
[105] C.Y. Wang, J.D. Achenbach, Three-dimensional time-harmonic elastodynamic Green's functions for anisotropic solids, Proceedings of the Royal Society of London, United Kingdom A-449 (1995) 441–458.
[106] C.Y. Wang, J.D. Achenbach, Lamb's problem for solids of general anisotropy, Wave Motion 24 (1996) 227–242.
[107] V.K. Tewary, C.M. Fortunko, Surface waves in three-dimensional half-space tetragonal solids, Journal of the Acoustical Society of America 100 (1) (1996) 86–88.
[108] A.G. Every, K.Y. Kim, A.A. Maznev, The elastodynamic response of a semi-infinite anisotropic solid to sudden surface loading, Journal of the Acoustical Society of America 102 (3) (1997) 1346–1354.
[109] A.G. Every, K.Y. Kim, A.A. Maznev, Surface dynamic response functions of anisotropic solids, Ultrasonics 36 (1998) 349–353.
[110] R.E. Camley, A.A. Maradudin, Phonon focusing at surfaces, Physical Review B 27 (4) (1983) 1959–1964.
[111] A.A. Kolomenskii, A.A. Maznev, Phonon-focusing effect with laser-generated ultrasonic surface waves, Physical Review B 48 (19) (1993) 14502–14512.
[112] A.A. Maznev, A.G. Every, Ray surface and focusing of surface acoustic waves on the basal plane of cubic crystals, Acta Acustica 1 (1994) 137–143.
[113] A.L. Shuvalov, A.G. Every, Transverse curvature of the acoustic slowness surface in crystal symmetry planes and associated phonon focusing cusps, Journal of the Acoustical Society of America 108 (5) (2000) 2107–2113.
[114] A. Maznev, A.M. Lomonosov, P. Hess, A.A. Kolomenskii, Anisotropic effects in surface acoustic wave propagation from a point source in a crystal, The European Physical Journal B 35 (2003) 429–439.
[115] L. Wang, Caustic and anticaustic points in the phonon focusing patterns of cubic crystals, Journal of the Acoustical Society of America 123 (6) (2008) 4140–4146.
[116] A.A. Maznev, A.G. Every, Time-domain dynamic surface response of an anisotropic elastic solid to an impulsive line force, International Journal of Engineering Science 35 (4) (1997) 321–327.
[117] P. Chadwick, G.D. Smith, Surface waves in cubic elastic materials, in: H.G. Hopkins, M.J. Sewell (Eds.), Mechanics of Solids, Pergamon Press, Oxford, United Kingdom, 1982, pp. 47–100.
[118] V.I. Alshits, J. Lothe, Elastic waves in triclinic crystals: (III) the problem of existence and some general properties of exceptional surface waves, Soviet Physics Crystallography 24 (1979) 644–648.
[119] V.I. Alshits, J. Lothe, Elastic waves in triclinic crystals: (I) general theory and the degeneracy problem, Soviet Physics Crystallography 24 (1979) 387–392.
[120] V.I. Alshits, J. Lothe, Elastic waves in triclinic crystals: (II) topology of polarization fields and some general theorems, Soviet Physics Crystallography 24 (1979) 393–398.
[121] V.I. Alshits, V.N. Lyubimov, N.F. Naumenko, N.V. Perelomova, A.L. Shuvalov, Exceptional elastic body waves in crystals of various symmetries, Soviet Physics Crystallography 30 (1985) 123–126.
[122] J. Lothe, L. Wang, Properties of type 6 transonic states with respect to grazing incidence reflection of bulk waves at planar free or clamped surfaces of half-infinite elastically anisotropic media, Wave Motion 20 (1994) 41–56.
[123] A.M. Kosevich, Y.A. Kosevich, E.S. Syrkin, Generalized Rayleigh waves and the geometry of isofrequency surfaces of sound oscillation waves in crystals, Soviet Physics – Journal of Experimental and Theoretical Physics 61 (1985) 639–644.
[124] Y.A. Kosevich, E.S. Syrkin, A.M. Kosevich, Vibrations localized near surfaces and interfaces in non-traditional crystals, Progress in Surface Science 55 (1) (1997) 59–111.
[125] D. Royer, E. Dieulesaint, Rayleigh wave velocity and displacement in orthorhombic, tetragonal, hexagonal, and cubic crystals, Journal of the Acoustical Society of America 76 (5) (1984) 1438–1444.
[126] Y.A. Kosevich, E.S. Syrkin, Existence criterion and properties of deeply penetrating Rayleigh waves in crystals, Soviet Physics – Journal of Experimental and Theoretical Physics 62 (6) (1985) 1282–1286.
[127] L.M. Brekhovskikh, O.A. Godin, Acoustics of layered media I, Springer Series on Wave phenomena, vol. 5, Springer-Verlag, Berlin, Germany, 1990.
[128] G. Stegeman, Normal-mode surface waves in pseudo-branch on (001) plane of gallium arsenide, Journal of Applied Physics 47 (1976) 1712–1713.

Bibliographie

[Aki et Richards, 2002] Aki, K. et Richards, P. (2002). *Quantitative seismology*. University Science Books, second édition. (Cit pages 12 et 15.)

[Ayzenberg *et al.*, 2007] Ayzenberg, M., Aizenberg, A., Helle, H., Klem-Musatov, K., Pajchel, J. et Ursin, B. (2007). 3D diffraction modeling of singly scattered acoustic wavefields based on the combination of surface integral propagators and transmission operators. *Geophysics*, 72(5):SM19–SM34. (Cit page 53.)

[Ayzenberg *et al.*, 2009] Ayzenberg, M., Aizenberg, A. et Ursin, B. (2009). Tip-wave superposition method with effective reflection and transmission coefficients : a new 3D Kirchhoff-based approach to synthetic seismic modeling. *The Leading Edge*, pages 582–588. (Cit pages 13 et 53.)

[Baik et Thompson, 1984] Baik, J.-M. et Thompson, R. (1984). Ultrasonic scattering from imperfect interfaces : a quasi-static model. *Journal of Nondestructive Evaluation*, 4(3/4):177–196. (Cit pages 21 et 39.)

[Bardainne, 2005] Bardainne, T. (2005). *Etude de la sismicité de Lacq et analyse des formes d'onde par décomposition en chirplets*. Thèse de doctorat, Université de Pau et des Pays de l'Adour. (Cit page 37.)

[Berkhout, 1984] Berkhout, A. J. (1984). *Seismic migration : Imaging of acoustic energy by wavefield extrapolation*. Elsevier. (Cit page 10.)

[Bonneau *et al.*, 2010] Bonneau, L., Fink, M. et Tourin, A. (2010). Retournement temporel, source virtuelle et monitoring de réservoirs de stockage de CO2. *In Actes du 10ème Congrès Français d'Acoustique, Lyon, 12-16 Avril 2010*. (Cit page 28.)

[Born et Wolf, 1999] Born, M. et Wolf, E. (1999). *Principles of Optics*. Cambridge University Press, 7th expanded. édition. (Cit page 16.)

[Broseta *et al.*, 2009] Broseta, D., Khalid, P., Nichita, D., Favretto-Cristini, N. et Blanco, J. (2009). A new look at seismic properties of low gas-saturated reservoirs. *In* 71^{st} *EAGE (European Association of Geoscientists and Engineers) Conference & Exhibition, Amsterdam (The Netherlands), 8 - 11 June 2009*. (Cit page 38.)

[Carcione, 2007] Carcione, J. (2007). *Wave fields in real media : Theory and numerical simulation of wave propagation in anisotropic, anelastic, porous and electromagnetic media*. Elsevier Science, 2nd édition. (Cit page 30.)

[Castagna, 1993] Castagna, J.-P. (1993). AVO-analysis, tutorial and review. *In* Castagna, J.-P. et Backus, M., éditeurs : *Offset-dependent reflectivity, theory and practice of AVO analysis*, volume 8 de *Investigations in Geophysics*, pages 3–36. SEG. (Cit page 6.)

[Chadwick, 2008] Chadwick, A. (2008). *Best practice for the storage of CO2 in saline aquifers : Observations and guidelines from the SACS and CO2STORE projects*. British Geological Survey. (Cit page 34.)

[Crandall, 1970] Crandall, S. (1970). On the use of slowness diagrams to represent wave reflections. *Journal of the Acoustical Society of America*, 47(5):1338–1342. (Cit page 40.)

[Cristini et Komatitsch, 2007] Cristini, P. et Komatitsch, D. (2007). The spectral element method as a tool for simulations in underwater acoustics. *In 8th International Conference on Theoretical Computational Acoustics Heraklion, Crete (Greece) 2-5 July 2007*. (Cit page 53.)

[Danicki, 1999] Danicki, E. (1999). Resonant phenomena in bulk-wave scattering by in-plane periodic cracks. *Journal of the Acoustical Society of America*, 105(1):84–92. (Cit page 21.)

[de Coulon, 2000] de Coulon, F. (2000). *Théorie et traitement des signaux*. Presses Polytechniques et Universitaires Romandes. (Cit page 7.)

[Deplanté, 2009] Deplanté, C. (2009). Spectral Fusion : A tool to merge low and high frequency datasets. *In International Petroleum Technology Conference, Doha (Qatar), 7-9 December 2009*. (Cit page 8.)

[Deschamps et Huet, 2009] Deschamps, M. et Huet, G. (2009). Complex surface rays associated with inhomogeneous skimming and Rayleigh waves. *International Journal of Nonlinear Mechanics*, 44:469–477. (Cit pages 30 et 32.)

[Dettmer *et al.*, 2007] Dettmer, J., Dosso, S. et Holland, C. (2007). Full wave-field reflection coefficient inversion. *Journal of the Acoustical Society of America*, 122(6):3327–3337. (Cit page 13.)

[Favretto-Cristini, 2004] Favretto-Cristini, N. (2004). *Monografias del Seminario Matematico Garcia de Galdeano*, volume 31, chapitre Wave scattering by a periodic array of in-plane cracks at the interface between dissimilar media, pages 469–478. (Cit page 21.)

[Favretto-Cristini *et al.*, 2007a] Favretto-Cristini, N., Cristini, P. et de Bazelaire, E. (2007a). Influence on the Interface Fresnel zone on the reflected P-wave amplitude modelling. *Geophysical Journal International*, 171:841–846. (Cit page 12.)

[Favretto-Cristini *et al.*, 2007b] Favretto-Cristini, N., Cristini, P. et de Bazelaire, E. (2007b). Some reflections on reflectors and wave amplitudes. *Acta Acustica*, 93:909–916. (Cit page 12.)

[Favretto-Cristini *et al.*, 2008] Favretto-Cristini, N., Cristini, P. et de Bazelaire, E. (2008). On the influence of the Interface Fresnel Zone for estimating media parameters from seismic Amplitude-versus-Angle curves. *In* Taroudakis, M. et Papadakis, P., éditeurs : *Theoretical and Computational Acoustics '07*, pages 139–148. (Cit page 13.)

[Favretto-Cristini *et al.*, 2009] Favretto-Cristini, N., Cristini, P. et de Bazelaire, E. (2009). What is a seismic reflector like ? *Geophysics*, 75(1):T13–T23. (Cit pages 9, 10 et 12.)

[Favretto-Cristini et de Bazelaire, 2003] Favretto-Cristini, N. et de Bazelaire, E. (2003). Pp amplitude bias caused by interface scattering : are diffracted waves guilty ? *Geophysical Prospecting*, 51:99–115. (Cit pages 21 et 22.)

[Favretto-Cristini *et al.*, 2011] Favretto-Cristini, N., Komatitsch, D., Carcione, J. et Cavallini, F. (2011). Elastic surface waves in crystals. Part 1 : Review of the physics. *Ultrasonics*, 51:653–660. (Cit pages 29 et 30.)

[Foster *et al.*, 2010] Foster, D., Keys, R. et Lane, F. (2010). Interpretation of AVO anomalies. *Geophysics*, 75(5):75A3–75A13. (Cit page 6.)

[French, 1974] French, W. (1974). 2D and 3D migration of model-experiment reflection profiles. *Geophysics*, 39(3):265–277. (Cit page 53.)

[Henry, 1994] Henry, G. (1994). *Géophysique des bassins sédimentaires*. Editions Technip. (Cit page 27.)

[Hubral et Krey, 1980] Hubral, P. et Krey, T. (1980). *Internal velocities from seismic reflection time measurements*. SEG. (Cit page 11.)

[Ishimaru, 1978] Ishimaru, A. (1978). *Wave propagation and scattering in random media*. Academic Press. (Cit page 16.)

[Kallweit et Wood, 1982] Kallweit, R. et Wood, L. (1982). The limits of resolution of zero-phase wavelets. *Geophysics*, 47(7):1035–1046. (Cit page 7.)

[Khalid, 2011] Khalid, P. (2011). *Effets de la relaxation thermo-élastique et de la transition de phase liquide/vapeur sur les propriétés sismiques*. Thèse de doctorat, Université de Pau et des Pays de l'Adour. (Cit page 38.)

[Klem-Musatov et Aizenberg, 1985] Klem-Musatov, K. et Aizenberg, A. (1985). Seismic modeling by methods of the theory edge waves. *Journal of Geophysics*, 57:90–105. (Cit page 13.)

[Komatitsch *et al.*, 2000] Komatitsch, D., Barnes, C. et Tromp, J. (2000). Simulation of anisotropic wave propagation based upon a spectral element method. *Geophysics*, 65(4):1251–1260. (Cit page 30.)

[Komatitsch *et al.*, 2011] Komatitsch, D., Carcione, J., Cavallini, F. et Favretto-Cristini, N. (2011). Elastic surface waves in crystals. Part 2 : Cross-check of two full-wave numerical modeling methods. *Ultrasonics*. (Cit page 30.)

[Komatitsch *et al.*, 2002] Komatitsch, D., Ritsema, J. et Tromp, J. (2002). The spectral-element method, Beowulf computing,and three-dimensional seismology. *Science*, 298:1737–1742. (Cit page 53.)

[Komatitsch et Vilotte, 1998] Komatitsch, D. et Vilotte, J. (1998). The spectral-element method : an effcient tool to simulate the seismic response of 2D and 3D geological structures. *Bulletin of the Seismological Society of America*, 88(2):368–392. (Cit pages 30, 41 et 53.)

[Kravtsov et Orlov, 1990] Kravtsov, Y. et Orlov, Y. (1990). *Geometrical optics of inhomogeneous media*. Springer Series on Wave Phenomena. Springer-Verlag, NY. (Cit page 11.)

[Kvasnička et Červený, 1996] Kvasnička, M. et Červený, V. (1996). Analytical expressions for Fresnel volumes and interface Fresnel zones of seismic body waves. Part 1 : Direct and unconverted reflected waves. *Studia Geophysica et Geodetica*, 40:136–155. (Cit page 11.)

[Lebon *et al.*, 2004] Lebon, F., Rizzoni, R. et Ronel-Idrissi, S. (2004). Asymptotic analysis of some non-linear soft thin layers. *Computers and Structures*, 82:1929–1938. (Cit page 52.)

[Levanon et Mozeson, 2004] Levanon, N. et Mozeson, E. (2004). *Radar signals*. John Wiley Sons. (Cit page 7.)

[Lindsey, 1989] Lindsey, J. (1989). The Fresnel zone and its interpretative significance. *The Leading Edge*, 8(10):33–39. (Cit page 10.)

[Lumley *et al.*, 2008] Lumley, D., Adams, D., Wright, R., Markus, D. et Cole, S. (2008). Seismic monitoring of CO2 geo-sequestration : realistic capabilities and limitations. *In SEG Annual Meeting - Las Vegas*. (Cit page 41.)

[Makindé, 2004] Makindé, W. (2004). *Amélioration de l'imagerie sismique sous des sédiments sous-compactés et des argiles mobiles en Delta du Niger*. Thèse de doctorat, Université de Pau et des Pays de l'Adour. (Cit page 17.)

[Makindé *et al.*, 2005] Makindé, W., Favretto-Cristini, N. et de Bazelaire, E. (2005). Numerical modeling of interface scattering of seismic wavefield from a random rough interface in acoustic medium : comparison between 2D and 3D cases. *Geophysical Prospecting*, 53(3): 373–397. (Cit page 18.)

[Margetan *et al.*, 1988] Margetan, F., Thompson, R. et Gray, T. (1988). Interfacial spring model for ultrasonic interactions with imperfect interfaces : theory of oblique incidence and applications to diffusion bonded butt joints. *Journal of Nondestructive Evaluation*, 7(3/4): 131–152. (Cit page 21.)

[Meur *et al.*, 2010] Meur, D. L., Benjamin, N., Twigger, L., Garceran, K., Delmas, L. et Poulain, G. (2010). Adaptive attenuation of surface-wave noise. *First Break*, 28:83–88. (Cit page 28.)

[Nichita *et al.*, 2010] Nichita, D., Khalid, P. et Broseta, D. (2010). Calculation of isentropic compressibility and sound velocity in two-phase fluids. *Fluid Phase Equilibria*, 291(1):95–102. (Cit page 38.)

[Ogilvy, 1991] Ogilvy, J. (1991). *Theory of wave scattering from random rough surfaces.* Institute of Physics Publishing. (Cit pages 16, 17 et 18.)

[Priolo *et al.*, 1994] Priolo, E., Carcione, J. et Seriani, G. (1994). Numerical simulation of interface waves by high-order spectral modeling techniques. *Journal of the Acoustical Society of America*, 95(2):681–693. (Cit page 30.)

[Rappin et Barnes, 2008] Rappin, D. et Barnes, C. (2008). Contribution to the understanding of field-specific seismic attenuation. *In SEG Annual Meeting Las Vegas.* (Cit page 16.)

[Rappin *et al.*, 2009a] Rappin, D., Barnes, C. et Samyn, K. (2009a). Contribution to the discrimination of field-specific seismic amplitude attenuation causes. *In EAGE/SEG Research Workshop "Frequency attenuation and resolution of seismic data", Barcelona (Spain), 14-15 september 2009*, Barcelona, Spain. (Cit page 16.)

[Rappin *et al.*, 2009b] Rappin, D., Castex, T., Paternoster, B. et Deplanté, C. (2009b). Seismic wavelet spectral enhancement : quantity or quality ? *In EAGE/SEG "Frequency attenuation and resolution of seismic data", Barcelona (Spain), 14-15 september 2009.* (Cit page 7.)

[Revaux, 2005] Revaux, C. (2005). *Simplification des modéles et du tracé de rais en sismique via la Théorie de l'Information et le Traitement du Signal : Application en tectonique complexe.* Thèse de doctorat, Université de Pau et des Pays de l'Adour. (Cit page 7.)

[Rokhlin et Wang, 1991] Rokhlin, S. et Wang, Y. (1991). Analysis of boundary conditions for elastic wave interaction with an interface between two solids. *Journal of the Acoustical Society of America*, 80(2):585–590. (Cit page 21.)

[Schleicher *et al.*, 2001] Schleicher, J., Tygel, M., Ursin, B. et Bleistein, N. (2001). The Kirchhoff-Helmholtz integral for anisotropic elastic media. *Wave Motion*, 34:353–364. (Cit page 53.)

[Schulbaum, 1996] Schulbaum, L. (1996). *Traduction des surfaces stratigraphiques et des géométries deltaiques lors du passage de l'échelle puits á l'échelle sismique.* Thèse de doctorat, Université Henri Poincaré Nancy I. (Cit page 19.)

[Sheriff, 1975] Sheriff, R. (1975). Factors affecting the amplitudes. *Geophysical Prospecting*, 23:125–138. (Cit page 15.)

[Sheriff, 1977] Sheriff, R. (1977). Limitations on resolution of seismic reflections and geological detail derivable from them. *AAPG Memoir*, 26:3–14. (Cit page 7.)

[Sheriff, 1997] Sheriff, R. (1997). Seismic resolution : a key element. *Geophysical Corner.* (Cit page 7.)

[Strobbia *et al.*, 2009] Strobbia, C., Glushchenko, A., Laake, A., Vermeer, P., Papworth, S. et Ji, Y. (2009). Arctic near surface challenges : the point receiver solution to coherent noise and statics. *First Break*, 27:69–76. (Cit page 31.)

[Touzé *et al.*, 2010] Touzé, G. L., Cristini, P., Favretto-Cristini, N. et Blanco, J. (2010). Wavefield extraction using multi-channel chirplet decomposition. *Journal of the Acoustical Society of America*, 127(4):EL140–EL145. (Cit page 37.)

[Tygel et Ursin, 1999] Tygel, M. et Ursin, B. (1999). Weak-contrast edge and vertex diffractions in anisotropic elastic media. *Wave Motion*, 29:363–373. (Cit page 53.)

[Ursin, 2004] Ursin, B. (2004). Tutorial : Parameter inversion and angle migration in anisotropic elastic media. *Geophysics*, 69:1125–1142. (Cit page 53.)

[Ursin et Tygel, 1997] Ursin, B. et Tygel, M. (1997). Reciprocal volume and surface scattering integrals for anisotropic elastic media. *Wave Motion*, 26:31–42. (Cit page 53.)

[Welford et Rongfeng, 2004] Welford, J. et Rongfeng, Z. (2004). Ground-roll suppression from deep crustal seismic reflection data using a wavelet-based approach : a case study from western Canada. *Geophysics*, 69(3):877–884. (Cit page 27.)

[Widess, 1973] Widess, M. (1973). How thin is a bed ? *Geophysics*, 38(6):1176–1180. (Cit page 7.)